DISSERTATION

TRIFLUOROMETHYLATED FULLERENES AND POLYCYCLIC AROMATIC HYDROCARBONS AND ANAEROBICALLY MILLED SILICON NANOPARTICLES

Submitted by

Karlee P. Castro

Department of Chemistry

In partial fulfillment of the requirements

For the Degree of Doctor of Philosophy

Colorado State University

Fort Collins, Colorado

Fall 2015

Doctoral Committee:

Advisor: Steven. H. Strauss

Melissa M. Reynolds
Delphine K. Farmer
Martin J. McCullagh
Howard S. Ramsdell

ABSTRACT

TRIFLUOROMETHYLATED FULLERENES AND POLYCYCLIC AROMATIC HYDROCARBONS AND ANAEROBICALLY MILLED SILICON NANOPARTICLES

Well characterized molecules and materials are essential to understand trends and predict future performance. Fundamental studies provide information about molecular properties which may be useful in other applications such as electronic devices. The focus of this dissertation is the characterization of three different classes of molecules/materials with the goal of understanding the fundamental underlying reasons for any trends observed.

The first chapter of this dissertation examines the photophysical properties of $C_{70}(CF_3)_n$ (n = 8 or 10) molecules. Four of the compounds exhibited quantum yields higher than for any previously reported C_{70} derivative and three exceeded 0.24, the highest fluorescence quantum yield for any fullerene or fullerene derivative. A difference in the location of only one CF_3 group in $C_{70}(CF_3)_8$ and $C_{70}(CF_3)_{10}$ isomers resulted in 200-fold and 14-fold increases in fluorescence quantum yields respectively. The isomer of $C_{70}(CF_3)_{10}$ with the highest fluorescence quantum yield (0.68 in toluene) also exhibited the longest fluorescence lifetime (51 ns). Formation of the S_1 state in one of the $C_{70}(CF_3)_{10}$ isomers occurred within 0.6 ps and its nanosecond-long decay was monitored by ultrafast transient absorption spectroscopy. Time-dependent density functional theory calculations provide a physically meaningful understanding of the photophysical properties. High fluorescence quantum yields are correlated with high oscillator strengths for the $S_0 \rightarrow S_1$ transition, large Δ_{S1-T1} energy gaps, and small spatial extension of the $S_0 \rightarrow S_1$ excitation.

The second chapter of this dissertation explores trifluoromethyl derivatives of polycyclic aromatic hydrocarbons ($PAH(CF_3)_n$). First, the effects of PAH size and shape on the product distribution are examined. Second, the electronic properties, including reduction potential and

gas-phase electron affinity, are examined. Third, the influence of number and orientation of the CF_3 groups on the crystalline morphologies of these compounds is explored. Finally, charge-transfer complexes made with $PAH(CF_3)_n$ molecules mixed with PAHs are prepared and examined spectroscopically and crystallographically. From this work it was determined that when PAHs with 8–10 substitutable carbons are reacted with at least 10 equivalents of CF_3I gas the $PAH(CF_3)_n$ products had *n* values of 4–6 regardless of the size or shape of the PAH core. The reduction potential and gas-phase electron affinity exhibit a regular, incremental increase as a function of the number of trifluoromethyl groups. The number and position of CF_3 groups influences the π-π stacking and crystalline morphologies and typically the more CF_3 groups added, the lower the intermolecular overlap. Charge-transfer complexes made from mixing $PAH(CF_3)_n$ and PAH form mixed stacks in the solid-state and exhibit weak association constants in solution.

The third chapter of this dissertation examines the effects of oxygen and aromatic molecules on stirred media milling of silicon. Metallurgical-grade silicon was wet-milled in a stirred media mill to produce nanoparticles. Several milling fluids, additives, and milling parameters have been tested and compared between aerobic and anaerobic milling. It was determined that oxygen and aromatic molecules serve as surface passivating additives and lead to higher specific surface areas, indicating smaller particles. Particle amorphization occurs rapidly in a stirred media mill, within two hours crystallite size is on the order of 2-50 nm regardless of whether surface passivating additives are present. In all milling experiments, even in the presence of oxygen, new Si–C bonds are formed, the most Si–C bonds are formed when aromatic molecules are present during the milling process.

ACKNOWLEDGMENTS

First and foremost I would like to thank my husband, Rick. You supported me from the time I declared I wanted to quit my job and go to graduate school and you've kept supporting me through all the ups and downs of the process. Thank you for being my design consultant. I truly appreciate all the hard work you have put in to put me through school twice now. You are the best and have done so much for me I can't list it all.

The past and present members of the Strauss-Boltalina research group have enriched my graduate school experience. Eric V. Bukovsky has been an excellent collaborator on multiple projects, diagnosed my shingles, got most of my Simpsons references, and didn't get too upset when I rained on his parades. Long K. San always answered my random question text messages, sent out morale boosting funny e-mails, and tried to make the lab a cleaner place. Tyler T. Clikeman always has (or at least pretends to have) an excellent attitude and he's always willing to help. Thanks to all three of you for showing me how graduate school is done. Brent M. Wyatt brought me coupon books and root beer and was there with me on the longest day of graduate school. No less important are those who helped me get through the first couple of years: Amanda M. Pluntze, Dr. Bryon W. Larson, and Dr. Igor V. Kuvychko. Thanks for the advice, the fun, and the camaraderie. Thank you to the unofficial Strauss-Boltalina group member Desirée Bukovsky for giving me a home away from home.

My sincere appreciation goes to my advisors Prof. Steven H. Strauss and Dr. Olga V. Boltalina. You believe in me more than I believe in myself. Olga has been indispensible with reading drafts, ideas for experiments, general support, and so much more. Steve pushes for the best, finds new angles in my research that I have overlooked, and has boundless enthusiasm for science. Thank you for the baked goods and pizza at group meetings and group trips to Breckenridge. I appreciate that you accepted my commuting and were understanding of the resulting odd schedules.

Excellent collaborators have made my work possible. Dr. Jeffrey J. Rack and Dr. Yuhuan Jin were excellent hosts in Ohio an instrumental in making time-resolved spectroscopic measurements. Dr. Alexey A. Popov provided theoretical calculations and spearheaded the writing of the fullerene fluorophores paper. Dr. Xue-Bin Wang and co-workers measured gas-phase electron affinities. Dr. Yu-Sheng Chen hosted the Synchrotron Charge Density School and assisted a number of my colleagues with synchrotron X-ray crystallography. Dr. Andrew J. Ferguson and Dr. Jeffrey L. Blackburn taught me how to use the instrument I used to collect singlet oxygen quantum yields and were very accommodating every time I wanted to come back and do more measurements. Dr. Stephen A. Rolfe and Dr. Andrew J. Fleming presented the idea of using fluorescent fullerenes as leaf imaging agents and their co-workers completed the proof of concept testing.

My family provides much needed love and support. I don't think I can ever adequately express my gratitude to or repay my mom for all she has done for me. Thank you to my dad for being interested in my work, helping try out ideas for science projects for elementary school students, and the AAA membership which provided peace of mind for my commutes. Thank you to my cousin, Amanda Faux, for packing up her kids and driving me to Fort Collins to see the eye doctor. Thank you to the rest of my family and Rick's family for all the ways you have helped me through the years.

I want to acknowledge my friends who have supported me for years. To all the other raging balls of angry smart kids thanks for starting my cult and continuing to support me. Thanks in particular to Heather Gannon for editing this dissertation, any mistakes are mine and were made after her deft editing. My dear friend Sara Allen has leant her ear and her pen and has inspired me. Joyce Miyagishima, thank you for being a great aisle-mate and friend (FPS). Erin Stuckert and Morgan Hawker threw me a birthday party when I really needed it, always attended my practice talks, discussed science with me, and shared my enjoyment of game nights.

My committee members have been excellent teachers. Thank you for both scientific discussions and practical graduate school advice. Thank you to all of the support staff in the CSU

Department of Chemistry. You all do a million things and I'm sure I don't even know half of what you do. Korina Brim and Karen Kahler were especially helpful at the end of a trying project and Korina provided some much needed laughs. I appreciate Dr. Johnna Bontadelli in the CSU Health Network for helping save my sight when I had shingles.

I would like to acknowledge my undergraduate professors who got me interested in chemistry. Dr. Eric Ball was the best instructor I ever had and helped cement my interest in analytical and inorganic chemistry. Thanks to Dr. Niels Schonbeck for making me think, exposing me to new ideas, and encouraging my continued education. Dr. Susan Schelble helped me to become the first student at Metro to complete an honors thesis in chemistry and encouraged me to attend graduate school.

Thank you to the artists who helped me get through graduate school without even knowing it. These include Cold Cave, Depeche Mode, Nitzer Ebb, Joy Division, the team behind Orphan Black, the team behind The Simpsons, Wolf Pupy, Neil Gaiman, William Gibson, and others I'm sure I forgot.

Finally, I would like to once again thank my husband, Rick. Just one thank you would not be enough. I appreciate you. It has not been a particularly easy 4 years, but we've made it. Thank you from the bottom of my heart.

TABLE OF CONTENTS

ABSTRACT ii

ACKNOWLEDGMENTS iv

TABLE OF CONTENTS vii

LIST OF TABLES xi

LIST OF FIGURES xii

LIST OF COMMONLY USED ABBREVIATIONS AND SYMBOLS xiv

INTRODUCTION 1

BACKGROUND AND MOTIVATION 1

INTRODUCTION REFERENCES 3

CHAPTER 1: PHOTOPHYSICAL PROPERTIES OF TRIFLUOROMETHYLFULLERENES 4

1.1. INTRODUCTION 4

1.2. RESULTS AND DISCUSSION 7

1.2.1. STEADY-STATE SPECTROSCOPY 7

1.2.2. TIME-RESOLVED SPECTROSCOPY 12

1.2.3. COMPUTATIONAL STUDIES 14

1.2.4. LEAF AIR-SPACE IMAGING 18

1.2.5. SINGLET OXYGEN YIELDS 19

1.3. SUMMARY AND CONCLUSIONS 20

1.4. EXPERIMENTAL DETAILS 21

1.4.1. REAGENTS AND SOLVENTS 21

1.4.2. PREPARATION OF TMFs 22

1.4.3. SEPARATION, PURITY CHARACTERIZATION, AND ISOMER IDENTIFICATION 22

1.4.4. FLUORESCENCE SPECTROSCOPY 24
1.4.5. FLUORESCENCE LIFETIMES 26
1.4.6. ULTRAFAST TRANSIENT ABSORPTION 26
1.4.7. THEORETICAL CALCULATIONS 26
1.4.8. LEAF IMAGING EXPERIMENTS 27
1.4.9. SINGLET OXYGEN QUANTUM YIELDS 27
CHAPTER 1 REFERENCES 28
CHAPTER 2: TRIFLUOROMETHYL POLYCYCLIC AROMATIC HYDROCARBONS AND CHARGE-TRANSFER COMPLEXES 32
2.1. INTRODUCTION 32
2.2. RESULTS AND DISCUSSION 35
2.2.1. PRODUCT COMPOSITION, SEPARATION, AND IDENTIFICATION 35
2.2.2. ELECTROCHEMISTRY AND ELECTRON AFFINITY 58
2.2.3. CRYSTAL STRUCTURE ANALYSIS 64
2.2.4. REACTIONS OF PHNZ$(CF_3)_n$ WITH TRIETHYLALUMINUM 68
2.2.5. CHARGE-TRANSFER COMPLEX CHARACTERIZATION 69
2.3. SUMMARY AND CONCLUSIONS 88
2.4. EXPERIMENTAL DETAILS 89
2.4.1. REAGENTS AND SOLVENTS 89
2.4.2. REACTIONS OF PAH WITH CF_3I 89
2.4.3. SEPARATION OF PAH$(CF_3)_n$ COMPOUNDS 89
2.4.4. CHARACTERIZATION OF NEWLY IDENTIFIED COMPOUNDS 90
2.4.5. X-RAY CRYSTALLOGRAPHY OF PAH$(CF_3)_n$ COMPOUNDS 91
2.4.6. REACTION OF PHNZ$(CF_3)_n$ WITH TRIETHYLALUMINUM 92
2.4.7. CHARACTERIZATION OF CHARGE-TRANSFER COMPLEXES 93
2.4.8. GAS-PHASE ELECTRON AFFINITY 94
CHAPTER 2 REFERENCES 95

CHAPTER 3: STRICTLY ANAEROBIC STIRRED MEDIA MILLING: THE EFFECT OF OXYGEN ON MILLING DYNAMICS, CRYSTALLITE SIZE, AND SURFACE COMPOSITION OF SILICON NANOPARTICLES 101
3.1. INTRODUCTION 101
3.2. RESULTS 107
3.2.1. GENERAL 107
3.2.2. ANAEROBIC POWDER XRD 111
3.2.3. ANAEROBIC MILLING IN HEPTANE 113
3.2.4. ANAEROBIC MILLING IN MESITYLENE WITH PYRENE ADDITIVE 120
3.2.5. AEROBIC MILLING IN HEPTANE 123
3.2.6. AEROBIC MILLING IN MESITYLENE WITH PYRENE ADDITIVE 124
3.2.7. DLS PARTICLE SIZE ANALYSIS OF SAMPLES 124
3.3. DISCUSSION 125
3.3.1. GENERAL 125
3.3.2. ANAEROBIC VS AEROBIC WITHOUT SURFACE PASSIVATING ADDITIVES 126
3.3.3. ANAEROBIC MILLING WITHOUT SURFACE PASSIVATING ADDITIVES VS ANAEROBIC MILLING WITH SURFACE PASSIVATING ADDITIVIES 129
3.3.4. MILLING TIME FOR ANAEROBIC MILLING WITHOUT SURFACE PASSIVATING ADDITIVES VS ANAEROBIC WITH SURFACE PASSIVATING ADDITIVES 129
3.3.5. ANAEROBIC MILLING WITH SURFACE PASSIVATING ADDITIVES VS AEROBIC MILLING WITH SURFACE PASSIVATING ADDITIVES 131
3.3.6. COMPARING DLS RESULTS WITH BET SURFACE AREAS 132
3.4. CONCLUSIONS 134
3.5. EXPERIMENTAL DETAILS 135

3.5.1. GENERAL 135
3.5.2. ANAEROBIC MILLING IN HEPTANE 136
3.5.3. ANAEROBIC MILLING IN MESITYLENE WITH PYRENE ADDITIVE 137
3.5.4. AEROBIC MILLING IN HEPTANE 137
3.5.5. AEROBIC MILLING IN MESITYLENE WITH PYRENE ADDITIVE 138
3.5.6. BET 138
3.5.7. H_2O AND O_2 GAS UPTAKE EXPERIMENTS 139
3.5.8. POWDER XRD 139
3.5.9. AIR-FREE POWDER XRD 140
3.5.10. TEM 140
3.5.11. SEM 141
3.5.12. XPS 141
3.5.13. DLS 143
CHAPTER 3 REFERENCES 144
SUMMARY/CONCLUSIONS AND FUTURE CONSIDERATIONS 148
SUMMARY/CONCLUSIONS 148
FUTURE CONSIDERATIONS 149

LIST OF TABLES

TABLE 1.1. PRINCIPAL SPECTROSCOPIC PARAMETERS OF TMFs 10
TABLE 1.2. EXPERIMENTAL AND CALCULATED ENERGIES AND OSCILLATOR STRENGTS OF TMFs 15
TABLE 1.3. TD-DFT VERTICAL EXCITATION ENERGIES AND OSCILLATOR STRENGTHS 18
TABLE 2.1. REACTION CONDITIONS FOR PAH + CF_3I REACTIONS 36
TABLE 2.2. NMR SHIFTS OF ALL PAH$(CF_3)_n$ COMPOUNDS 56
TABLE 2.3. REDUCTION POTENTIALS AND GAS-PHASE ELECTRON AFFINITIES 59
TABLE 2.4. ELECTRON AFFINITY, IONIZATION POTENTIAL, AND SPECTROSCOPIC DATA FOR CTCs 71
TABLE 2.5. X-RAY STRUCTURE PARAMETERS FOR CTCs 78
TABLE 3.1. LITERATURE REPORTED XPS SHIFTS 107
TABLE 3.2. SUMMARY OF MILLING EXPERIMENTAL DETAILS 110
TABLE 3.3. ELEMENTAL COMPOSITION OF MILLED SILICON SAMPLES 117
TABLE 3.4. PARTICLE SIZES FROM BET ESTIMATES AND DLS 129

LIST OF FIGURES

FIGURE 1.1. STRUCTURE OF I_h-C_{60} AND D_{5h}-C_{70} 4
FIGURE 1.2. SCHLEGEL DIAGRAMS OF TMFs STUDIED 7
FIGURE 1.3. ABSORPTION AND FLUORESCENCE SPECTRA OF TMFs 8
FIGURE 1.4. ABSORPTION SPECTRA OF TMFs REPORTED IN 2008 9
FIGURE 1.5. ^{19}F NMR SPECTRA OF TMFs 9
FIGURE 1.6. TRANSIENT ABSORPTION SPECTRA OF **70-10-2** 13
FIGURE 1.7. TD-DFT COMPUTED DIFFERENCE ELECTRON DENSITIES 17
FIGURE 1.8. LEAF AIR-SPACE IMAGES 19
FIGURE 1.9. BUCKYPREP STATIONARY PHASE 23
FIGURE 1.10. JABLONSKI DIAGRAM 25
FIGURE 2.1. PAH CORES 35
FIGURE 2.2. HPLC CHROMATOGRAM OF ANTH$(CF_3)_n$ SEPARATION 37
FIGURE 2.3. HPLC CHROMATOGRAM OF ANTH-4-1 AND ANTH-5-1 SEPARATION 37
FIGURE 2.4. HPLC CHROMATOGRAM OF ANTH-6-2 ISOLATION 38
FIGURE 2.5. HPLC CHROMATOGRAMS OF FLUR-5-1 SEPARATION 39
FIGURE 2.6. HPLC CHROMATOGRAM OF FLRA$(CF_3)_n$ SEPARATION 40
FIGURE 2.7. HPLC CHROMATOGRAM OF FLRA-3-1 AND FLRA-3-2 SEPARATION 41
FIGURE 2.8. HPLC CHROMATOGRAM OF PHEN$(CF_3)_n$ SEPARATION 42
FIGURE 2.9. HPLC CHROMATOGRAMS OF PHEN-4-1 AND PHEN-4-2 SEPARATIONS 43
FIGURE 2.10. HPLC CHROMATOGRAM OF SEPARATION OF SMALL-SCALE PHNZ$(CF_3)_n$ REACTION 44
FIGURE 2.11. HPLC CHROMATOGRAMS OF STAGE 2 AND STAGE 3 SEPARATION OF SMALL-SCALE PHNZ$(CF_3)_n$ REACTION 44
FIGURE 2.12. HPLC CHROMATOGRAMS OF SEPARATION OF PHNZ-3-1 45
FIGURE 2.13. HPLC CHROMATOGRAM OF SEPARATION OF LARGE-SCALE PHNZ$(CF_3)_n$ REACTION 46
FIGURE 2.14. HPLC CHROMATOGRAM OF PHNZ-6-1 AND PHNZ-6-2 SEPARATION 47
FIGURE 2.15. STRUCTURES OF PHNZ-6-1 AND PHNZ-6-2 47
FIGURE 2.16. HPLC CHROMATOGRAM OF STAGE 2 SEPARATION OF LARGE-SCALE PHNZ$(CF_3)_n$ REACTION 48
FIGURE 2.17. HPLC CHROMATOGRAM OF PYRN$(CF_3)_n$ SEPARATION 49
FIGURE 2.18. HPLC CHROMATOGRAM OF PYRN-6-1 SEPARATION 50
FIGURE 2.19. HPLC CHROMATOGRAMS OF PYRN-6-3 SEPARATION 52
FIGURE 2.20. NMR SPECTRA OF ANTH-6-2 55
FIGURE 2.21. NMR SPECTRA OF PYRN-6-1 55
FIGURE 2.22. PAH$(CF_3)_n$ STRUCTURES PREDICTED FROM NMR SPECTRA 58
FIGURE 2.23. CYCLIC VOLTAMMOGRAMS OF PHNZ$(CF_3)_n$ 60
FIGURE 2.24. PHOTOELECTRON SPECTRA OF ANTH-6-2 AND PHNZ-6 62
FIGURE 2.25. CHANGE IN $E_{1/2}$ AND EA AS A FUNCTION OF THE NUMBER OF CF_3 GROUPS FOR ANTH AND PHNZ 63
FIGURE 2.26. $E_{1/2}$ VS. GAS-PHASE EA FOR PAH AND PAH$(CF_3)_n$ 64

FIGURE 2.27. THERMAL ELLIPSOID PLOT FOR ALL CRYSTALLIZED PAH(CF_3)$_n$ 65
FIGURE 2.28. COMPARISON OF THE X-RAY STRUCTURES OF ANTH-5-1 AND ANTH-6-1 AND PYRN-5-1 AND PYRN-5-2 66
FIGURE 2.29. COMPARISON OF OVERLAP BETWEEN PHNZ-3-1 AND PHNZ-3-2 67
FIGURE 2.30. MOLECULAR PACKING OF PHNZ(CF_3)$_n$ 68
FIGURE 2.31. VISIBLE SPECTRA FOR CHARGE-TRANSFER COMPLEXES 72
FIGURE 2.32. RAW AND CORRECTED VISIBLE SPECTRA OF PERY/ANTH-6-1 COMPLEX AT DIFFERENT CONCENTRATIONS 74
FIGURE 2.33. JOB'S PLOTS FOR CTCs 75
FIGURE 2.34. SCOTT AND SEAL PLOTS FOR ANTH-5-1 AND ANTH-6-1 75
FIGURE 2.35. PSEUDOHEXAGONAL PACKING OF 1/1 D/A CTCs 79
FIGURE 2.36. PSEUDOHEXAGONAL PACKING OF D_2/A AND D/A_2 CTCs 80
FIGURE 2.37. STRUCTURE OF PYRN/(ANTH-6-1)$_2$ 81
FIGURE 2.38. PACKING OF PYRN/(ANTH-6-1)$_2$ 82
FIGURE 2.39. UNIT CELL FOR ANTH/ANTH-6-1 AND PLANARITY OF ANTH-6-1 83
FIGURE 2.40. MAJOR AND MINOR AXES OF ANTH/ANTH-6-1 84
FIGURE 2.41. VIEWS LOOKING DOWN ANTH/ANTH-6-1 STACKS 85
FIGURE 2.42. FLAT PROJECTION OF ANTH/ANTH-6-1 86
FIGURE 2.43. PACKING OF ANTH/ANTH-6-1 AND ANTH/ANTH-6-2 87
FIGURE 3.1. SUFACE POTENTIAL REGIONS FOR A SUSPENDED PARTICLE 104
FIGURE 3.2. SEM IMAGES A-H/M-5.5h 108
FIGURE 3.3. TEM IMAGES A-H/M-5.5h 109
FIGURE 3.4. POWDER XRD PATTERNS FOR SAMPLES ON SILICON GREASE AND MIXED IN APIEZON GREASE 112
FIGURE 3.5. POWDER XRD PATTERNS OF AA-H-1h 113
FIGURE 3.6. POWDER XRD PATTERNS OF HAND-GROUND MGS AND AA-H-1–5h 114
FIGURE 3.7. TEM IMAGES OF AA-H-1h 115
FIGURE 3.8. TEM IMAGES OF AA-H-5h 116
FIGURE 3.9. XPS OF AA-H-1h, AA-H-3h, AND AA-H-5h 117
FIGURE 3.10. XPS OF AA-H-3h AS MADE AND SPUTTERED 118
FIGURE 3.11. TREATMENT OF AA-H/M-5.5h WITH O_2 119
FIGURE 3.12. POWDER XRD OF HAND-GROUND MGS AND AA-M/P-1–6h 121
FIGURE 3.13. TREATMENT OF AA-M/P-5h WITH O_2 122
FIGURE 3.14. XPS OF A-M/P-5h AND AA-M/P-5h 123
FIGURE 3.15. XPS OF A-H-5h AND AA-H-5h 124
FIGURE 3.16. DLS OF AA-H-1h, AA-H-5h, AA-M/P-1h, AA-M/P-5h, AND A-H-5h 125
FIGURE 3.17. POWDER XRD OF SAMPLES MILLED FOR 5–5.5 h 132
FIGURE 3.18. SCHEMATIC OF NETZSCH MINICER LABORATORY MILL 135

LIST OF COMMONLY USED ABBREVIATIONS AND SYMBOLS

abbrev./symbol	full name
TMF	trifluoromethylfullerene
TD-DFT	time dependent density functional theory
HPLC	high pressure liquid chromatography
NMR	nuclear magnetic resonance spectroscopy
UV-vis	ultraviolet-visible spectroscopy
HOMO	highest occupied molecular orbital
LUMO	lowest unoccupied molecular orbital
ISC	intersystem crossing
Φ_F	fluorescence quantum yield
τ_F	fluorescence lifetime
SB	Strickler-Berg
f	oscillator strength
PAH	polycyclic aromatic hydrocarbon
EA	electron affinity
IE	ionization energy
CTC	charge-transfer complex
CT	charge-transfer
ANTH	anthracene
AZUL	azulene
CORO	coronene
FLUR	fluorene
FLRA	fluoranthene
PERY	perylene
PHEN	phenanthrene
PHNZ	phenazine
PYRN	pyrene
CV	cyclic voltammetry or cyclic voltammogram
DCE	1,2-dichloroethane
D	donor
A	acceptor
LSP	least-squares plane
K_{CT}	association constant for CT complex
$\odot$	centroid
XPS	X-ray photoelectron spectroscopy
MGS	metallurgical grade silicon
XRD	X-ray diffraction
TEM	transmission electron microscopy
SEM	scanning electron microscopy
DLS	dynamic light scattering

INTRODUCTION

Background and Motivation

Well-characterized molecules and materials are essential to understand structure-property relationships predict future performance of new molecules or materials. This work endeavors to characterize three different classes of molecules/materials to better understand their properties and elucidate the underlying chemical reasons for those properties. Each class of molecules/materials have been investigated using different methods and is targeted for different applications spanning from energy storage and conversion or optoelectronics to biological imaging and theranostics.

The first class of molecules investigated herein is trifluoromethylfullerenes (TMFs). TMFs are one of the most well-studied classes of fullerene derivatives and many dozens of isomerically pure TMFs with a wide variety of addition patterns have been produced which have provided insight into a number of properties that arise as a result of the addition pattern.[1] Fullerenes and fullerene derivatives typically exhibit low fluorescence quantum yields due to the efficiency of transfer to the triplet state, except for a few examples. Nakamura and co-workers have discovered a number of fluorescent fullerene derivatives[2-5] and, based on the derivatives studied, they hypothesized that the shape of the remaining pi system was the determining factor for fluorescence quantum yields. In this work, a family of highly fluorescent fullerene derivatives comprised of structurally similar $C_{70}(CF_3)_n$ (n = 8 or 10) compounds has been discovered and the reasons for differences in the fluorescence quantum yields have been examined based on the results of experimental spectroscopy and theoretical study. The photophysical properties of TMFs may make them attractive for use in electroluminescence, photodynamic therapy, or imaging the air-spaces in leaves.

The second class of molecules studied is trifluoromethyl derivatives of polycyclic aromatic hydrocarbons (PAHs). The introduction of electron-withdrawing groups onto the PAH

core is known to tune the properties, particularly the electrochemical properties, of the PAH derivative.[6-8] Since selective organic functionalization of a PAH core typically involves multi-step synthesis procedure, previous studies of PAHs substituted with electron-withdrawing groups have typically focused on characterizing either a single compound or a small number of molecules per study, which made elucidation of more general trends and relationships difficult to achieve.[8,9] The goal of this work is to build selected libraries of new PAH$(CF_3)_n$ compounds to find trends in PAH size or shape, number of CF_3 substitutions, or substitution pattern, and, in particular, the effect of these differences on the electrochemical properties. The enhanced electron acceptor properties of PAH$(CF_3)_n$ compounds may make them attractive for use in field effect transistors , organic photovoltaics, or other optoelectronic devices.

The third and final class of materials studied is silicon nanoparticles produced by wet stirred media milling. Peukert and co-workers have extensively investigated the effects of changing milling parameters such as milling time, amount of milling media, agitator tip velocity, and temperature and they have also looked into a selection of fluids or additives to stabilize the milled particles.[10-15] Despite this interest in stirred media mills there has been a distinct lack of research into the effects oxygen plays in the milling process. The goal of this work is to wet mill silicon and compare the effects of milling solvent with and without presence of oxygen during the milling process. Silicon nanoparticles are being researched for use in lithium-ion batteries, optoelectronic devices, and fluorescent biomarkers.

The methods used to characterize the materials investigated in this dissertation depend on the properties being evaluated and included fluorescence spectroscopy, density functional theory calculations, high performance liquid chromatography, cyclic voltammetry, NMR spectroscopy, mass spectrometry, photoelectron spectroscopy to measure gas-phase electron affinity, single crystal X-ray diffraction, powder X-ray diffraction, Brunauer, Emmet, and Teller surface area analysis, and X-ray photoelectron spectroscopy.

INTRODUCTION REFERENCES

(1) Boltalina, O. V.; Popov, A. A.; Kuvychko, I. V.; Shustova, N. B.; Strauss, S. H.: Perfluoroalkylfullerenes. *Chem. Rev.* **2015**, *115*, 1051-1105.

(2) Fujita, T.; Matsuo, Y.; Nakamura, E.: Synthesis of Tetradeca- and Pentadeca(organo) 60 fullerenes Containing Unique Photo- and Electroluminescent pi-Conjugated Systems. *Chem. Mater.* **2012**, *24*, 3972-3980.

(3) Matsuo, Y.; Sato, Y.; Hashiguchi, M.; Matsuo, K.; Nakamura, E.: Synthesis, Electrochemical and Photophysical Properties, and Electroluminescent Performance of the Octa- and Deca(aryl) 60 fullerene Derivatives. *Adv. Funct. Mater.* **2009**, *19*, 2224-2229.

(4) Li, C. Z.; Matsuo, Y.; Nakamura, E.: Luminescent Bow-Tie-Shaped Decaaryl 60 fullerene Mesogens. *J. Am. Chem. Soc.* **2009**, *131*, 17058-+.

(5) Matsuo, Y.; Tahara, K.; Morita, K.; Matsuo, K.; Nakamura, E.: Regioselective eightfold and tenfold additions of a pyridine-modiried organocopper reagent to 60 fullerene. *Angew. Chem., Int. Ed.* **2007**, *46*, 2844-2847.

(6) Jones, B. A.; Ahrens, M. J.; Yoon, M. H.; Facchetti, A.; Marks, T. J.; Wasielewski, M. R.: High-mobility air-stable n-type semiconductors with processing versatility: Dicyanoperylene-3,4 : 9,10-bis(dicarboximides). *Angew. Chem., Int. Ed.* **2004**, *43*, 6363-6366.

(7) Jones, B. A.; Facchetti, A.; Wasielewski, M. R.; Marks, T. J.: Tuning orbital energetics in arylene diimide semiconductors. Materials design for ambient stability of n-type charge transport. *J. Am. Chem. Soc.* **2007**, *129*, 15259-15278.

(8) Anthony, J. E.: Functionalized acenes and heteroacenes for organic electronics. *Chem. Rev.* **2006**, *106*, 5028-5048.

(9) Sun, H. R.; Putta, A.; Kloster, J. P.; Tottempudi, U. K.: Unexpected photostability improvement of aromatics in polyfluorinated solvents. *Chem. Commun.* **2012**, *48*, 12085-12087.

(10) Stenger, F.; Mende, S.; Schwedes, J.; Peukert, W.: Nanomilling in stirred media mills. *Chem. Eng. Sci.* **2005**, *60*, 4557-4565.

(11) Mende, S.; Stenger, F.; Peukert, W.; Schwedes, J.: Mechanical production and stabilization of submicron particles in stirred media mills. *Powder Technol.* **2003**, *132*, 64-73.

(12) Peukert, W.; Schwarzer, H.-C.; Stenger, F.: Control of aggregation in production and handling of nanoparticles. *Chem. Eng. Processing: Process Intensification* **2005**, *44*, 245-252.

(13) Sommer, M.; Stenger, F.; Peukert, W.; Wagner, N. J.: Agglomeration and breakage of nanoparticles in stirred media mills—a comparison of different methods and models. *Chem. Eng. Sci.* **2006**, *61*, 135-148.

(14) Knieke, C.; Sommer, M.; Peukert, W.: Identifying the apparent and true grinding limit. *Powder Technol.* **2009**, *195*, 25-30.

(15) Knieke, C.; Romeis, S.; Peukert, W.: Influence of process parameters on breakage kinetics and grinding limit at the nanoscale. *AIChE J.* **2011**, *57*, 1751-1758.

CHAPTER 1. PHOTOPHYSICAL PROPERTIES OF TRIFLUOROMETHYLFULLERENES

1.1. Introduction

Fullerenes, closed cage molecules composed exclusively of carbon atoms, were first reported in 1985.[1] The two fullerenes obtained in the highest abundance are I_h-C_{60} and D_{5h}-C_{70} shown in Figure 1.1. These fullerene structures obey the "isolated pentagon rule" which predicts higher stability for fullerene structures in which the pentagons are isolated from one another by hexagons.[2,3] Both C_{60} and C_{70} have 12 pentagons, but have different numbers of hexagons which leads to the different shapes of these two fullerenes. The flatter equatorial region of C_{70} is a result of the addition of 10 extra carbon atoms while still only having 12 pentagons and obeying the isolated pentagon rule.

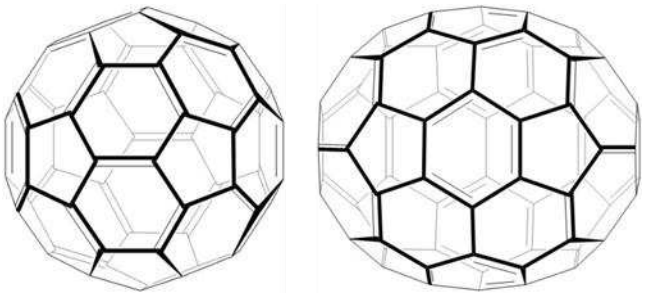

Figure 1.1. Structure of I_h-C_{60} (left) and D_{5h}-C_{70} (right).

Initially, fullerenes were produced by laser vaporization of graphite which resulted in very small quantities. Subsequently new methods of synthesis, such as arc discharge of graphite, were discovered that led to much higher amounts, sufficient for research into the chemistry of these new molecules. Although all of the carbon atoms are included in the pi electron system, fullerenes behave more like electron deficient olefins than as aromatic molecules. Since their discovery fullerenes have been derivatized in many different ways.[4] One of the most well studied classes of fullerene derivatives are trifluoromethylfullerenes (TMFs).[5]

The photophysical properties of fullerenes have been exploited for use in photovoltaics, photodynamic therapy, and electroluminescence.[6-8] Despite the potential usefulness of fullerenes in these applications, still mostly confined to research studies, they typically show poor performance in fluorescence. Both C_{60} and C_{70} show high rates of intersystem crossing and therefore low fluorescence quantum yields, Φ_F.[9-11] Derivatization of the fullerenes reduces the symmetry and changes the π system. Thus, absorptions of the derivatives are usually optically allowed and hence higher radiative rate constants, k_f, can be reached. However, the relatively small perturbation of the fullerene π-system at the early stages of functionalization results in relatively low $S_0 \rightarrow S_1$ absorption intensities and, hence, relatively low fluorescence rate. Intersystem crossing (ISC) also remains efficient, thus preserving rather low Φ_F values in fullerene derivatives (albeit higher than those of bare fullerenes).

More extensive derivatization opens the possibilities for more pronounced changes in the fullerene π-system. Fujita et al. showed that the Φ_F values in multiply phenylated/alkylated C_{60} can be as high as 24% for $C_{60}Ph_{10}(CH_2Ph)_3Me_2H$, much higher than for all fullerene derivatives reported prior to their work.[12] In comparison the highest reported Φ_F for a C_{70} derivative, $C_{70}Ph_{10}$, is 2.5%.[13] Photophysical studies of $C_{70}Ph_n$ showed that ISC remains the primary mechanism of S_1 decay and even for the most highly fluorescent compound ($C_{70}Ph_{10}$), the yield of the triplet state is nearly quantitative.[13]

In conjunction with the low quantum yields the fluorescence lifetime is also low for fullerenes. The fluorescence lifetimes of C_{60} and C_{70} are 0.65 ns and 1.1 ns respectively.[14] The fluorescence lifetime of fullerene derivatives is also generally low, but this too can be altered with derivatization. Matsuo et al. reported lifetimes up to 67 ns for $C_{60}Ph_5(p\text{-}t\text{-butyl-}C_6H_4)_5Me_2$.[8]

Fullerenes and fullerene derivatives that exhibit low fluorescence quantum yields and retain high ISC yields have been investigated for use as photodynamic therapy agents.[7,15,16] Several groups have derivatized the fullerenes to improve their water solubility which makes them more attractive for biological use.[17-21] Red absorption is one of the characteristics of an ideal photosensitizer[22] and can be difficult to achieve with fullerenes or fullerene derivatives. Singlet

oxygen sensitizers that are not suitable for photodynamic therapy can still be used for photocatalysis or photodisinfection.[23-26]

TMFs are one of the most thoroughly characterized classes of fullerene derivatives with a number of useful properties.[5,27-32] i) TMFs are air stable and can be stored, handled, and used under ambient conditions. ii) TMFs are thermally stable, which allows them to be used in high-temperature applications. iii) TMFs can be sublimed without decomposition, so high-quality thin films can be fabricated by vapor-deposition. iv) They are freely soluble in many organic solvents, allowing films to be fabricated by spin-casting or spray methods. iv) Libraries of TMFs with different numbers of CF_3 groups and different isomeric structures for a given number of CF_3 groups can be prepared in a single reaction followed by one- or two-step HPLC separation. v) Electrochemical studies of 18 $C_{60}(CF_3)_n$ and 17 $C_{70}(CF_3)_n$ derivatives with n = 2–12 showed that varying the value of n and, even more importantly, varying the addition pattern for a given value of n, allows for versatile tuning of their electronic properties (e.g., the ranges of first reduction potentials for $C_{60}(CF_3)_n$ and $C_{70}(CF_3)_n$ compounds are 0.73 and 0.45 V, respectively).[27,28]

Fluorescence spectra were reported for a selection of $C_{60}(CF_3)_n$ compounds in 2007.[27] The fluorescence spectrum and quantum yield have been reported for one isomer of $C_{70}(CF_3)_{10}$.[33] The majority of this work, except the leaf air-space imaging and singlet oxygen quantum yields, has already been published.[34] The goal of this work was to examine the photophysical properties of a series of selected $C_{70}(CF_3)_n$ compounds, whose Schelgel diagrams are shown in Figure 1.2. Compounds were selected that had visible fluorescence when excited with a handheld 405 nm laser. Additionally, between isomers there was a difference in the position of only one CF_3 group so the impact of small structural changes on photophysical properties could be examined. The methods used to examine the photophysical properties include: steady-state UV-vis and fluorescence spectroscopy, time-resolved fluorescence spectroscopy, ultrafast transient absorption spectroscopy, time-dependent density functional theory (TD-DFT), and steady-state singlet oxygen emission spectroscopy.

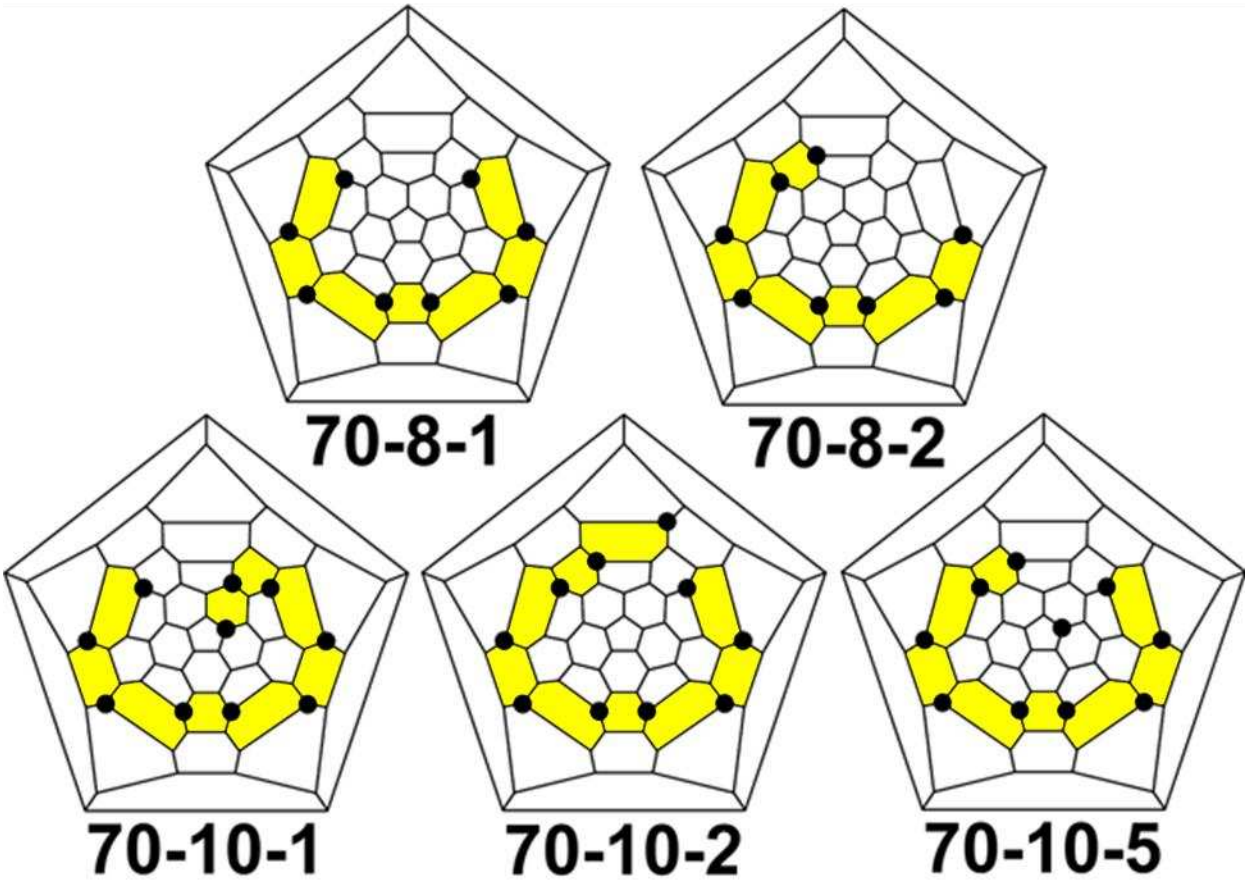

Figure 1.2. Schlegel diagrams of TMFs studied in this work. Black dots indicate the position of trifluoromethyl groups and the shaded spaces indicate ribbons of trifluoromethyl groups.

1.2. Results and Discussion

1.2.1 Steady State Spectroscopy.

The UV-vis spectra of the compounds studied in this work, **70-8-1**, **70-8-2**, **70-10-1**, **70-10-2**, and **70-10-5**, have been previously reported in dichloromethane.[28] For this work the absorption and emission spectra of **70-8-1** and **70-8-2** were collected in cyclohexane. For the isomers **70-10-1**, **70-10-2**, and **70-10-5** the spectra were collected in cyclohexane, hexafluorobenzene, perfluorodecalin, and toluene. Absorption and fluorescence spectra of **70-8-1** and **70-8-2** in cyclohexane and **70-10-1**, **70-10-2**, and **70-10-5** in toluene are shown in Figure 1.3. The spectrum of **70-10-2** presented in 2008[28] showed absorption at wavelengths longer than 550 nm which line up with the absorption of other TMFs (Figure 1.4). To obtain reliable fluorescence

quantum yield measurements, the compounds studied should be pure so extra care was taken in the separation to obtain pure compounds. The isomeric purity was assessed using ^{19}F NMR spectroscopy shown in Figure 1.5 and was determined to be 95 mol% or higher.

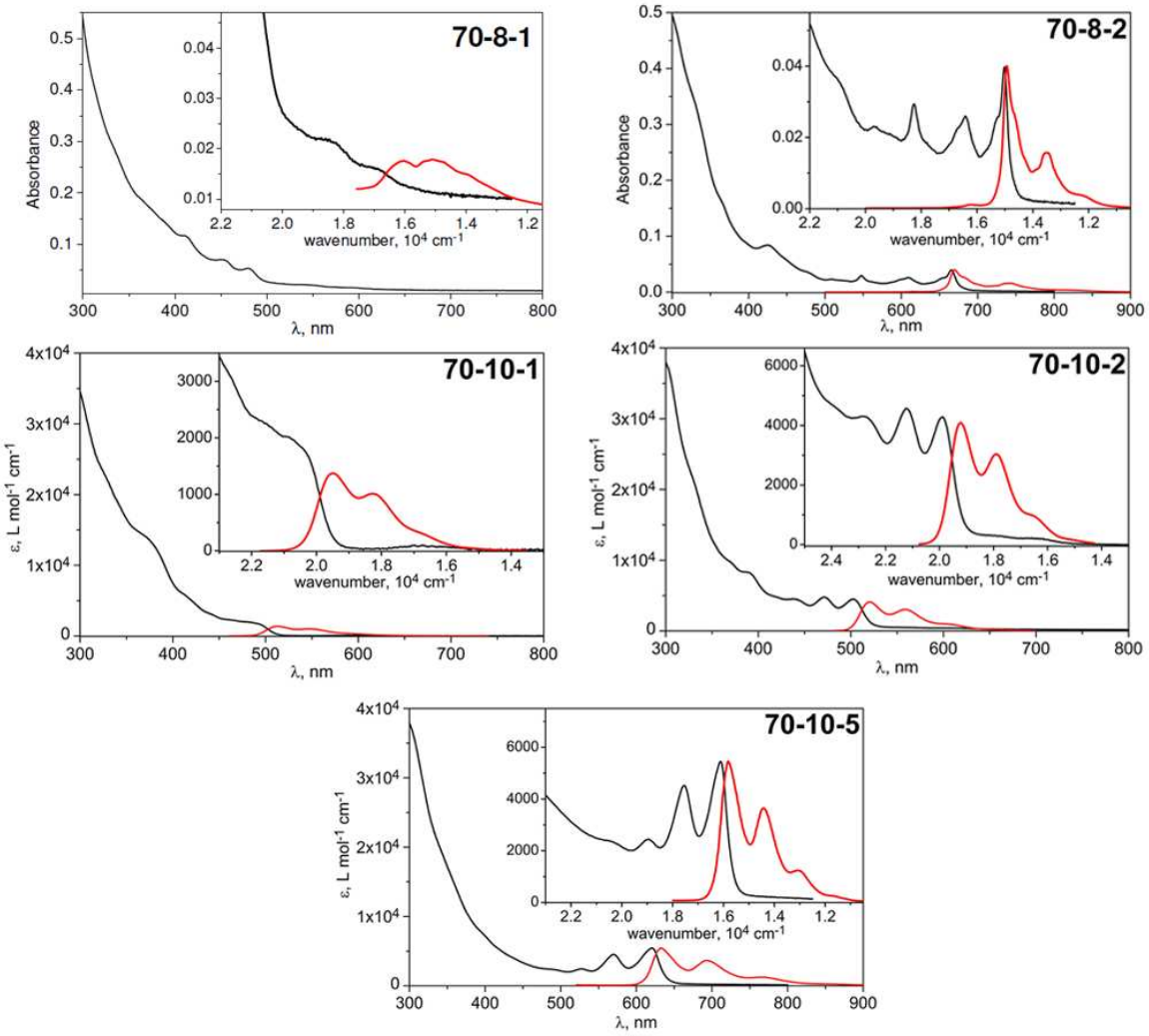

Figure 1.3. Absorption (black) and fluorescence (red) spectra of **70-8-1** (λ_{ex} = 481 nm) **70-8-2** (λ_{ex} = 444 nm), **70-10-1** (λ_{ex} = 449 nm), **70-10-2** (λ_{ex} = 468 nm), and **70-10-5** (λ_{ex} = 570 nm). The insets show vertically-expanded spectra for the lowest energy absorption and fluorescence bands. The wavenumber scale is used in the insets to more readily provide visual evidence of the mirror-image rule.

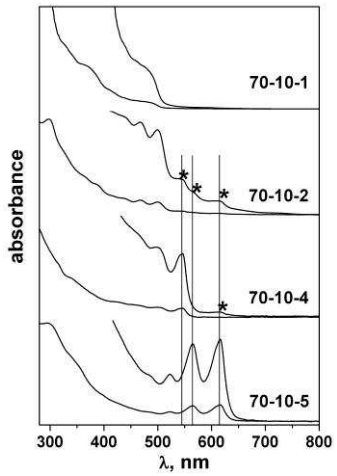

Figure 1.4. Absorption spectra of TMFs reported in 2008[28] plotted to show the likely presence of **70-10-5** and **70-10-4** in the sample of **70-10-2**. The asterisks mark the absorption peaks which are suspected to originate from TMFs other than the main compound present in the sample.

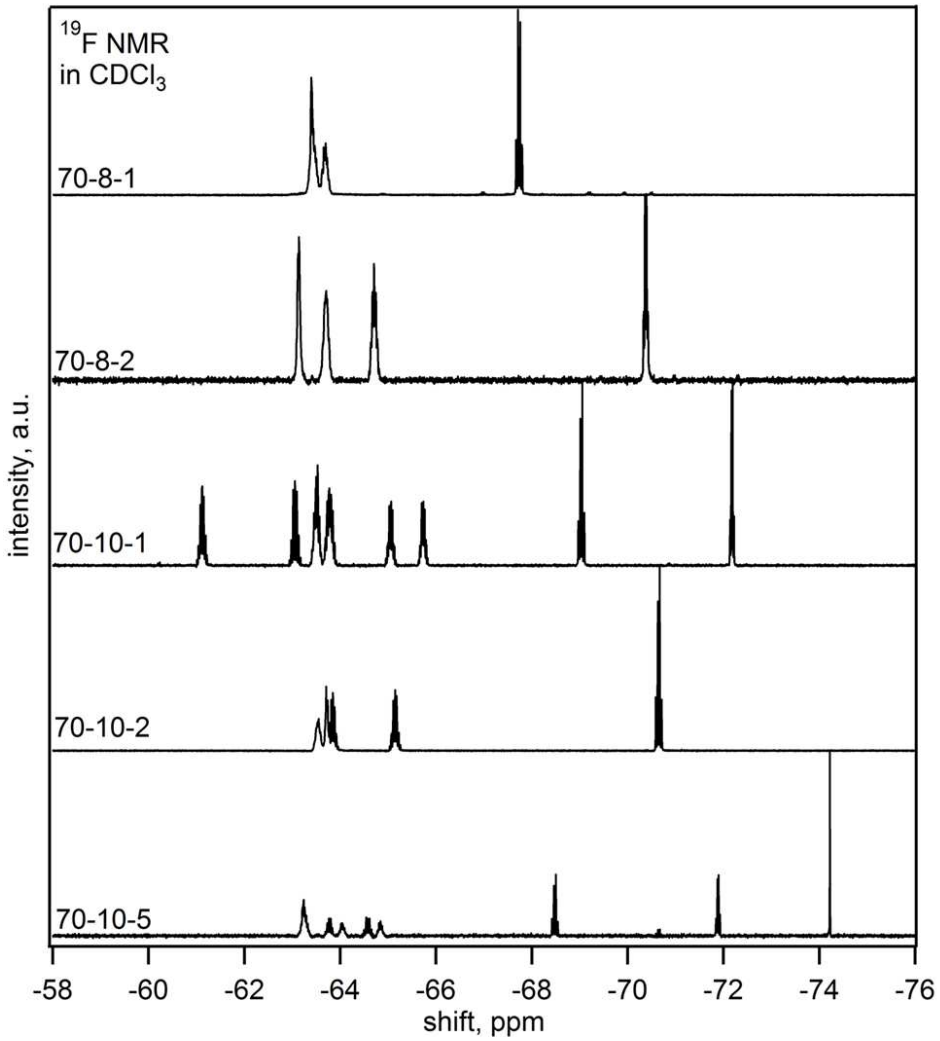

Figure 1.5. Fluorine-19 NMR spectra of TMFs (376 MHz, $CDCl_3$, C_6F_6 int. std. (δ −164.9)).

Table 1.1. Absorption and emission maxima (λ), Stokes shifts (Δ), fluorescence quantum yields (Φ_F), fluorescence lifetimes (τ_F), and fluorescence decay rate constants (k_F) for $C_{70}(CF_3)_8$ and $C_{70}(CF_3)_{10}$ compounds in different solvents.[a]

cmpd	solv	λ_{abs} nm	λ_F nm	Δ[b] cm^{-1}	Φ_F [c]	τ_F ns	$10^6 k_F$ s^{-1}
70-8-1	chx	595	613	495	0.0012(8)	–	–
70-8-2	chx	666	670	90	0.27(3)	–	–
70-10-1	chx	–	506	–	0.041(5)	4.0	10.2
	hfb	–	504	–	0.033(4)	12	2.8
	pfd	–	501	–	0.030(4)	3.5	8.5
	tol	–	513	–	0.047(5)	5.6	8.4
70-10-2	chx	499	514	585	0.24(3)	4.5	53.3
	hfb	497	512	590	0.22(3)	6.6	33.4
	pfd	496	510	550	0.20(2)	2.0	99.5
	tol	503	520	650	0.29(3)	3.2	90.6
70-10-5	chx	616	623	182	0.50(5)	55	9.1
	hfb	613	620	180	0.46(5)	55	8.3
	pfd	612	617	130	0.51(6)	66	7.7
	tol	621	632	280	0.68(7)	51	13.4

[a] Solvents are abbreviated as follows: chx – cyclohexane, hfb – hexafluorobenzene, pfd – perfluorodecalin, tol – toluene; [b] Δ denotes the Stokes shift; [c] Uncertainties in the least significant digit are shown in parentheses; uncertainties are determined from measurements of three independently prepared solutions.

Table 1.1 lists the principal spectroscopic parameters. The spectra show a weak solvent effect and the S_1 energies for toluene were lower than for any other solvent. All of the compounds exhibited fluorescence spectra with well-defined vibronic structure comprising the 0-0 transition and its 2–3 descending equidistant replicas, each at ca 1350 cm^{-1}. These features were well matched by the analogous bands in the lowest-energy part of the absorption spectra, showing that the mirror-image rule is fulfilled and enabling precise determination of the energies of the first

excited singlet states. The Stokes shifts are relatively small and span the range 90–650 cm^{-1}. The largest shifts were found for toluene solutions, and the smallest for cyclohexane solutions. The compound **70-10-1** was the only compound that showed an apparent deviation from the mirror-image rule. Its absorption spectrum has no distinct vibronic structure, presumably due to the overlap with higher-energy excitations, and its Stokes shift could not be determined precisely.

Although all of the $C_{70}(CF_3)_n$ derivatives studied in this work have a common addition-pattern motif (i.e., a belt of 8 CF_3 groups around the C_{70} equator), the Φ_F values vary from 0.0012 to 0.68, demonstrating that small addition-pattern variations can have very large effects. Both **70-8-1** (C_s symmetry) and **70-8-2** (C_2 symmetry) have addition patterns that can be described as a ribbon of seven edge-sharing $C_6(CF_3)_2$ hexagons, and differ by the position of only one CF_3 group. Nevertheless, this change results in the increase of Φ_F from 0.0012 to 0.24, respectively. A similar situation was found for the $C_{70}(CF_3)_{10}$ isomers.

The structure of **70-10-5** is related to the structures of **70-10-1** and **70-10-2** by the position of one CF_3 group (a different one in each case), but these seemingly small structural differences are sufficient to change Φ_F from 0.05 for **70-10-1** to 0.25 for **70-10-2** to 0.68 for **70-10-5**. The latter value is now the highest value reported for any fullerene derivative and is almost 3 times larger than the 0.24 value for previous record holder, $C_{60}Ph_{10}(CH_2Ph)_3(CH_3)_3H$.[12] Furthermore, the addition patterns of **70-10-5** and $C_{70}Ph_{10}$ also differ by the position of only one substituent, but their Φ_F values differ by more than 50 times, 0.68 for **70-10-5** and 0.025 for $C_{70}Ph_{10}$.[13] That this Φ_F disparity is due to the minor addition-pattern difference and not to the electronic or steric properties of the CF_3 and Ph substituents is shown by comparing the Φ_F values in cyclohexane for **70-8-1** (0.0012) and $C_{70}Ph_8$ (0.0013),[13] which have the same addition pattern. It is now apparent that the luminescence efficiencies and the HOMO-LUMO gaps of $C_{70}(CF_3)_n$ derivatives, and not only their reduction potentials,[28] can be conveniently tuned by the proper choice of addition pattern.

1.2.2. Time Resolved Spectroscopy.

Further insight into the photophysical properties of the $C_{70}(CF_3)_{10}$ derivatives was obtained by time-resolved measurements using 355 nm excitation from a pulsed Nd:YAG laser. The fluorescence lifetimes (τ_F) listed in Table 1.1 show that **70-10-5** has the longest lifetimes, up to 66 ns in perfluorodecalin, as well as the highest quantum yields, up to 0.68 in toluene. Its lifetime in toluene is more than 70 times longer than that of C_{70} in toluene (0.7 ns)[35] and is close to the 67 ns lifetime reported by Matsuo et al. for $C_{60}Ph_5(p\text{-}C_6H_4(^tBu)_5Me_2$, which has a cyclophenacene-like π-system and a Φ_F value of 0.185.[8]

The excited state behavior of one of these compounds was also studied by ultrafast transient absorption spectroscopy. To date only **70-10-2** was studied in perfluorodecalin. It was excited at 495 nm, which corresponds to the lowest energy absorption maximum in this solvent. Figure 1.6 shows transient absorption spectra recorded at different pump-probe delays. At delays shorter than 2 ps, the spectra exhibit an almost instantaneous rise throughout the visible region characterized by several absorption features and a shallow bleach (i.e., a negative peak) near 500 nm. The negative peak is ascribed to loss of the ground state, while the absorption bands are ascribed to the $S_1 \rightarrow S_n$ excited state transitions. This evolution was complete within 0.6 ps, and this state persisted for the next 100 ps.

More dramatic changes in the transient absorption spectra occurred at longer pump-probe delays. From 100 to 2990 ps, the spectra reveal an evolution from one electronic state to another with the emergence of four isosbestic points at 516, 537, 576 and 612 nm. The spectrum at 2,990 ps exhibits broad features at long wavelengths and sharp, narrow features from 440 to ca. 490 nm. The broad features are consistent with a triplet excited state. Based on the computational results, described in the next section, the longer-time spectral changes are ascribed to the conversion of the S_1 state to a T_1 state. Kinetic data at multiple wavelengths and a global fitting analysis revealed a lifetime of 1270 ± 150 ps, which is consistent with literature values for other fullerenes and their derivatives.[36-42] This lifetime is shorter by a factor of 2-3 as determined by fluorescence spectroscopy in cyclohexane or toluene solution. This difference in the measured

lifetime is ascribed to unspecified solvent interactions. It was also found that the relaxed S_1 state was formed within 0.6 ps.

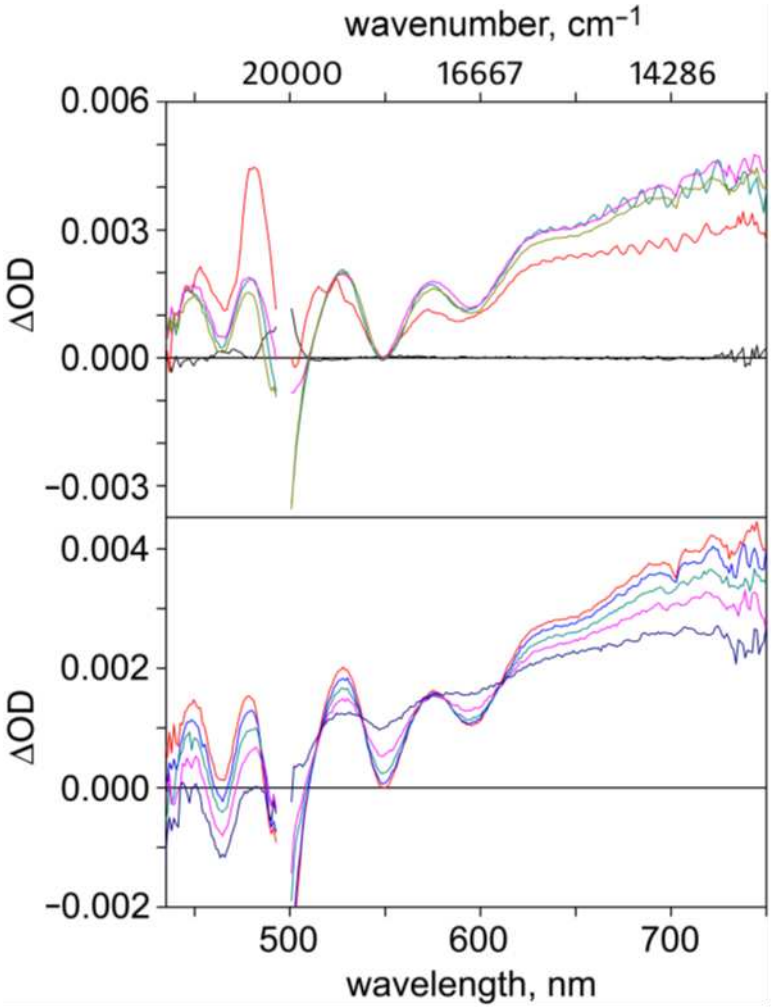

Figure 1.6. Transient absorption spectra of **70-10-2** in perfluorodecalin measured at different pump-probe delays. Top panel: −0.07 ps (black), 0.30 ps (red), 0.520 ps (blue), 1.97 ps (purple), 99.9 ps (green). Bottom panel: 99.9 ps (red), 299 ps (blue), 605 ps (green), 1.200 ns (purple), 2.99 ns (navy).

The transient absorption spectra in Figure 1.6 are also consistent with a number of other studies on fullerenes (no transient absorption spectra for C_{70} derivatives have been reported in the literature to date).[36-38,40,42] Of particular note is that many previous studies show an increase in the absorption of the excited state relative to the ground state. However, few of these studies show the absorption detail that was found in this work. It is not certain yet if these peaks are due

to more allowed transitions associated with the trifluoromethylated C_{70} studied here, or if it is due to differences in the spectral resolution of the instruments employed.

It is noted that the ground state absorption spectrum of **70-10-2**, shown in Figure 1.3, features low energy peaks separated by ca. 1500 cm^{-1}. For comparison, the transient absorption spectrum at a 2 ps delay (ascribed to $S_1 \rightarrow S_n$) exhibits peaks separated by 1351 cm^{-1} (449nm, 498 nm) and 1578 cm^{-1} (520 nm, 576 nm). It is likely that these peaks are due to the vibrational structure of the S_1 state.

1.2.3. Computational Studies.

To understand the reasons for the large variation in Φ_F values measured in this work, and in the future to propose addition patterns for fullerene derivatives with even higher quantum yields, time-dependent TD-DFT calculations at the PBE/TZ2P level were performed. The fluorescence quantum yield is related to the radiative and non-radiative decays of the S_1 state via the equation $\Phi_F = k_F/(k_F + k_{nr})$. To achieve the maximum quantum yield, the fluorescence rate constant k_F should be maximized and the cumulative rate constant of non-radiative processes, k_{nr}, should be minimized.

The Strickler-Berg (SB) rule connects k_F with the absorption intensity:[43,44]

$$k_F = 2900 \cdot n^2 \nu_{max}^2 \int_{S_0 \rightarrow S_1} \varepsilon d\nu = 0.125 \cdot n^2 \nu_{max}^2 f$$

where n is the refractive index of the solvent, ν_{max} is absorption maximum (in 10^4 cm^{-1}), and f is the oscillator strength of the $S_0 \rightarrow S_1$ excitation. According to the SB rule, a high fluorescence rate constant is expected for the molecules with high oscillator strength. Very good matches between the f values, listed in Table 1.2, which were obtained by direct integration of the absorption spectrum and from the k_F value determined in photophysical measurements shows that the SB rule holds for **70-10-5**. At the same time, **70-10-2** significantly deviates from the rule (its k_F value is ca 4 times higher than might be expected from the SB equation). The values listed in Table 1.2 show that the TD-PBE method underestimates excitation energies (adiabatic values by ca. 0.4 eV; vertical values by ca. 0.25 eV), but relative S_1 energies and, even more importantly, computed oscillator strengths agree very well with the experimental estimations. For **70-10-1**, the

Table 1.2. Experimental and calculated S_1 and T_1 energies and $S_0 \rightarrow S_1$ oscillator strengths *f*.[a]

	C_{70}	**70-8-1**	**70-8-2**	**70-10-1**	**70-10-2**	**70-10-5**
S_1-exp	1.93	2.02	1.86	2.42	2.38	1.96
S_1-vert	1.75	1.83	1.51	2.19	2.03	1.62
S_1-adb	1.69	1.62	1.43	2.05	1.89	1.51
f_{exp}-int					0.039	0.046
f_{exp}-SB				0.015	0.162	0.035
f_{calc}	0.000	0.003	0.012	0.011	0.036	0.041
τ_F-exp				5.6	3.2	50.9
τ_F-calc		1.1	72.7	7.8	12.1	45.9
T_1-adb	1.52	1.37	0.98	1.75	1.38	1.03
$\Delta_{S1\text{-}T1}$	0.16	0.25	0.44	0.29	0.51	0.48
$T_1 \rightarrow T_2$-vert		0.63	0.72	0.46	0.73	0.79

[a] all energies are in eV; S_1-exp is the energy of S_1 from fluorescence in toluene, S_1-vert and S_1-adb are vertical and adiabatic $S_0 \rightarrow S_1$ excitation energies computed at the TD-PBE/TZ2P level; f_{exp}-int and f_{exp}-SB are oscillator strengths determined experimentally by integration of the absorption spectrum (int) or from Strickler-Berg relation (SB) using experimental k_F values; f_{calc} denotes TD-DFT computed oscillator strengths; τ_F-exp are experimental lifetimes, τ_F-calc are lifetimes computed using experimental Φ_F and computed *f* values.

f value computed from the SB equation also fits the TD-DFT prediction very well. Hence, it is reasonable to use computed *f* values when their experimental determination is not possible, and then estimate the lifetimes using the experimental quantum yields. Comparison of the *f* values for **70-8-1** and **70-8-2** shows that their Φ_F difference can be explained, in part, by the very low oscillator strength of the $S_0 \rightarrow S_1$ excitation in **70-8-1**. In contrast, very long lifetimes would be expected for **70-8-2**. In principle, it appears that compounds with higher Φ_F tend to have higher oscillator strengths. However, the analysis of only *f* is not sufficient to explain the results here because, for example, **70-8-2** and **70-10-1** have similar *f* values for their respective $S_0 \rightarrow S_1$ excitations but have quantum yields that differ by more than a factor of 6.

Analysis of the rate of the non-radiative decay is more complicated and its direct prediction is hardly possible now. However, if $S_1 \rightarrow T_1$ ISC remains the main pathway for the non-radiative decay, the energy-gap law can be applied, which states that the rate of the ISC increases with the decrease of the energy gap between the states, Δ_{S1-T1}.[44] The Δ_{S1-T1} values listed in Table 1.2 show that the largest gap of 0.5 eV is found for **70-10-2** and **70-10-5** followed by **70-8-2** with 0.44 eV. In the series **70-10-1** to **70-8-1** to C_{70} the Δ_{S1-T1} values decrease from 0.29 to 0.25 to 0.16 eV. Thus, it is clear that compounds with high fluorescence quantum yield have the largest Δ_{S1-T1} gaps. To verify that $S_1 \rightarrow T_2$ ISC is unlikely, vertical $T_1 \rightarrow T_2$ excitation energies have been computed and found that in all compounds T_2 state is higher in energy than S_1.

Increase of the fluorescence yields for multiply functionalized C_{60} derivatives was earlier ascribed to the shrinking of the π-system.[8,12] The results in this work show that neither the size nor the location of the π-system itself is of such a high importance since there remain 60 $C(sp^2)$ atoms in very similar positions in the three $C_{70}(CF_3)_{10}$ isomers. Presumably, the spatial extension of the $S_0 \rightarrow S_1$ excitation, which is visualized in Figure 1.7 by plotting the difference S_1/S_0 electron densities, is a factor that also plays a role. Larger Δ_{S1-T1} gaps are achieved when excitation is more localized (i.e., when the HOMO and LUMO are spatially localized in the same fragment of the molecule), as in **70-10-2** and **70-10-5**, whereas a larger spatial extension leads to smaller Δ_{S1-T1} gaps as in **70-10-1**. Since the addition pattern dictates the shape and localization of the frontier orbitals in functionalized fullerenes, including TMFs,[27] it follows that it should also determine their photophysical properties, as shown in this study.

Table 1.3 lists TD-DFT computed vertical excitation energies and oscillator strengths. In **70-10-2** and **70-10-5** the $S_0 \rightarrow S_1$ excitations are much more intense than all other excitations in the range of at least 0.5 eV (**70-10-2**) and even more (**70-10-5**). This agrees with the experimentally observed spectra, where $S_0 \rightarrow S_1$ band is clearly seen for both compounds, but for **70-10-2** the overlap with higher energy bands is stronger than for **70-10-5**. On the contrary, there is almost no gap between $S_0 \rightarrow S_1$ and other $S_0 \rightarrow S_n$ excitations of similar intensity in the computed spectrum of **70-10-1**, and hence the overlap in experimental spectrum is much stronger.

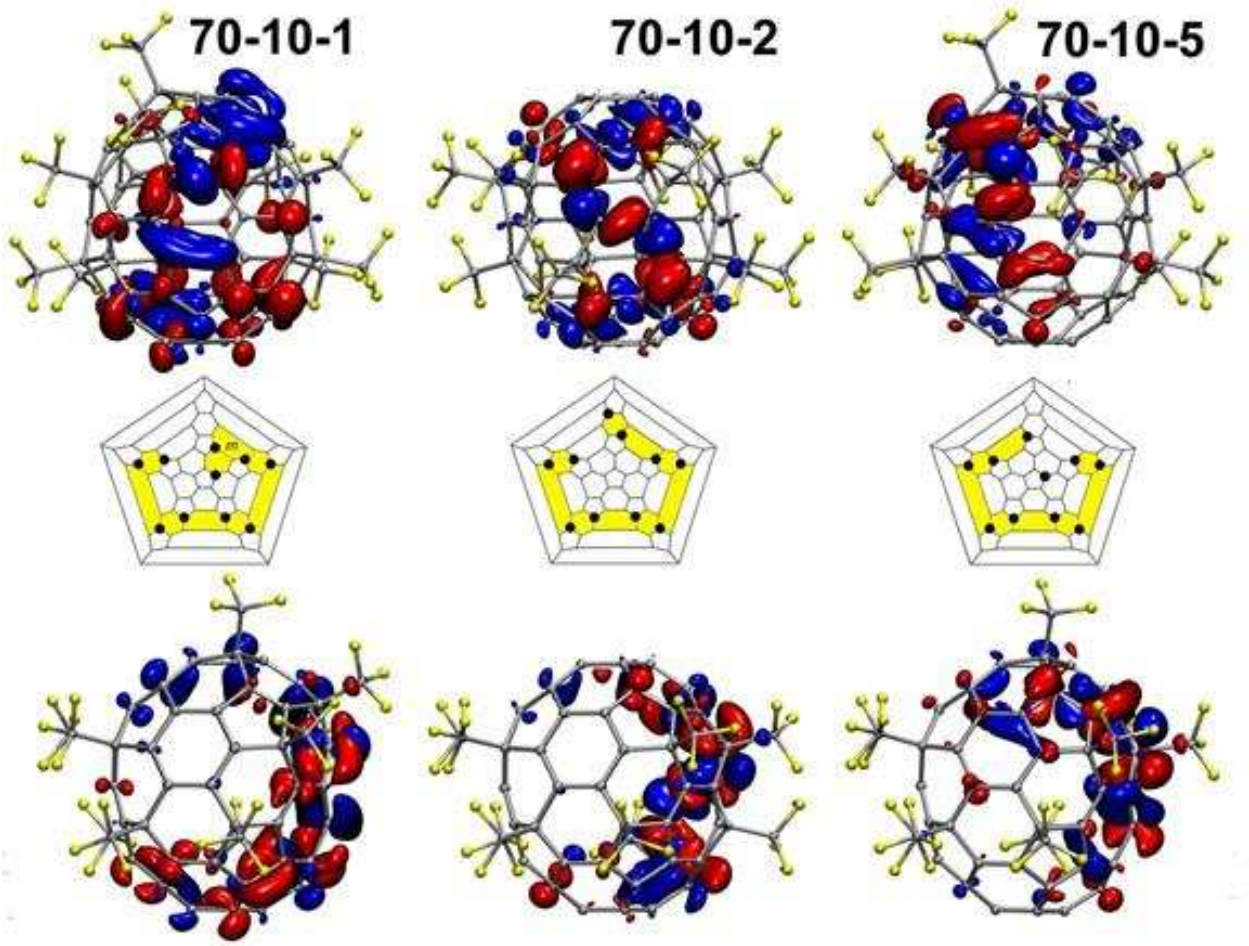

Figure 1.7. TD-DFT computed difference electronic densities for $S_0 \rightarrow S_1$ excitation, $\Delta\rho = \rho(S_1) - \rho(S_0)$, in **70-10-1** (left), **70-10-2** (middle), and **70-10-5** (right). Positive and negative $\Delta\rho$ lobes (i.e. spatial distribution of the electron and hole in the exciton formalism) are red and blue, respectively. Each molecule is shown in two orientations in the top and bottom rows with a Schelgel diagram in the middle row.

Table 1.3. TD-DFT computed vertical excitation energies, and oscillator strengths, *f*.

	70-10-1		**70-10-2**		**70-10-5**	
	E, eV	*f*	E, eV	*f*	E, eV	*f*
S1	2.19	0.011	2.03	0.036	1.62	0.041
S2	2.24	0.000	2.21	0.008	1.91	0.000
S3	2.25	0.002	2.24	0.001	1.98	0.001
S4	2.32	0.007	2.28	0.000	2.01	0.003
S5	2.38	0.000	2.35	0.003	2.07	0.004
S6	2.42	0.005	2.40	0.002	2.18	0.002
S7	2.49	0.001	2.49	0.022	2.23	0.009
S8	2.51	0.003	2.53	0.000	2.33	0.001
S9	2.53	0.004	2.56	0.005	2.34	0.001
S10	2.55	0.003	2.61	0.000	2.41	0.003
S11	2.58	0.007	2.63	0.004	2.41	0.006
S12	2.64	0.001	2.66	0.001	2.45	0.005
S13	2.67	0.001	2.67	0.001	2.47	0.007
S14	2.69	0.003	2.67	0.004	2.54	0.004
S15	2.70	0.004	2.69	0.003	2.56	0.000
S16	2.72	0.011	2.72	0.001	2.60	0.006
S17	2.75	0.001	2.74	0.001	2.65	0.001
S18	2.78	0.003	2.81	0.000	2.65	0.004
S19	2.79	0.003	2.84	0.000	2.70	0.003
S20	2.82	0.002	2.85	0.001	2.71	0.001
S21	2.83	0.001	2.85	0.001	2.76	0.008
S22	2.85	0.004	2.87	0.000	2.80	0.011
S23	2.87	0.005	2.87	0.001	2.84	0.005
S24	2.87	0.003	2.92	0.004	2.87	0.003

1.2.4. Leaf Air-Space Imaging

The fluorescence and solubility properties of TMFs, particularly **70-10-2**, make them suitable for use as leaf air-space imaging agents. Perfluorodecalin has been investigated for use in imaging the interior of leaves.[45,46] The use of perfluorodecalin as an imaging medium leads to high quality images of the interior structure of leaves. When perfluorodecalin alone is applied to the leaf air-spaces must be manually distinguished from vacuoles. Littlejohn et al. reported using a suspension of green fluorescent protein in perfluorodecalin to distinguish air-spaces, which were flooded with green fluorescent protein, from vacuoles.[45,46] A perfluorodecalin soluble molecule should provide a more stable imaging medium which is not prone to the fluorescent molecule settling out of solution. The structure and size of the air-spaces within leaves may

impact their photosynthetic efficiency, by providing efficient access of photosynthetic cells to CO_2 while minimizing water losses due to transpiration. Visualization of the air-spaces will therefore allow for improved modeling of the structure-function relationship between air-spaces and photosynthetic efficiency.

The use of perfluorodecalin soluble molecules as leaf imaging agents has not yet been reported in the literature. Preliminary studies on the use of **70-10-2** as a leaf air-space imaging agent in *Arabidopsis thaliana* leaves have been conducted. Shown in Figure 1.8 are images of a wild-type leaf and a leaf from plant with a mutated *reticulata* gene. Plants with mutated *reticulata* genes (*re-6*) are known to have lower mesophyll cell density, but on the exterior the leaves appear the same.[47] Work to model the structure-function relationship between air-spaces and photosynthetic efficiency are ongoing.

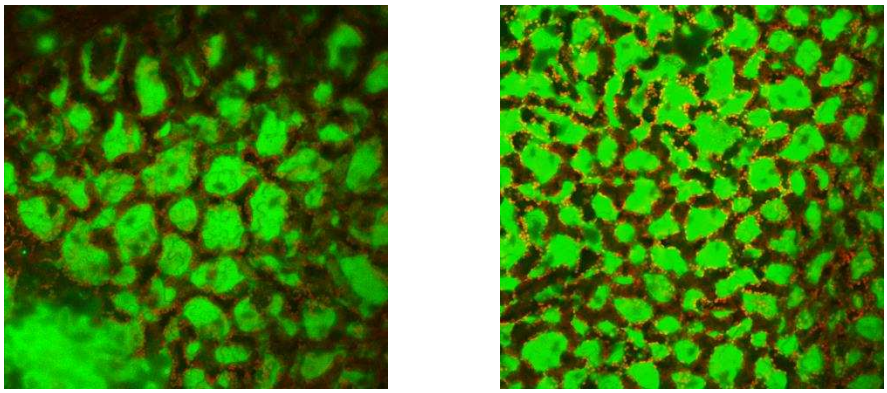

A **B**

Figure 1.8. A) Wild-type *Arabidopsis thaliana* leaf interior. B) *re-6* mutant *Arabidopsis thaliana* leaf interior. Both images taken from the under-side of the leaf, green areas are air-spaces flooded with dye in PFD, red portions are chloroplasts, and black portions are cell interiors. Note that the air-spaces are smaller and more numerous in the *re-6* mutant.

1.2.5. Singlet Oxygen Yields

TMFs are soluble in both hexafluorobenzene and perfluorodecalin. Fluorous solvents have high oxygen solubility relative to typical organic solvents.[48,49] Since photodynamic therapy depends on the sensitization of oxygen in the surrounding area, solvents with higher oxygen

content may result in more effective therapy. The measured solubility of **70-10-1** in perfluorodecalin was 0.7 mM.

All three $C_{70}(CF_3)_{10}$ compounds studied (**70-10-1**, **70-10-2**, and **70-10-5**) are fluorescent in hexafluorobenzene and perfluorodecalin, with quantum yields similar to the fluorescence quantum yields in cyclohexane. Therefore, it is reasonable to expect fluorescence quantum yields of $C_{70}(CF_3)_8$ compounds to be similar to the yields measured in cyclohexane. Despite the relatively high fluorescence, all five TMFs sensitize the production of singlet oxygen. The singlet oxygen yields in hexafluorobenzene are **70-8-1** 0.12 ± 0.02, **70-8-2** 0.7 ± 0.2, **70-10-1** 0.6 ± 0.1, **70-10-2** 0.17 ± 0.04, and **70-10-5** 0.18 ± 0.05. Given the low fluorescence quantum yield of **70-8-1**, the low singlet oxygen yield was unexpected. Benasson et al. studied $C_{70}(Ph)_8$ with the same addition pattern and determined a singlet oxygen yield of 0.18 ± 0.02;[50] this is further proof that the photophysical properties are largely due to the addition pattern and not the electronic properties of the substituents. Taken together these results suggest that this addition pattern on C_{70} undergoes significant non-radiative decay. Singlet oxygen yields must be measured in the same solvent as the standard and so yields have not been determined in perfluorodecalin, however, they are expected to be similar given the fluorescence quantum yields in these solvents.

Many singlet oxygen generating fullerenes have been reported in the literature, but this is the first report of TMF sensitizers and one of very few reports in fluorous solvent.[51] Wilson et al. reported one compound they called the C_3 tris-R_F, $C_{60}(C(CO_2CH_2CH_2CH_2C_8F_{17})_2)_3$, which was soluble in perfluorohexane and had a singlet oxygen yield of 0.45. The C_3 tris-R_F compound has a lower singlet oxygen yield than **70-8-2** or **70-10-1** and its fluorescence spectrum and yield have never been reported.

1.3 Summary and Conclusions

Three TMFs meet or exceed the highest previously reported fluorescence quantum yield for a fullerene derivative. One of these, **70-10-5**, is more than 2.8 times higher than any other fullerene or fullerene derivative. Fluorescence quantum yields and lifetimes show a weak dependence on the solvent with Φ_F generally being slightly lower in fluorous solvents. The ultrafast transient

absorption spectrum of **70-10-2** shows the transition to the vibrational states of the S_1 excited state and, at longer pump-probe delays, conversion to the triplet state. High fluorescence quantum yields are correlated with high oscillator strength, large Δ_{S1-T1} energy gaps, and smaller spatial extension of the $S_0 \rightarrow S_1$ excitation. DFT calculation of these values can provide a method for screening potential fullerene fluorophores in the future. A difference in the location of only one CF_3 group in $C_{70}(CF_3)_8$ and $C_{70}(CF_3)_{10}$ isomers resulted in 200-fold and 14-fold increases in Φ_F, respectively. By comparing the fluorescence and singlet oxygen quantum yields of **70-8-1** and the values reported for $C_{70}Ph_8$,[13,50] which has the same addition pattern with different substituents, it was determined that it is highly probable that the addition pattern and not the identity of the substituents that affects the photophysical properties of fullerenes.

The TMFs studied in this work sensitize the production of singlet oxygen. Two of these compounds, **70-8-2** and **70-10-5**, also absorb red wavelengths and one of these, **70-8-2**, even absorbs 630 nm, the wavelength typically used for photodynamic therapy and has a high singlet oxygen yield. Compounds that have both an appreciable fluorescence quantum yield and singlet oxygen yield could be used as dual purpose photosensitizers to determine cellular localization using fluorescence while still generating sufficient singlet oxygen to kill cancer cells.

1.4. Experimental Details

1.4.1. Reagents and Solvents.

Silver trifluoroacetate (Aldrich), C_{70} (MTR Ltd.), 4-(dicyanomethylene)-2-methyl-6-(4-dimethylaminostyryl)-4H-pyran (Aldrich), absolute ethanol (Pharmco-Aaper), cyclohexane (Mallinckrodt), hexafluorobenzene (Oakwood Products or Aldrich), perfluorodecalin (SynQuest Labs), heptane (Fisher Scientific), and toluene (Fisher Scientific or Burdick & Jackson) were used as received. All TMFs were isolated from the products of high-temperature reactions performed by Mr. Travis C. Folsom or the students in CHEM 462 Spring 2012, of C_{70} with CF_3I in a flow-tube apparatus.[28,52] In addition to the flow tube reactions, the compounds **70-8-1** and **70-8-2** were prepared by the author in a reaction of C_{70} with silver trifluoroacetate in a copper tube.[53]

1.4.2. Preparation of TMFs.

Mr. Travis Folsom prepared $C_{70}(CF_3)_n$ in a flow-tube using 101 mg C_{70} and 24 equivalents of copper powder under a flow of CF_3I gas at 540 °C for 1.25 hours. The students in CHEM 462 Spring 2012 prepared $C_{70}(CF_3)_n$ in a flow-tube using approximately 50 mg C_{70} and 24 equivalents of copper powder under a flow of CF_3I gas at 460 °C for 3 hours.

The compounds **70-8-1** and **70-8-2** were also prepared by the author in a reaction of C_{70} with silver trifluoroacetate, similar to reactions reported previously.[53] For this work 112 mg C_{70} and 10 equivalents of silver trifluoroacetate were ground with a mortar and pestle. The mixture was placed in a Pyrex tube which was loaded into a copper tube sealed at one end and a Swagelok fitting at the other end. The Swagelok fitting was closed tightly and the tube placed in a 340 °C tube furnace for 3 h. After cooling the products were transferred to a larger Pyrex tube which was placed in a Pyrex tube sealed at one end with a Teflon valve at the other end. The outer tube was connected to a vacuum pump and evacuated. The entire assembly was heated to 520 °C for 6 h. After cooling the inner Pyrex tube was removed and sealed below the sublimed TMFs. The TMFs were washed out of the Pyrex tube by dissolving them in toluene.

1.4.3. Separation, Purity Characterization, and Isomer Identification.

High performance liquid chromatography (HPLC) is used to isolate pure molecules. In HPLC, mobile phase flows, at high pressure, through a column filled with stationary phase. The stationary phase is typically small silica gel beads whose surface is modified to produce different interactions with the analytes. A mixture of analytes is injected into the system and flows onto the column. In the column the analytes partition between the mobile phase and the stationary phase. In a static system the analytes would come to equilibrium with a certain amount in the liquid and the rest interacting with the stationary phase. During separation the system is constantly perturbed by fresh mobile phase being pumped into the system and the analytes move along the length of the column. Compounds with a higher affinity for the stationary phase are retained on the column longer. The Buckyprep stationary phase is shown in Figure 1.9.

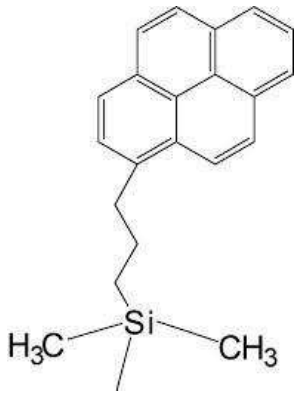

Figure 1.9. The stationary phase of the Buckyprep column is 3-(1-pyrenyl)propyl groups bonded to silica.

Isomers of $C_{70}(CF_3)_8$ were purified by the author using HPLC with a Cosmosil Buckyprep (Nacalai Tesque) semi-preparative column (250 × 10 mm i.d.) on an HPLC Prominence system (Shimadzu) comprised of LC-6AD pump, 2 mL sample loop, equipped with SPD-20A UV-vis detector, SPD-M20A diode array detector, and CBM-20A communications bus module. The first stage of separation used 100% toluene eluent at 4 mL min^{-1}; a fraction collected between 5.2-6.5 minutes contained both **70-8-1** and **70-8-2**. This fraction was further purified using 20:80 toluene:heptane eluent at of 5 mL min^{-1}; a fraction collected between 14.9-16.0 minutes contained **70-8-1** and a fraction collected between 20.2-21.7 minutes contained **70-8-2**.

Isomers of $C_{70}(CF_3)_{10}$ were purified by the author using HPLC with a Cosmosil Buckyprep (Nacalai Tesque) preparative column (250 × 20 mm i.d) on an HPLC Prominence system (Shimadzu) comprised of LC-8A pump, 20 mL sample loop, equipped with SPD-M20A diode array detector, DGU-20As degasser, CBM-20A communications bus module, and FRC-10A fraction collector. The first stage of separation used 100% toluene eluent at 16 mL min^{-1}, a fraction collected between 2.8-6.0 minutes contained all three isomers. The second stage of separation used with 20:80 toluene:heptane eluent at 16 mL min^{-1}; a fraction collected between 10-11.8 minutes contained **70-10-2** and **70-10-5** and a fraction collected between 12.3-15.5 minutes contained **70-10-1**. The fraction containing **70-10-2** and **70-10-5** was further purified using 100% heptane eluent at 16 mL min^{-1}; a fraction collected between 45.7-51.7 minutes

contained **70-10-5** and a fraction collected between 55.3-63.4 minutes contained **70-10-2**. TMF purity was determined to be 95 mol% or higher as shown by ^{19}F NMR spectroscopy in Figure 1.5 (Varian 400 spectrometer). UV-vis spectra were obtained on a Cary 500 UV/Vis/NIR spectrometer in a 1 cm quartz cuvette.

1.4.4. Fluorescence Spectroscopy.

Fluorescence spectroscopy is used to examine the emission of photons as excited electrons relax back to the ground state.[54] Electrons in the sample are excited by incoming photons of a selected wavelength. Typically no matter what energy level the electron is excited to it relaxes quickly via a process called internal conversion to the first excited state. The excited electrons can then relax back to the ground state in either a non-radiative or a radiative manner. Electrons that relax in a radiative manner emit photons which are detected by a photomultiplier tube in the fluorimeter. Since most electrons relax from the first excited ground state, the emitted photons are lower in energy than the absorbed photons. Figure 1.10 depicts the basic processes involved in absorption and fluorescence. The fluorescence spectrum is typically the mirror image of the low energy portion of the absorption spectrum because electrons can relax to any vibrational level within the ground state in the same way they can be excited to any vibrational level of the first excited state and these vibrational levels possess approximately the same energy spacing.

The fluorescence quantum yield is the ratio of photons emitted to photons absorbed. This value allows different fluorescent compounds to be compared for how fluorescent they are. The most common method used to measure fluorescence quantum yields is the relative method where the fluorescence intensity of the sample is compared to the fluorescence intensity a well-characterized quantum yield standard.

Steady-state fluorescence was measured by the author on an AVIV ATF-105 Auto-Titrating Differential/Ratio Spectrofluorimeter with 90^{o} measurement geometry. Sample solutions were degassed with a minimum of three freeze-pump-thaw cycles. The quartz cuvette size was 1 cm square. Each sample solution was independently prepared and measured three times. A blank

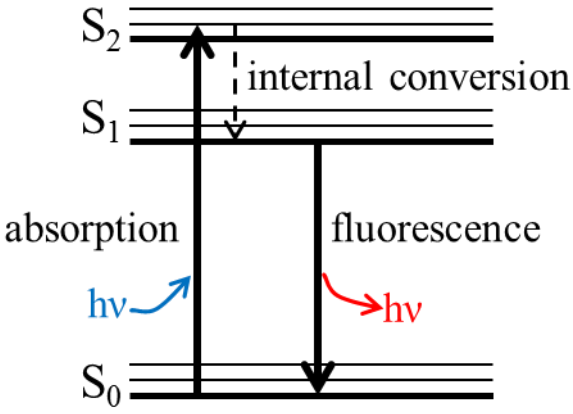

Figure 1.10. Jablonski diagram depicting absorption and fluorescence processes. S_0, S_1, and S_2 are the ground, first excited, and second excited singlet states respectively; within these states the thickest line represents the ground state and the thinner lines represent higher vibrational states.

solution of the pure solvent was also measured three times for each sample or standard solution. The absorbance of standard and sample were matched at the excitation wavelength and the absorbance at and above the excitation wavelength was kept below 0.1. Slit widths were 2 nm, the step size was 1 nm, and the temperature was 25.0 ± 0.2 ^{o}C. The spectra were corrected for wavelength dependent detector response using a correction curve generated by comparing the measured spectrum of tetraphenylporphyrin with published data.[55,56]

To ensure correct determination of fluorescence intensities in the NIR range, additional fluorescence measurements were performed by Dr. A. A. Popov (Leibniz Institute for Solid State and Materials Research, Dresden, Germany) on a home-made system comprised of a 405 nm laser (Omicron) and diode-array spectrometer AvaSpec-ULS2048XL (Avantes). The detector was calibrated versus the certified halogen lamp AvaLight-DH-CAL (Avantes). Corrected spectra measured independently on both systems were found to be virtually identical.

Fluorescence quantum yields were calculated using the equation:

$$\Phi_{x} = \Phi_{std}\left(\frac{\int F_x}{\int F_{std}}\right)\left(\frac{1-10^{-A_{std}}}{1-10^{-A_x}}\right)\left(\frac{\eta_x^2}{\eta_{std}^2}\right)$$

where *x* represents the sample, std represents the standard, Φ is the quantum yield, $\int F$ is the integrated fluorescence intensity, *A* is the absorbance at the excitation wavelength, and η is the

refractive index of the solvent. The standard used was 4-(dicyanomethylene)-2-methyl-6-(4-dimethylaminostyryl)-4H-pyran in absolute ethanol which has a published Φ_F value of 0.44 ± 0.02.[57]

1.4.5. Fluorescence Lifetimes.

Fluorescence lifetimes were measured by the author in the laboratory of Dr. Jeffrey J. Rack (Ohio University) with an Edinburgh LP920 Spectrometer equipped with an Edinburgh TM300 monochromator and an Edinburgh LP900 PMT using a Surelite Continuum Nd:YAG laser with a Surelite SSP. The excitation wavelength was 355 nm. Detection occurred at the fluorescence emission maximum. During the measurements, two laser pulses were discarded and three were averaged for one output. The instrument response was also recorded for each sample using a 1-cm cuvette filled with the relevant solvent. Using Edinburgh L900 software, a reconvolution fit was calculated using the sample signal and the instrument response. From this fit the fluorescence lifetime of the sample was determined. Samples were measured in the same solvents as those used in the fluorescence quantum-yield measurements.

1.4.6. Ultrafast Transient Absorption.

Ultrafast transient absorption spectroscopy was performed by Dr. Yuhuan Jin and Dr. Jeffrey J. Rack (Ohio University). For ultrafast transient absorption measurements, excitation was at 495 nm and a sapphire crystal was employed to generate the white light continuum with a detection range of ca. 450 to 800 nm

1.4.7. Theoretical Calculations.

DFT is a theoretical approach to model the electronic properties of materials and was introduced by Kohn and co-workers.[58,59] The two theorems underlying DFT calculations are: 1) the ground state electron density determines all of the properties of a system and 2) the energy of the system can be described as a functional of the electron density. In this work time-dependent DFT (TD-DFT), an extension of ground-state DFT, is used to examine excitations of the electrons in the system. While the absolute values obtained from some calculations underestimate the experimental data, the relative energy levels can be used for comparisons

between molecules. TD-DFT calculations were performed by Dr. Popov with the PBE functional and TZ2P basis set using the Priroda code.[60,61]

1.4.8. Leaf Imaging Experiments.

The compound **70-10-2** was isolated by the author. Leaf imaging experiments were conducted in the laboratories of Dr. Andrew J. Fleming and Dr. Stephen A. Rolfe (The University of Sheffield). A solution of **70-10-2** in perfluorodecalin was prepared, at the limit of solubility, by sonication. Leaves were immersed in the solution and then examined via confocal microscopy.

1.4.9. Singlet Oxygen Quantum Yields.

Experiments were carried out by the author with the assistance of Dr. Andrew J. Ferguson in the laboratory of Dr. Jeffrey L. Blackburn (National Renewable Energy Laboratory) on a home-built instrument which used front face detection, a 250 W halogen lamp, a monochromator (Acton Research Corp.), a modified Thermo-Nicolet FT-960 liquid nitrogen cooled germanium detector, and run by a home written LabView program. Sample and standard (tetraphenylporphyrin) were dissolved in hexafluorobenzene (Aldrich or Synquest Laboratories) and the absorbance values were matched at the excitation wavelength. Measurements were taken in a 1 cm quartz cuvette.

Singlet oxygen quantum yields were calculated according to the following equation:

$$\Phi_{\Delta,x} = \Phi_{\Delta,std}\left(\frac{slope_x}{slope_{std}}\right)\left(\frac{1-10^{-A_{std}}}{1-10^{-A_x}}\right)$$

Where x represents the sample and std represents the standard (tetraphenylporphyrin in hexafluorobenzene $\Phi_\Delta = 0.57$),[62] A is the absorbance at the excitation wavelength. Slopes were determined in the following manner: responses were recorded with increasing neutral density filters placed before the sample and peak areas were plotted against the transmission of the filter.

CHAPTER 1: REFERENCES

(1) Kroto, H. W.; Heath, J. R.; Obrien, S. C.; Curl, R. F.; Smalley, R. E.: C_{60} - Buckminsterfullerene. *Nature* **1985**, *318*, 162-163.

(2) Schmalz, T. G.; Seitz, W. A.; Klein, D. J.; Hite, G. E.: C_{60} carbon cages. *Chem. Phys. Lett.* **1986**, *130*, 203-207.

(3) Kroto, H. W.: The stability of the fullerenes C_n, with n = 24, 28, 32, 36, 50, 60 and 70. *Nature* **1987**, *329*, 529-531.

(4) Hirsch, A. D. r. n.: *Fullerenes chemistry and reactions*; Wiley-VCH: Weinheim ;, 2005.

(5) Boltalina, O. V.; Popov, A. A.; Kuvychko, I. V.; Shustova, N. B.; Strauss, S. H.: Perfluoroalkylfullerenes. *Chem. Rev.* **2015**, *115*, 1051-1105.

(6) Dennler, G.; Scharber, M. C.; Brabec, C. J.: Polymer-Fullerene Bulk-Heterojunction Solar Cells. *Adv. Mater.* **2009**, *21*, 1323-1338.

(7) Mroz, P.; Tegos, G. P.; Gali, H.; Wharton, T.; Sarna, T.; Hamblin, M. R.: Photodynamic therapy with fullerenes. *Photochem. Photobiol. Sci.* **2007**, *6*, 1139-1149.

(8) Matsuo, Y.; Sato, Y.; Hashiguchi, M.; Matsuo, K.; Nakamura, E.: Synthesis, Electrochemical and Photophysical Properties, and Electroluminescent Performance of the Octa- and Deca(aryl) 60 fullerene Derivatives. *Adv. Funct. Mater.* **2009**, *19*, 2224-2229.

(9) Arbogast, J. W.; Darmanyan, A. P.; Foote, C. S.; Rubin, Y.; Diederich, F. N.; Alvarez, M. M.; Anz, S. J.; Whetten, R. L.: Photophysical Properties of C_{60}. *J. Phys. Chem.* **1991**, *95*, 11-12.

(10) Arbogast, J. W.; Foote, C. S.: Photophysical Properties of C_{70}. *J. Am. Chem. Soc.* **1991**, *113*, 8886-8889.

(11) Catalan, J.; Elguero, J.: Fluorescence of C_{60} and C_{70}. *J. Am. Chem. Soc.* **1993**, *115*, 9249-9252.

(12) Fujita, T.; Matsuo, Y.; Nakamura, E.: Synthesis of Tetradeca- and Pentadeca(organo) 60 fullerenes Containing Unique Photo- and Electroluminescent pi-Conjugated Systems. *Chem. Mater.* **2012**, *24*, 3972-3980.

(13) Schwell, M.; Gustavsson, T.; Marguet, S.; de la Vaissiere, B.; Wachter, N. K.; Birkett, P. R.; Mialocq, J. C.; Leach, S.: The fluorescence properties of the phenylated fullerenes $C_{70}Ph_4$, $C_{70}Ph_6$, $C_{70}Ph_8$, and $C_{70}Ph_{10}$ in room temperature solutions. *Chem. Phys. Lett.* **2001**, *350*, 33-38.

(14) Foley, S.; Berberan-Santos, M. N.; Fedorov, A.; McGarvey, D. J.; Santos, C.; Gigante, B.: Photophysical properties of pseudo-dihydro derivatives of C_{70}. *J. Phys. Chem. A* **1999**, *103*, 8173-8178.

(15) Chen, Z. Y.; Ma, L. J.; Liu, Y.; Chen, C. Y.: Applications of Functionalized Fullerenes in Tumor Theranostics. *Theranostics* **2012**, *2*, 238-250.

(16) Bosi, S.; Da Ros, T.; Spalluto, G.; Prato, M.: Fullerene derivatives: an attractive tool for biological applications. *Eur. J. Med. Chem.* **2003**, *38*, 913-923.

(17) Hu, Z.; Zhang, C. H.; Huang, Y. D.; Sun, S. F.; Guan, W. C.; Yao, Y. H.: Photodynamic anticancer activities of water-soluble C_{60} derivatives and their biological consequences in a He La cell line. *Chemico-Biological Interactions* **2012**, *195*, 86-94.

(18) Liu, J. A.; Tabata, Y.: Photodynamic Antitumor Activity of Fullerene Modified with Poly(ethylene glycol) with Different Molecular Weights and Terminal Structures. *J. Biomater. Sci., Polym. Ed.* **2011**, *22*, 297-312.

(19) Kwag, D. S.; Oh, N. M.; Oh, Y. T.; Oh, K. T.; Youn, Y. S.; Lee, E. S.: Photodynamic therapy using glycol chitosan grafted fullerenes. *Int. J. Pharm.* **2012**, *431*, 204-209.

(20) Fan, J.; Fang, G.; Zeng, F.; Wang, X.; Wu, S.: Water-Dispersible Fullerene Aggregates as a Targeted Anticancer Prodrug with both Chemo- and Photodynamic Therapeutic Actions. *Small* **2013**, *9*, 613-621.

(21) Rancan, F.; Rosan, S.; Boehm, F.; Cantrell, A.; Brellreich, M.; Schoenberger, H.; Hirsch, A.; Moussa, F.: Cytotoxicity and photocytotoxicity of a dendritic C_{60} mono-adduct and a malonic acid C_{60} tris-adduct on Jurkat cells. *J. Photochem. Photobio. B* **2002**, *67*, 157-162.

(22) Allison, R. R.; Downie, G. H.; Cuenca, R.; Hu, X. H.; Childs, C. J. H.; Sibata, C. H.: Photosensitizers in clinical PDT. *Photodiagn. Photodyn. Ther.* **2004**, *1*, 27-42.

(23) Lee, J.; Mackeyev, Y.; Cho, M.; Wilson, L. J.; Kim, J. H.; Alvarez, P. J. J.: C_{60} Aminofullerene Immobilized on Silica as a Visible-Light-Activated Photocatalyst. *Environ. Sci. Technol.* **2010**, *44*, 9488-9495.

(24) Wainwright, M.: The emerging chemistry of blood product disinfection. *Chem. Soc. Rev.* **2002**, *31*, 128-136.

(25) Kammerlander, G.; Assadian, O.; Eberlein, T.; Zweitmuller, P.; Luchsinger, S.; Andriessen, A.: A clinical evaluation of the efficacy and safety of singlet oxygen in cleansing and disinfecting stagnating wounds. *J. Wound Care* **2011**, *20*, 149-+.

(26) Moor, K. J.; Kim, J.-H.: Simple Synthetic Method Toward Solid Supported C_{60} Visible Light-Activated Photocatalysts. *Environ. Sci. Technol.* **2014**, *48*, 2785-2791.

(27) Popov, A. A.; Kareev, I. E.; Shustova, N. B.; Stukalin, E. B.; Lebedkin, S. F.; Seppelt, K.; Strauss, S. H.; Boltalina, O. V.; Dunsch, L.: Electrochemical, spectroscopic, and DFT study of $C_{60}(CF_3)_n$ frontier orbitals (n=2-18): The link between double bonds in pentagons and reduction Potentials. *J. Am. Chem. Soc.* **2007**, *129*, 11551-11568.

(28) Popov, A. A.; Kareev, I. E.; Shustova, N. B.; Lebedkin, S. E.; Strauss, S. H.; Boltalina, O. V.; Dunsch, L.: Synthesis, spectroscopic and electrochemical characterization, and DFT study of Seventeen $C_{70}(CF_3)_n$ derivatives (n=2, 4, 6, 8, 10, 12). *Chem. - Eur. J.* **2008**, *14*, 107-121.

(29) Shustova, N. B.; Kuvychko, I. V.; Bolskar, R. D.; Seppelt, K.; Strauss, S. H.; Popov, A. A.; Boltalina, O. V.: Trifluoromethyl Derivatives of Insoluble Small-HOMO-LUMO-Gap Hollow Higher Fullerenes. NMR and DFT Structure Elucidation of C_2-(C_{74}-D_{3h})$(CF_3)_{12}$, C_s-(C_{76}-T_d(2))$(CF_3)_{12}$, C_2-(C_{78}-D_{3h}(5))$(CF_3)_{12}$, C_s-(C_{80}-C_{2v}(5))$(CF_3)_{12}$, and C_2-(C_{82}-C_2(5))$(CF_3)_{12}$. *J. Am. Chem. Soc.* **2006**, *128*, 15793-15798.

(30) Shustova, N. B.; Newell, B. S.; Miller, S. M.; Anderson, O. P.; Bolskar, R. D.; Seppelt, K.; Popov, A. A.; Boltalina, O. V.; Strauss, S. H.: Discovering and Verifying Elusive Fullerene Cage Isomers: Structures of C_2–p^{11}–(C_{74}–D_{3h})$(CF_3)_{12}$ and C_2–p^{11}–(C_{78}–D_{3h}(5))$(CF_3)_{12}$. *Angew. Chem., Int. Ed.* **2007**, *46*, 4111-4114.

(31) Kareev, I. E.; Lebedkin, S. F.; Bubnov, V. P.; Yagubskii, E. B.; Ioffe, I. N.; Khavrel, P. A.; Kuvychko, I. V.; Strauss, S. H.; Boltalina, O. V.: Trifluoromethylated endohedral metallofullerenes: Synthesis and characterization of Y@$C_{82}(CF_3)_5$. *Angew. Chem., Int. Ed.* **2005**, *117*, 1880-1883.

(32) Shustova, N. B.; Chen, Y.-S.; Mackey, M. A.; Coumbe, C. E.; Phillips, J. P.; Stevenson, S.; Popov, A. A.; Boltalina, O. V.; Strauss, S. H.: Sc_3N@(C_{80}-I_h(7))$(CF_3)_{14}$ and

$Sc_3N@(C_{80}\text{-}I_h(7))(CF_3)_{16}$. Endohedral Metallofullerene Derivatives with Exohedral Addends on Four and Eight Triple-Hexagon Junctions. Does the Sc_3N Cluster Control the Addition Pattern or Vice Versa? *J. Am. Chem. Soc.* **2009**, *131*, 17630-17637.

(33) Takano, Y.; Herranz, M.; Martín, N.; de Miguel Rojas, G.; Guldi, D. M.; Kareev, I. E.; Strauss, S. H.; Boltalina, O. V.; Tsuchiya, T.; Akasaka, T.: Electron Donor–Acceptor Interactions in Regioselectively Synthesized $exTTF_2$–$C_{70}(CF_3)_{10}$ Dyads. *Chem. - Eur. J.* **2010**, *16*, 5343-5353.

(34) Castro, K. P.; Jin, Y.; Rack, J. J.; Strauss, S. H.; Boltalina, O. V.; Popov, A. A.: Perfluoroalkyl [70]-Fullerenes as Robust Highly-Luminescent Fluorocarbons, or Position of One CF_3 Group Matters. *J. Phys. Chem. Lett.* **2013**, *4*, 2500-2507.

(35) Kim, D.; Lee, M.; Suh, Y. D.; Kim, S. K.: Observation of fluorescence emission from solutions of C_{60} and C_{70} fullerenes and measurement of their excited-state lifetimes. *J. Am. Chem. Soc.* **1992**, *114*, 4429-4430.

(36) Clements, A. F.; Haley, J. E.; Urbas, A. M.; Kost, A.; Rauh, R. D.; Bertone, J. F.; Wang, F.; Wiers, B. M.; Gao, D.; Stefanik, T. S.: Photophysical properties of C_{60} colloids suspended in water with Triton X-100 surfactant: Excited-state properties with femtosecond resolution. *J. Phys. Chem. A* **2009**, *113*, 6437-6445.

(37) Lembo, A.; Tagliatesta, P.; Guldi, D. M.: Synthesis and Photophysical Investigation of New Porphyrin Derivatives with β-Pyrrole Ethynyl Linkage and Corresponding Dyad with [60] Fullerene. *J. Phys. Chem. A* **2006**, *110*, 11424-11434.

(38) Fraelich, M.; Weisman, R.: Triplet states of fullerene C_{60} and C_{70} in solution: long intrinsic lifetimes and energy pooling. *J. Phys. Chem.* **1993**, *97*, 11145-11147.

(39) Hung, R. R.; Grabowski, J. J.: C_{70}: intersystem crossing and singlet oxygen production. *Chem. Phys. Lett.* **1992**, *192*, 249-253.

(40) Hope, M. J.; Higlett, M. P.; Andrews, D. L.; Meech, S. R.; Hands, I. D.; Dunn, J. L.; Bates, C. A.: Observation of ultrafast internal conversion in fullerene anions in solution. *Chem. Phys. Lett.* **2009**, *474*, 112-114.

(41) Tanigaki, K.; Ebbesen, T. W.; Kuroshima, S.: Picosecond and nanosecond studies of the excited state properties of C_{70}. *Chem. Phys. Lett.* **1991**, *185*, 189-192.

(42) Ebbesen, T. W.; Tanigaki, K.; Kuroshima, S.: Excited-state properties of C_{60}. *Chem. Phys. Lett.* **1991**, *181*, 501-504.

(43) Strickler, S.; Berg, R. A.: Relationship between absorption intensity and fluorescence lifetime of molecules. *J. Chem. Phys.* **1962**, *37*, 814.

(44) Klán, P.; Wirz, J.: *Photochemistry of organic compounds: From concepts to practice*; John Wiley & Sons Ltd., 2009.

(45) Littlejohn, G. R.; Gouveia, J. D.; Edner, C.; Smirnoff, N.; Love, J.: Perfluorodecalin enhances in vivo confocal microscopy resolution of *Arabidopsis thaliana* mesophyll. *New Phytol.* **2010**, *186*, 1018-1025.

(46) Littlejohn, G. R.; Love, J.: A Simple Method for Imaging *Arabidopsis* Leaves Using Perfluorodecalin as an Infiltrative Imaging Medium. *J. Vis. Exp.* **2012**.

(47) González-Bayón, R.; Kinsman, E. A.; Quesada, V.; Vera, A.; Robles, P.; Ponce, M. R.; Pyke, K. A.; Micol, J. L.: Mutations in the RETICULATA gene dramatically alter internal architecture but have little effect on overall organ shape in *Arabidopsis* leaves. *J. Exp. Bot.* **2006**, *57*, 3019-3031.

(48) Evans, F. D.; Battino, R.: Solubility of Gases in Liquids 3. Solubilities of Gases in Hexafluorobenzene and in Benzene. *J. Chem. Thermodyn.* **1971**, *3*, 753-&.

(49) Dias, A. M. A.; Freire, M.; Coutinho, J. A. P.; Marrucho, I. M.: Solubility of oxygen in liquid perfluorocarbons. *Fluid Phase Equilib.* **2004**, *222*, 325-330.

(50) Benasson, R. V.; Schwell, M.; Fanti, M.; Wachter, N. K.; Lopez, J. O.; Janot, J. M.; Birkett, P. R.; Land, E. J.; Leach, S.; Seta, P.; Taylor, R.; Zerbetto, F.: Photophysical properties of the ground and triplet state of four multiphenylated 70 fullerene compounds. *Chemphyschem* **2001**, *2*, 109-114.

(51) Wilson, S. R.; Yurchenko, M. E.; Schuster, D. I.; Yurchenko, E. N.; Sokolova, O.; Braslavsky, S. E.; Klihm, G.: Preparation and photophysical studies of a fluorous phase-soluble fullerene derivative. *J. Am. Chem. Soc.* **2002**, *124*, 1977-1981.

(52) Kareev, I. E.; Kuvychko, I. V.; Lebedkin, S. F.; Miller, S. M.; Anderson, O. P.; Seppelt, K.; Strauss, S. H.; Boltalina, O. V.: Synthesis, structure, and ^{19}F NMR spectra of 1,3,7,10,14,17,23,28,31,40-$C_{60}(CF3)_{10}$. *J. Am. Chem. Soc.* **2005**, *127*, 8362-8375.

(53) Dorozhkin, E. I.; Ignat'eva, D. V.; Tamm, N. B.; Goryunkov, A. A.; Khavrel, P. A.; Ioffe, I. N.; Popov, A. A.; Kuvychko, I. V.; Streletskiy, A. V.; Markov, V. Y.: Synthesis, characterization, and theoretical study of stable isomers of $C_{70}(CF_3)_n$ (n= 2, 4, 6, 8, 10). *Chem. Eur. J.* **2006**, *12*, 3876-3889.

(54) Lakowicz, J. R.: *Principles of Fluorescence Spectroscopy*; 3rd ed.; Springer: New York, 2006.

(55) Dixon, J. M.; Taniguchi, M.; Lindsey, J. S.: PhotochemCAD 2: A Refined Program with Accompanying Spectral Databases for Photochemical Calculations. *Photochem. Photobio.* **2005**, *81*, 212-213.

(56) Prahl, S.: Tetraphenylporphyrin. Oregon Medical Laser Center: http://omlc.ogi.edu/spectra/PhotochemCAD/html/099.html, 2012; Vol. 2012.

(57) Rurack, K.; Spieles, M.: Fluorescence Quantum Yields of a Series of Red and Near-Infrared dyes Emitting at 600-1000 nm. *Anal. Chem.* **2011**, *83*, 1232-1242.

(58) Hohenberg, P.; Kohn, W.: Inhomogeneous electron gas. *Phys. Rev.* **1964**, *136*, B864.

(59) Kohn, W.; Sham, L. J.: Self-consistent equations including exchange and correlation effects. *Phys. Rev.* **1965**, *140*, A1133.

(60) Laikov, D.; Ustynyuk, Y. A.: PRIRODA-04: a quantum-chemical program suite. New possibilities in the study of molecular systems with the application of parallel computing. *Russ. Chem. Bull.* **2005**, *54*, 820-826.

(61) Laikov, D. N.: Fast evaluation of density functional exchange-correlation terms using the expansion of the electron density in auxiliary basis sets. *Chem. Phys. Lett.* **1997**, *281*, 151-156.

(62) Schmidt, R.; Afshari, E.: Effect of solvent on the phosphorescence rate constant of singlet molecular oxygen ($^1\Delta_G$). *J. Phys. Chem.* **1990**, *94*, 4377-4378.

CHAPTER 2: TRIFLUOROMETHYL POLYCYCLIC AROMATIC HYDROCARBONS AND CHARGE-TRANSFER COMPLEXES

2.1. Introduction

Small molecule electron acceptors, such as polycyclic aromatic hydrocarbons (PAHs), are being increasingly studied for use in organic electronics. Despite the growing market for and interest in organic electronics there remains an acknowledged need for electron acceptors and n-type semiconductors that are air-stable even in the presence of light. The term air-stable is generally used in the field of organic electronics to mean that charge carrier mobilities are the same, within an order of magnitude, under inert atmosphere and upon exposure to air. Electron affinities (EAs) have been shown to be correlated with air-stability and offer a method to evaluate candidates for acceptor materials without full device fabrication. Chang and co-workers found that compounds with DFT calculated EAs > 2.8 eV tend to be air-stable.[1]

One method of tuning the properties, including air-stability, of PAHs for use in organic electronics is functionalization, particularly fluorination or perfluoroalkylation.[2-4] Sun and co-workers predicted that the addition of perfluoroalkyl groups to the PAH substrate anthracene would not only "tune" the HOMO and LUMO levels and their gap, but would also improve the hydrophobicity and air-stability of PAH thin films.[5] Furthermore, Sun and co-workers demonstrated that perfluorooctyl PAH compounds were more photostable in the presence of air than parent PAHs or hydrocarbon analogs.[6]

Alterations to the electronic properties of PAHs can also occur through the introduction of heteroatoms into the PAH core. A common heteroatom is nitrogen and the potential semiconducting capabilities of nitrogen-containing acenes, or azaacenes, have been investigated by a few groups.[7-9] Compared to their all carbon analogues azaacenes have higher electron affinities (EAs).[9] For example, phenazine (PHNZ) a diazaacene analogue of anthracene has an EA of 1.3 ± 0.1 eV,[10] more than twice that anthracene at 0.53 ± 0.02 eV.[11,12] Aside from increased EAs, improved electron mobilities have been observed when nitrogens are substituted

into other, non-acene, PAHs.[13,14] Derivatives of PHNZ have been identified as natural products,[15,16] and other derivatives have found applications in dyes,[17,18] sensors,[19] and light-emitting diodes.[20]

For most organic electronic applications charge transport is an important consideration. Altering the electronic properties of the molecules under consideration can impact the charge transport as can the solid-state packing and it has been found that some packing motifs are more favorable than others.[21,22] Nitrogen-containing heterocycles exhibit different stacking than the corresponding all-carbon PAH.[23] Attaching electron-withdrawing groups, such as perfluoroalkyl groups, changes the electrostatic potential distribution thereby changing intermolecular interactions and potentially the packing motif.[24,25] Electron-poor PAHs derivatized with electron-withdrawing groups can also be co-crystallized with underivatized PAHs resulting in electron-rich and electron-deficient interactions.[22,26,27]

When electron acceptors and electron donors are mixed there is a possibility of forming a charge transfer complex (CTC). Aromatic electron donor-acceptor CTCs have been the subject of many reviews and book chapters because they are relatively well studied.[28-30] Conductivity in CTCs has been known since the discovery of superconductivity in tetrathiafulvalene/7,7,8,8-tetracyanoquinodimethane (TTF/TCNQ).[31,32] The TTF/TCNQ complex crystallizes in segregated stacks where the donor molecules are separate from the acceptors. Mixed stack complexes which crystallize with alternating donor and acceptor molecules have also demonstrated conductivity and carrier mobility.[33-35] Additional useful properties investigated in CTCs include: fluorescence[36,37] antimicrobial activity,[38] thermoelectric performance,[39] and photoconductivity.[40-42] Investigation into the properties of CTCs reveals information about the intermolecular interactions both in solution and in the solid state.

Previous attempts to produce electron acceptors by directly perfluoroalkylating one or two ring PAH cores generally resulted in products with low numbers of substitutions, low yields, and poor regioselectivity.[43-45] For PHNZ there are no examples of direct perfluoroalkylation. The

literature examples of PHNZ$(CF_3)_n$ all contained one or two trifluoromethyl groups substituted on the core and were synthesized from trifluoromethyl containing non-PAH precursors.[46-49]

Some of the work carried out by the author of this dissertation and described in the first part of this chapter, including the synthesis and characterization of ANTH$(CF_3)_n$, PERY$(CF_3)_n$, PHEN$(CF_3)_n$, and PYRN$(CF_3)_n$ derivatives, has already been published.[50] Subsequent to that publication the effects of multiple CF_3 groups on the properties of the two-ring PAHs naphthalene and azulene were investigated by other members of the Strauss-Boltalina group.[51,52] The goals of the work described in this chapter were (i) to isolate and characterize new trifluoromethyl derivatives of three- and four-ring PAHs and a three-ring heteroatom-PAH and (ii) to study their ability to serve as acceptors in the formation of CTCs with PAH donors. The PAH substrates studied in this work, their abbreviations, and their IUPAC locants are shown in Figure 2.1. The substrates for the synthesis of PAH$(CF_3)_n$ derviatives were chosen to provide insight into the effects of: shape (i.e., ANTH vs PHEN), the presence of heteroatoms (i.e., ANTH vs. PHNZ), three- vs four-ring (i.e., ANTH and PHEN vs PYRN), and the presence of five member rings (i.e., PHEN vs. FLUR and PYRN vs FLRA) on direct PAH trifluoromethylation. The substrates studied for CTC formation were selected to investigate the effects of electronic differences (i.e., EA and reduction potential), PAH shape and size, and substitution pattern of the PAH$(CF_3)_n$ compounds. The methods used to isolate and characterize new PAH$(CF_3)_n$ compounds in this work are HPLC, ^{1}H and ^{19}F NMR, mass spectrometry, single crystal X-ray diffraction, UV-vis spectroscopy, electrochemistry, and gas-phase electron affinity. The CTCs were studied using UV-vis spectroscopy and single crystal X-ray diffraction.

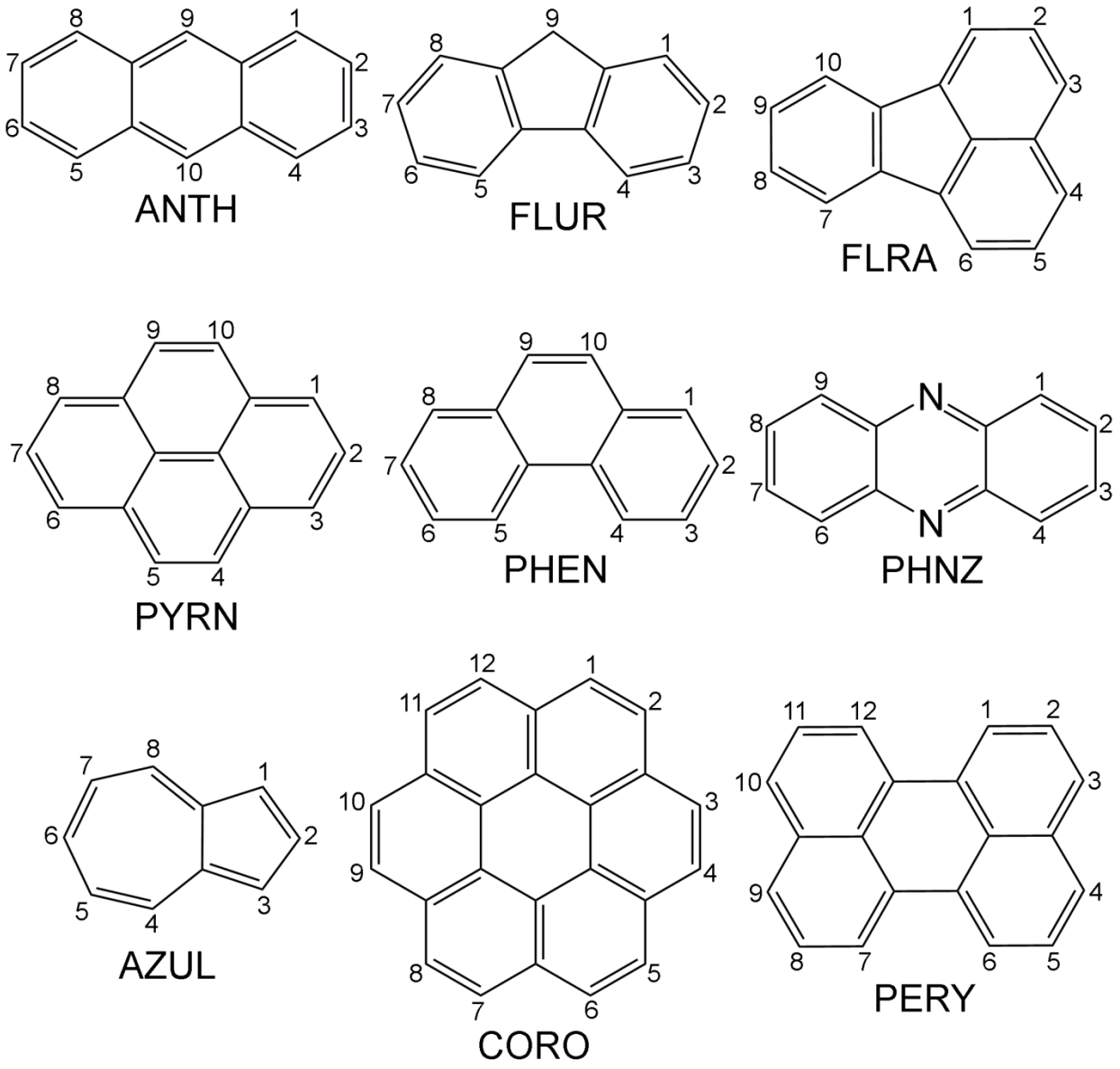

Figure 2.1. PAH cores derivatized with CF_3 groups and/or used to form CTCs in this work: anthracene (ANTH), fluorene (FLUR), fluoranthene (FLRA), pyrene (PYRN), phenanthrene (PHEN), phenazine (PHNZ), azulene (AZUL), coronene (CORO), and perylene (PERY). IUPAC locants for the C atoms available for substitution (i.e., bearing H atoms in the parent PAH) are shown.

2.2. Results and Discussion

2.2.1. Product Composition, Separation, and Identification

Eight trifluoromethylation reactions were performed. The reaction conditions are detailed in Table 2.1. Variables include starting amount of PAH substrate, mole ratio of CF_3I gas, sealed glass ampoule size, reaction temperature and reaction time.

Table 2.1. Reaction conditions for PAH + CF_3I reactions

rxn number	PAH substrate	mass PAH used, mg	n(CF_3I)[a]	$V_{ampoule}$, mL	$V_{headspace}$, mL	T, °C	reaction time
1	ANTH	97	21	350	350	360	18 h
2	ANTH	178	12	215	215	350	18 h
3	FLUR	182	7	220	220	350	25 min
4	FLRA	33	5	35	35	360	17 min
5	PHEN	18	20	50	50	360	24 h
6	PHNZ	28	8	35	35	310	33 min
7	PHNZ	216	10	373	373	330	20 h
8	PYRN	20	30	60	60	360	20 h

[a] n = mole ratio of CF_3I with respect to the number of moles of PAH

The trifluromethylation of ANTH was performed twice. The reaction conditions differed in the number of equivalents of CF_3I used and the size of the sealed glass ampoule (see Table 2.1 for details). In spite of these differences, both reactions produced a very similar crude product mixture. The products were mainly ANTH$(CF_3)_{5,6}$ isomers; a small amount of ANTH$(CF_3)_4$ isolated from Rxn 1 (Table 2.1). Mass spectrometry analysis identified ANTH$(CF_3)_7$ as a product, but a pure isomer has not been isolated. From Rxn 1 there was 302.2 mg crude product and the isolated yields were <1 mol% ANTH-4-1, 5 mol% ANTH-5-1 and 20 mol% ANTH-6-1, based on the amount of starting ANTH. From Rxn 2 there was 455.9 mg crude product and the yield was only calculated for ANTH-6-2 which was 2 mol%, based on the amount of starting ANTH. The ANTH$(CF_3)_n$ crude reaction mixtures were separated by HPLC and all identified products have been isolated in 2 steps. In the first step, the mixture was separated on a Buckyprep semipreparative column using 100% acetonitrile eluent at 5 mL min^{-1} as shown in Figure 2.2. The fraction collected between 6.3–6.9 min contained ANTH-5-1 and, in one case, ANTH-4-1. The fraction collected between 7.4–8.0 min contained a mixture of ANTH-6-2, ANTH-6-3, and ANTH-6-4. The fraction collected between 9.0–9.8 min contained 98+ mol% pure ANTH-6-1. No pure compounds were isolated from the fraction that eluted between 3–4.2 min, but mass spectrometry indicated it contained one or more ANTH$(CF_3)_7$ derivatives.

The fraction containing ANTH-4-1 and ANTH-5-1 was further purified on a FluoroFlash analytical column using 100% acetonitrile eluent at 2 mL min^{-1} (Figure 2.3). The chromatogram

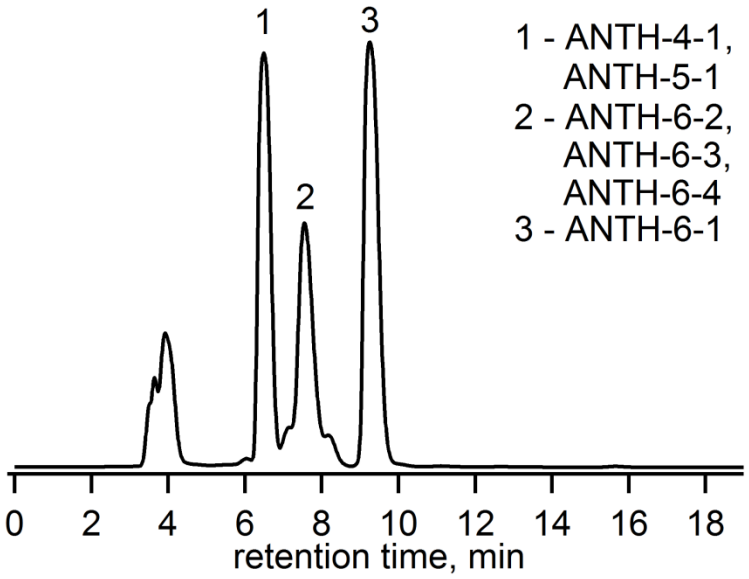

Figure 2.2. HPLC chromatogram of the ANTH$(CF_3)_n$ crude product mixture Rxn 1 in Table 2.1. Separation conditions: Buckyprep semipreparative, 100% acetonitrile eluent at 5 mL min^{-1}, 370 nm detection.

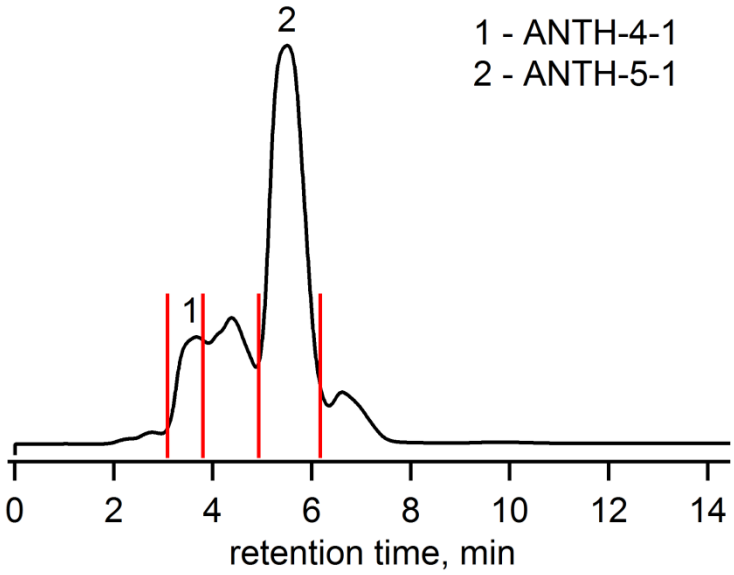

Figure 2.3. HPLC chromatogram of ANTH-4-1 and ANTH-5-1 separation. Mixture was from the 6.3–6.9 min fraction from the first separation stage of the crude product mixture from Rxn 1 in Table 2.1 (see Figure 2.2). Separation conditions: FluoroFlash analytical, 100% acetonitrile eluent, 2 mL min^{-1}, 300 nm detection. Vertical lines represent where the fractions were collected.

was obtained during separation of the Rxn 1 (Table 2.1) and was the only example where a detectable quantity of ANTH-4-1 has been isolated. The fraction collected between 3.2–4.0 min

contained 95 mol% pure ANTH-4-1 and the fraction collected between 5.0–6.3 min contained 98 mol% pure ANTH-5-1. No other pure compounds have been isolated from this separation.

Further purification of ANTH-6-2 from ANTH-6-3 and ANTH-6-4 was performed on a FluoroFlash analytical column using 95:5 v:v acetonitrile:water eluent at 1 mL min^{-1} (Figure 2.4). The fraction collected between 15.0–16.7 min contained 98 mol% pure ANTH-6-2 and the fraction collected between 17.1–18.4 min contained 40 mol% ANTH-6-3 and 60 mol% ANTH-6-4.

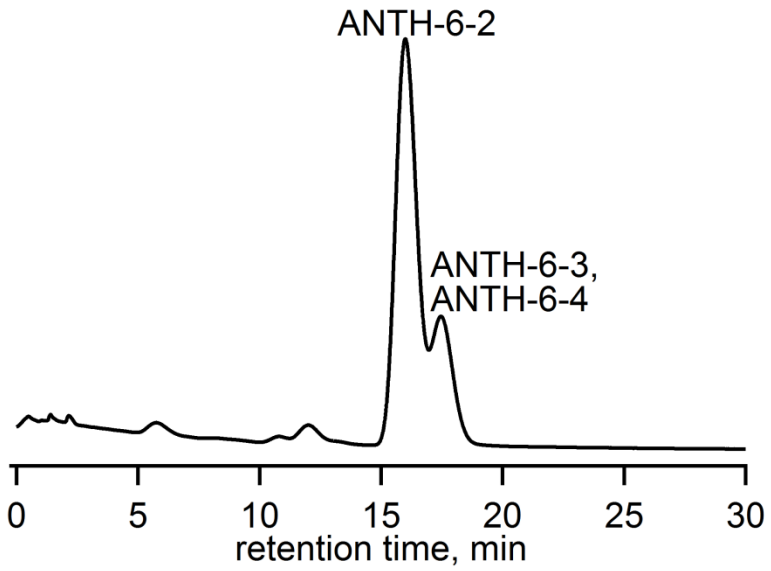

Figure 2.4. HPLC chromatogram for separation of ANTH-6-2 from ANTH-6-3 and ANTH-6-4. Mixture was from the 7.4–8.0 min fraction from the first separation stage of the crude product mixture from Rxn 1 in Table 2.1 (see Figure 2.2). Separation conditions: FluoroFlash analytical, 95:5 v:v acetonitrile:water eluent, 1 mL min^{-1}, 370 nm detection.

The reaction of FLUR with CF_3I was performed once and yielded 317.2 mg of crude FLUR$(CF_3)_n$ product (Rxn 3 Table 2.1). Based on mass spectrometry the mixture had a maximum *n* value of 5 and a predominant *n* value of 4. Despite the relatively large mass of crude material, only one pure compound, FLUR-5-1, was isolated in < 1 mol% yield, based on starting FLUR. Both ANTH and FLUR are three-ring PAHs, but FLUR has a C(sp^3) atom in the central ring. The trifluoromethylation of FLUR appears to be much less selective than most of the other reactions listed in Table 2.1.

Three stages of separation were required to isolate FLUR-5-1 in < 1 mol% isolated yield, as shown in Figure 2.5. Stage 1 utilized a Buckyprep preparative column with 100% acetonitrile eluent at 20 mL min^{-1} and the fraction of interest was collected between 3.3–4.1 min. Stage 2 separation was performed on a Buckyprep semipreparative column with 10:90 v:v toluene:heptane eluent at 5 mL min^{-1} and the fraction of interest was collected between 6.9–7.6 min. Stage 3 separation was performed on a FluoroFlash analytical column with 95:5 v:v acetonitrile:water eluent at 2 mL min^{-1} and 90 mol% pure FLUR-5-1 was collected between 5.7–6.8 min. All of the larger peaks in the chromatograms contained multiple compounds that were not isolated after several attempts to separate them. Many other separation methods were attempted including the use of a Buckyprep semiprep column with mixtures of toluene and heptane as eluents, a FluoroFlash column with mixtures of acetonitrile and water as eluents, and a FluoroFlash column with mixtures of acetonitrile and methanol as eluents. The trifluoromethylation of FLUR would have to be studied in greater detail in order to achieve better selectivity. It is possible that a longer reaction time and/or a larger excess of CF_3I may improve the conversion and selectivity.

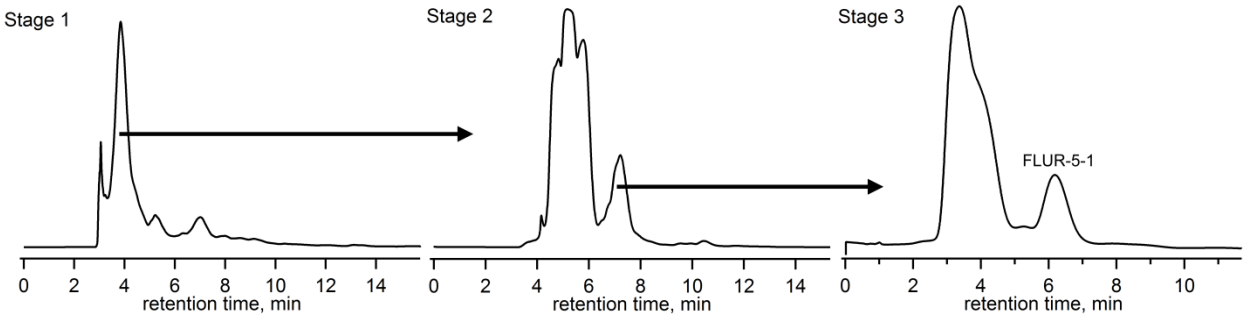

Figure 2.5. Three stages of isolation of FLUR-5-1 from Rxn 3 in Table 2.1. Stage 1 (left) conditions: Buckyprep preparative, 100% acetonitrile eluent, 20 mL min^{-1}, 300 nm detection. Stage 2 (middle) conditions: Buckyprep semipreparative, 10:90 v:v toluene:heptane eluent, 5 mL min^{-1}, 300 nm detection. Stage 3 (right) conditions: FluoroFlash analytical, 95:5 v:v acetonitrile:water eluent, 2 mL min^{-1}, 300 nm detection.

One trifluoromethylation reaction with FLRA was performed (Table 2.1 Rxn 4) and yielded 28.5 mg of crude product. Based on mass spectrometry the FLRA$(CF_3)_n$ products contained a

maximum n = 6 and a predominant n value of 5. Three compounds were isolated after 2 stages of HPLC separation: FLRA-3-1, FLRA-3-2, and FLRA-4-1. However, only some of the fractions yielded pure compounds. Other fractions that could not be separated further (see below) probably contain these putative FLRA$(CF_3)_5$ and FLRA$(CF_3)_6$ derivatives.

The first stage of FLRA$(CF_3)_n$ separation was completed on a Buckyprep semipreparative column with 100% acetonitrile eluent at 5 mL min^{-1} (Figure 2.6). The fraction collected between 8.4–9.3 min contained a mixture of FLRA-3-1 and FLRA-3-2. The fraction collected between 15.4–16.8 min contained 90 mol% pure FLRA-4-1 in 7 mol% isolated yield. The compounds FLRA-3-1 and FLRA-3-2 were purified in a second stage separation on a Buckyprep semipreparative column with 100% methanol eluent at 5 mL min^{-1} (Figure 2.7). The fraction collected between 18.2–19.3 min contained 98 mol% pure FLRA-3-1 in 1 mol% isolated yield. The fraction collected between 19.7–21.3 min contained 92 mol% pure FLRA-3-2 contaminated with FLRA-3-1 in 1 mol% isolated yield.

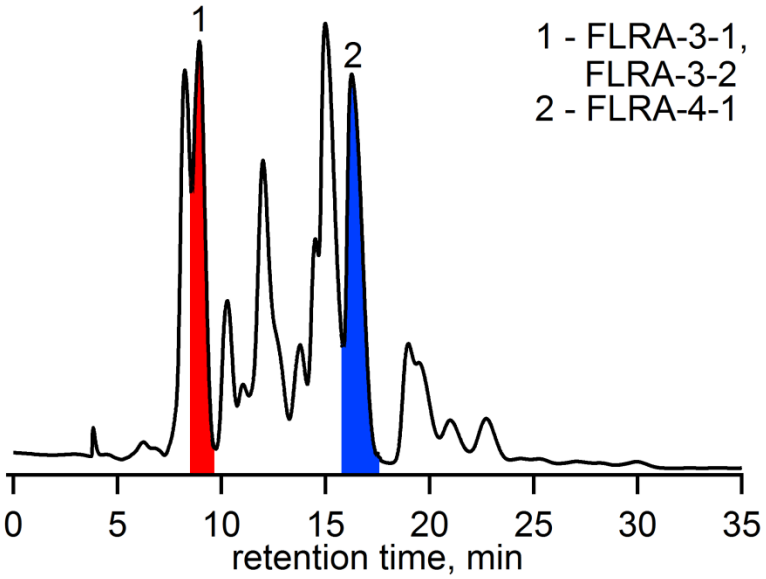

Figure 2.6. HPLC chromatogram of the FLRA$(CF_3)_n$ crude product mixture Rxn 4 in Table 2.1. The peak highlighted in red contained FLRA-3-1 and FLRA-3-2 and the peak highlighted in blue contained FLRA-4-1. Separation conditions: Buckyprep semiprep, 100% acetonitrile eluent, 5 mL min^{-1}, 300 nm detection.

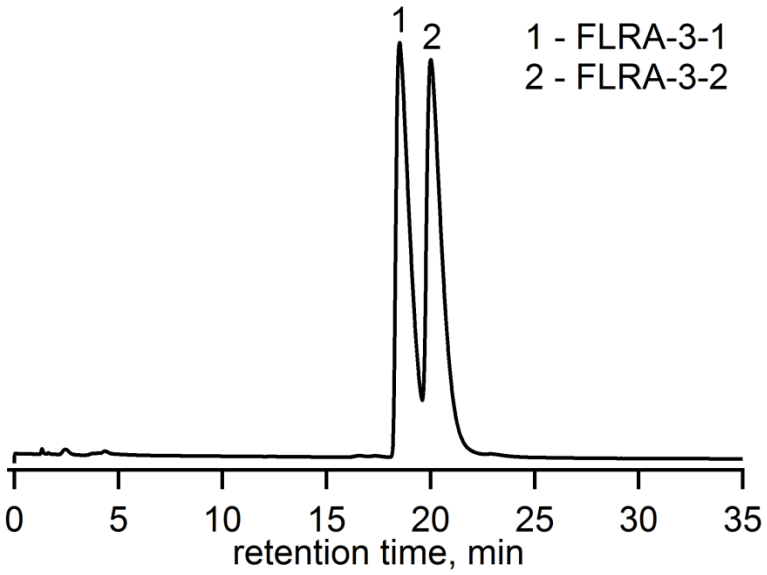

Figure 2.7. Second stage separation of FLRA-3-1 and FLRA-3-2. Mixture was from the 8.4–9.3 min fraction from the first separation stage of the crude product mixture from Rxn 4 in Table 2.1 (see Figure 2.6). Separation conditions: Buckyprep semiprep, 100% methanol eluent, 5 mL min^{-1}, 300 nm detection.

Attempts to separate the other predominant peaks from the first stage separation involved the use of a FluoroFlash column with mixtures of acetonitrile and water as the eluent. It is possible that using methanol eluent with the Buckyprep column could result in additional purified products, perhaps including some products where $n \geq 5$. When acetonitrile was used as the eluent fractions containing compounds with retention times > 20 min were observed and if methanol were to be used as the eluent these retention times would likely be longer due to the likely lower affinity of FLRA$(CF_3)_n$ for the more polar eluent. Therefore, it is still recommended that the first stage separation be completed in acetonitrile.

One trifluoromethylation of PHEN was performed (Table 2.1, Rxn 5) and produced 255.3 mg of crude product. According to analysis by mass spectrometry the crude mixture had a maximum value of $n = 6$ and a predominant n value of 5. The first stage of separation was performed on a Buckyprep preparative column with 100% acetonitrile eluent at 16 mL min^{-1} (Figure 2.8). The fraction collected between 8.5–9.9 min contained impure PHEN-4-1. The fraction collected

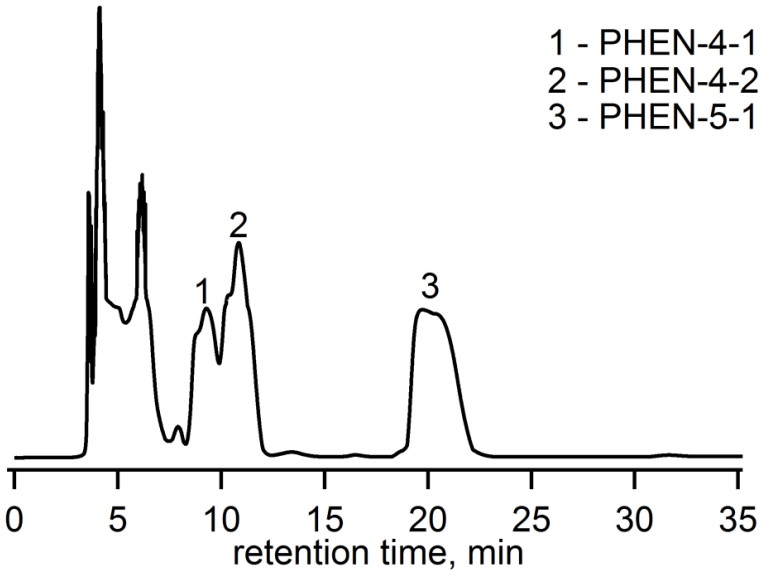

Figure 2.8. HPLC chromatogram of the PHEN$(CF_3)_n$ crude product mixture Rxn 5 in Table 2.1. Separation conditions: Buckyprep preparative, 100% acetonitrile eluent, 16 mL min^{-1}, 300 nm detection. The unusual shapes of the peaks are believed to be artifacts due to defects in the column packing.

between 9.9–11.7 min contained impure PHEN-4-2. The fraction collected between 18.8–21.0 min contained 95 mol% pure PHEN-5-1 in 13 mol% yield, based on starting PHEN.

The compounds PHEN-4-1 and PHEN-4-2 were ca. 90 mol% pure after the first stage of separation, so a second stage separation was attempted to increase the purity. These fractions were separated on a FluoroFlash analytical column with 100% acetonitrile eluent at 2 mL min^{-1} (Figure 2.9). In the second stage separation of PHEN-4-1, a fraction was collected between 3.4–4.5 min which contained 93 mol% pure PHEN-4-1 in 4 mol% yield based on starting PHEN, the main impurity is PHEN-4-2. In the second stage separation of PHEN-4-2, a fraction was collected between 3.3–4.5 min which contained 95 mol% pure PHEN-4-2 in 11 mol% yield, based on starting PHEN.

Two trifluoromethylation reactions were performed on the substrate PHNZ (Table 2.1 Rxns 6 and 7). The two reactions differed in the amount of starting PHNZ, the number of CF_3I equivalents, the temperature, and, most significantly, the reaction time. Rxn 6, the smaller-scale of the two reactions produced 41.3 mg of crude product which, based on mass spectrometry

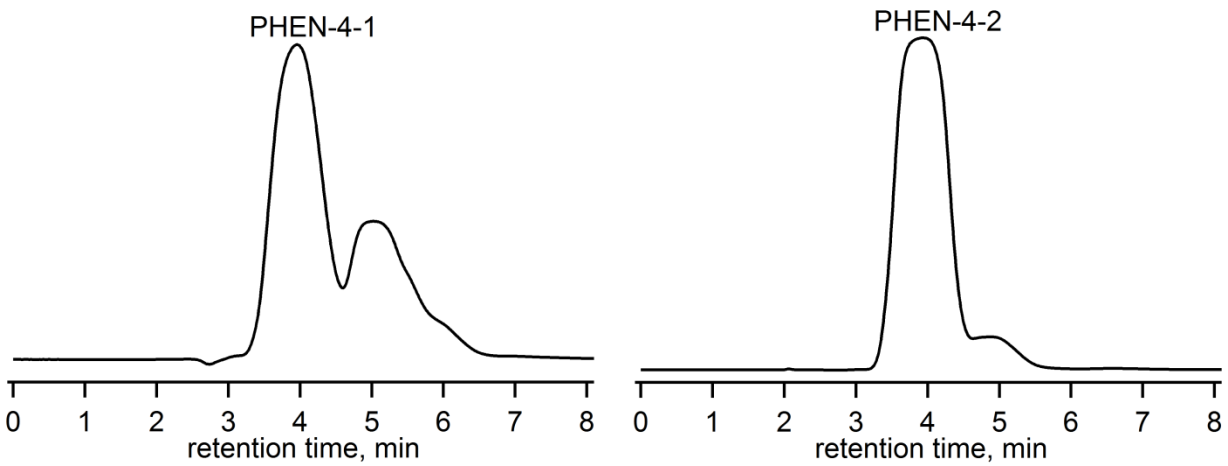

Figure 2.9. HPLC chromatograms of second stage separation of PHEN-4-1 and PHEN-4-2. PHEN-4-1 was from the 8.5–9.9 min fraction from the first separation stage of the crude product mixture from Rxn 5 in Table 2.1 (see Figure 2.8). PHEN-4-2 was from the 9.9–11.7 min fraction from the first separation stage of the crude product mixture from Rxn 5 in Table 2.1 (see Figure 2.8). Separation conditions were the same in both instances: FluoroFlash analytical, 100% acetonitrile eluent, 2 mL min^{-1}, 350 nm detection.

analysis, contained a maximum $n = 5$, and predominantly had a n value of 4. The first stage of separation of Rxn 6 was performed on a Buckyprep semipreparative column with 100% acetonitrile eluent at 5 mL min^{-1} (Figure 2.10). A fraction collected between 5.1–5.9 min contained a mixture of compounds. A fraction collected between 6.7–7.2 min contained impure PHNZ-3-1.

The first fraction collected in the first stage PHNZ$(CF_3)_n$ separation between 5.1–5.9 min was subjected to a second stage of separation on a Buckyprep semipreparative column with 80:20 v:v toluene:heptane eluent at 5 mL min^{-1} (Figure 2.11). A fraction was collected between 3.5–4.2 min which was still a mixture of compounds. This fraction underwent a third stage of separation on a Buckyprep semipreparative column with 100% methanol eluent at 5 mL min^{-1} (Figure 2.11). Four fractions were collected. Fraction 1 was collected between 8.5–9.3 min and contained 65 mol% PHNZ-2-1 and 35 mol% PHNZ-2-2 in a total yield of 3 mol%. Fraction 2 was collected between 11.7–12.5 min and contained 95 mol% pure PHNZ-3-2 in 6 mol% isolated yield, based on starting PHNZ. Fraction 3 was collected between 13.3–14.1 min and contained 98 mol% pure PHNZ-4-1 in 2 mol% isolated yield, based on starting PHNZ. Fraction

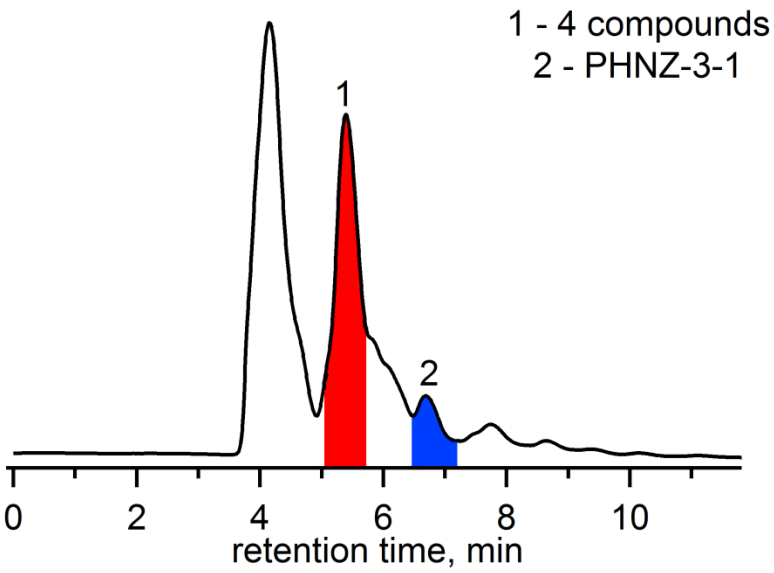

Figure 2.10. HPLC chromatogram of the PHNZ$(CF_3)_n$ crude product mixture Rxn 6 in Table 2.1. Separation conditions: Buckyprep semiprep, 100% acetonitrile eluent, 5 mL min^{-1}, 300 nm detection.

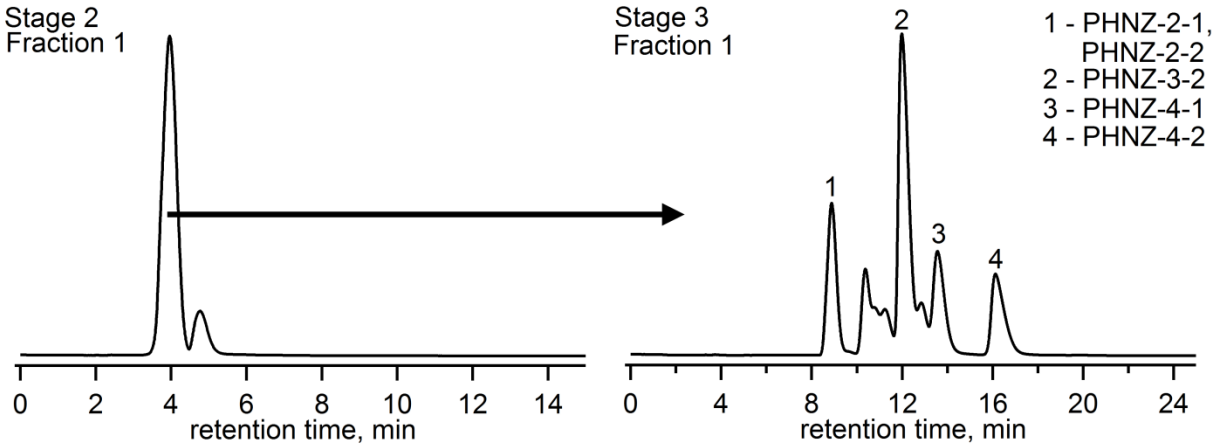

Figure 2.11. HPLC chromatograms of stage 2 (left) and stage 3 (right) separation of of the 5.1–5.9 min fraction from the first separation stage of the crude product mixture from Rxn 6 in Table 2.1 (see Figure 2.10). Stage 2 separation conditions: Buckyprep semiprep, 80:20 v:v toluene:heptane eluent, 5 mL min^{-1}, 300 nm detection. Stage 3 separation conditions: Buckyprep semiprep 100% methanol eluent, 5 mL min^{-1}, 370 nm detection.

4 was collected between 15.9–16.8 min and contained 98 mol% pure PHNZ-4-2 in 2 mol% yield, based on starting PHNZ. In the future the second stage separation could likely be skipped since all four isolated compounds co-eluted.

The second fraction collected between 6.7–7.2 min in the first stage PHNZ$(CF_3)_n$ separation (Rxn 6, Table 2.1) underwent a second stage separation on a Buckyprep semipreparative column using 80:20 v:v toluene:heptane eluent at 5 mL min^{-1} (Figure 2.12). A fraction was collected between 4.4–5.0 min and was still impure so a third stage of separation was performed. The third stage of separation used a Buckyprep semipreparative column with 100% methanol eluent at 5 mL min^{-1} (Figure 2.12). A fraction collected between 15.7–16.6 min contained 98 mol% pure PHNZ-3-1 in 1 mol% yield, based on starting PHNZ. For the isolation of PHNZ-3-1 the second stage separation could likely be omitted since only minor improvements in purity were gained. Overall, for PHNZ$(CF_3)_n$ separations with the Buckyprep and FluoroFlash columns it is likely that two stages of separation will remain necessary since, in methanol, on the Buckyprep column PHNZ-3-2 and PHNZ-4-2 would co-elute, but are separated in acetonitrile. The separation could likely be performed with either eluent to start, but would then require a second stage separation.

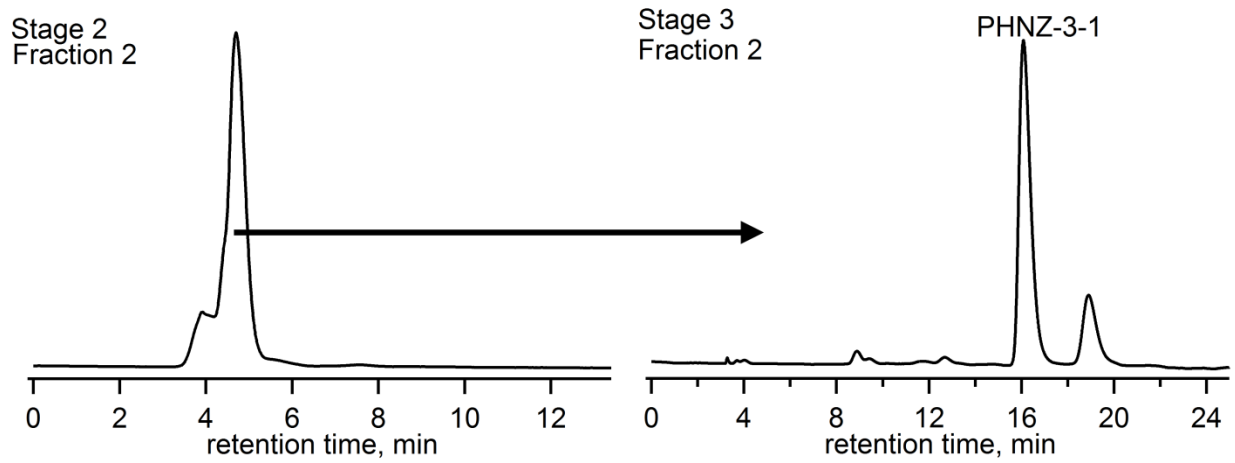

Figure 2.12. HPLC chromatograms of stage 2 (left) and stage 3 (right) separation of PHNZ-3-1 from Rxn 6 (Table 2.1). Mixture was from the 6.7–7.2 min fraction from the first separation stage of the crude product mixture from Rxn 6 in Table 2.1 (see Figure 2.10). Stage 2 separation conditions: Buckyprep semiprep 80:20 v:v toluene:heptane eluent, 5 mL min^{-1}, 300 nm detection. Stage 3 separation conditions: Buckyprep semiprep 100% methanol eluent, 5 mL min^{-1}, 370 nm detection.

The large-scale PHNZ trifluoromethylation reaction (Rxn 7, Table 2.1) produced 352.2 mg of crude product which, based on mass spectrometry analysis, contained a maximum $n = 6$ and a

predominant *n* value of 5. The first stage of separation was performed on a Buckyprep preparative column with 100% acetonitrile eluent at 20 mL min^{-1} (Figure 2.13). A fraction (1) collected between 4.0–4.4 min contained impure PHNZ-6-1 and PHNZ-6-2. A fraction (2) collected between 4.4–5.4 min contained a mixture of PHNZ-4-1, PHNZ-4-2, and PHNZ-5-1.

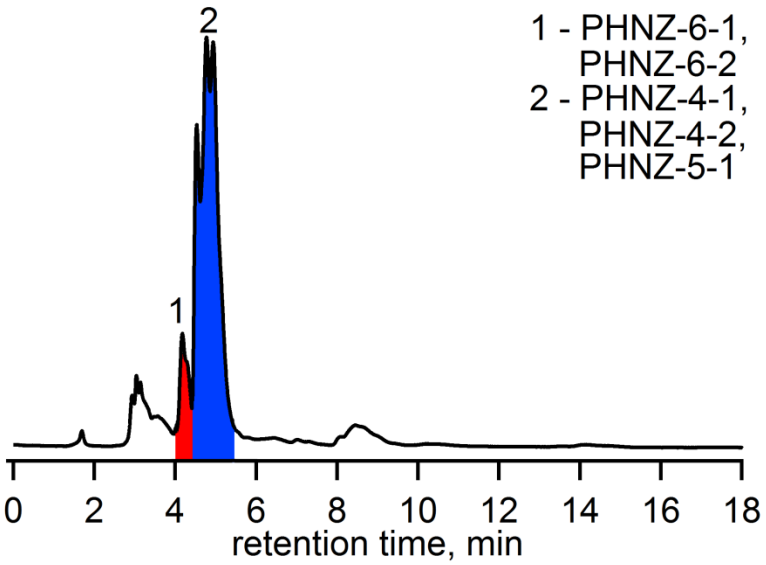

Figure 2.13. HPLC chromatogram of the large-scale PHNZ$(CF_3)_n$ crude product mixture Rxn 7 in Table 2.1. Separation conditions: Buckyprep prep, 100% acetonitrile eluent, 20 mL min^{-1}, 370 nm detection.

Fraction 1, which was collected between 4.0–4.4 min in the first stage separation, underwent a second stage of separation using a Buckyprep semipreparative column with 100% methanol eluent at 5 mL min^{-1} (Figure 2.14). A fraction collected between7.7–8.6 min contained 75 mol% PHNZ-6-1 and 25 mol% PHNZ-6-2 with a combined yield of 3 mol%, based on starting PHNZ. Crystals of PHNZ-6-1 were grown from this mixture and the substitution pattern of PHNZ-6-2 has been predicted based on the NMR spectra. From this information, the structures of PHNZ-6-1 and PHNZ-6-2 differ by the placement of only one CF_3 group (i.e., 1,2,4,6,8,9-PHNZ$(CF_3)_6$ and 1,2,4,6,7,9-PHNZ$(CF_3)_6$ Figure 2.15). It is expected that PHNZ-6-1 would be more polar and it is possible that these compounds could be isolated from each other on the basis of polarity, but this separation has not been attempted at this time.

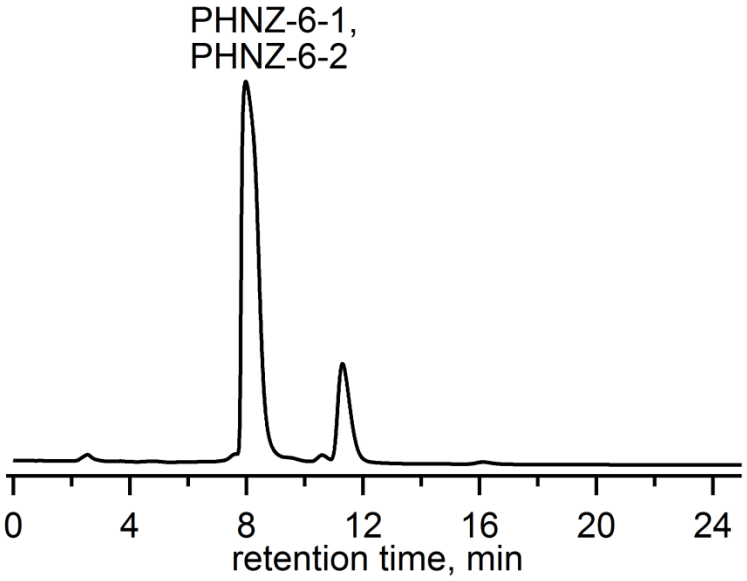

Figure 2.14. HPLC chromatogram from separation of PHNZ-6-1 and PHNZ-6-2. Mixture was from the 4.0–4.4 min fraction from the first separation stage of the crude product mixture from Rxn 7 in Table 2.1 (see Figure 2.13). Separation conditions: Buckyprep semiprep, 100% methanol eluent, 5 mL min^{-1}, 370 nm detection.

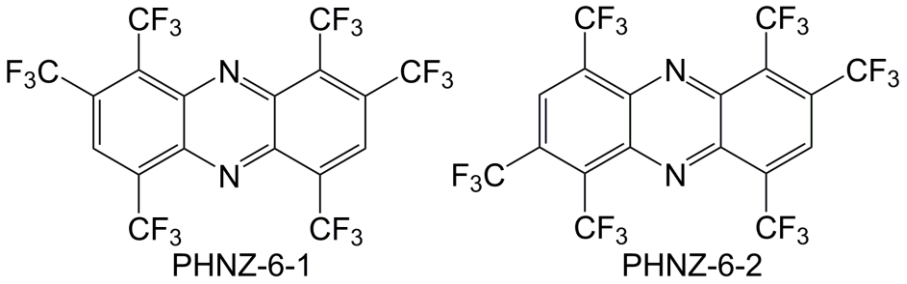

Figure 2.15. Drawings of the structures of PHNZ-6-1 and PHNZ-6-2. The structure of PHNZ-6-1 has been confirmed by single crystal X-ray diffraction. The structure of PHNZ-6-2 is predicted based on NMR spectra. These two compounds differ in the position of one CF_3 group.

Fraction 2, which was collected from 4.4–5.4 min in the first stage separation of the large-scale PHNZ$(CF_3)_n$ reaction (Rxn 7, Table 2.1), underwent a second stage separation using a Buckyprep semipreparative column with 100% methanol eluent at 4 mL min^{-1} (Figure 2.16). A fraction collected between 14.5–15.8 min contained 95 mol% pure PHNZ-5-1 in 6 mol% yield, based on starting PHNZ. A fraction collected between 16.1–17.5 min contained 97 mol% pure PHNZ-4-1 in 4 mol% yield, based on starting PHNZ. A fraction collected between 18.6–20.4 min contained 98 mol% pure PHNZ-4-2 in 7 mol% yield, based on starting PHNZ. The peak

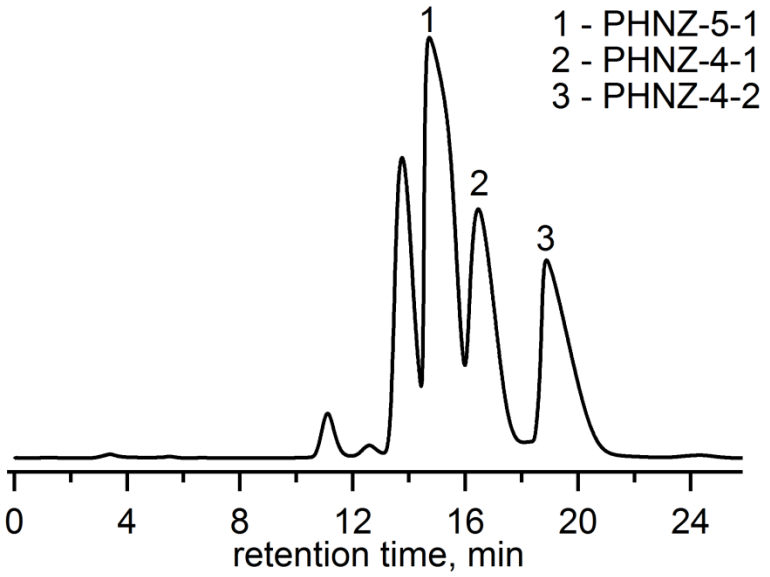

Figure 2.16. HPLC chromatograms of stage 2 separation of of the 4.4–5.4 min fraction from the first separation stage of the crude product mixture from Rxn 7 in Table 2.1 (see Figure 2.13). Separation conditions: Buckyprep semiprep, 100% methanol eluent, 4 mL min^{-1}, 370 nm detection.

collected between 13.3–14.3 min contains two PHNZ$(CF_3)_5$ compounds, based on NMR analysis, but these compounds have not been isolated.

The large-scale and small-scale PHNZ$(CF_3)_n$ reactions produced different product compositions. The large-scale reaction produced products with n values ≥ 4, whereas the small-scale reaction produced products with n values ≤ 4. From the small-scale to the large-scale the number of CF_3I equivalents increased from 8 to 10, the reaction temperature increased from 310 °C to 330 °C, and the reaction time increased from 33 min to 20 h. It is difficult to separate the effects of these changes, but it is clear that the reaction conditions impact the product composition and conditions designed to increase the n value such as higher equivalents, higher temperatures, and longer times resulted, in this case, in the desired higher n value products.

One reaction of PYRN with CF_3I was performed (Rxn 8, Table 2.1) and produced 180 mg of crude product. According to mass spectrometry the maximum number of additions was 7 and the predominant products had n = 5 and 6. Five PYRN$(CF_3)_n$ compounds were isolated from this reaction mixture over the course of three stages of separation. Stage 1 separation occurred using

a Buckyprep preparative column, 100% acetonitrile eluent at 20 mL min^{-1} (Figure 2.17). A fraction collected between 2.8–4.5 min contained impure PYRN-6-1. A fraction collected between 15.8–18.2 min contained 95 mol% pure PYRN-5-1 in 18 mol% yield, based on starting PYRN. A fraction collected between 20.1–22.8 min contained 70 mol% PYRN-5-2 and 30 mol% PYRN-5-3, with a combined yield of 9 mol% yield, based on starting PYRN. A fraction collected between 28.2–34.6 min contained impure PYRN-6-3. Based on NMR analysis, the large peak between 35–40 min contains $PYRN(CF_3)_4$, but these compounds have not been further separated.

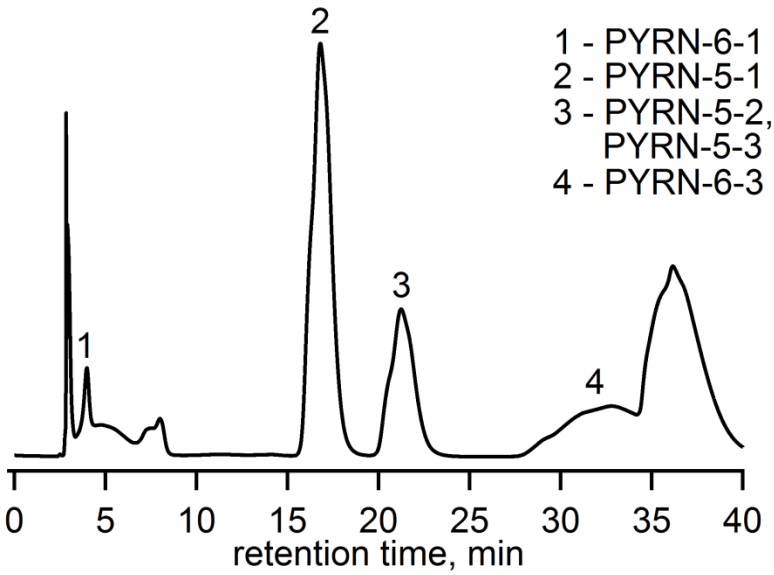

Figure 2.17. HPLC chromatogram of the $PYRN(CF_3)_n$ crude product mixture Rxn 8 in Table 2.1.. Separation conditions: Buckyprep preparative, 100% acetonitrile eluent, 20 mL min^{-1}, 370 nm detection. The unusual shapes of the peaks are believed to be artifacts due to defects in the column packing.

PYRN-6-1 was further purified using a FluoroFlash analytical column with 100% acetonitrile eluent at 2 mL min^{-1} (Figure 2.18). The fraction collected between 4.8–6.0 min contained 95 mol% pure PYRN-6-1 in 1 mol% isolated yield, based on starting PYRN. No other pure compounds have been isolated from this separation.

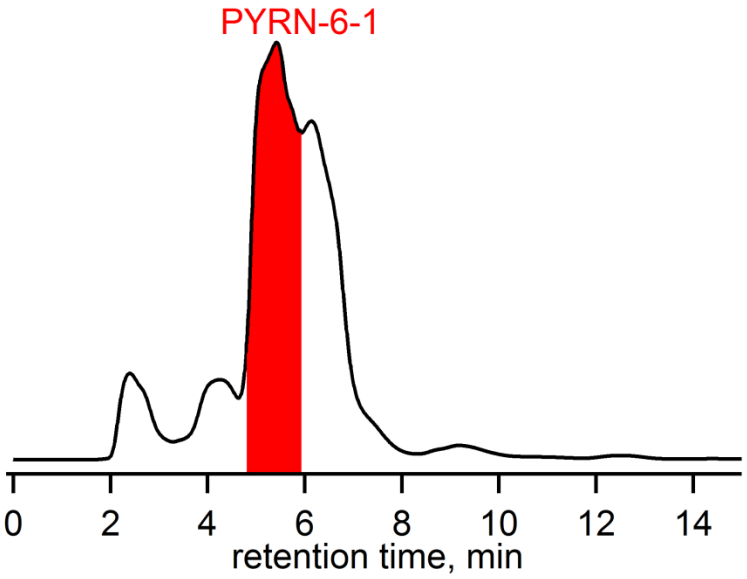

Figure 2.18. HPLC chromatogram of stage 2 separation of PYRN-6-1, PYRN-6-1 containing fraction highlighted in red. Mixture was from the 2.8–4.5 min fraction from the first separation stage of the crude product mixture from Rxn 8 in Table 2.1 (see Figure 2.17). Separation conditions: FluoroFlash analytical, 100% acetonitrile eluent, 2 mL min^{-1}, 300 nm detection.

The additional separation stages used to isolate pure PYRN-6-3 are shown in Figure 2.19. The second stage of separation was done on a FluoroFlash analytical column with 100% acetonitrile eluent at 2 mL min^{-1}. A fraction was collected between 6.1–6.7 minutes which contained impure PYRN-6-3. This fraction underwent a third stage of separation on a Buckyprep semipreparative column with 60:40 v:v toluene:heptane eluent at 5 mL min^{-1}. A fraction collected between 3.5–3.8 min contained 90 mol% pure PYRN-6-3 in < 1 mol% yield, based on starting PYRN. The other peak may contain another PYRN$(CF_3)_5$ compound, but the identity has not been confirmed. For future separations the second stage separation could be eliminated since separation of pure compounds was ineffective at this stage.

Based on the work performed here, the shape of the PAH core does play a minor role in the resulting products. For the reactions of ANTH and PHEN (Rxns 1 and 4 Table 2.1) the number of CF_3I equivalents was similar as was the reaction temperature and reaction time. Despite these similarities the product composition was different, with ANTH$(CF_3)_n$ products being comprised

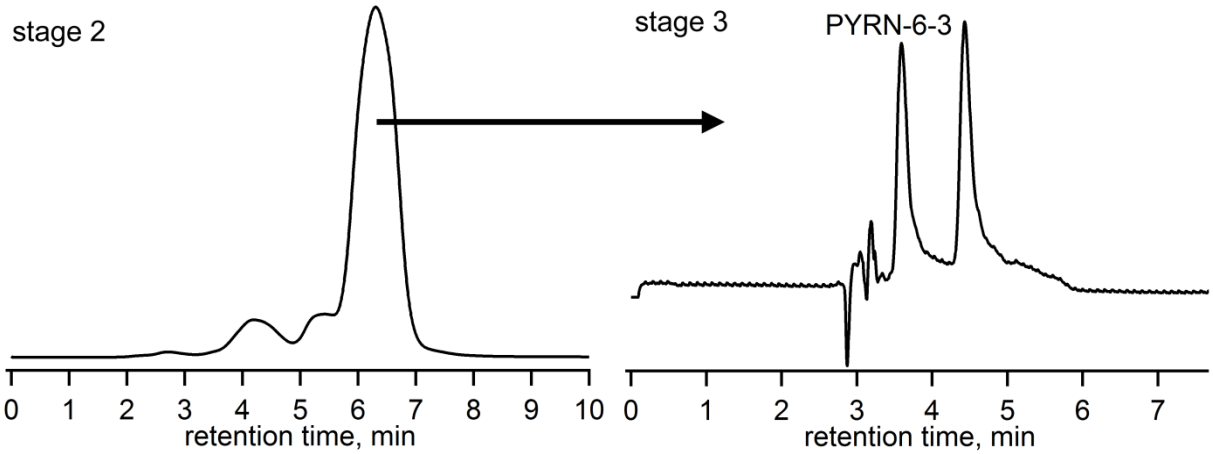

Figure 2.19. Stages 2 (left) and 3 (right) of the isolation of PYRN-6-3. Mixture was from the 28.2–34.6 min fraction from the first separation stage of the crude product mixture from Rxn 8 in Table 2.1 (see Figure 2.17). Stage 2 separation conditions: FluoroFlash analytical, 100% acetonitrile eluent, 2 mL min^{-1}, 300 nm detection. Stage 3 separation conditions: Buckyprep semiprep, 60:40 v:v toluene:heptane eluent, 5 mL min^{-1}, 370 nm detection.

mostly of n = 5, 6 whereas PHEN$(CF_3)_n$ products exhibited n values of 4 and 5. In the PHEN derivatives presented in this work there were no examples of CF_3 groups adding to the C4 or C5 position of the core. In contrast, there were examples of substitutions at every position in the ANTH derivatives studied in this work. There is a report in the literature[53] of radical attack on the C4 position of PHEN, suggesting that the C4 and C5 positions are not exempt from radical attack. A more exhaustive separation of the PHEN$(CF_3)_n$ reaction mixture may yield products with substitution at the C4 and/or C5 position, but these were not the major products. If CF_3 radicals have a low probability of adding to the C4 and C5 positions this means there are 8 carbons which are likely to experience CF_3 substitution. Substituting 6 CF_3 groups onto 8 carbons would lead to ≥ 75% substitution, which is rare, based on the PAH$(CF_3)_n$ products identified in the Strauss-Boltalina research group.

The presence of heteroatoms also impacted the product composition, likely because the number of carbons available for substitution has decreased. Even with fewer equivalents of CF_3I in the PHNZ large-scale reaction (Rxn 7 Table 2.1) than in the ANTH reactions (Rxns 1 and 2 Table 2.1), PHNZ derivatives with n = 6 were isolated. As mentioned previously ≥ 75%

substitution is rare, but it was observed in PHNZ$(CF_3)_6$ which is 75% substituted, leaving only 2 unsubstituted carbons. In comparison, ANTH$(CF_3)_6$ is only 60% substituted and this difference in the relative amount of substitution was likely at least partially responsible for the different abundances of these products in the two different reactions.

The product composition of PYRN$(CF_3)_n$ was similar to that ANTH$(CF_3)_n$ with n = 5 and 6. Although PYRN has 4 rings compared to 3 rings in ANTH, there were 10 carbons available for substitution in both compounds. However, substitution on the C2 and C7 positions is typically rare for PYRN derivatives because there is no HOMO and LUMO density on these positions in underivatized PYRN.[54] From the low probability of substitution onto 2 carbons one would expect a lower degree of substitution, as was observed in the PHEN$(CF_3)_n$ derivatives, but this was not the case as PYRN$(CF_3)_n$ derivatives maintained a higher degree of substitution (i.e., n values of 5 or 6). In the identified PYRN$(CF_3)_n$ products there was an example, PYRN-6-3, of a compound with substitution at the C2 position. Although this was a minor product, it means that substitution at these positions is possible and they are not completely unreactive. It is likely that the positions of the HOMO and LUMO change as the core is derivatized.

The presence of a 5 membered ring which contains a C(sp^3) atom, as observed in FLUR, produced products that were difficult to separate and only one pure product has been identified. The identified product had 5 CF_3 groups and was 50% substituted, including one substituent on the C(sp^3) atom. The short time (25 min) and low (7) number of equivalents of CF_3I that were used in the FLUR reaction (Rxn 3 Table 2.1) could lead to products with low n values and a large number of isomers for each composition. When reactions are run for a short time there is less time for molecules with low n values to react further. The proposed reaction mechanism involves a CF_3 radical adding to a carbon and subsequently another CF_3 radical removing the hydrogen from the same carbon. For this mechanism one CF_3 substitution would require two equivalents of CF_3I. Based on the results from the other reactions presented here, it seems likely that a narrower product distribution could be achieved by running a reaction with more CF_3I, pushing the products to higher n values which typically have fewer isomers. For both

PHEN$(CF_3)_n$ and FLUR$(CF_3)_n$ no products with CF_3 groups in the bay region have been identified. Trifluoromethyl groups have been identified on the bay region of perylene[50] so substitutions are possible on bay regions, but so far are considered unlikely on smaller (i.e., 3 ring) PAH cores.

The reaction of FLRA with CF_3I (Rxn 4 Table 2.1) also ran for a short time (17 min) and used a low (5) number of equivalents of CF_3I, and despite having 10 substitutable carbons, the only products identified so far have n = 3, 4. Due to the significantly different reaction conditions it is difficult to compare the two 4 ring systems studied here. For a better comparison the FLRA reaction should be repeated with 30 equivalents of CF_3I. It is recommended to make the FLRA reaction equivalent to the PYRN reaction because it is hypothesized that adding more equivalents will narrow the product distribution while also adding more electron-withdrawing groups and thereby increasing the EA of the products.

The Buckyprep stationary phase consists of 3-(1-pyrenyl)propyl groups bonded to silica and has a larger π system than the more typical phenol stationary phase. A larger π system can interact more strongly with the PAH$(CF_3)_n$ compounds and provide improved separation. Buckyprep columns are sold for fullerene separations which are typically done in relatively non-polar solvents such as toluene and hexane due, in part, to the very low solubility of fullerenes in polar solvents. The PAH$(CF_3)_n$ molecules investigated here have solubility in aromatic solvents as well as increased solubility, relative to fullerenes, in more polar solvents such as acetonitrile or methanol. Therefore, PAH$(CF_3)_n$ compounds have a wider variety of separation methodologies on a Buckyprep column than do fullerenes. It was found that typically by using a polar, non-aromatic solvent the PAH$(CF_3)_n$ molecules interacted more with the column. Only four separations were performed using toluene or toluene mixtures as the eluent and only one of those led to the isolation of a pure compound, PYRN-6-3.

The FluoroFlash stationary phase is perfluorooctylethylsilyl bonded to silica and is reported to separate compounds based on fluorine content.[55] This reported separation is based on increasing fluoroalkyl chain length. In this work the FluoroFlash column did not routinely show

increased retention time for increased number of CF_3 groups. In this work seven separations were completed on the FluoroFlash column, and six of these separations resulted in the isolation of pure compounds. The FluoroFlash column can be useful for isolating pure PAH$(CF_3)_n$ compounds, however, frequently the peaks of interest are not well separated under the conditions investigated here (Figures 2.3, 2.9, 2.18, and 2.19) and therefore peaks must be selected carefully and collection times must be controlled to decrease contamination from overlapping peaks and may result in lower isolated yields than would be possible with improved separation techniques. For some separations methanol eluent on a Buckyprep column may be productive and should be investigated further.

Once pure compounds have been isolated, the CF_3 groups provide insight, via ^{19}F NMR spectroscopy, into the substitution pattern of the PAH derivative. Examples of the way NMR spectra are used in structure assignments are shown in Figures 2.20 and 2.21. Trifluoromethyl groups within three carbons of each other result in quartets in the ^{19}F NMR and CF_3 groups with two CF_3 neighbors present an apparent septet, or quartet of quartets. This fluorine-fluorine coupling can even occur across a fissure as seen in PYRN-6-1 (Figure 2.21). The shift of the groups is also determined by the position on the PAH core, similar to what is observed in ^1H NMR for non-substituted PAHs, the relationship between position and being shielded or deshielded follows a similar pattern for ^{19}F NMR and ^1H NMR spectra. For example, in ANTH$(CF_3)_n$ structures, any CF_3 groups on the 9 or 10 position are more deshielded (δ −50 to −51) than those on the outer rings (δ −63 to −67). The ^{19}F and ^1H shifts of all isolated PAH$(CF_3)_n$ compounds are listed in Table 2.2. Structures which were predicted based on NMR spectra, but not yet confirmed by X-ray are shown in Figure 2.22. Structures confirmed by X-ray diffraction will be discussed later.

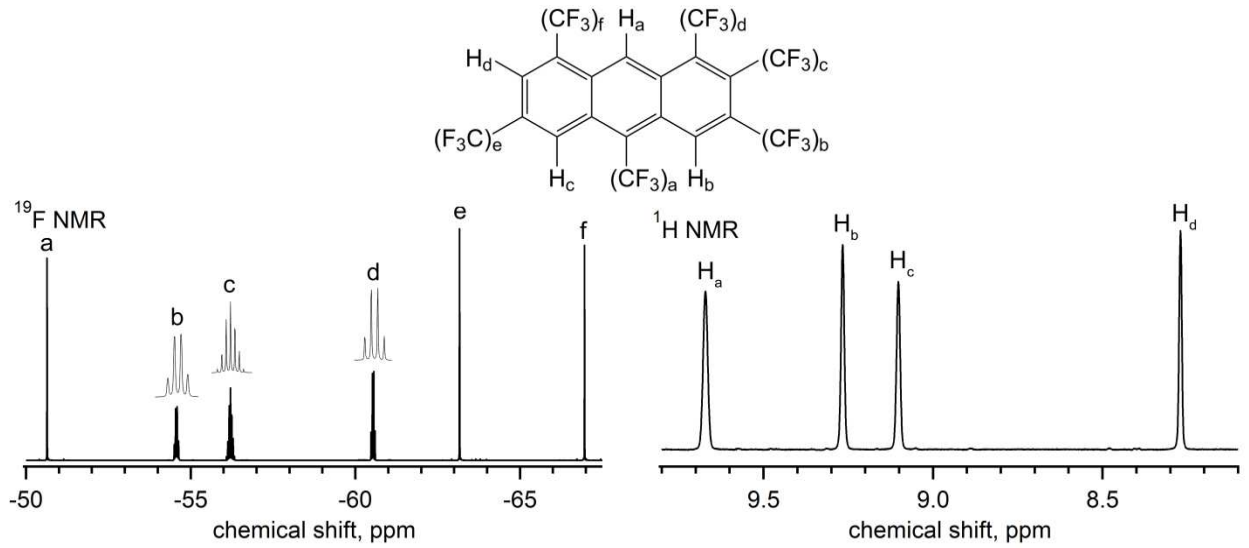

Figure 2.20. Assignment of NMR peaks for ANTH-6-2. The ANTH-6-2 molecule is shown at the top. The ^{19}F NMR spectrum ($CDCl_3$, 376 MHz, $\delta(C_6F_6) = -164.9$) is shown on the left (insets show the structure of the multiplets) and the ^{1}H NMR spectrum ($CDCl_3$, 399 MHz, $\delta(CHCl_3) = 7.27$) is shown on the right.

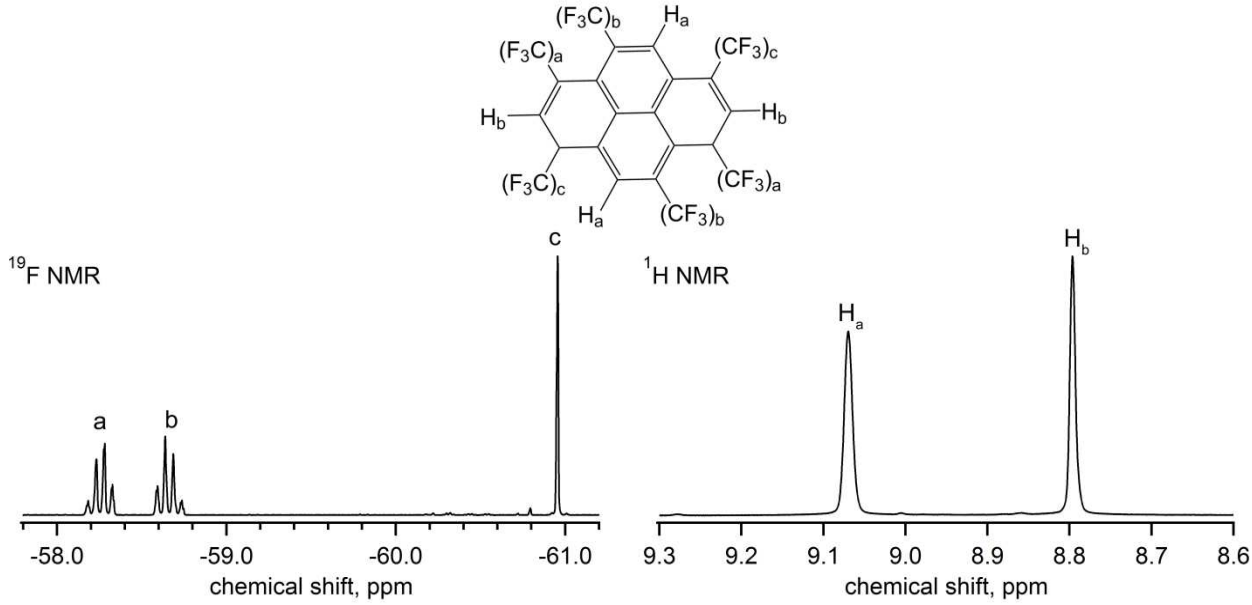

Figure 2.21. Assignment of NMR peaks for PYRN-6-1. The PYRN-6-1 molecule is shown at the top. The ^{19}F NMR spectrum ($CDCl_3$, 376 MHz, $\delta(C_6F_6) = -164.9$) is shown on the left and the ^{1}H NMR spectrum ($CDCl_3$, 399 MHz, $\delta(CHCl_3) = 7.27$) is shown on the right. Notice that fluorine-fluorine coupling occurs across the fissure for $(CF_3)_a$ and $(CF_3)_b$.

Table 2.2. ^{19}F and ^{1}H shifts of all identified PAH$(CF_3)_n$ compounds[a]

ANTH-4-1 ^{19}F: −62.4 (s, $2CF_3$), −65.4 (s, $2CF_3$) ^{1}H: 9.22 (s, 2H), 8.46 (s, 2H), 8.32 (s, 2H)	ANTH-5-1 ^{19}F: −50.4 (s, $1CF_3$), −63.3 (s, $2CF_3$), −66.8 (s, $2CF_3$) ^{1}H: 9.55 (s, 1H), 9.11 (s, 2H), 8.23 (s, 2H)	ANTH-6-1 ^{19}F: −51.2 (s, $2CF_3$), −63.5 (s, $4CF_3$) ^{1}H: 9.17 (s, $4CF_3$)	ANTH-6-2 ^{19}F: −50.6 (s, $1CF_3$), −54.6 (q, 15 Hz, 1 CF_3), −56.2 (as/qq, 15 Hz, $1CF_3$), −60.5 (q, 15 Hz, $1CF_3$) −63.2 (s, $1CF_3$), −67.0 (s, $1CF_3$) ^{1}H: 9.67 (s, 1H), 9.27 (s, 1H), 9.10 (s, 1H), 8.27 (s, 1H)
ANTH-6-3 ^{19}F: −56.3 (q, 16 Hz, $1CF_3$), −60.1 (q, 16 Hz, $1CF_3$), −64.0 (s, $1CF_3$) ^{1}H: 9.79 (s, 1H) 9.36 (s, 1H) 8.41 (s, 2H)	ANTH-6-4 ^{19}F: −56.5 (q, 16 Hz, $1CF_3$), −60.2 (q, 16 Hz, $1CF_3$), −63.8 (s, $1CF_3$), ^{1}H: 9.58 (s, 2H) 8.39 (s, 2H)	FLRA-3-1 ^{19}F: −61.1 (s, $1CF_3$), −62.9 (s, $1CF_3$), −65.9 (s, $1CF_3$) ^{1}H: 8.39 (d, 8 Hz, 1H), 8.35 (d, 8 Hz, 1H), 8.25 (d, 8 Hz, 1H), 8.11 (d, 8 Hz, 1H), 8.00 (d, 9 Hz, 1H), 7.76 (d, 8 Hz, 1H), 7.59 (t, 7 Hz, 1H)	FLRA-3-2 ^{19}F: −61.1 (s, $1CF_3$), −63.5 (s, $1CF_3$), −63.8 (s, $1CF_3$) ^{1}H: 8.23 (s, 1H), 8.15 (d, 8 Hz, 1H) 8.17 (um, 2H), 7.99 (d, 9 Hz, 1H), 7.51 (um, 2H)
FLRA-4-1 ^{19}F: −61.2 (s, $1CF_3$), −63.2 (s, $1CF_3$), −63.4 (s, $1CF_3$), −66.2 (s, $1CF_3$) ^{1}H: 8.39 (s, 1H), 8.32 (d, 1H), 8.30 (s, 1H), 8.26 (um, 1H) 8.06 (d, 1H) 7.78 (um, 1H)	FLUR-5-1 ^{19}F: −62.4 (q, 12 Hz, $1CF_3$), −62.7 (q, 12 Hz, $1CF_3$), −64.8 (s, $1CF_3$) −65.8 (s, $1CF_3$) −69.9 (d, 8 Hz, $1CF_3$) ^{1}H: 8.66 (s, 1H), 8.27 (s, 1H), 8.24 (s, 1H), 8.17 (s, 1H) 4.87 (q, 8 Hz, 1H)	PHEN-4-1 ^{19}F: −62.4 (s, $2CF_3$), −65.4 (s, $2CF_3$) ^{1}H: 9.22 (s, 2H), 8.46 (s, 2H), 8.32 (s, 2H)	PHEN-4-2 ^{19}F: −62.0 (s, $1CF_3$), −63.9 (s, $1CF_3$), −65.6 (s, $1CF_3$), −65.6 (s, $1CF_3$) ^{1}H: 9.19 (s, 1H), 9.03 (s, 1H) 8.67 (s, 1H) 8.46 (d, 9 Hz, 1H), 8.31 (s, 1H), 8.06 (d, 9Hz, 1H)

[a] ^{19}F NMR: 376.5 MHz, $CDCl_3$,shifts referenced to internal standard: C_6F_6 (δ −164.9) or 1,4-bis(trifluoromethyl)benzene (δ −66.4). ^{1}H NMR 399 MHz, $CDCl_3$, shifts referenced to residual $CHCl_3$ (δ 7.27). Abbreviation: s, singlet; d, doublet; t, triplet; q, quartet; as/qq, apparent septet or quartet of quartets; um, broad unresolved multiplet. Table continues on next page.

PHEN-5-1 ^{19}F: −62.0 (s, 1CF_3), −62.3 (q, 12 Hz, 1CF_3), −62.6 (q, 12 Hz, 1CF_3) −63.7 (s, 1CF_3), −65.7 (s, 1CF_3) ^{1}H: 9,26 (s, 1H), 9.23 (s, 1H), 8.82 (s, 1H), 8.80 (s, 1H), 8.41 (s, 1H)	PHNZ-2-1 ^{19}F: −63.4 (s, 2CF_3) ^{1}H: d: 8.55 (9 Hz, 1H), d: 8.29 (7 Hz, 1H) t: 7.95 (8 Hz, 1H)	PHNZ-2-2 ^{19}F: −63.9 (s, 2CF_3) ^{1}H: 8.37 (um, 2H), 8.25 (s, 2H) 7.98 (um, 2H)	PHNZ-3-1 ^{19}F: −64.1 (s, 1CF_3), −64.3 (s, 1CF_3), −66.6 (s, 1CF_3) ^{1}H: 8.80 (s, 1H), 8.50 (d, 9 Hz, 1H), 8.40 (s, 1H) 8.37 (d, 7 Hz, 1H) 8.04 (t, 8 Hz, 1H)
PHNZ-3-2 ^{19}F: −64.0 (s, 1CF_3), −64.0 (s, 1CF_3), −64.5 (s, 1CF_3) ^{1}H: 8.56 (d, 9 Hz, 1H), 8.35 (d, 7 Hz, 1H), 8.32 (s, 2 H), 8.03 (t, 8 Hz, 1H)	PHNZ-4-1 ^{19}F: −64.0 (s, 1CF_3), −64.3 (s, 1CF_3), −64.5 (s, 1CF_3), −66.7 (s, 1CF_3) ^{1}H: 8.91 (s, 1H), 8.46 (s, 1H), 8.41 (s, 2H)	PHNZ-4-2 ^{19}F: −64.5 (s, 4CF_3) s: 8.40 (s, 4H)	PHNZ-5-1 ^{19}F: −57.4 (q, 15 Hz, 1CF_3), −60.4 (q, 15 Hz, 1CF_3) −64.5 (s, 1CF_3), −64.6 (s, 2CF_3) ^{1}H: 8.67 (s, 1H), 8.46 (um, 2H)
PHNZ-6-1 ^{19}F: −57.5 (q, 15 Hz, 2CF_3), −60.4 (q, 15 Hz, 2CF_3) −64.6 (s, 2CF_3) ^{1}H: 8.71 (s, 1H)	PHNZ-6-2 ^{19}F: −57.5 (q, 16 Hz, 2CF_3), −60.5 (q, 16 Hz, 2CF_3) −64.6 (s, 2CF_3) ^{1}H: 8.69 (s, 1H)	PYRN-5-1 ^{19}F: −57.6 (q, 19 Hz, 1CF_3), −58.4 (q, 19 Hz, 1CF_3) −60.3 (s, 1CF_3), −60.7 (s, 1CF_3), −60.9 (s, 1CF_3) ^{1}H: 9.12 (s, 1H), 8.84 (s, 1H), 8.83 (s, 1H), 8.80 (um, 2H)	PYRN-5-2 ^{19}F: −57.9 (q, 18 Hz, 1CF_3), −58.4 (q, 19 Hz, 1CF_3) −60.4 (s, 1CF_3), −60.7 (s, 1CF_3), −63.6 (s, 1CF_3) ^{1}H[b]
PYRN-5-3 ^{19}F: −57.7 (q, 19 Hz, 1CF_3), −58.3 (q, 19 Hz, 1CF_3), −60.6 (s, 1CF_3), −60.9 (s, 1CF_3), −63.5(s, 1CF_3) ^{1}H[b]	PYRN-6-1 ^{19}F: −58.3 (q, 17 Hz, 2CF_3), −58.7 (q, 17 Hz, 2CF_3), −60.5 (s, 2CF_3) ^{1}H: 9.07 (s, 2H), 8.80 (s, 2H)	PYRN-6-3 ^{19}F: −53.9 (q, 16 Hz, 1CF_3), −58.3 (q, 16 Hz, 1CF_3), −58.9 (q, 19 Hz, 1CF_3), −60.4 (q, 15 Hz, 1CF_3), −60.7 (s, 1CF_3), −63.5 (s, 1CF_3) ^{1}H: 9.21 (s, 1H), 9.15 (um, 1H), 9.11 (s, 1H), 8.88 (s, 1H)	

[a] ^{19}F NMR: 376.5 MHz, $CDCl_3$, shifts referenced to internal standard: C_6F_6 (δ −164.9) or 1,4-bis(trifluoromethyl)benzene (δ −66.4). ^{1}H NMR 399 MHz, $CDCl_3$, shifts referenced to residual $CHCl_3$ (δ 7.27). [b] These two compounds have not been isolated from each other and the ^{1}H NMR signals could not be distinguished. Abbreviation: s, singlet; d, doublet; t, triplet; q, quartet; as/qq, apparent septet or quartet of quartets; um, broad unresolved multiplet.

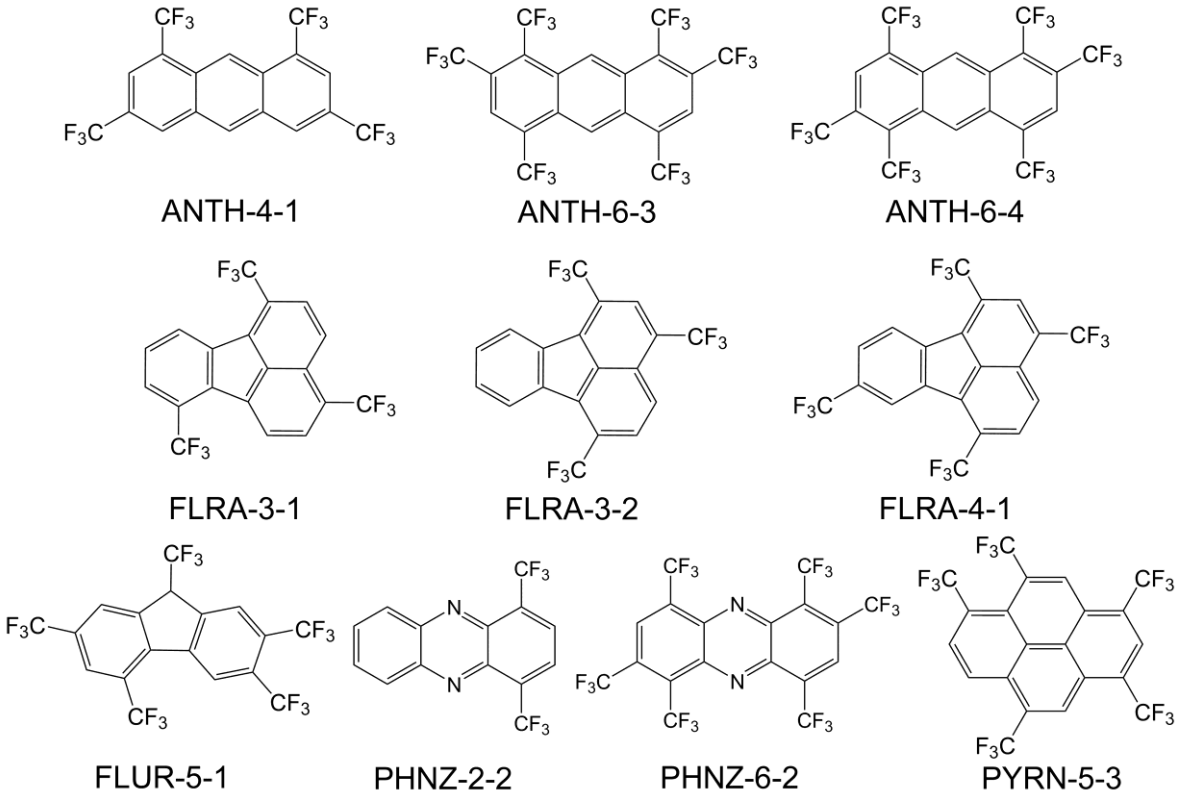

Figure 2.22. Drawings of structures for PAH$(CF_3)_n$ predicted based on NMR spectra. These predictions have not yet been confirmed by single crystal X-ray diffraction.

2.2.2. Electrochemistry and Electron Affinity

The substitution of an electron-withdrawing group onto a PAH core is known to result in molecules with enhanced electron acceptor properties, better air-stability, and improved solid-state charge-carrier mobilities.[5,56-59] In this work the reduction potential, $E_{1/2}$, and the gas-phase EA of CF_3 derivatives of ANTH, FLRA, PHEN, PHNZ, and PYRN have been studied. From these studies it has been determined there is a regular, linear increase in both the $E_{1/2}$ and the EA with the number of CF_3 substitutions on the PAH core. The effect of substitution pattern on $E_{1/2}$ and EA values depends on the PAH core. All of the reduction potentials and electron affinity measurements are listed in Table 2.3. IUPAC locants used in Table 2.3 are defined in Figure 2.1.

For the unsubstituted PAH cores studied in this work $E_{1/2}$ values range from −3.10 to −1.74 V vs $Fe(Cp)_2^{+/0}$. In contrast, for PAH$(CF_3)_n$ compounds the $E_{1/2}$ values range from −1.71 to −0.46 V vs $Fe(Cp)_2^{+/0}$. Some representative cyclic voltammograms (CVs) are shown in Figure

Table 2.3. Reduction potentials and electron affinity measurements

cmpd	abbreviation	gas-phase EA,[a] eV	$E_{1/2}$, V vs $Fe(Cp)_2^{+/0}$
anthracene	ANTH	0.53(2)[11,12]	−2.52
1,3,6,8,10-ANTH$(CF_3)_5$	ANTH-5-1	2.40(2)	−1.24
2,3,6,7,9,10-ANTH$(CF_3)_6$	ANTH-6-1	2.81(2)	−0.92
1,2,3,6,8,10-ANTH$(CF_3)_6$	ANTH-6-2	2.68(2)	−0.98
fluoranthene	FLRA	0.630[b,60]	−2.31
FLRA$(CF_3)_3$[c]	FLRA-3-1	—	−1.58
FLRA$(CF_3)_3$[c]	FLRA-3-2	—	−1.45
FLRA$(CF_3)_4$[c]	FLRA-4-1	2.28(1)	−1.26
phenanthrene	PHEN	−0.01(4)[61]	−3.10
1,3,6,8-PHEN$(CF_3)_4$	PHEN-4-1	—	−1.96
1,3,6,9-PHEN$(CF_3)_4$	PHEN-4-2	—	−1.83
1,3,6,7,9-PHEN$(CF_3)_5$	PHEN-5-1	1.95(2)	−1.71
phenazine	PHNZ	1.3(1)[10]	−1.74[d]
PHNZ$(CF_3)_2$	mixture of isomers	2.00(2)	−1.21
2,4,6-PHNZ$(CF_3)_3$	PHNZ-3-1	2.37(2)	−1.07
1,4,6-PHNZ$(CF_3)_3$	PHNZ-3-2	2.30(2)	−1.12
1,4,6,8-PHNZ$(CF_3)_4$	PHNZ-4-1	2.65(1)	−0.92
1,4,6,9-PHNZ$(CF_3)_4$	PHNZ-4-2	2.60(1)	−0.97
1,2,4,6,9-PHNZ$(CF_3)_5$	PHNZ-5-1	2.93(1)	−0.71
PHNZ$(CF_3)_6$	mixture of isomers	3.24(2)	−0.46
pyrene	PYRN	0.41(1)[62]	−2.65
1,3,4,6,8-PYRN$(CF_3)_5$	PYRN-5-1	2.44(2)	−1.25
1,3,4,6,9-PYRN$(CF_3)_5$	PYRN-5-2	2.38(2)	−1.27
1,3,4,6,8,9-PYRN$(CF_3)_6$	PYRN-6-1	2.71(2)	−1.01
1,2,4,6,8,9-PYRN$(CF_3)_6$	PYRN-6-3	—	−1.05

[a] Uncertainty in the least significant digit shown in parentheses. [b] Uncertainty not reported. [c] Substitution pattern not known at this time. [d] Irreversible reduction, $E_{1/2}$ estimated from square wave voltammetry.

2.23. The change in reduction potential as a function of the number of CF_3 groups is dependent on the core. The trend for the 3 and 4 ring systems ANTH (3 ring), PHEN (3 ring), FLRA (4 ring), and PYRN (4 ring) are 0.26 V/CF_3 group, 0.29 V/CF_3 group, 0.26 V/CF_3 group, and 0.27 V/CF_3 group respectively.

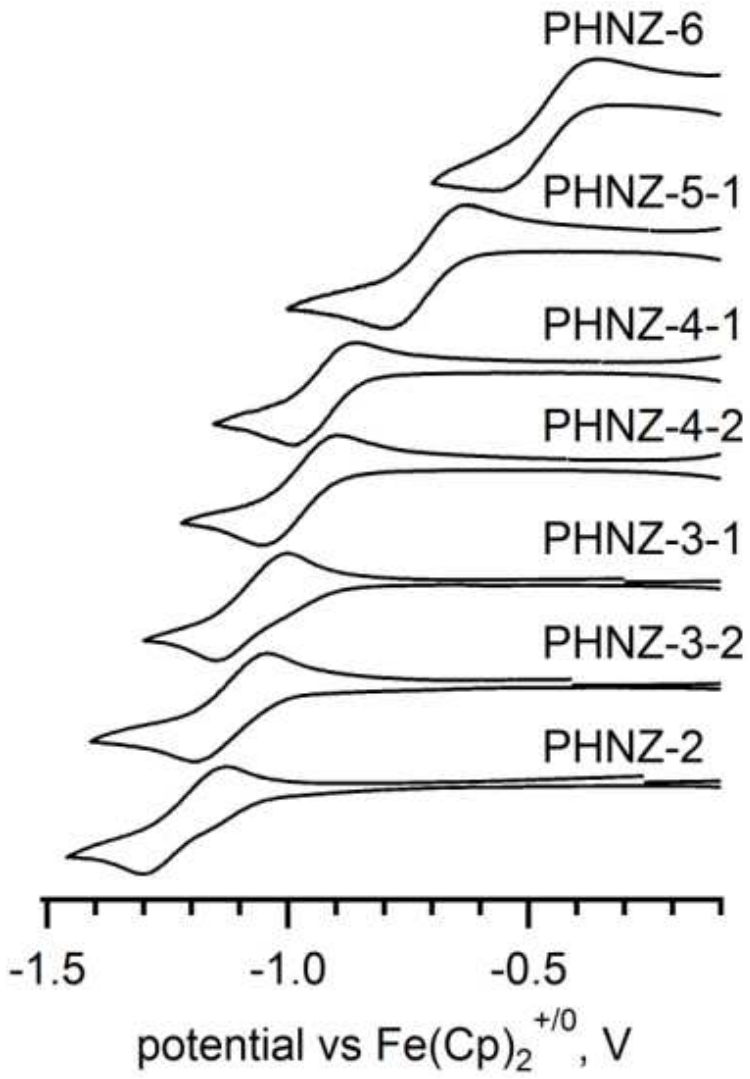

Figure 2.23. Representative cyclic voltammograms of PHNZ$(CF_3)_n$ compounds. (0.1 M N(*n*-Bu)$_4ClO_4$ in dimethoxyethane, 500 mV sec^{-1})

Among these 3 and 4 ring systems, with 12–16 total C atoms, the trend in reduction potential as a function of the number of CF_3 groups is very similar and does not appear to be dependent on shape or the number of rings in the system.

The effect of the number of CF_3 groups is much higher in the two-ring system, naphthalene$(CF_3)_n$ ($C_{10}H_{8-n}(CF_3)_n$) with a change of 0.37 V/CF_3.[51] In contrast the effect is less for the larger five ring system, PERY$(CF_3)_n$ ($C_{20}H_{12-n}(CF_3)_n$), where the change is 0.20 V/CF_3.[50] Aside from the similarity in 3 and 4 ring systems, in general, as the PAH core gets larger the CF_3 groups are less effective at withdrawing electron

density from the aromatic rings leading to lower magnitude increases in the reduction potential as a function of the number of CF_3 groups. The heterocyclic PHNZ core does not follow the same trend as the 3 and 4 ring systems, instead these derivatives show a 0.20 V/CF_3 group change in reduction potential (Figure 2.23). This suggests that the N atoms in the core diminish the electron-withdrawing effect of the CF_3 groups possibly by donating electron density back into the aromatic system.

The effect of substitution pattern on the reduction potential is dependent on the PAH core. The substitution pattern had a significant impact on the $E_{1/2}$ of derivatives of FLRA and PHEN. Between isomers of FLRA$(CF_3)_3$ and PHEN$(CF_3)_4$ the $E_{1/2}$ values changed by 0.13 V. In contrast, for derivatives of ANTH, PHNZ, and PYRN the difference between isomers was ≤ 0.06 V. For a selection of PERY$(CF_3)_5$ isomers the $E_{1/2}$ values differed by up to 0.14 V.[50] These data suggest that PAH cores that only have fissures between rings exhibit less pronounced isomer effects on the solution reduction potential.

The EA values, shown in Table 2.3, for the all-carbon PAH cores are very low, all less than 0.6 eV, the azaacene PHNZ exhibits a much higher EA of 1.31 eV. Importantly, the CF_3 derivatives of PAHs show a nearly-linear incremental increase in EA with increasing number of CF_3 groups substituted on the core. This regular increase in EA allows for the EA of a new compound to be predicted, as long as the increase per CF_3 group is known for a given core. The increase in EA with increasing number of CF_3 groups in PAHs was dependent, to some extent, on the size of the parent PAH, similar to the change in reduction potential. The fewer C atoms in the PAH core the larger the increase in EA. For 6 ring corannulene derivatives ($C_{20}H_{10-n}(CF_3)_n$) the DFT-predicted change is 0.20 eV/CF_3 group.[63] Derivatives of a 20 carbon PAH with only 5 rings, PERY ($C_{20}H_{12-n}(CF_3)_n$) showed a change of 0.25 eV/CF_3 group.[50] For 3 ring ANTH ($C_{14}H_{10-n}(CF_3)_n$), 3 ring PHEN ($C_{14}H_{10-n}(CF_3)_n$), 4 ring FLRA ($C_{16}H_{10-n}(CF_3)_n$, and 4 ring PYRN ($C_{16}H_{10-n}(CF_3)_n$) derivatives the change was 0.37 eV/CF_3, 0.39 eV/CF_3, 0.41 V/CF_3, and 0.39 eV/CF_3, respectively. The EA increase values for FLRA and PHEN derivatives are each based on the two data points available at this time and may change if additional EA data is collected. Similar to the $E_{1/2}$ trend the presence of heteroatoms in the PAH core affected the EA trend. For

PHNZ ($C_{12}H_{8-n}(CF_3)_n$) derivatives the EA trend was attenuated to 0.32 V/CF_3 group. This result supports the hypothesis that the N atoms are donating electron density back into the aromatic system. Representative photoelectron spectra are shown in Figure 2.24. The experimental result of 0.37 eV/CF_3 for ANTH$(CF_3)_n$ matched well with a theoretical prediction of 0.35 eV/CF_3 group from Sun and co-workers.[5]

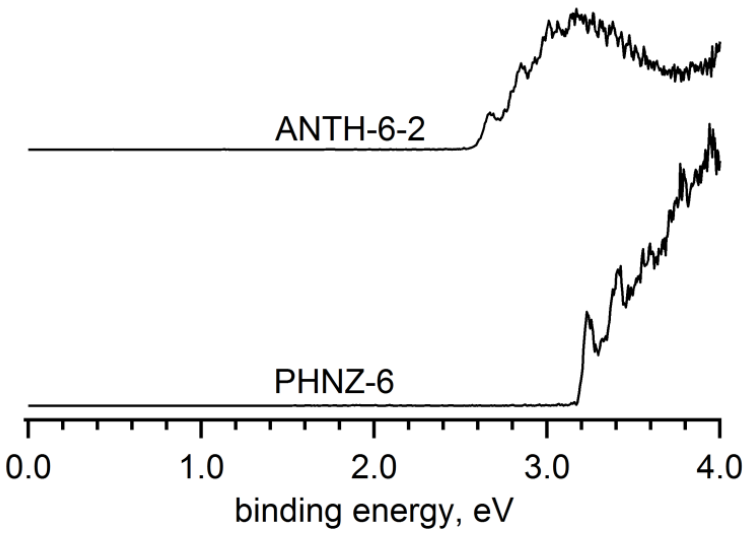

Figure 2.24. Low-temperature photoelectron spectra (20 K, 266 nm) of ANTH-6-2 and PHNZ-6.

The effect the N atoms have on the electronic properties can be investigated most directly by comparing PHNZ and its all-carbon analog ANTH (Figure 2.25). The relative difference in $E_{1/2}$ between ANTH$(CF_3)_n$ and PHNZ$(CF_3)_n$ is attenuated as additional groups are added to the core, the difference started at 0.81 V when there are no CF_3 groups and decreased to 0.46 or 0.52 V for ANTH$(CF_3)_6$ and PHNZ$(CF_3)_6$. The difference in EA as a function of the number of CF_3 groups for ANTH$(CF_3)_n$ and PHNZ$(CF_3)_n$ compounds was also attenuated as more CF_3 groups are added, it started at 0.78 eV for n = 0 and decreased to 0.43 or 0.56 eV for n = 6.

The effect of substitution pattern on EA can be assessed for ANTH, PHNZ, and PYRN. The largest difference is observed for ANTH$(CF_3)_6$ compounds which differ by 0.13 eV. The rest of the isomer pairs differ by ≤ 0.07 eV. Trifluoromethyl derivatives of PERY show a similar insensitivity of the EA value to the substitution pattern with a series of PERY$(CF_3)_5$ isomers

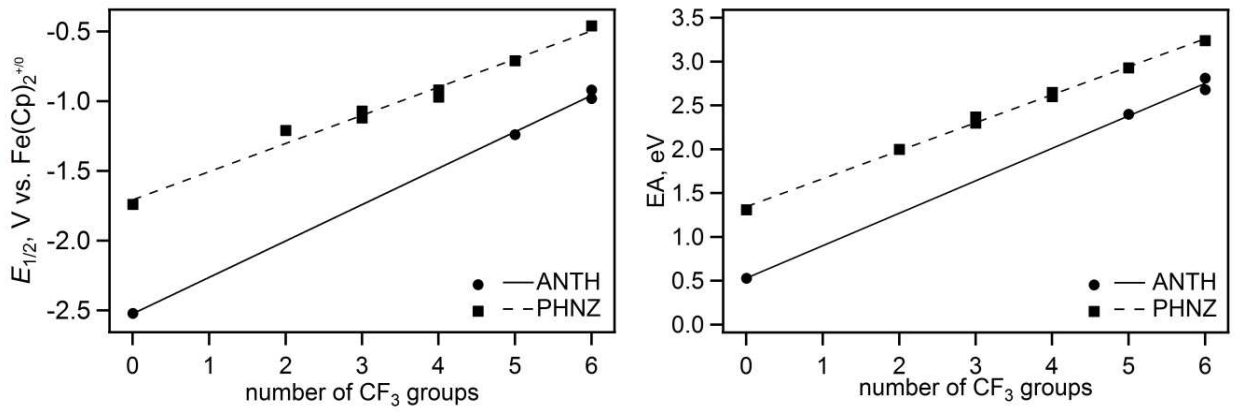

Figure 2.25. Comparison of change in $E_{1/2}$ and EA for ANTH$(CF_3)_n$ and PHNZ$(CF_3)_n$ compounds. In both instances the relative change for PHNZ$(CF_3)_n$ compounds is attenuated relative to the relative change for ANTH$(CF_3)_n$ compounds.

differing up to 0.04 eV, which is within the uncertainty of the measurement.[50] Aside from the ANTH$(CF_3)_6$ outliers, the solution $E_{1/2}$ was more sensitive to changes in the substitution pattern and the structure of the PAH core than the gas-phase EA. In the future, measuring the EA of isomers of FLRA$(CF_3)_3$ and PHEN$(CF_3)_4$ may help elucidate these patterns further.

A plot of $E_{1/2}$ vs EA for all PAH and PAH$(CF_3)_n$ compounds discussed in this work and some additional compounds from ref 50 is shown in Figure 2.26. The plot is nominally linear with a slope of 0.74 V eV^{-1}. This demonstrates, for a broad set of PAHs and PAH$(CF_3)_n$ derivatives, that the incremental change in $E_{1/2}$ from one compound to the next is, on average, attenuated by 26% relative to the change in EA from one compound to the next. Designers of new electron acceptors with targeted EAs will find this correlation useful, because reduction potentials are much easier to measure than precise values of gas-phase electron affinities. Significantly, the 0.74 V eV^{-1} slope stands in contrast to the 1.0 V eV^{-1} slope for a similar plot for aromatic hydrocarbons published by Ruoff et al. in 1994.[64]

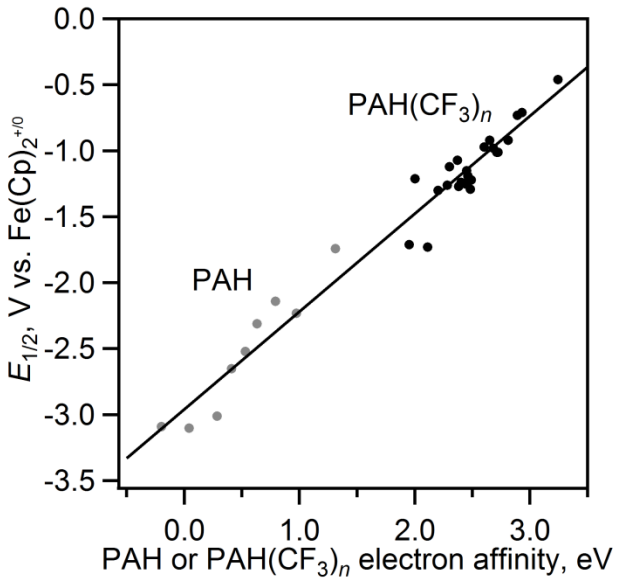

Figure 2.26. Plot of $E_{1/2}$ vs gas-phase EA for PAH and PAH$(CF_3)_n$ compounds. Data points for PAHs are gray and data points for PAH$(CF_3)_n$ are black The slope of the least squares fit of the data is 0.74 V eV^{-1}.

2.2.3. Crystal Structure Analysis

Thermal ellipsoid plots for all PAH$(CF_3)_n$ compounds crystallized during the course of this work are shown in Figure 2.27. The collection of PAH$(CF_3)_n$ molecules identified in this work with varying *n* values and differing substitution patterns provide interesting crystal structure comparisons. The first comparison is the impact of different numbers of CF_3 groups, illustrated with ANTH-5-1 and ANTH-6-1. Drawings of two neighboring pairs of molecules of ANTH-5-1 and ANTH-6-1 are shown in Figure 2.28. For both derivatives the upper aromatic core is rigorously parallel to the aromatic core below it. The packing varies along both the short and long axis of the ANTH core. The most dramatic difference is along the long axis, where the slippage for ANTH-5-1 is ca. 0.6 Å and for ANTH-6-1 is ca. 4.0 Å. The ANTH core is only 7.3 Å, so each ANTH-6-1 overlaps less than half of the neighboring molecule.

Another comparison to be made among the crystal structures studied in this work is the difference between two isomers of the same composition. Shown in Figure 2.28 are drawings of PYRN-5-1 and PYRN-5-2, which have nearly identical EA and $E_{1/2}$ values and four of their five CF_3 groups in the same positions, but exhibit very different solid-state packings. For PYRN-5-1,

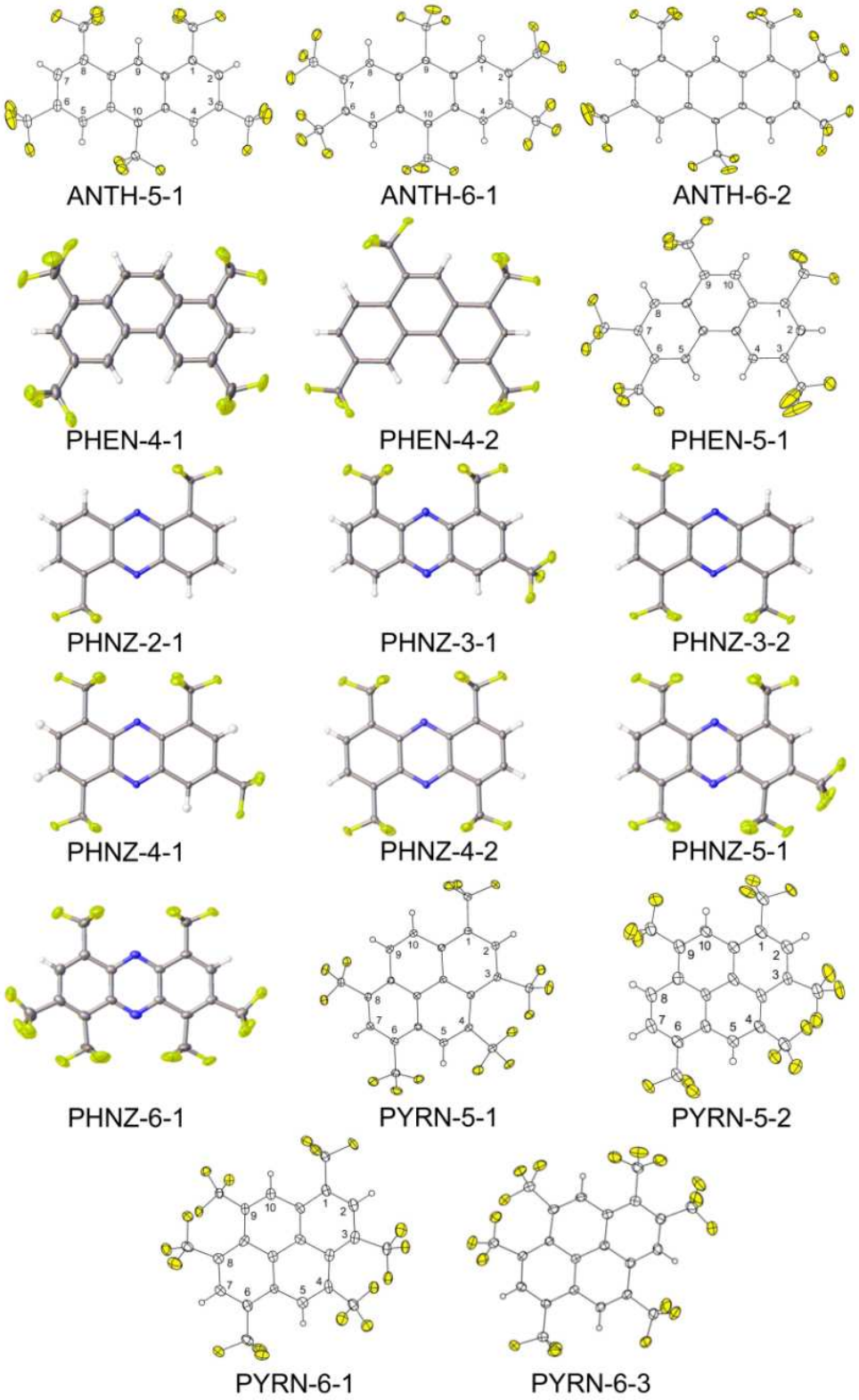

Figure 2.27. Thermal ellipsoids shown at the 50% probability level for all PAH$(CF_3)_n$ compounds crystallized and structurally characterized by X-ray diffraction in the course of this work. (F atoms are colored yellow, N atoms are colored blue, and H atoms are shown as spheres of arbitrary size).

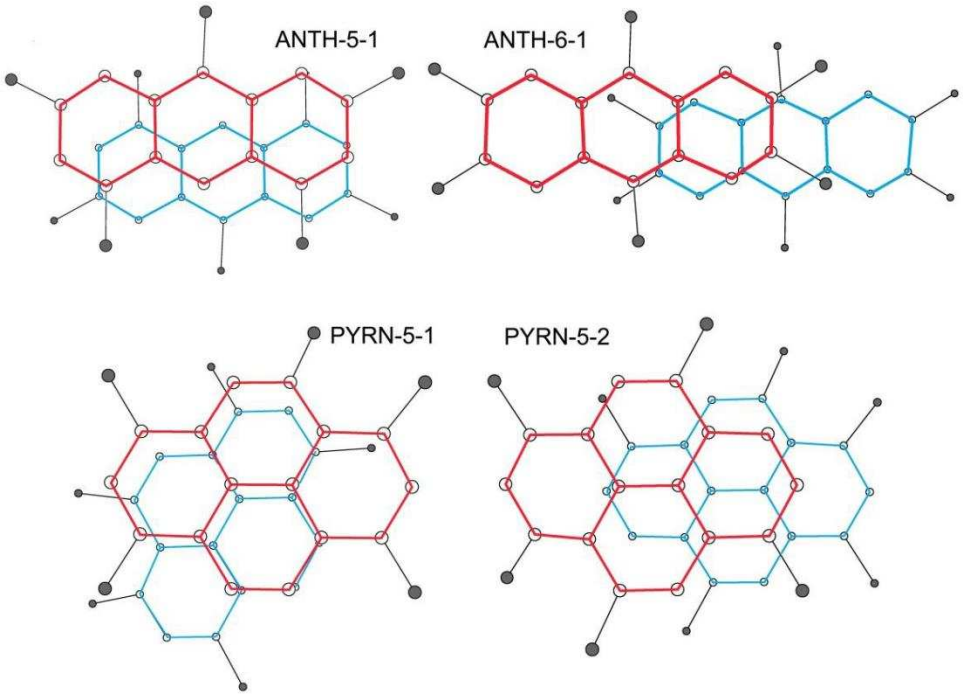

Figure 2.28. Comparison of portions of the X-ray structures of ANTH-5-1 and ANTH-6-1 (top) and PYRN-5-1 and PYRN-5-2 (bottom). Both F and H atoms have been omitted for clarity, and the C atoms are shown as spheres of arbitrary size. The CF_3 C atoms are shaded gray. Each drawing is oriented so that the least-squares plane of the lower aromatic core is in the plane of the page. For ANTH-5-1, ANTH-6-1, and PYRN-5-2, the least-squares planes of the upper aromatic cores are rigorously parallel to the planes of the lower cores. For PYRN-5-1, the least-squares plane of the upper aromatic core is tilted 5.2° with respect to the plane of the lower core.

the two aromatic cores are nearly parallel, but the second molecule is rotated by 45° resulting in three of the rings being nearly superimposed when viewed normal to the least-squares plane (LSP) of one of the molecules. The two molecules are not rigorously parallel: the upper molecule is tilted by 5.2° relative to the LSP of the lower molecule. The two aromatic cores are separated by 3.5–3.7 Å. In contrast, the molecules of PYRN-5-2 are rigorously parallel and are not rotated relative to one another. Instead, the molecules are slipped by half the distance of an aromatic ring. The result is that there is much less π overlap between adjacent molecules. The distance between aromatic cores is also greater with distances ranging from 4.1 to 4.3 Å.

The series of PHNZ$(CF_3)_n$ compounds crystallized for this work allow for a more detailed examination of the effect of the number of CF_3 groups on packing distances. Introducing

multiple CF_3 groups, which repel each other, onto the PHNZ core is expected to reduce PHNZ core interactions between adjacent molecules. Indeed, PHNZ$(CF_3)_{2,3}$ derivatives stack in columns that exhibit significant core overlap while PHNZ$(CF_3)_{4,5,6}$ derivatives exhibit no core overlap. Adjacent molecules of PHNZ-3-1 and PHNZ-3-2 adopt opposite orientations within the columns, as shown in Figure 2.29, but molecules of PHNZ-2-1 are all oriented in the same direction within columns. The average perpendicular distances between mean planes of neighboring PHNZ core atoms are 3.56, 3.44, and 3.55 Å in PHNZ-2-1, PHNZ-3-1, and PHNZ-3-2, respectively (Figure 2.30). For comparison, the interplanar distance between PHNZ cores is 3.49 Å.[65] Repulsion between CF_3 groups in both the C1 and C5 positions cause less favorable stacking interactions in PHNZ-2-1 and PHNZ-3-2 compared to when CF_3 groups are at C1 and C3, as in PHNZ-3-1, which actually packs closer than bare PHNZ. Having two isomers with different packing distances allows for a means of choosing molecules with the same electron-withdrawing strength, but with potentially different charge transport pathways. Some core planes in the crystal structures of PHNZ-4-2 and PHNZ-5-1 are also parallel to adjacent molecules (perpendicular distances are 4.00 and 4.09 Å, respectively), but the bulky CF_3 groups cause such a shift that there is actually no core overlap. In the most extreme case, PHNZ-6-1, all molecules pack in a herringbone fashion where no cores are parallel to the nearest neighbors.

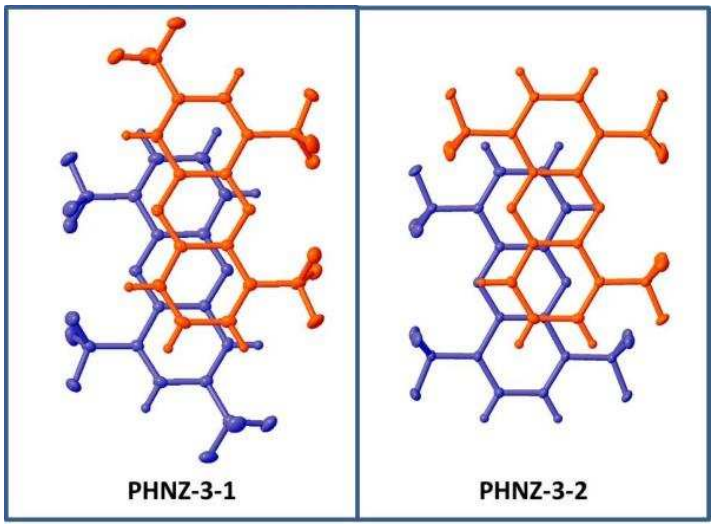

Figure 2.29. Comparison of overlap between PHNZ-3-1 and PHNZ-3-2. For both compounds adjacent molecules adopt opposite orientations, but the position of the CF_3 groups in PHNZ-3-1 allows for more overlap between molecules.

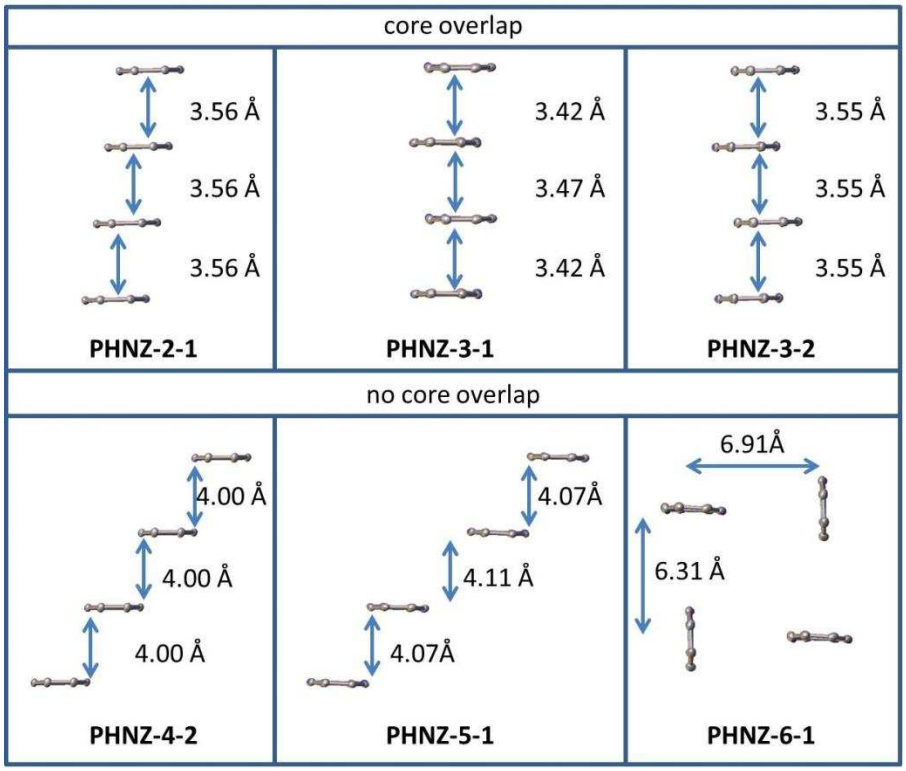

Figure 2.30. Molecular packing of four molecular cores of PHNZ$(CF_3)_n$ (n = 2–6) viewed down the long axis of the PHNZ core. Distances between nearest parallel cores are given. H atoms and CF_3 groups were removed for clarity.

2.2.4. Reactions of PHNZ$(CF_3)_n$ with Triethylaluminum

Shuster et al. reported a reaction between PHNZ and triethylaluminum, $AlEt_3$, in which they suggest that PHNZ promoted homolytic Al–C cleavage and acted as a radical monoanion.[66] It was hypothesized that PHNZ$(CF_3)_n$ compounds would be more stable than PHNZ as radical monoanions and would therefore form a similar complex intermediate with $AlEt_3$. Three reactions, described in the Experimental Details as Reactions A, B, and C, were performed. Reaction A involved crude PHNZ$(CF_3)_n$ to assess whether a reaction with any of the PHNZ$(CF_3)_n$ derivatives would occur, which would warrant further study with individual, purified PHNZ$(CF_3)_n$ compounds. Crude PHNZ$(CF_3)_n$ was yellow in solution and 30 min after adding $AlEt_3$ the reaction mixture turned orange. After 16 h the solution turned red and remained that color for the next 80 hours. Changes in the ^{19}F NMR spectra of the PHNZ$(CF_3)_n$ precursor and the reaction mixture were observed including different splitting and shifted peaks. It was

determined, based on the color change and the NMR spectral changes, that this reaction was promising to attempt with purified PHNZ$(CF_3)_n$ compounds.

Reactions B and C were performed with PHNZ-4-1 and PHNZ-4-2, respectively. Both reaction mixtures were initially yellow solutions and over the course of 1 day became light orange in color. In both cases the NMR spectra after 4 days looked nearly identical to the spectra of the starting materials indicating that this reaction does not work for PHNZ$(CF_3)_4$ compounds. This is possibly due to (i) steric hindrance blocking the Al atom from interacting with the N atom and/or (ii) the four electron withdrawing groups weakening a putative Al–N bond. Given the NMR spectral changes observed for Reaction A, it is possible that a PHNZ$(CF_3)_n$/$AlEt_3$ reaction with $n \leq 3$ would be worth studying in the future.

2.2.5. Charge-Transfer Complex Characterization

Table 2.4 lists the names, formulas, and abbreviations of the PAH and PAH$(CF_3)_n$ compounds studied as components of CTCs in this work, their gas-phase ionization energies (IEs) and/or EAs, and their solution and/or solid-state visible absorption maxima. The IUPAC locants used in this table are defined in Figure 2.1. Compounds with electron-withdrawing groups are better electron acceptors than the underivatized parent compound. When electron acceptors are mixed with electron donors, such as some parent PAHs, partial charge transfer can occur, which frequently leads to new absorption bands referred to as charge-transfer (CT) bands

These new absorption bands resulted in color changes for most mixtures of PAH and PAH$(CF_3)_n$ compounds studied in this work. Some of the CTC colors appeared to be different in 1,2-dichloroethane (DCE) solution than in the solid-state, but in some cases these differences might be a function of the concentration of the CTC (i.e., low concentration in solution vs high concentration in the solid state). For example, ANTH/ANTH-5-1 was golden-yellow in solution and orange in the solid state (single crystals as well as thin films). Both ANTH/ANTH-6-1 and ANTH/ANTH-6-2 were pink in solution and orange as solids. The CTC CORO/ANTH-6-1 was orange-red in solution and red in the solid-state. The most pronounced, and unambiguous, color change was observed for PERY/ANTH-6-1 which was yellow-green in solution, similar to the

color of a solution of PERY itself, and blue-green in the solid state. In contrast, all three CTCs with PYRN as the donor were the same color in solution and in the solid state: PYRN/ANTH-6-1 was pink, PYRN/AZUL-5-1 was red-purple, and PYRN/PYRN-6-3 was orange.

UV-vis spectra of DCE solutions were recorded for all CTCs other than a mixture of CORO and ANTH-6-1, for which toluene was the solvent, and solid-state UV-vis spectra were recorded for ANTH/ANTH-5-1, ANTH/ANTH-6-1, PERY/ANTH-6-1, and PYRN/ANTH-6-1 (Figure 2.31). Solution and solid-state spectra appeared similar for all CTCs investigated with both methods. Typically the solid-state CT bands were broader and the absorption maxima were slightly different than those in solution. A longer wavelength absorption in the solid was most pronounced for PERY/ANTH-6-1, which, as mentioned previously, in solution was nearly the same color as PERY alone, but as a solid adopted a dark blue-green color. A shift to longer wavelength absorption in the solid has previously been observed by Berionni et al. in a CTC with ANTH as the donor.[67] For PYRN/AZUL-5-1, it appears that CT occurred between the ground state of PYRN and the S_2 state of AZUL-5-1 because the CT band maximum is at a shorter wavelength than the S_0–S_1 absorption band maximum in AZUL-5-1 alone.

Table 2.4. Electron affinity, ionization potential, and spectroscopic data[a]

compound or CTC stoichiometry in single crystals	abbreviation	gas-phase EA, eV	gas-phase IP, eV	gas-phase Δ(IP/EA), eV[b]	longest wavelength λ_{max} value, nm [eV]	
					soln	solid
anthracene	ANTH	0.53(2)[c]	7.439(6)[c]	—	< 400 [>3.11]	< 400 [>3.11]
azulene	AZUL	0.790(8)[c]	7.42(2)[c]	—	579 [2.14]	—
perylene	PERY	0.973(5)[c]	6.960(1)[c]	—	523 [2.37]	467 [2.655]
pyrene	PYRN	0.41(1)[c]	7.426(1)[c]	—	< 400 [>3.11]	< 400 [>3.11]
coronene	CORO	0.47(9)[c]	7.26(5)[c]	—	451 [2.75]	—
1,3,6,8,10-ANTH$(CF_3)_5$	ANTH-5-1	2.40(2)[d]	—	—	< 400 [>3.11]	< 400 [>3.11]
2,3,6,7,9,10-ANTH$(CF_3)_6$	ANTH-6-1	2.81(2)[d]	—	—	< 400 [>3.11]	< 400 [>3.11]
1,2,3,6,8,10-ANTH$(CF_3)_6$	ANTH-6-2	2.68(2)[i]	—	—	< 400 [>3.11]	—
1,2,3,5,7-AZUL$(CF_3)_5$	AZUL-5-1	2.890(5)[d]	—	—	536 [2.31]	—
1,2,4,6,8,9-PYRN$(CF_3)_6$	PYRN-6-3	—	—	—	< 400 [>3.11]	—
ANTH/(ANTH-5-1)$_2$	—	—	—	5.04(2)	467 [2.66]	456 [2.72]
ANTH/ANTH-6-1	—	—	—	4.63(2)	523 [2.37]	530 [2.34]
ANTH/ANTH-6-2	—	—	—	4.76(2)	506 [2.45]	—
PERY/ANTH-6-1	—	—	—	4.15(2)	595 [2.08][e]	655 [1.90]
PYRN/(ANTH-6-1)$_2$	—	—	—	4.62(2)	510 [2.43]	494 [2.51][f]
PYRN/AZUL-5-1	—	—	—	4.54(2)	—[g]	—
PYRN/PYRN-6-3	—	—	—	—	454 [2.73]	—
(CORO)$_2$/ANTH-6-1	—	—	—	4.45(5)	504 [2.46]	—

[a] All λ_{max} values were determined by the author of this dissertation. The solution CTC stoichiometries were determined to be 1:1 for ANTH/ANTH-5-1, ANTH/ANTH-6-1, PERY/ANTH-6-1, and PYRN/ANTH-6-1 and are assumed to be 1:1 in solution for the other CTC combinations [b] Δ(IP/EA) = IP(PAH) − EA(PAH$(CF_3)_n$) [c] From NIST Webbook (http://webbook.nist.gov/chemistry). [d] From ref [50] [e] Shoulder at ca. 640 nm [ca. 1.94 eV]. [f] This is the maximum of the CT band. [g] There was no clear CT band maximum (see text).

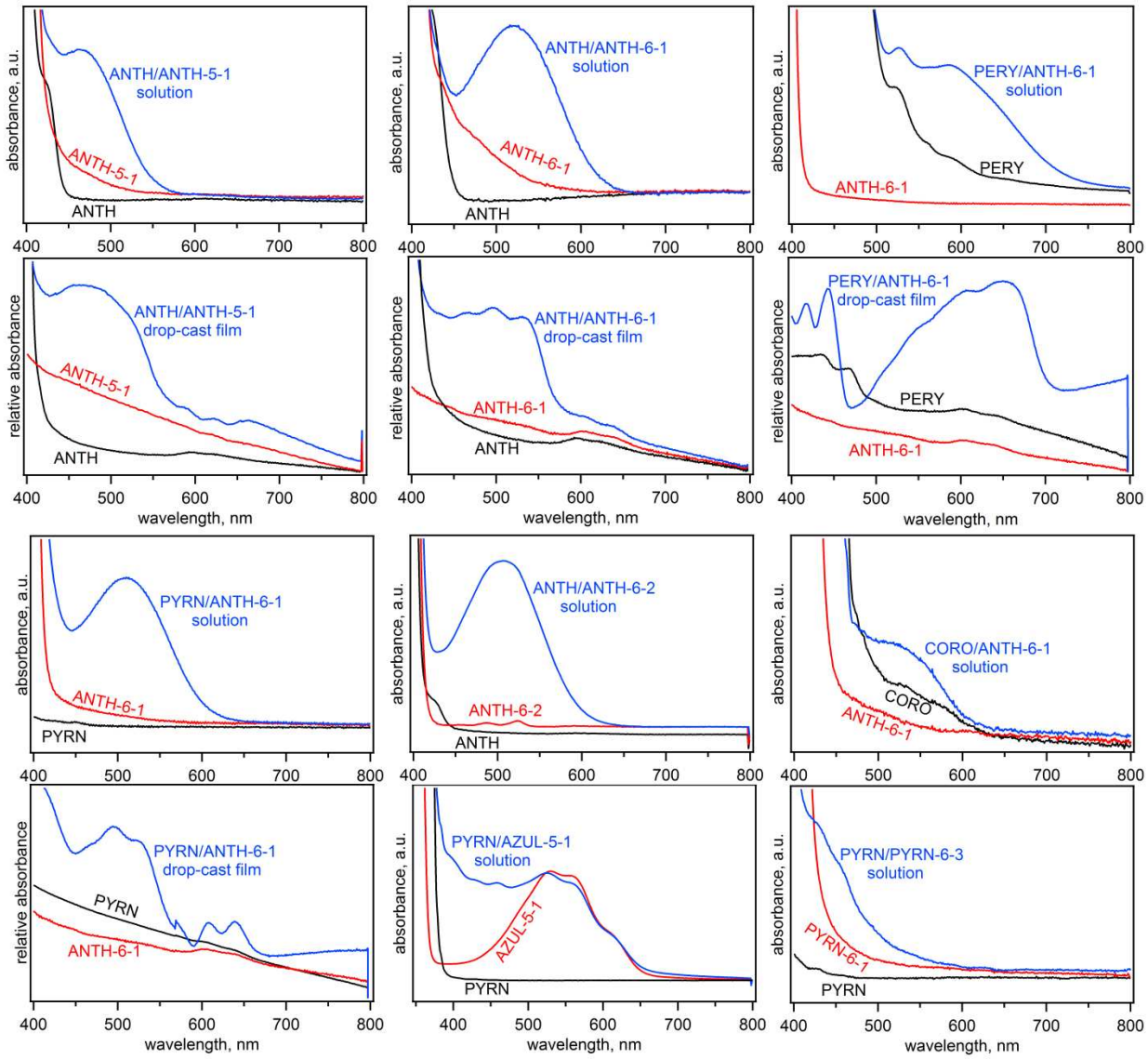

Figure 2.31. Visible spectra showing CT band absorptions. Solution spectra are presented for all D/A combinations as DCE solutions, except CORO/ANTH-6-1, for which the solvent was toluene. Solid-state spectra are presented for four D/A combinations as thin films drop-cast from 1:1 DCE solutions. The spectrum of PYRN/PYRN-6-3 was compared with the spectrum of PYRN-6-1 because no purified sample of PYRN-6-3 was available after PYRN/PYRN-6-3 single crystals had been prepared (several crystals were dissolved in DCE to record the spectrum of PYRN/PYRN-6-3). The spectrum of PYRN-6-3 is probably similar, but not identical, to the spectrum of PYRN-6-1.

Determination of the solution stoichiometry for PERY/ANTH-6-1 was complicated by the overlap of the trailing edge of PERY absorption and the CT band. This overlap was addressed by taking the absorbance of the mixture and subtracting out the contribution of PERY, (i.e., the equation used was $Abs_{D/A}-\%D\times Abs_D$). A comparison of the raw spectra and the PERY-absorbance-subtracted spectra is shown in Figure 2.32. Job's plots[68] for ANTH/ANTH-5-1, ANTH/ANTH-6-1, PERY/ANTH-6-1, and PYRN/ANTH-6-1, showing the formation of 1/1 donor/acceptor (D/A) complexes in solutions for which $[D]_{max} = [A]_{max} \leq 10$ mM, are shown in Figure 2.33. Plots of spectral data used to determine the equilibrium quotients (K_{CT} values) for the ANTH + ANTH-5-1 $\rightleftharpoons$ ANTH/ANTH-5-1 and the ANTH + ANTH-6-1 $\rightleftharpoons$ ANTH/ANTH-6-1 equilibria at 20 °C in DCE and the molar extinction coefficients of the 1/1 D/A complexes are shown in Figure 2.34.[69,70] The K_{CT} values are 1.7(1) and 2.8(1) M^{-1}, respectively. The DCE ε and λ_{max} values were found to be 7.7(4) × 10^2 cm^{-1} M^{-1} and 468 nm, respectively, for ANTH/ANTH-5-1 and 6.3(3) × 10^2 cm^{-1} M^{-1} and 523 nm, respectively for ANTH/ANTH-6-1.

The CTCs formed between ANTH and ANTH-5-1 and between PYRN and ANTH-6-1 were both found to have 1:1 stoichiometries in solution, but both combinations crystallized as 1:2 complexes, although with significantly different morphologies (the structures will be discussed in more detail below). In contrast, the solution and solid-state stoichiometries were the same for ANTH/ANTH-6-1 and PERY/ANTH-6-1. No obvious reasons for the discrepancy have been identified. It has been suggested that solvent choice is important in determining solid-state stoichiometry,[30] but this has not been looked into at this time.

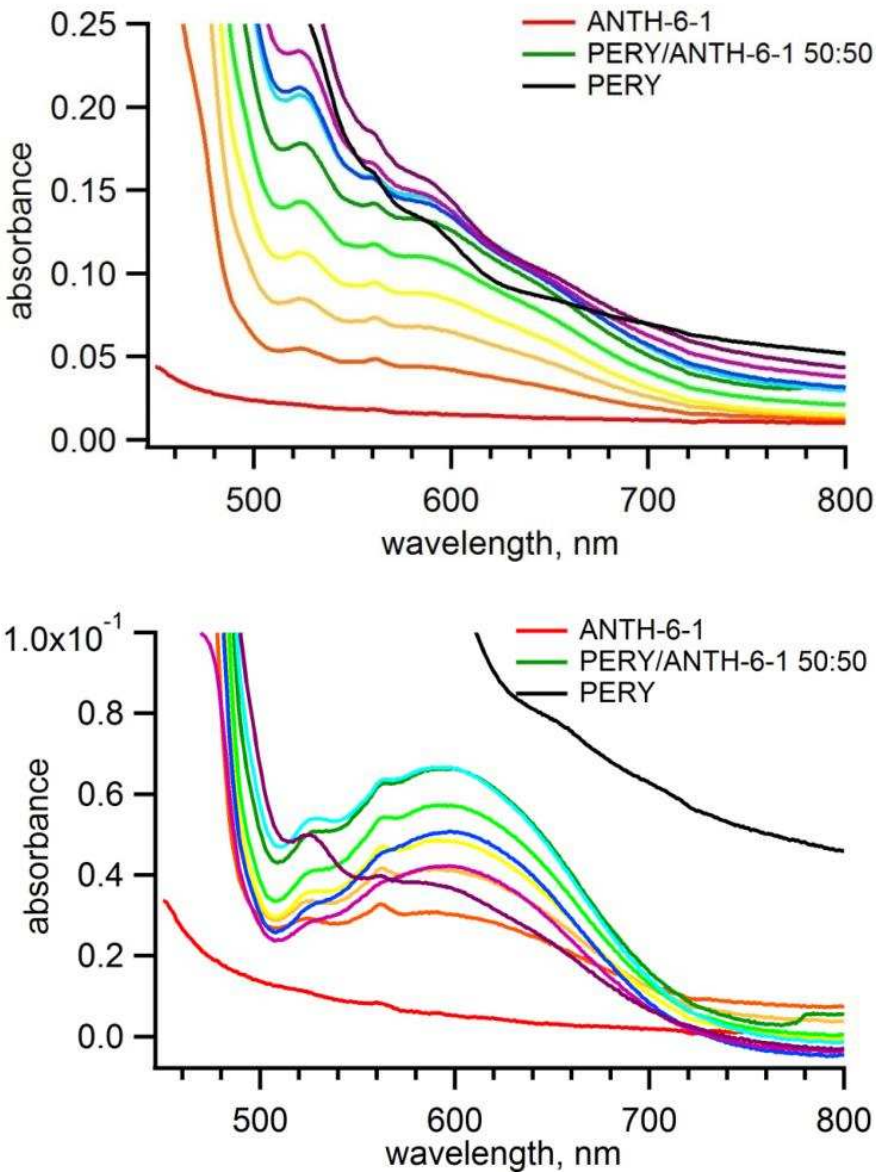

Figure 2.32. Comparison of the absorption spectra of solution of PERY and ANTH-6-1 with the mol% PERY varying from 0% (red spectrum, 100% ANTH-6-1) to 100% (black spectrum, 0% ANTH-6-1, top) with the corresponding PERY-absorbance-subtracted spectra (bottom). The latter spectra allowed an approximate CT band λ_{max} value for the CTC PERY/ANTH-6-1 of 595 nm to be determined. As the mol% of PERY increased from 0 to 100% in increments of 10%, the CT band absorbance at λ_{max} first increased (e.g., orange spectrum 10% PERY, yellow spectrum 30% PERY, green and teal spectra 50% and 60% PERY respectively) and then decreased (e.g., blue spectrum 70% PERY, indigo spectrum 80% PERY, etc.).

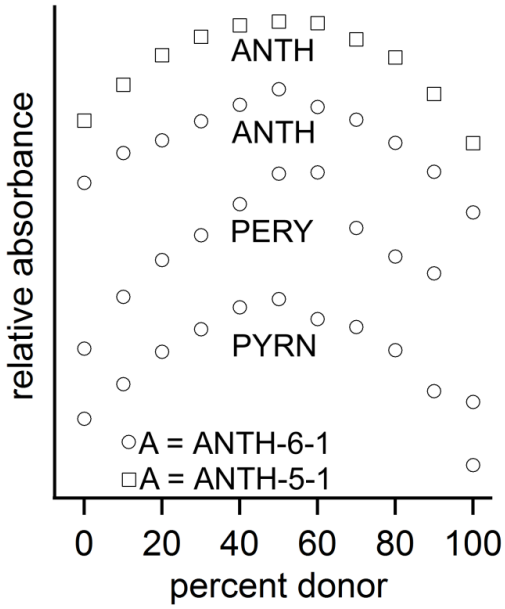

Figure 2.33. Job's plots indicating 1/1 charge transfer D/A CTC formation in DCE. From top to bottom: ANTH/ANTH-5-1 (λ_{max} = 467 nm), ANTH/ANTH-6-1 (λ_{max} = 523 nm), PERY/ANTH-6-1 (λ_{max} = 595 nm), and PYRN/ANTH-6-1 (λ_{max} = 510 nm).

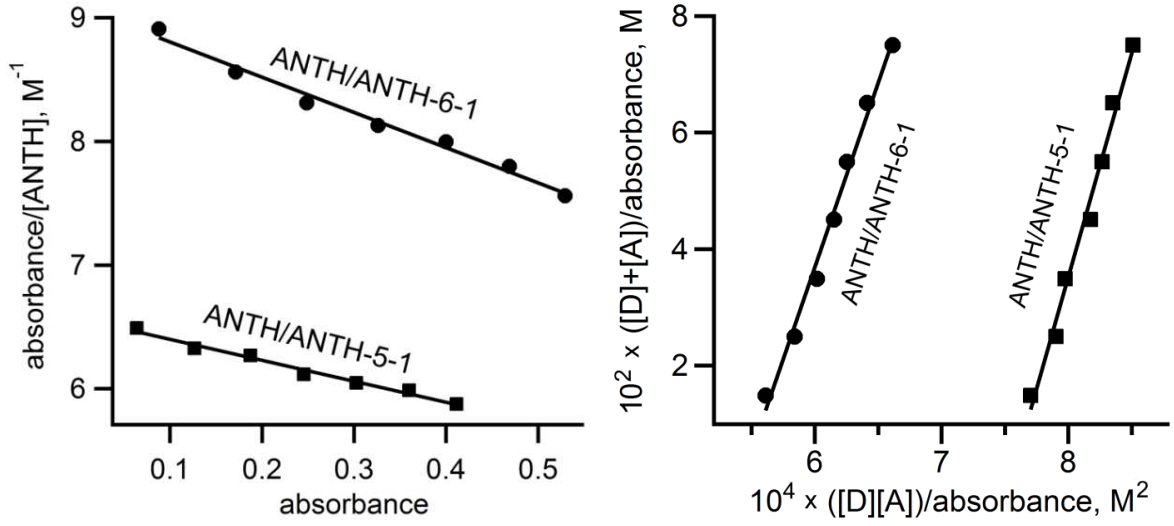

Figure 2.34. Scott plots (left) and Seal plots (right) for ANTH/ANTH-5-1 and ANTH/ANTH-6-1 titrations in DCE. The acceptor concentration was 5.0×10^{-3} M and the donor concentration was varied between 1.0×10^{-2} and 7.0×10^{-2} M. The K_{eq} values for ANTH/ANTH-5-1 and ANTH/ANTH-6-1 were found to be 1.7(1) and 2.8(1) M^{-1}, respectively. The DCE ε and λ_{max} values were found to be $7.7(4) \times 10^2$ cm^{-1} M^{-1} and 468 nm, respectively, for ANTH/ANTH-5-1 and $6.3(3) \times 10^2$ cm^{-1} M^{-1} and 523 nm, respectively for ANTH/ANTH-6-1.

Relatively low association constants of 1.7(1) and 2.8(1) M^{-1} were determined for the CTCs ANTH/ANTH-5-1 and ANTH/ANTH-6-1 respectively. These association constants suggest that the intermolecular interaction is relatively weak in DCE solution. For these two complexes the association constant appears to be directly correlated to the EA, however the ratio between EAs is not the same as the ratio between K_{CT} values. The EA of ANTH-6-1 is higher than that ANTH-5-1 and ANTH/ANTH-6-1 has a correspondingly higher association constant.[50] Low association constants have been observed for other CTCs with ANTH as the donor. For example, a mixture of ANTH and chloranil exhibits a K_{CT} of 1.7 M^{-1} in chloroform.[71] In another example CTC, the association constant for a mixture of ANTH and 4-nitrobenzodifuroxan is reported to be 5.5 M^{-1}.[67]

The energy-level differences between the solution-based CT absorption bands, solution redox potentials, and gas-phase EAs and IEs can be compared. For example, consider ANTH/ANTH-5-1 vs ANTH/ANTH-6-1. The EAs of the two acceptors differ by 0.41 eV, their reduction potentials differ by 0.32 V, and their CT λ_{max} values differ by 0.284 eV. The two solution-phase differences are in close agreement; the gas-phase EA difference is ca. 26% higher. This is in close agreement with the 0.74 V eV^{-1} relationship found between gas-phase electron affinities and solution-phase reduction potentials found for PAH and PAH$(CF_3)_n$ compounds. In other words, differences in gas-phase EAs for a series of compounds are attenuated, in this case by 26%, when their "electron affinities" (i.e., their reduction potentials are measured in solution). A similar attenuation, ca. 20%, was reported for $C_{60}(CF_3)_n$ compounds in 2007.[72]

A similar analysis can be performed for a given acceptor (ANTH-6-1) and different donors (ANTH, PERY, and PYRN). Consider ANTH/ANTH-6-1 vs PERY/ANTH-6-1. The IEs of ANTH (7.439(6) eV) and PERY (6.960(1) eV) differ by ca. 0.5 eV.[73,74] However, their +/0 reduction potentials differ by only ca. 0.3 V[75] and their CT band λ_{max} values with ANTH-6-1 as the acceptor differ by only 0.287 eV. Once again, the condensed-phase CT band λ_{max} more closely corresponds to the difference in solution (i.e., the difference in "donor ability" of ANTH and PERY in solution, $E_{1/2}$ values) than to the difference in the gas-phase (i.e., the difference in

"donor ability" of ANTH and PERY in the gas-phase, IEs). In this case the attenuation is ca. 40% (i.e., 0.3 eV/0.5 eV = 0.6). A similar comparison can be made for the pair of CTCs ANTH/ANTH-6-1 and PYRN/ANTH-6-1, but in this case the two donors, ANTH and PYRN, have similar "donor abilities" and the comparison is less compelling because the differences are so small. Ignoring the uncertainties in the measured values, the IEs of ANTH (7.439(6) eV) and PYRN (7.426(1) eV) differ by 0.013 eV,[73] their +/0 $E_{1/2}$ values differ by 0.03 V,[75] and the CT band λ_{max} values differ by 0.06 eV.

Selected geometric parameters for the seven D_x/A_y X-ray structures reported in this work and for the structure of PYRN/AZUL-5-1 reported previously[52] are listed in Table 2.5. Seven of the eight structures contain $(D_x/A_y/)_\infty$ columns, with six parallel columns surrounding each column in pseudohexagonal arrays. Five of these structures consist of infinite columns with alternating donors and acceptors (i.e., $(D/A/)_\infty$ columns): ANTH/ANTH-6-1, ANTH/ANTH-6-2, PERY/ANTH-6-1, PYRN/AZUL-5-1, and PYRN/PYRN-6-3. Drawings of the column stacking in these five structures are shown in Figure 2.35. Two of the other structures, ANTH/(ANTH-5-1)$_2$ and (CORO)$_2$/ANTH-6-1, consist of $(D/A_2/)_\infty$ or $(D_2/A/)_\infty$ columns, respectively, also arranged in pseudohexagonal arrays. Drawings of these two structures are shown in Figure 2.36. The eighth structure, PYRN/(ANTH-6-1)$_2$, consists of discrete D/A_2 units arranged so that (i) each PYRN molecule is sandwiched between two "domed" ANTH-6-1 molecules and (ii) the D/A_2 sandwiches are arranged in herringbone-like layers which are virtually superimposed on each other, as shown in Figures 2.37 and 2.38.

Table 2.5. X-ray Structure Geometric Parameters for D_x/A_y Co-crystals[a]

structure	major axis, Å; ∠ to ⊙···⊙	minor axis, Å; ∠ to ⊙···⊙	D/A LSP dihedral ∠	A→D(LSP) OOP's (i.e., π–π overlap), Å	rotation of D/A major axes	D major axis slip, Å [%]	D minor axis slip, Å [%]
ANTH/(ANTH-5-1)$_2$	D: 7.296; 14.8° A: 7.301; 9.3°	D: 2.784; 7.6° A: 2.800; 12.9°	2.2°	3.76–3.86	17.1°	2.42 [33]	1.07 [38]
ANTH/ANTH-6-1	D: 7.296; 17.5° A: 7.344; 16.4°	D: 2.809; 3.0° A: 2.832; 5.9°	2.4°	3.47–3.66	20.7°	2.20 [30]	0.44 [16]
ANTH/ANTH-6-2	D: 7.301; 18° A: 7.342; 16°	D: 2.804; 4° A: 2.806; 2°	1.9°	3.39–3.62	14.8°	2.24 [31]	0.49 [18]
PERY/ANTH-6-1	D: 5.727; 7.2° A: 7.353; 0.7°	D: 2.493; 18.9° A: 2.849; 15.1°	1.0°	3.48–3.66	23.2°	0.89 [16]	2.42 [97]
PYRN/(ANTH-6-1)$_2$	D: 7.006; 6.7° A: 7.300; 11.6°	D: 4.919; 3.4° A: 2.816; 0.5°	1.6°	3.36–3.73	33.0°	0.99 [14][b]	0[b]
PYRN/AZUL-5-1	D: 7.027; 7.0° A: 5.236; 3.1°	D: 4.917; 5.2° A: 3.164[c]; 1.8°	0.8°	3.58–3.67	3.85°	0	0
PYRN/PYRN-6-3	D: 7.009; 17.6° A: 7.041; 15.9°	D: 4.904; 7.0° A: 4.900; 11.4°	3.1°	3.45–3.60	22.8°	—[d]	—[d]
(CORO)$_2$/ANTH-6-1	D: 7.359; 1.2° A: 7.353; 0.7°	D: 5.676; 24° A: 2.844; 22.7°	4.8°	3.45–3.76	2.6°	0	2.49 [44]
ANTH/NAPH(F)$_8$[e]	D: 7.296; 14.8° A: 7.301; 9.3°	D: 2.784; 7.6° A: 2.800; 12.9°	2.7°	3.34–3.42	19.9°	D: 0.26 [3.5] A: 0.12 [2.5]	D: 1.07 [38] A: 1.08 [26]

[a] All data from this work unless otherwise indicated. [b] Structure is comprised of acceptor-donor-acceptor isolated triads so donor to donor slip axis is not possible. [c] Minor axis taken as longest distance across 7-membered ring perpendicular to major axis. [d] Major and minor axis slip dimensions are meaningless in this case since the donor molecules on either side of the acceptor are rotated almost perpendicular to each other (86.1°). [e] from Collings et al.[76]

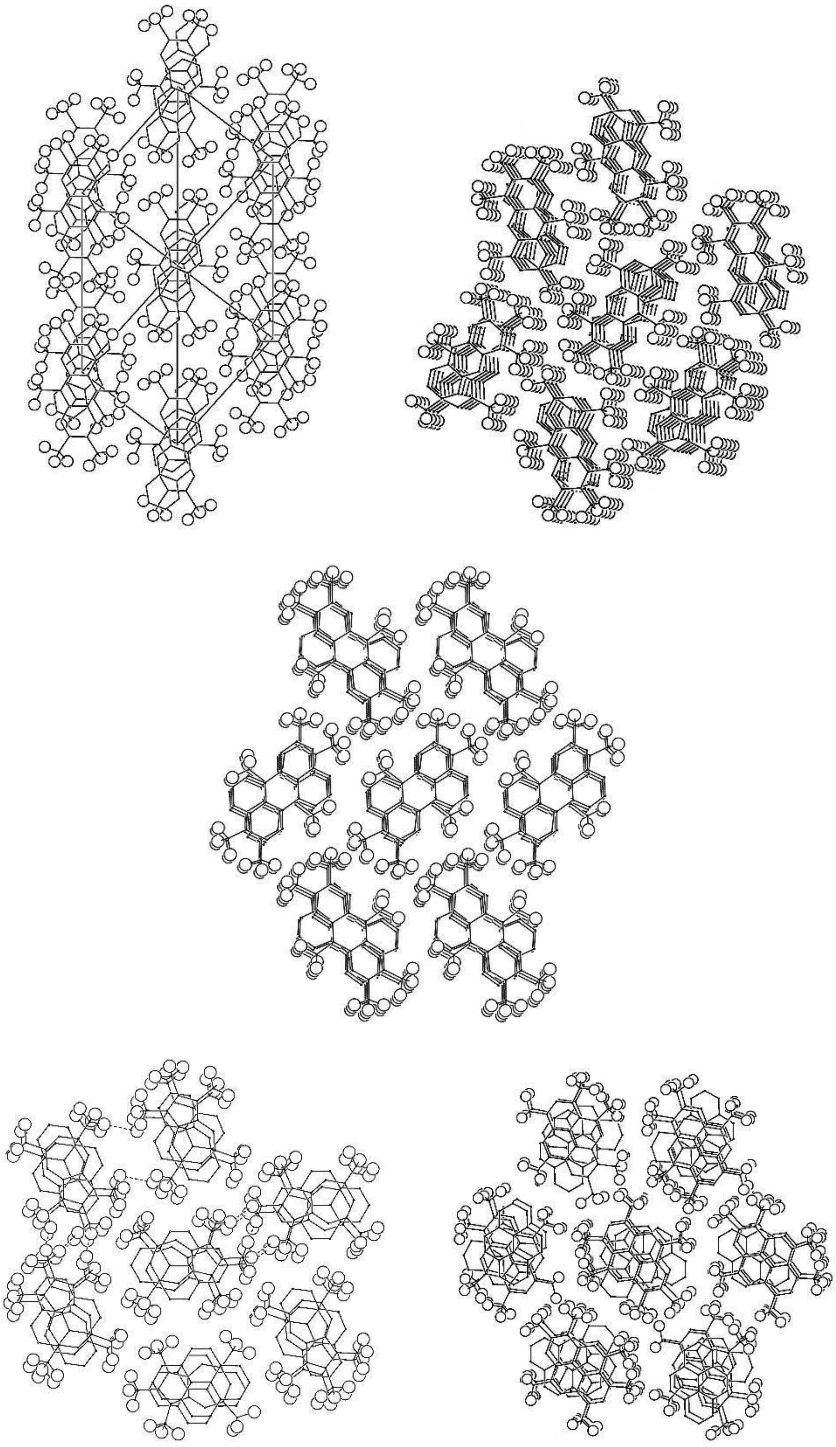

Figure 2.35. Pseudohexagonal packing of the $(D/A/)_\infty$ columns in the structures of ANTH/ANTH-6-1 (top left), ANTH/ANTH-6-2 (top right), PERY/ANTH-6-1 (middle), PYRN/AZUL-5-1 (bottom left), and PYRN/PYRN-6-3 (bottom right). The H atoms have been omitted for clarity. The F atoms are depicted as large spheres so that the "Teflon-like" insulation between the columns can be appreciated.

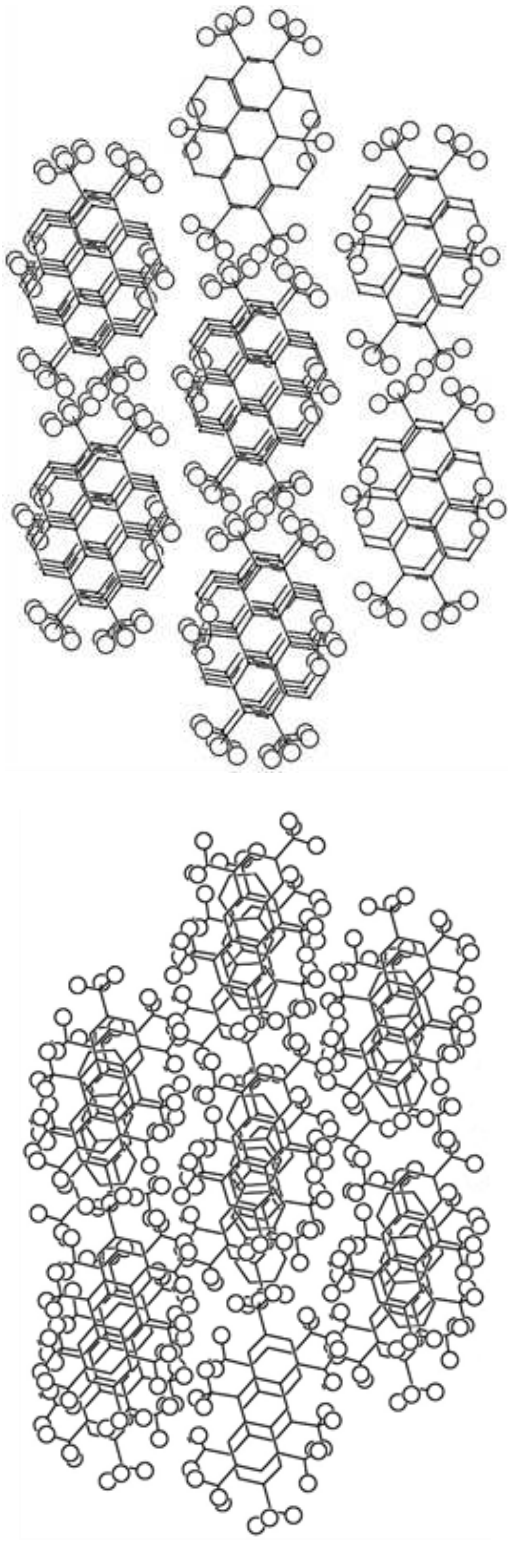

Figure 2.36. Pseudohexagonal packing of the $(D_2/A/)_\infty$ or $(D/A_2/)_\infty$ columns in the structure of $(CORO)_2$/ANTH-6-1 (top) and ANTH/$(ANTH\text{-}5\text{-}1)_2$ (bottom). The H atoms have been omitted for clarity. The F atoms are depicted as large spheres so that the "Teflon-like" insulation between the columns can be appreciated.

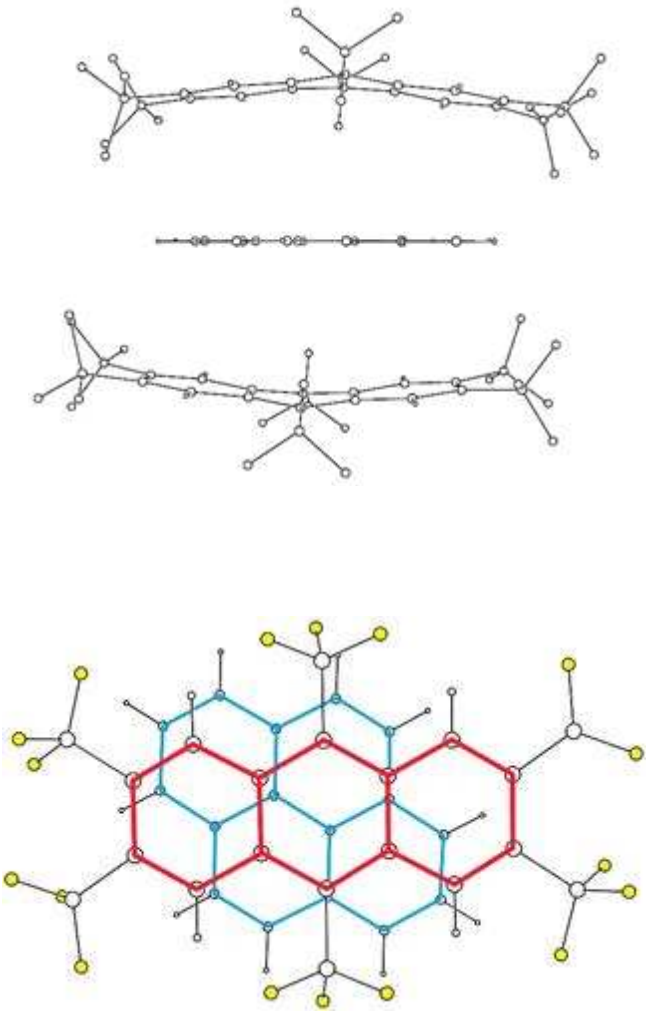

Figure 2.37. Drawings of the structure of PYRN/(ANTH-6-1)$_2$, showing (i) how the PYRN donor is sandwiched between two domed ANTH-6-1 acceptors (top) and (ii) the overlap between the π systems of the PYRN and one of its two nearest-neighbor ANTH-6-1 molecules (bottom). The atoms are depicted as spheres of arbitrary size, and the F atoms in the bottom drawing are highlighted in yellow.

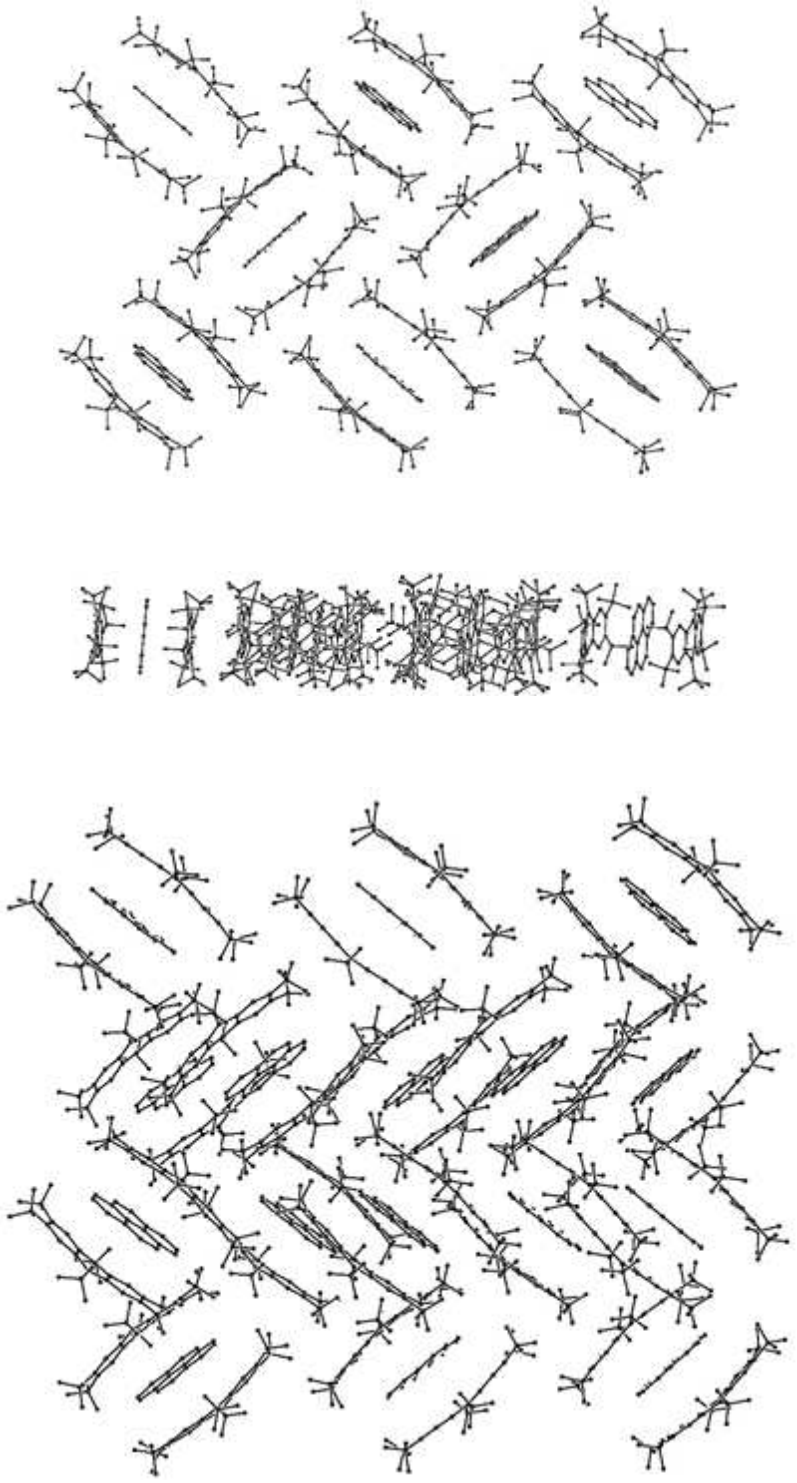

Figure 2.38. Drawings showing the herringbone-like layers of the CTC A/D/A sandwiches in the structure of PYRN/(ANTH-6-1)$_2$. The top and middle drawings show a single layer of sandwiches in two perpendicular orientations. The bottom drawing shows two superimposed layers. The H atoms have been omitted for clarity and the C and F atoms are depicted as spheres of arbitrary size.

As an example of the way the stacking within and the packing of the $(D_x/A_y/)_\infty$ columns can be analyzed, the structure of ANTH/ANTH-6-1 will now be described in detail. The ANTH and ANTH-6-1 molecules have crystallographic inversion symmetry, so only half of each molecule is unique. In each (ANTH/ANTH-6-1/) column the centroids (⊙) of the ANTH donors and ANTH-6-1 acceptors lie on a rigorously straight line that is parallel to the crystallographic *a* axis, as shown in Figure 2.39. The distance along the ⊙···⊙ vector between ANTH centroids or between ANTH-6-1 centroids is the unit cell *a* dimension, 7.3206(3) Å.

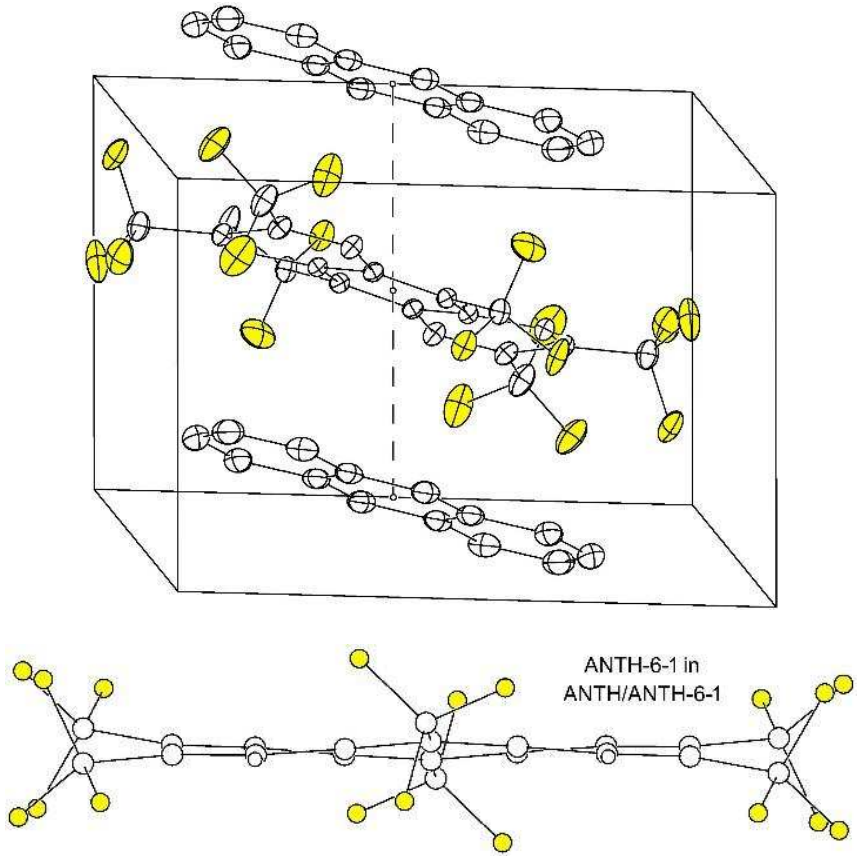

Figure 2.39. (Top) The unit cell for the structure of ANTH/ANTH-6-1 showing that the centroids of both ANTH and ANTH-6-1 lie on a straight line that is parallel to the crystallographic *a* axis (50% probability ellipsoids). (Bottom) Drawing of the ANTH-6-1 molecule in the structure of ANTH/ANTH-6-1 showing that the C(sp^2) aromatic core is only approximately planar (the atoms are shown as spheres of arbitrary size). In both drawings the H atoms have been omitted for clarity.

The ANTH molecule is essentially planar. The range and average out-of-plane deviations (OOP's) from the LSP of the 14 C(sp^2) atoms are ±0.002–0.012 Å and 0.005 Å, respectively. The

aromatic core of the ANTH-6-1 molecule is only approximately planar, as also shown in Figure 2.36. The range and average OOP's from the LSP of the ANTH-6-1 C(sp^2) atoms are ±0.024–0.132 Å and ±0.066 Å, respectively. The C(sp^2) LSP's of ANTH and ANTH-6-1 are nearly parallel; the interplane dihedral angle is 2.4°.

Figure 2.40 shows the orientations of the major and minor axes of the ANTH and ANTH-6-1 molecules with respect to the ⊙···⊙ vector, which is not normal to the LSP of either molecule. The major axis of each molecule is defined here as the line which connects the centroids of (i) C2 and C3 and (ii) C6 and C8 and the minor axis as the line connecting C9 and C10. The angles between the ⊙···⊙ vector and the major and minor axes of ANTH are 17.5 and 3.0°, respectively; for ANTH-6-1 these angles are 16.4 and 5.9°, respectively. Two views of ANTH/ANTH-6-1 stacking in each $(D/A/)_\infty$ column, one looking down the ⊙···⊙ vector and one looking down the normal to the ANTH LSP, are shown in Figure 2.41.

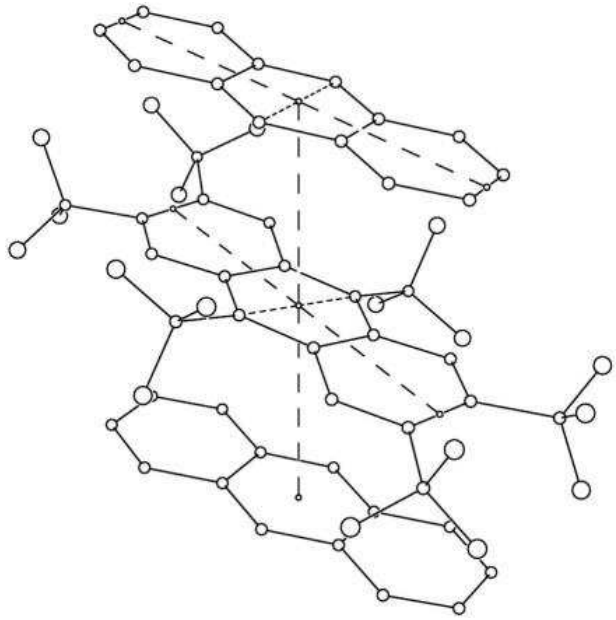

Figure 2.40. Drawing of the structure of ANTH/ANTH-6-1 showing the orientations of the major and minor axes of the ANTH and ANTH-6-1 molecules (shown as dashed lines) with respect to the vertical dashed line through the ⊙ of the 14 C(sp^2) atoms of each molecule (the ⊙'s are shown as small circles; H atoms omitted for clarity; C and F atoms are shown as spheres of arbitrary size). The angles between the ⊙···⊙ vector and the major and minor axes of ANTH are 17.5 and 3.0°, respectively; for ANTH-6-1 these angles are 16.4 and 5.9°, respectively.

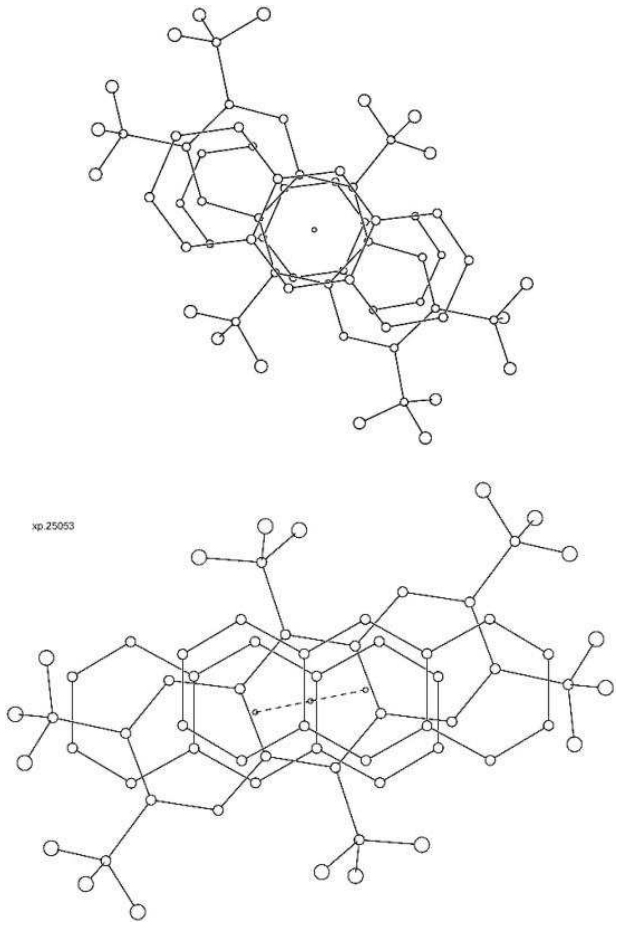

Figure 2.41. (Top) View looking down the centroid···centroid (⊙···⊙) vector, which is parallel to the crystallographic *a* axis, of two ANTH and one ANTH-6-1 molecules in one of the $(D/A)_\infty$ columns in the structure of ANTH/ANTH-6-1 (H atoms omitted for clarity; C and F atoms shown as spheres of arbitrary size). Note that the three ⊙'s, which are depicted as small circles, are superimposed in this view. (Bottom) View looking down the normal to the ANTH least-squares planes. The three ⊙'s are connected with dashed lines.

A flat projection of one pair of adjacent ANTH donor and ANTH-6-1 acceptor molecules along the $(D/A/)_\infty$ columns in the structure of ANTH/ANTH-6-1 is shown in Figure 2.42. The projection of the ANTH-6-1 major axis onto the ANTH LSP is rotated 20.7° relative to the ANTH major axis. The numbered $C(sp^2)$ atoms of ANTH-6-1 that appear "within" or nearly within the red lines of the ANTH π-electron cloud have the following perpendicular out-of-plane displacements from the ANTH least-squares plane: C1, 3.63 Å; C2, 3.66 Å; C5, 3.34 Å; C11, 3.49 Å; C12, 3.46 Å; C13, 3.48 Å; and C14, 3.50 Å. Note that the standard errors for C–C distances in this structure are no more than ±0.002 Å.

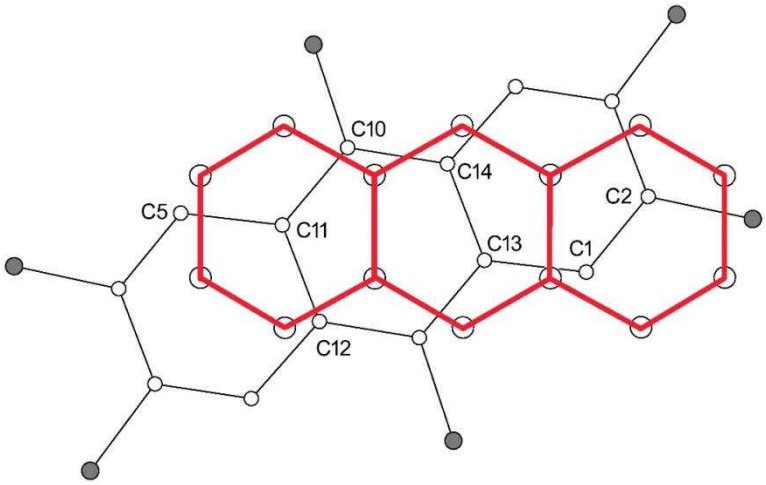

Figure 2.42. A flat projection of one pair of adjacent ANTH and ANTH-6-1 molecules along the $(D/A)_\infty$ columns in the ANTH/ANTH-6-1 co-crystal (H and F atoms omitted for clarity; CF_3 carbon atoms are highlighted as dark circles; the LSP of the ANTH $C(sp^2)$ atoms is coincident with the plane of the page). The projection of the ANTH-6-1 major axis onto the ANTH LSP is rotated 20.7° relative to the ANTH major axis. The numbered $C(sp^2)$ atoms of ANTH-6-1 that appear "within" or nearly within the red lines of the ANTH π-electron cloud have the following perpendicular out-of-plane displacements from the ANTH least-squares plane: C1, 3.63 Å; C2, 3.66 Å; C5, 3.34 Å; C11, 3.49 Å; C12, 3.46 Å; C13, 3.48 Å; and C14, 3.50 Å. Note that the standard errors for C–C distances in this structure are no more than ±0.002 Å.

As predicted by Sun and co-workers,[77] mixing of CF_3 containing substituents with underivatized PAHs led to mainly π-π stacking. Similar mixed stacks have been seen many times for co-crystals of fluorine-containing substituents with electron donors.[26,76,78,79]

Two interesting comparisons in solid-state packing can be made when there is little to no difference in gas-phase ion energetics. The CTCs ANTH/ANTH-6-1 and ANTH/ANTH-6-2 had no difference in donor IE (i.e., ANTH is the donor in both cases) and little difference in acceptor EA (2.81(2) eV for ANTH-6-1 and 2.68(2) eV for ANTH-6-2). Their solid-state packing is similar with infinite stacks of alternating donors and acceptors and with the stacks organized in pseudohexagonal arrays. However, in ANTH/ANTH-6-1 these stacks were parallel to each other, whereas in ANTH/ANTH-6-2 adjacent stacks were tilted from one another by 33.7° as shown in Figure 2.43. Given the minimal differences in ion energetics, the most likely explanation is the difference in structure between the centrosymetric molecule, ANTH-6-1, and the

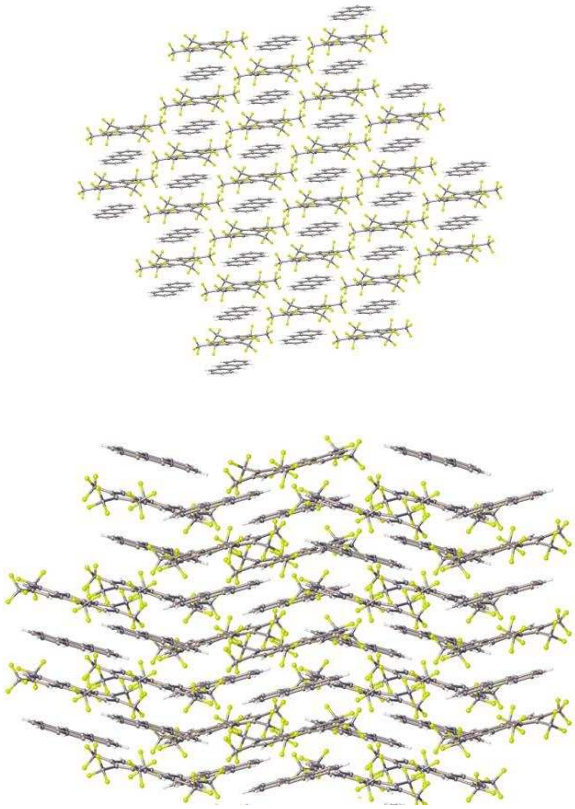

Figure 2.43. (Top) Packing of ANTH/ANTH-6-1 co-crystal. Adjacent stacks are parallel. (Bottom) Packing of ANTH/ANTH-6-2 co-crystals. Adjacent stacks have a 33.7° angle of corrugation between them. This is most apparent in the top three molecules of the bottom image where there are two ANTH molecules around an ANTH-6-2 molecule, the angle is measured between the central ANTH-6-2 molecule and one of the adjacent ANTH molecules. F atoms are colored yellow.

non-centrosymmetric molecule, ANTH-6-2. It is likely that the differences in intermolecular F···F interactions may be the reason for the different interstack orientations.

The next comparison is between ANTH/ANTH-6-1 and PYRN/ANTH-6-1. The difference in donor IE is only 0.013 eV and both CTCs have the same acceptor. The difference in solid-state packing is significant. As described above the structure of ANTH/ANTH-6-1 consists of parallel infinite alternating D/A stacks whereas the structure of PYRN/ANTH-6-1 consists of A/D/A sandwiches in herringbone-like planes superimposed on one another in the third dimension (Figures 2.37 and 2.38). This difference may have been due to the rotation between PYRN and ANTH-6-1 which may have induced a bend in the ANTH-6-1 core leading to the observed structure.

2.3. Summary and Conclusions

The sealed-ampoule reaction between a PAH and CF_3I can be used to produce PAH$(CF_3)_n$ compounds with a variety of compositions and isomers. It has also been demonstrated that this method can be used to add CF_3 groups to PHNZ, which has not been post-synthetically trifluoromethylated in the past. In general, when PAHs with 8–10 carbons available for substitution are reacted with at least 10 equivalents of CF_3I the main PAH$(CF_3)_n$ products will have a range of n values from 4 to 6. Most of the products are ≤ 60% substituted, but higher levels of substitution can be achieved. The shape of the PAH does play a role: the predominant PHEN$(CF_3)_n$ products had lower n values than derivatives of the linear acene, ANTH. Changing the number of rings in the parent PAH from 3 to 4 (i.e., ANTH vs PYRN) did not significantly impact the product distribution, likely because both PAHs have the same number of C(sp^2) atoms available for substitution. Finally, reaction times of less than 1 h and using ≤ 8 equivalents of CF_3I in the reaction led to a wider product distribution and lower n values.

The addition of electron-withdrawing CF_3 groups to PAHs resulted in a regular, incremental increase in both the $E_{1/2}$ values and EAs as a function of the number of CF_3 groups. PAHs with 3 or 4 rings have very similar trends in $E_{1/2}$ and EA as a function of the number of CF_3 groups. The presence of heteroatoms in the PAH core decreases the electron-withdrawing ability of the CF_3 groups and results in lower changes in $E_{1/2}$ or EA per CF_3 group added. The substitution pattern impacts the $E_{1/2}$ more than the EA and the largest impacts of substitution pattern are observed for PAHs with bay or fjord regions, such as FLRA, PHEN, and PERY. Reduction potentials and EAs can also be correlated and for a broad selection of PAH and PAH$(CF_3)_n$ the approximately linear plot exhibited a slope of 0.74 V eV^{-1}. The significance of this is that differences in gas-phase acceptor properties of PAH$(CF_3)_n$ compounds are attenuated in solution, and presumably would also be attenuated in the solid state.

CTCs are formed when solutions of PAHs and PAH$(CF_3)_n$ compounds are mixed. A color change is typically observed and many PAH/PAH$(CF_3)_n$ CTCs pack in pseudohexagonal arrays of alternating donor-acceptor. The association constants for ANTH/ANTH-5-1 and

ANTH/ANTH-6-1 were found to be 1.7(1) and 2.8(1) M^{-1} in DCE solution. The energy of the CT band is more closely approximated by the difference in solution oxidation/reduction potentials of the donors and acceptors than by the difference in gas-phase IEs and EAs of the donors and acceptors.

2.4. Experimental Details

2.4.1. Reagents and Solvents. All reagents and solvents were reagent grade or better. Anthracene (TCI America, 94%), coronene (TCI America, 95.0%) fluorene (Aldrich, 98%), fluoranthene (Aldrich, 98%), pyrene (Alfa Aesar, 98%), phenanthrene (Aldrich, 98%), phenazine (Aldrich, 98%), perylene (Aldrich, 99%), ACS grade toluene (Fisher), Spectroscopy grade toluene (Burdick & Jackson), HPLC grade heptane (Fisher Scientific), HPLC grade acetonitrile (EMD or Fisher), HPLC grade methanol (Fisher), ACS grade dichloromethane (Fisher), triethylaluminum 25 wt% in toluene (Aldrich), hexafluorobenzene (Aldrich), 1,4-bis(trifluoromethyl)benzene (Central Glass), chloroform-D (Cambridge Isotopes Laboratories), and 1,2-dichloroethane (Acros or Fisher Scientific) were used as received. AZUL-5-1 was prepared by Mr. Tyler T. Clikeman as previously described.[52] For the reaction of PHNZ$(CF_3)_n$ with triethylalumium ACS grade toluene was refluxed over sodium metal under N_2 for 3 h followed by distillation under N_2. For NMR analysis of the reaction of PHNZ$(CF_3)_n$ with triethylaluminum: d8-toluene (Cambridge Isotopes Laboratories) and hexafluorobenzene (Oakwood Products) were dried over activated 3 Å molecular sieves and distilled under N_2.

2.4.2. Reactions of PAH with CF_3I. Reactions were performed by Strauss-Boltalina postdoc Dr. Igor V. Kuvychko as previously described.[50] Reaction conditions for each PAH substrate are listed in Table 2.1.

2.4.3. Separation of PAH$(CF_3)_n$ Compounds.

PAH$(CF_3)_n$ compounds were separated by the author using an HPLC Prominence system (Shimadzu) comprised of LC-6AD pump, 2 mL sample loop, equipped with SPD-20A UV-vis detector, SPD-M20A diode array detector, and CBM-20A communications bus module. Three columns were used for separations (i) Cosmosil Buckyprep (Nacalai Tesque) preparative column

(250 × 20 mm i.d), (ii) Cosmosil Buckyprep (Nacalai Tesque) semi-preparative column (250 × 10 mm i.d.), and (iii) FluoroFlash (Fluorous Technologies, Inc.) analytical column (150 × 4.6 mm i.d.). Separation conditions and compounds isolated at each step are detailed in the results and discussion.

2.4.4. Characterization of Newly Identified Compounds

Preliminary isomer identification was performed by the author using ^{19}F and ^{1}H NMR spectroscopy. Fluorine-19 (376 MHz) and proton (399 MHz) NMR spectra of samples dissolved in $CDCl_3$ were recorded on a Varian Innova 400 MHz instrument using a 1 s relaxation time and a 45° pulse angle. The ^{19}F chemical shifts were referenced using either hexafluorobenzene (δ −164.9) or 1,4-bis(trifluoromethyl)benzene as an internal standard (δ −66.4). The ^{1}H chemical shifts were referenced using the resonance of the residual $CHCl_3$ in $CDCl_3$ as an internal standard (δ 7.27).

UV-vis spectra were recorded by the author using a Cary 500 UV/Vis/NIR spectrophotometer. Mass spectra were recorded by the author with the assistance of Dr. Olga V. Boltalina or Dr. Kuvychko using an electrospray ionization source on either a 2000 Finnigan LCQ Duo or a Finnigan LTQ instrument. For mass spectrometry the carrier solvent was acetonitrile at 0.3 mL min^{-1}; the samples were injected as solutions in dichloromethane or acetonitrile.

In this work solution reduction potentials have been determined by cyclic voltammetry (CV) using a three electrode system. The platinum working electrode is where oxidation and reduction of the analytes occur. Current flows into the system through the platinum auxiliary electrode. The potential is controlled as the energy difference between the working electrode and a reference electrode. A silver wire quasi-reference electrode was used because the measurements were made in non-aqueous solutions. Since the potential between the working and reference electrodes is then a function of the composition of the system, ferrocene ($Fe(Cp)_2$) was used as an internal standard for the potential of the system and all reduction potentials are reported versus $Fe(Cp)_2^{+/0}$. In a CV experiment the potential is scanned, at a set scan rate, to a set value,

then the potential is scanned in the opposite direction, back to the initial. The current in the system changes as species are either oxidized or reduced. A cyclic voltammogram is produced by plotting the current as a function of the potential. For the electron acceptors studied in this work the reduction potential is a measure of the electron accepting capabilities of the molecule; as the reduction potential increases, i.e., becomes less negative, the molecule is easier to reduce and is therefore a better electron acceptor. CV measurements were carried out in a purified dinitrogen-atmosphere glovebox using a PAR 263 potentiostat/galvanostat. CV measurements utilized 0.1 M tetrabutylammonium perchlorate in dimethoxyethane with platinum working and counter electrodes and a silver wire quasi-reference electrode at a scan rate of 500 mV s^{-1} using ferrocene as an internal standard. Electrochemical measurements for ANTH-6-2, all FLRA$(CF_3)_n$ compounds, PHEN-4-1, PHEN-4-2, all PHNZ$(CF_3)_n$ compounds, and PYRN-6-3 were performed by the author. All other electrochemical measurements were performed by Dr. Kuvychko.

2.4.5. X-ray Crystallography of PAH$(CF_3)_n$ Compounds

To perform single crystal X-ray diffraction, the molecule of interest must be grown as a single crystal, typically from solution. The crystal is then mounted onto the instrument in the path of the X-ray beam. Incident X-rays are diffracted by the electrons in the crystal lattice and produce a diffraction spot when Bragg's Law is satisfied. Many diffraction spots are generated as the crystal is rotated in the X-ray beam. A Fourier transform of the diffraction pattern results in an electron density map of the crystal. Larger molecules with more electrons will have a higher electron density. The molecular structure is then modeled by fitting atoms to the electron density. The model is refined to minimize discrepancy between the model and the data, while also minimizing the data-to-parameter ratio.

All crystals were grown by the author via slow solvent evaporation. X-ray crystallographic studies were performed by Dr. Kuvychko, Mr. Eric V. Bukovsky, and Mr. Clikeman. Some crystal structures were collected at Colorado State University using a Bruker APEX-II CCD diffractometer with a Mo Kα X-ray tube source and graphite monochromator. Other crystal structures were collected at the Advanced Photon Source synchrotron instrument at Argonne

National Laboratory, Argonne IL, on beamline 15ID-B with a wavelength of 0.40651 Å, employing a diamond 1 1 1 monochromator and a Bruker D8 goniometer with the assistance of Dr. Yu-Sheng Chen. Diffraction data for PHNZ-6-1 were collected during the 2014 American Crystallographic Association Summer Course in Chemical Crystallography at the University of Notre Dame using a Bruker Kappa APEX II CCD diffractometer employing Cu Kα radiation and a graphite monochromator.

Unit cell parameters were obtained from least-squares fits to the angular coordinates of all reflections, and intensities were integrated from a series of frames (ω and ϕ rotation) covering more than a hemisphere of reciprocal space. Absorption and other corrections were applied using SCALE.[80] The structure was solved using direct methods and refined (on F^2, using all data) by a full-matrix, weighted least-squares process. Standard Bruker control and integration software (APEX II) was employed[81] and Bruker SHELXTL software was used with Olex 2 for structure solution, refinement, and molecular graphics for PHEN-4-1, PHEN-4-2, and all PHNZ$(CF_3)_n$ compounds.[82,83] The data for PHNZ-6-1 were indexed with three twin components and absorption and other corrections were applied using TWINABS.[84] A small amount of twinning in PHNZ-6-1 was accounted for by modeling disorder near one F atom.

2.4.6. Reaction of PHNZ$(CF_3)_n$ with Triethylaluminum

Three reactions of PHNZ$(CF_3)_n$ with triethylaluminum were performed by the author. The proposed reaction is shown below.

$$\text{PHNZ}(CF_3)_n + 2 \text{ eq. } AlEt_3 \xrightarrow[\text{rt, } N_2\text{, 4 d}]{\text{toluene}} 2 \text{ PHNZ}(CF_3)_nAlEt_2 + 2\ C_4H_{10}$$

Reaction A was performed with crude PHNZ$(CF_3)_n$ reaction mixture from Reaction 7 (Table 2.1) mixed with 2 equivalents (assuming n = 4) of $AlEt_3$, stirred at room temperature, under inert atmosphere in a N_2 glovebox for 4 days. Reaction B was performed with PHNZ-4-1, 2 equivalents of $AlEt_3$, stirred at room temperature in a N_2 glovebox for 3 days. Reaction C was performed with pure PHNZ-4-2 and 2 equivalents of $AlEt_3$, stirred at room temperature in a N_2

glovebox for 4 days. For all reactions, after the stirring was stopped the reaction mixture was dried under vacuum and redissolved in d8-toluene for NMR analysis.

2.4.7. Characterization of Charge-Transfer Complexes

Solution spectra of the CTCs were recorded by the author. Unless otherwise noted the spectra were recorded using a 1 cm quartz cuvette containing DCE solutions. For PYRN/PYRN-6-3 several diffraction-quality single crystals were re-dissolved in DCE and the spectrum was recorded using a 10 cm quartz cuvette. For CORO/ANTH-6-1 the spectra were recorded in toluene due to the low solubility of CORO in DCE. Solid-state UV-vis spectra were obtained by Mr. Bukovsky. Solutions of 1/1 D/A were drop-cast onto a quartz slide and the experiment was performed in dual-beam mode with another quartz slide in the background subtraction beam. The stoichiometry of the CTCs in solution was determined, by the author, using Job's method of continuous variation.[68] Solutions of donor and acceptor with concentrations of 1×10^{-2} M were prepared and subsequently mixed to cover the range of 0% donor to 100% donor in increments of 10%. Measurements were taken in a 1 cm quartz cuvette. The absorbance of each solution was plotted versus the D/A ratio.

Association constants for ANTH/ANTH-5-1 and ANTH/ANTH-6-1 were determined, by the author, by measuring the absorbance at the charge transfer band maximum as a function of changing donor concentration. Measurements were taken in a 1 cm quartz cuvette. The concentration of the acceptor was held constant at 5×10^{-3} M and the concentration of the donor, ANTH, was varied between 1×10^{-2} M and 7×10^{-2} M. The resulting data were used in a Scott analysis, Equation 2.1, where the absorbance at the charge transfer maximum is plotted versus the absorbance and the slope of the fitted line gives the association constant.[69] The same data were analyzed according to Seal's equation, Equation 2.2, where the sum of the donor and acceptor concentrations are plotted versus the product of the concentrations divided by the absorbance and the slope of the fitted line is the molar absorptivity.[70]

$$\frac{Abs^{CT}}{[D]_0} = -K^{CT} Abs^{CT} + K^{CT}[A]_0 \varepsilon_\lambda^{CT} \qquad \text{(Equation 2.1)}$$

$$[A]_0 + [D]_0 = \frac{[A]_0[D]_0\varepsilon_\lambda^{CT}}{Abs^{CT}} - \frac{1}{K^{CT}} \qquad \text{(Equation 2.2)}$$

2.4.8. Gas-Phase Electron Affinity

Electron affinities were measured by Strauss-Boltalina collaborator Dr. Xue-Bin Wang and his co-workers at the Pacific Northwest National Laboratory. The measurement of gas-phase electron affinities provides direct information on the molecule of interest without solvation effects. Photoelectron spectra are collected after the molecules are at low-temperatures (ca. 12–20 K) to reduce molecular vibration and therefore eliminate what is known as the hot band which is observed at the low binding energy side of the spectrum.

The instrument is operated and functions in the following manner. A dilute solution of the molecule of interest is chemically reduced by tetrakis(dimethylamino)ethylene. This solution is injected into the instrument through a desolvation capillary heated to ca. 80 °C. The desolvated anions pass through a series of skimmers and ion guides to the 3D Paul ion trap where ions are thermalized to low temperatures (ca. 12–20 K) by collisions with 0.1 to 1 mTorr helium with 20% H_2 gas. Cooled ions are then sent through a time-of-flight mass spectrometry flight tube after which the ion of interest is selected by a mass gate. The selected ions interact with a laser which leads to the photodetachment of electrons, which are then collected by a magnetic bottle, guided through an electron flight tube and detected by three multi-channel plates. The photoelectron time-of-flight spectra are converted to kinetic energy spectra through calibration by known spectra. Finally, the binding energies are obtained by subtracting the kinetic energy spectra from the energy of the photodetachment laser used. The electron affinity of each compound was directly measured from the first peak maximum which is produced by the 0–0 transition in the corresponding photoelectron spectrum.[85] The energy resolution ($\Delta E/E$) was ca. 2% (i.e., ca. 20 meV for 1 eV electrons).

CHAPTER 2 REFERENCES

(1) Chang, Y. C.; Kuo, M. Y.; Chen, C. P.; Lu, H. F.; Chao, I.: On the Air Stability of n-Channel Organic Field-Effect Transistors: A Theoretical Study of Adiabatic Electron Affinities of Organic Semiconductors. *J. Phys. Chem. C* **2010**, *114*, 11595-11601.

(2) Anthony, J. E.: Functionalized acenes and heteroacenes for organic electronics. *Chem. Rev.* **2006**, *106*, 5028-5048.

(3) Jones, B. A.; Facchetti, A.; Wasielewski, M. R.; Marks, T. J.: Tuning orbital energetics in arylene diimide semiconductors. Materials design for ambient stability of n-type charge transport. *J. Am. Chem. Soc.* **2007**, *129*, 15259-15278.

(4) Jones, B. A.; Ahrens, M. J.; Yoon, M. H.; Facchetti, A.; Marks, T. J.; Wasielewski, M. R.: High-mobility air-stable n-type semiconductors with processing versatility: Dicyanoperylene-3,4 : 9,10-bis(dicarboximides). *Angew. Chem., Int. Ed.* **2004**, *43*, 6363-6366.

(5) Sun, H. R.; Putta, A.; Billion, M.: Arene Trifluoromethylation: An Effective Strategy to Obtain Air-Stable n-Type Organic Semiconductors with Tunable Optoelectronic and Electron Transfer Properties. *J. Phys. Chem. A* **2012**, *116*, 8015-8022.

(6) Sun, H. R.; Putta, A.; Kloster, J. P.; Tottempudi, U. K.: Unexpected photostability improvement of aromatics in polyfluorinated solvents. *Chem. Commun.* **2012**, *48*, 12085-12087.

(7) Miao, S.; Brombosz, S. M.; Schleyer, P. V.; Wu, J. I.; Barlow, S.; Marder, S. R.; Hardcastle, K. I.; Bunz, U. H. F.: Are N,N-dihydrodiazatetracene derivatives antiaromatic? *J. Am. Chem. Soc.* **2008**, *130*, 7339-7344.

(8) Bunz, U. H. F.: N-Heteroacenes. *Chem. - Eur. J.* **2009**, *15*, 6780-6789.

(9) Winkler, M.; Houk, K. N.: Nitrogen-rich oligoacenes: Candidates for n-channel organic semiconductors. *J. Am. Chem. Soc.* **2007**, *129*, 1805-1815.

(10) Dillow, G. W.; Kebarle, P.: Electron affinities of aza-substituted polycyclic aromatic hydrocarbons. *Can. J. Chem.* **1989**, *67*, 1628-1631.

(11) Schiedt, J.; Weinkauf, R.: Photodetachment photoelectron spectroscopy of mass selected anions: anthracene and the anthracene-H_2O cluster. *Chem. Phys. Lett.* **1997**, *266*, 201-205.

(12) Ando, N.; Mitsui, M.; Nakajima, A.: Comprehensive photoelectron spectroscopic study of anionic clusters of anthracene and its alkyl derivatives: Electronic structures bridging molecules to bulk. *J. Chem. Phys.* **2007**, *127*.

(13) Lemaur, V.; da Silva Filho, D. A.; Coropceanu, V.; Lehmann, M.; Geerts, Y.; Piris, J.; Debije, M. G.; van de Craats, A. M.; Senthilkumar, K.; Siebbeles, L. D. A.; Warman, J. M.; Brédas, J.-L.; Cornil, J.: Charge Transport Properties in Discotic Liquid Crystals: A Quantum-Chemical Insight into Structure−Property Relationships. *J. Am. Chem. Soc.* **2004**, *126*, 3271-3279.

(14) Kaafarani, B. R.; Kondo, T.; Yu, J.; Zhang, Q.; Dattilo, D.; Risko, C.; Jones, S. C.; Barlow, S.; Domercq, B.; Amy, F.; Kahn, A.; Brédas, J.-L.; Kippelen, B.; Marder, S. R.: High Charge-Carrier Mobility in an Amorphous Hexaazatrinaphthylene Derivative. *J. Am. Chem. Soc.* **2005**, *127*, 16358-16359.

(15) Turner, J. M.; Messenger, A. J.: Occurrence, Biochemistry and Physiology of Phenazine Pigment Production. *Adv. Microb. Physiol.* **1986**, *27*, 211-275.

(16) Laursen, J. B.; Nielsen, J.: Phenazine Natural Products: Biosynthesis, Synthetic Analogues, and Biological Activity. *Chem. Rev.* **2004**, *104*, 1663-1686.

(17) Singh, M. K.; Pal, H.; Bhasikuttan, A. C.; Sapre, A. V.: Dual solvatochromism of neutral red. *Photochem. Photobiol.* **1998**, *68*, 32-38.

(18) Swan, G. A.; Felton, D. G. I.: Phenazines. In *The Chemistry of Heterocyclic Compounds*; Weissberger, A., Ed.; Interscience: London, 1957; Vol. XI.

(19) Pauliukaite, R.; Ghica, M. E.; Barsan, M. M.; Brett, C. M. A.: Phenazines and Polyphenazines In Electrochemical Sensors and Biosensors. *Anal. Lett.* **2010**, *43*, 1588-1608.

(20) Gu, P.-Y.; Zhao, Y.; He, J.-H.; Zhang, J.; Wang, C.; Xu, Q.-F.; Lu, J.-M.; Sun, X. W.; Zhang, Q.: Synthesis, Physical Properties, and Light-Emitting Diode Performance of Phenazine-Based Derivatives with Three, Five, and Nine Fused Six-Membered Rings. *J. Org. Chem.* **2015**, *80*, 3030-3035.

(21) Wang, C.; Dong, H.; Hu, W.; Liu, Y.; Zhu, D.: Semiconducting π-Conjugated Systems in Field-Effect Transistors: A Material Odyssey of Organic Electronics. *Chem. Rev.* **2011**, *112*, 2208-2267.

(22) Martinez, C. R.; Iverson, B. L.: Rethinking the term "pi-stacking". *Chem. Sci.* **2012**, *3*, 2191-2201.

(23) Maly, K. E.: Acenes vs N-Heteroacenes: The Effect of N-Substitution on the Structural Features of Crystals of Polycyclic Aromatic Hydrocarbons. *Cryst. Growth Des.* **2011**, *11*, 5628-5633.

(24) Sun, H. R.; Tottempudi, U. K.; Mottishaw, J. D.; Basa, P. N.; Putta, A.; Sykes, A. G.: Strengthening pi-pi Interactions While Suppressing C_{sp2}-H center dot center dot center dot pi (T-Shaped) Interactions via Perfluoroalkylation: A Crystallographic and Computational Study That Supports the Beneficial Formation of 1-D pi-pi Stacked Aromatic Materials. *Cryst. Growth Des.* **2012**, *12*, 5655-5662.

(25) Putta, A.; Putta, J. D.; Mottishaw, Z.; Wang, H.; Sun, A.: Rational Design of Lamellar π–π Stacked Organic Crystalline Materials with Short Interplanar Distance *Cryst. Growth Des.* **2014**, *14*, 350-356.

(26) Collings, J. C.; Roscoe, K. P.; Robins, E. G.; Batsanov, A. S.; Stimson, L. M.; Howard, J. A.; Clark, S. J.; Marder, T. B.: Arene–perfluoroarene interactions in crystal engineering 8: structures of 1:1 complexes of hexafluorobenzene with fused-ring polyaromatic hydrocarbons. *New J. Chem.* **2002**, *26*, 1740-1746.

(27) Yu, W.; Wang, X. Y.; Li, J.; Li, Z. T.; Yan, Y. K.; Wang, W.; Pei, J.: A photoconductive charge-transfer crystal with mixed-stacking donor-acceptor heterojunctions within the lattice. *Chem. Commun.* **2013**, *49*, 54-56.

(28) Herbstein, F. H.: *Crystalline molecular complexes and compounds*; Oxford University Press, 2005; Vol. 2.

(29) Mori, T.; Kawamoto, T.: Organic conductors-from fundamentals to nonlinear conductivity. *Annu. Rep. Prog. Chem., Sect. C: Phys. Chem.* **2007**, *103*, 134-172.

(30) Goetz, K. P.; Vermeulen, D.; Payne, M. E.; Kloc, C.; McNeil, L. E.; Jurchescu, O. D.: Charge-transfer complexes: new perspectives on an old class of compounds. *J. Mater. Chem. C* **2014**, *2*, 3065-3076.

(31) Ferraris, J.; Cowan, D. O.; Walatka, V.; Perlstein, J. H.: Electron transfer in a new highly conducting donor-acceptor complex. *J. Am. Chem. Soc.* **1973**, *95*, 948-949.

(32) Coleman, L. B.; Cohen, M. J.; Sandman, D. J.; Yamagishi, F. G.; Garito, A. F.; Heeger, A. J.: Superconducting fluctuations and the peierls instability in an organic solid. *Solid State Comm.* **1973**, *12*, 1125-1132.

(33) Karl, N.; Ziegler, J.: Generation and transport of charge carriers in the charge-transfer complex anthracene-pyromellitic-dianhydride. *Chem. Phys. Lett.* **1975**, *32*, 438-442.

(34) Rao, K. V.; George, S. J.: Supramolecular Alternate Co-Assembly through a Non-Covalent Amphiphilic Design: Conducting Nanotubes with a Mixed D–A Structure. *Chem. - Eur. J.* **2012**, *18*, 14286-14291.

(35) Zhu, L.; Yi, Y.; Li, Y.; Kim, E.-G.; Coropceanu, V.; Brédas, J.-L.: Prediction of Remarkable Ambipolar Charge-Transport Characteristics in Organic Mixed-Stack Charge-Transfer Crystals. *J. Am. Chem. Soc.* **2012**, *134*, 2340-2347.

(36) Mataga, N.; Murata, Y.: Electron donor-acceptor interactions in the fluorescent state of tetracyanobenzene-aromatic hydrocarbon complexes. *J. Am. Chem. Soc.* **1969**, *91*, 3144-3152.

(37) Lei, Y.-L.; Jin, Y.; Zhou, D.-Y.; Gu, W.; Shi, X.-B.; Liao, L.-S.; Lee, S.-T.: White-Light Emitting Microtubes of Mixed Organic Charge-Transfer Complexes. *Adv. Mater.* **2012**, *24*, 5345-5351.

(38) Eldaroti, H. H.; Gadir, S. A.; Refat, M. S.; Adam, A. M. A.: Charge Transfer Complexes of the Donor Acriflavine and the Acceptors Quinol, Picric acid, TCNQ and DDQ: Synthesis, Spectroscopic Characterizations and Antimicrobial Studies. *Int. J. Electrochem. Sci.* **2013**, *8*, 5774-5800.

(39) Harada, K.; Sumino, M.; Adachi, C.; Tanaka, S.; Miyazaki, K.: Improved thermoelectric performance of organic thin-film elements utilizing a bilayer structure of pentacene and 2,3,5,6-tetrafluoro-7,7,8,8-tetracyanoquinodimethane (F4-TCNQ). *Appl. Phys. Lett.* **2010**, *96*, 253304.

(40) Alves, H.; Pinto, R. M.; Maçôas, E. S.: Photoconductive response in organic charge transfer interfaces with high quantum efficiency. *Nat. Commun.* **2013**, *4*, 1842.

(41) Tsutsumi, J. y.; Yamada, T.; Matsui, H.; Haas, S.; Hasegawa, T.: Competition between Charge-Transfer Exciton Dissociation and Direct Photocarrier Generation in Molecular Donor-Acceptor Compounds. *Phys. Rev. Lett.* **2010**, *105*, 226601.

(42) Tsutsumi, J. y.; Matsui, H.; Yamada, T.; Kumai, R.; Hasegawa, T.: Generation and Diffusion of Photocarriers in Molecular Donor–Acceptor Systems: Dependence on Charge-Transfer Gap Energy. *J. Phys. Chem. C* **2012**, *116*, 23957-23964.

(43) Tiers, G. V. D.: Perfluoroalkylation Of Aromatic Compounds. *J. Am. Chem. Soc.* **1960**, *82*, 5513-5513.

(44) Cowell, A. B.; Tamborski, C.: Fluoroalkylation of Aromatic Compounds. *J. Fluorine Chem.* **1981**, *17*, 345-356.

(45) Bravo, A.; Bjorsvik, H. R.; Fontana, F.; Liguori, L.; Mele, A.; Minisci, F.: New methods of free-radical perfluoroalkylation of aromatics and alkenes. Absolute rate constants and partial rate factors for the homolytic aromatic substitution by n-perfluorobutyl radical. *J. Org. Chem.* **1997**, *62*, 7128-7136.

(46) Chernetsky, V.; Yagupolsky, L.; Serebryany, S.: Synthesis of Some Fluorine Derivatives of Phenazine, Azobenzene, and Diphenylamine. *Zh. Obschch. Khim.* **1959**, 14.

(47) Banks, R. E.; Prakash, A.: Studies in Azide Chemistry 6 Some Reactions of Perfluoroazidobenzene and Perfluoro-4-Azidotoluene. *J. Chem. Soc. Perkin Trans. 1* **1974**, 1365-1371.

(48) Banks, R. E.; Madany, I. M.; Pritchard, R. G.: 1,2,4-Trifluoro-6,8-dimethyl-3-trifluromethylphenazine, $C_{15}H_8F_6N_2$, produced via thermolysys of perfluoro-4-azidotoluene in the presence of 2,4,6-trimethylaniline. *Acta Crystallogr., Sect. C: Cryst. Struct. Comm.* **1993**, *49*, 1988-1990.

(49) Matsui, M.; Suzuki, M.; Nunome, I.; Kubota, Y.; Funabiki, K.; Shiro, M.; Matsumoto, S.; Shiozaki, H.: Reaction, identification, and fluorescence of aminoperfluorophenazines. *Tetrahedron* **2008**, *64*, 8830-8836.

(50) Kuvychko, I. V.; Castro, K. P.; Deng, S. H. M.; Wang, X. B.; Strauss, S. H.; Boltalina, O. V.: Taming Hot CF_3 Radicals: Incrementally Tuned Families of Polyarene Electron Acceptors for Air-Stable Molecular Optoelectronics. *Angew. Chem., Int. Ed.* **2013**, *52*, 4871-4874.

(51) San, L. K.; Bukovsky, E. V.; Kuvychko, I. V.; Popov, A. A.; Strauss, S. H.; Boltalina, O. V.: Single-Step Gas-Phase Polyperfluoroalkylation of Naphthalene Leads to Thermodynamic Products. *Chem. Eur. J.* **2014**, *20*, 4373-4379.

(52) Clikeman, T. T.; Bukovsky, E. V.; Kuvychko, I. V.; San, L. K.; Deng, S. H.; Wang, X.-B.; Chen, Y.-S.; Strauss, S. H.; Boltalina, O. V.: Poly (trifluoromethyl) azulenes: structures and acceptor properties. *Chem. Commun.* **2014**, *50*, 6263-6266.

(53) Lee, J.; Lane, D. A.: Formation of oxidized products from the reaction of gaseous phenanthrene with the OH radical in a reaction chamber. *Atmos. Environ.* **2010**, *44*, 2469-2477.

(54) Crawford, A. G.; Dwyer, A. D.; Liu, Z. Q.; Steffen, A.; Beeby, A.; Palsson, L. O.; Tozer, D. J.; Marder, T. B.: Experimental and Theoretical Studies of the Photophysical Properties of 2-and 2,7-Functionalized Pyrene Derivatives. *J. Am. Chem. Soc.* **2011**, *133*, 13349-13362.

(55) Curran, D. P.: Fluorous reverse phase silia gel. A new tool for preparative separations in synthetic organic and organofluorine chemistry. *Synlett* **2001**, *2001*, 1488-1496.

(56) Tang, M. L.; Bao, Z. A.: Halogenated Materials as Organic Semiconductors. *Chem. Mater.* **2011**, *23*, 446-455.

(57) Yoon, M. H.; Facchetti, A.; Stern, C. E.; Marks, T. J.: Fluorocarbon-modified organic semiconductors: Molecular architecture, electronic, and crystal structure tuning of arene-versus fluoroarene-thiophene oligomer thin-film properties. *J. Am. Chem. Soc.* **2006**, *128*, 5792-5801.

(58) Babudri, F.; Farinola, G. M.; Naso, F.; Ragni, R.: Fluorinated organic materials for electronic and optoelectronic applications: the role of the fluorine atom. *Chem. Commun.* **2007**, 1003-1022.

(59) Anthony, J. E.; Facchetti, A.; Heeney, M.; Marder, S. R.; Zhan, X. W.: n-Type Organic Semiconductors in Organic Electronics. *Adv. Mater.* **2010**, *22*, 3876-3892.

(60) Michl, J.: Electronic structure of non-alternant hydrocarbons: Their analogues and derivatives: XVIII. The electronic spectrum and electron affinity of fluoranthene. *J. Mol. Spectrosc.* **1969**, *30*, 66-76.

(61) Tschurl, M.; Boesl, U.; Gilb, S.: The electron affinity of phenanthrene. *J. Chem. Phys.* **2006**, *125*.

(62) Ando, N.; Kokubo, S.; Mitsui, M.; Nakajima, A.: Photoelectron spectroscopy of pyrene cluster anions, $(pyrene)^{-n}$ (n=1-20). *Chem. Phys. Lett.* **2004**, *389*, 279-283.

(63) Kuvychko, I. V.; Spisak, S. N.; Chen, Y. S.; Popov, A. A.; Petrukhina, M. A.; Strauss, S. H.; Boltalina, O. V.: A Buckybowl with a Lot of Potential: C_5-$C_{20}H_5(CF_3)_5$. *Angew. Chem., Int. Ed.* **2012**, *51*, 4939-4942.

(64) Ruoff, R. S.; Kadish, K. M.; Boulas, P.; Chen, E.: Relationship between the electron affinities and half-wave reduction potentials of fullerenes, aromatic hydrocarbons, and metal complexes. *J. Phys. Chem.* **1995**, *99*, 8843-8850.

(65) Woźniak, K.; Kariuki, B.; Jones, W.: Structure of phenazine. *Acta Cryst. C* **1991**, *47*, 1113-1114.

(66) Shuster, V.; Gambarotta, S.; Nikiforov, G. B.; Korobkov, I.; Budzelaar, P. H. M.: Radical Cleavage of Al–C Bonds Promoted by Phenazine: From Noninnocent Ligand to Radical Abstractor. *Organometallics* **2012**, *31*, 7011.

(67) Berionni, G.; Bertelle, P. A.; Marrot, J.; Goumont, R.: X-ray Structure of a CT Complex Relevant to Diels-Alder Reactivity of Anthracenes. *J. Am. Chem. Soc.* **2009**, *131*, 18224-+.

(68) Job, P.: Studies on the formation of complex minerals in solution and on their stability. *An. Chim. Fr.* **1928**, *9*, 113-203.

(69) Scott, R. L.: Some Comments on the Benesi-Hildebrand Equation. *Recl. Trav. Chim. Pays-Bas* **1956**, *75*, 787-789.

(70) Seal, B. K.; Sil, H.; Mukherjee, D. C.: Independent Determination of Equilibrium-Constant and Molar Extinction Coefficient of Molecular-Complexes From Spectrophotometric Data By a Graphical-Method. *Spectrochim. Acta Part A* **1982**, *38*, 289-292.

(71) Lotfi, M.; Roberts, R. M. G.: Correlation of thermodynamic stabilities of charge transfer complexes of anthracene and chloranil with those of tetra-cyanoethylene. *Tetrahedron* **1979**, *35*, 2123-2129.

(72) Popov, A. A.; Kareev, I. E.; Shustova, N. B.; Stukalin, E. B.; Lebedkin, S. F.; Seppelt, K.; Strauss, S. H.; Boltalina, O. V.; Dunsch, L.: Electrochemical, spectroscopic, and DFT study of $C_{60}(CF_3)_n$ frontier orbitals (n=2-18): The link between double bonds in pentagons and reduction Potentials. *J. Am. Chem. Soc.* **2007**, *129*, 11551-11568.

(73) Hager, J. W.; Wallace, S. C.: Two-laser photoionization supersonic jet mass spectrometry of aromatic molecules. *Anal. Chem.* **1988**, *60*, 5-10.

(74) Shchuka, M. I.; Motyka, A. L.; Topp, M. R.: Two-photon threshold ionization spectroscopy of perylene and van der waals complexes. *Chem. Phys. Lett.* **1989**, *164*, 87-95.

(75) Dietrich, M.; Heinze, J.: On the determination of redox potentials of highly reactive aromatic mono- and multications. *J. Am. Chem. Soc.* **1990**, *112*, 5142-5145.

(76) Collings, J. C.; Roscoe, K. P.; Thomas, R. L.; Batsanov, A. S.; Stimson, L. M.; Howard, J. A.; Marder, T. B.: Arene-perfluoroarene interactions in crystal engineering. Part 3. Single-crystal structures of 1: 1 complexes of octafluoronaphthalene with fused-ring polyaromatic hydrocarbons. *New J. Chem.* **2001**, *25*, 1410-1417.

(77) Mottishaw, J. D.; Sun, H.: Effects of Aromatic Trifluoromethylation, Fluorination, and Methylation on Intermolecular π–π Interactions. *J. Phys. Chem. A* **2013**, *117*, 7970-7979.

(78) Reichenbacher, K.; Suss, H. I.; Hulliger, J.: Fluorine in crystal engineering-"the little atom that could". *Chem. Soc. Rev.* **2005**, *34*, 22-30.

(79) Weck, M.; Dunn, A. R.; Matsumoto, K.; Coates, G. W.; Lobkovsky, E. B.; Grubbs, R. H.: Influence of Perfluoroarene–Arene Interactions on the Phase Behavior of Liquid Crystalline and Polymeric Materials. *Angew. Chem., Int. Ed.* **1999**, *38*, 2741-2745.

(80) Sheldrick, G. M.: SADABS - A program for area detector absorption corrections. 2004.

(81) Sheldrick, G. M.: Crystallography Program APEX2, v. 5-0. Bruker AXS: Madison,WI, 2014.

(82) Sheldrick, G. M.: Crystallography Software Package SHELXTL, v. 6.14 UNIX. Bruker AXS: Madison, WI, 2001.
(83) Dolomanov, O. V.; Bourhis, L. J.; Gildea, R. J.; Howard, J. A.; Puschmann, H.: OLEX2: a complete structure solution, refinement and analysis program. *J. Appl. Cryst.* **2009**, *42*, 339-341.
(84) Sheldrick, G. M.: TWINABS v. 2012/1. 2012.
(85) Wang, X. B.; Wang, L. S.: Development of a low-temperature photoelectron spectroscopy instrument using an electrospray ion source and a cryogenically controlled ion trap. *Rev. Sci. Instrum.* **2008**, *79*.

CHAPTER 3: STRICTLY ANAEROBIC STIRRED MEDIA MILLING: THE EFFECT OF OXYGEN ON MILLING DYNAMICS, CRYSTALLITE SIZE, AND SURFACE COMPOSITION OF SILICON NANOPARTICLES

3.1. Introduction

Comminution by mechanical attrition (grinding) is a routine method to reduce particle size which is beneficial for: increasing surface area and reactivity of a material, increasing solubility, maximizing solids loading, thickening and stabilizing slurries/suspensions, intimate homogenization of powdered materials, homogenizing particle size and morphology, and top down manufacture of nanoparticles.[1-8] The desirability of nanoparticles for a host of reasons makes them attractive synthetic targets; however, commonly employed bottom-up synthesis, while well-established, is sensitive to many variables and requires exceptional control over solvent, reagents and any possible contaminants (known or otherwise), temperatures, reaction time, pH, surfactants, and other additives for reproducibility.[9-11] Top-down grinding of materials to form nanoparticles is attractive from the standpoint of cost and, in certain applications, irregular morphologies and larger size distributions of milled nanoparticles can be tolerated.[5,7,12] The properties that make nanoparticles attractive (rapid solubility, increased suspension properties, rapid reaction rates, high surface areas) also make them difficult to synthesize in high purity. For example, nanoparticles possess the inherent property of having a significant portion of the per-mass or per-volume composition of the material as surface material which necessitates exacting control of all components that could affect the surface chemistry during nanoparticle formation. Whether via solution based bottom-up synthesis or top-down grinding based methods; in both cases any and all compounds that can interact with the nascent surface have the possibility of reacting and contaminating the particle surface. Simple, top-down grinding methods with precise control over all reagents and contaminants are required to make further strides in this field.

The grinding method most discussed in literature which is easily adapted to anaerobic conditions is a ball mill either inside an inert atmosphere glovebox, or charging a ball mill jar in an inert atmosphere and then sealing with an inert gas. While it is simple to adapt a ball mill to a glovebox, presumably without even opening the glovebox face, ball mills themselves are ill-suited for efficient production of high purity nanoparticles.[1-3,13] First, ball mills are known to have poor efficiency when grinding a material below ca. 1 μm. This is due to simple statistics, the chances of a ball in the milling jar striking a particle in such a way that particle fracture occurs decreases as the particle size decreases, requiring considerably longer milling times for marginal decrease in particle size.[3,13] Second, a ball mill relies on high-energy impact to fracture particles and, in the process, damaging the milling balls and milling jar over time and is known to contaminate the sample with measurable amounts of the milling balls or milling jar materials.[1-3] Due to contamination concerns milling balls and jars must be chosen carefully in order to not inadvertently react with or contaminate the sample.

A mill design well suited to efficiently grinding materials to fine particulate size, 10–1 μm and easily into the nm range, is a stirred media mill, sometimes called an attritor mill or a stirred ball mill.[1,13,14] The attritor mill imparts energy to fine milling media in a stationary vessel through a rotating mixer, maximizing the mechanical energy imparted to the milling media and material.[1,3] It has been claimed that a stirred media mill can grind a material up to 10 times faster compared to a conventional ball mill.[3,15] The grinding process occurs by a cyclic mechanism of increasing lattice defects generated through severe plastic deformation of the sample particles during grinding via various particle- mill, media, and particle interactions until a critical potential energy point in an individual particle is reached, such that further imparted energy from the mill causes particle fracture. A stirred media mill can operate with a solvent-covered or dry sample allowing fine control over what materials contact the freshly exposed reactive material during the grinding process. However, the stirred media mill is not without its problems. Due to its high-energy transfer and rapid grinding of a sample, rapid amorphization can occur if care is not taken to prevent aggregation and agglomeration of fine particles that limit further particle fracture.

Factors affecting grinding rate, ultimate grinding limit, and other grinding dynamics of a stirred media mill have been explored by Peukert et al. and others at length.[13,14,16-24] Peukert et al. show that grinding efficiency in stirred media mill applications depends on multiple variables including milling time, mill media loading percent, agitator tip velocity, temperature, and the ability of the milling fluid and additives to stabilize the particles against agglomeration.[14,16-18,20,23] Various additives to stabilize the suspension and mitigate agglomeration by means of electrostatic, steric, or electrosteric stabilization have been shown to allow further particle size reduction to occur compared to systems without such additives.[14,17,23] This concept is logical from the stand point of the system changing to minimize the surface potential (Figure 3.1).[25,26] The nascent particle surfaces generated during grinding are quite reactive and therefore the surface potential is greatly increased during milling. At some point it becomes more favorable (under the conditions created during grinding) for a sample to agglomerate into larger particles, thereby reducing the generated surface potential. In many respects this shift to minimize surface potential is similar to micelles in a solution forming a predictable size based on properties of the aqueous and lipid portions, type and quantity of surfactant and any additives for salts, the system will change to minimize the surface potential under that particular set of conditions. The major difference being that during comminution of a sample in a mill the set of conditions is dynamic throughout the milling cycle, i.e., as more fresh surface is exposed, chemical reactions, physisorption, and particle agglomeration can augment the surface and can further change the overall surface potential.

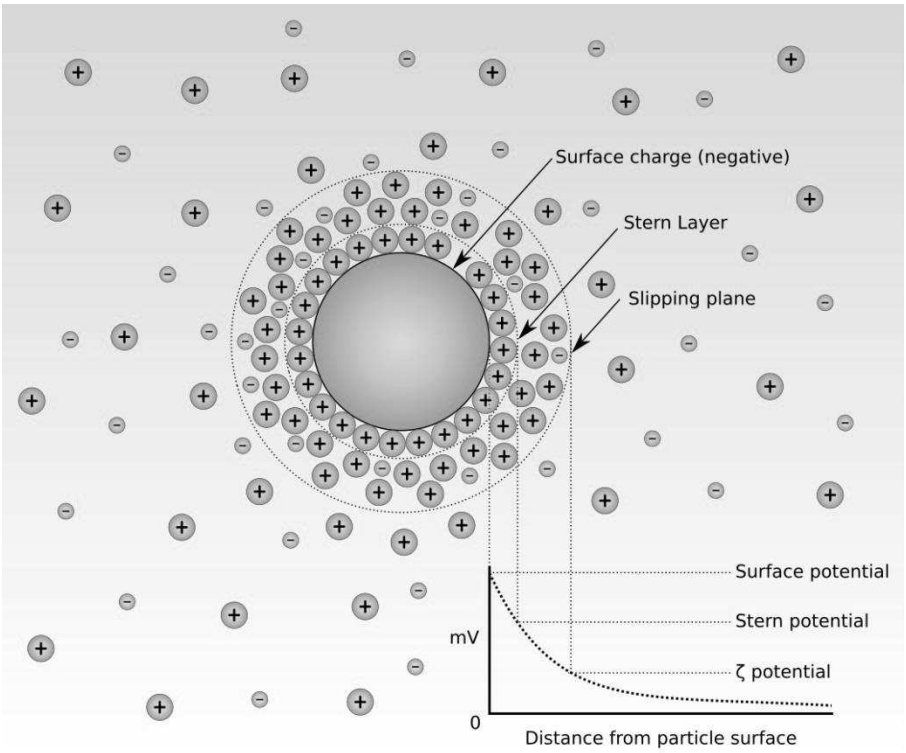

Figure 3.1. Diagram showing different regions of surface potential of a particle suspended in a solution. In this diagram the particle is negatively charged attracting positive charges to the immediate surface that slowly (if at all) exchange with the solution, this layer is known as the Stern Layer, and has a related Stern potential. Outside the Stern Layer is a more labile layer that exchanges more rapidly with the solution and has its own associated potential known as the Zeta potential (ζ – potential). The ζ – potential can be measured directly and is determined by the suspended particle (which determines the Stern layer), the solvent, any additives (buffers, surfactants and other physiochemical interacting species) and other particles and their associated layers suspended in solution. The ζ – potential also dictates how stable a suspension is with low values of ζ indicative of rapid flocculation and high values indicative of a stable suspension/colloid.[25,27]

Peukert et al. also describe a "true" grinding limit that is reached when crystallites become too small for a critical number of lattice defects to be generated in the particle.[20] It is necessary to know the true grinding limit of a particular system to minimize significant amorphization. Peukert et al. go on to describe an "apparent" grinding limit that is controlled by the stability of the suspension and how the suspension can hinder reaching the true grinding limit by being too viscous decreasing energy transfer from milling media to particles and significant inter-particle interaction leading to agglomeration. While stirred media mills have been used extensively to produce nanoparticles, and other groups have investigated what experimental factors are

important for reaching the smallest particle size, no examples have been found of another group adapting a stirred media mill to an inert atmosphere for complete inert atmosphere operation. In this work it will be demonstrated that even though the milling slurry in a stirred media mill under aerobic conditions is constantly covered with solvent (and any possible additives) atmospheric oxygen can have a significant impact on the resultant product.

The quite reactive element oxygen, in ca 20% abundance in air, readily reacts with most metals and metalloids, especially with the freshly exposed surfaces produced during grinding. Butyagin and coworkers showed that Si ball milled in an atmosphere of 100 Torr of O_2, will irreversibly bind (likely through chemical reaction) 17.5 wt% oxygen, and silicon powder activated by ball milling in vacuum and then exposed to the same amount of O_2 still irreversibly bound 1.1% oxygen.[28] Top-down production of nanoparticles via an anaerobic method is quite attractive for many applications: formation of metal nanoparticles for increased volumetric energy densities of liquid and solid fuels and explosives,[4,29-33] formation of cold-welded single component powders and multi-component intermetallic powders,[15,34,35] and quantum confined suspension-stable nanoparticles.[36-38] The effect on milling efficacy caused by adventitious oxygen present during the grinding of metals (no matter the mill design) is of interest since most metals form a surface oxide coating that would affect the agglomeration rates of these particles, affecting the ultimate particle size as well as the purity of the sample. In some cases this highly-reactive, nascent particle surface has been exploited to form new chemical bonds. The purity and surface composition of the new species would be affected by any undesired side reactions. Mitchell and Koch et al. used silicon with oxygen or various reactive organic solvents in a ball mill to concurrently mill the silicon into nanoparticles and form Si–C and Si–O bonds on the surface of the particles to produce a variety of air-stable, luminescent, passivated silicon nanoparticles.[36-38]

What species passivate the surface and other details of surface composition were investigated with X-ray photoelectron spectroscopy (XPS). The binding energy of an electron in a molecule is dependent on the composition of the molecule, particularly what adjacent atoms are present in

the molecule. The peak positions in raw data must generally be corrected for charging in a sample which causes peaks to shift. This correction is applied by shifting all peaks based on a peak with a well-established binding energy, frequently researchers use the C–C/C–H peak at 284.8 eV or 285.0 eV due to the fact that nearly all samples have an adventitious carbon layer present.[39] However, this practice is not universal and depending on how the peaks are shifted there can be large variations in peak positions between literature references. For a given binding environment peak positions reported in the literature can vary up to 1.2 eV. Collected in Table 3.1 are literature reported peaks relevant to this work. Authors do not always report peak positions for all elements involved in a given binding environment; for example, none of the references[40-42] that report Si^{3+} 2p peaks provide the associated O 1s peak position. Despite these issues, XPS is a powerful tool to identify what binding environments are present on the surface, particularly for nanoparticles.

To determine the effects an oxygen containing atmosphere has on milling dynamics in a stirred media mill, herein is reported a strictly anaerobic milling setup and results of the treatment of metallurgical grade silicon (MGS). To accomplish this research a Netzsch MiniCer stirred media mill has been completely adapted to an enclosed inert gas glovebox and the effect oxygen had on the grinding dynamics of MGS have been investigated. MGS was chosen as the test material because, while it does have an initial surface covering of SiO_2, the large increase in surface area created by the milling process rendered this small amount of initial oxide coating insignificant. Also, freshly exposed Si would rapidly react with any available O_2, making surface oxide or other surface silicon bonds easily distinguished by XPS. The milling dynamics were further investigated by intentionally adding surface passivating aromatic compounds during the anaerobic grinding of MGS samples. Anaerobic experiments are compared to aerobic milled samples produced under similar conditions. Both anaerobic and aerobic samples were analyzed by BET N_2 specific surface area, aerobic and anaerobic powder X-ray diffraction (XRD), O_2 titration and reaction experiments, and XPS.

Table 3.1. Literature reported XPS shifts relevant to this work

binding environment	Si 2p position (eV)	C 1s peak position (eV)	O 1s peak position (eV)
Si^0 $2p_{3/2}$	99.3[40,43,44] 99.4[45] 99.5[42,46-48]	—	—
Si–C	99.9[49] 100–100.4[50] 100.3[44] 101.0[41,51]	282.2[50] 282.8, 283.4[51] 283.0[44] 283.2[41]	—
Si^{2+}	101.1[40] 101.5 ($Si–Si_2O_3$)[42] 101.7 (SiO)[42]	—	531.8 ($Si–Si_2O_3$)[42]
Si^{3+}	102.1[40] 102.1 (Si_2O_3)[41] 102.5 ($Si–SiO_3$)[42]	—	—
SiO_2	102.6[49] 103.0[43] 103.2[40,45] 103.3[44] 103.4[41] 103.5[42] 103.8[46]	—	532.4[45] 532.5[40,42,46]

3.2. Results

3.2.1. General

Handle all metals milled anaerobically with caution: samples were extremely pyrophoric; samples poured through air reacted rapidly ranging in severity from heating and glowing orange to igniting particulate mid-air causing a fireball. Unless otherwise noted, anaerobic samples were treated anaerobically and manipulated in a N_2 or Ar environment. Milled samples were analyzed by BET surface area analysis, powder X-ray diffraction (XRD), (sometimes as a paste in highly purified grease to protect from oxygen), scanning electron microscopy (SEM), transmission electron microscopy (TEM), and XPS to determine effects of milling time, solvent, additives, and oxygen content. Dynamic light scattering was used to determine approximate

particle size, compare size distribution, and to further substantiate the BET surface area measurements. It was known from SEM and TEM that the milled particles were solid particles that were irregular in shape (i.e. without internal surface area due to pores), SEM and TEM images of A-H/M-5.5h are shown in Figures 3.2 and 3.3. All of the samples inspected by SEM looked similar to A-H/M-5.5h. Collected data for all milled MGS samples are summarized in Table 3.2.

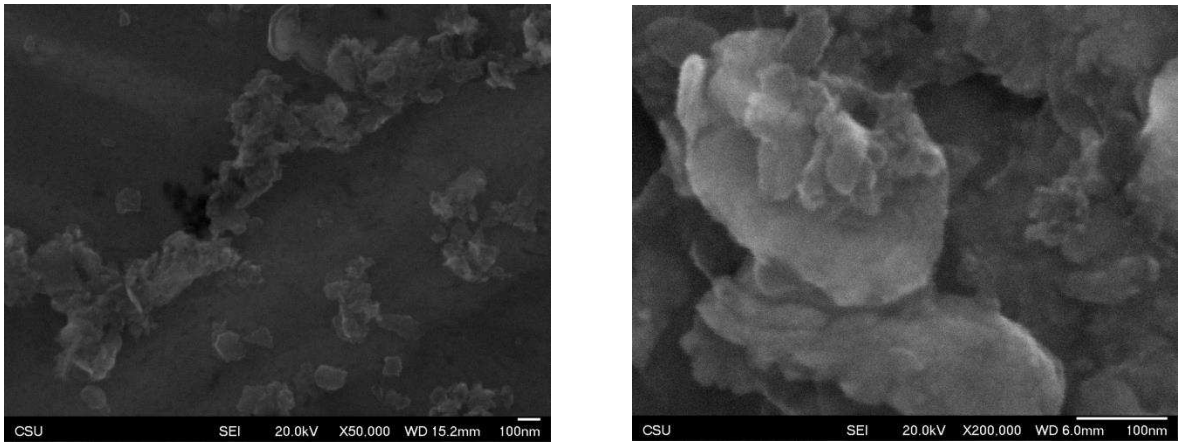

Figure 3.2. SEM images of A-H/M-5.5h aerobic milled MGS. Left image is 50,000X at 20.0 kV looking at many irregular shaped particles. Note the large distribution of sizes and that most particles appear to have flat jagged surfaces. Right, 200,000X at 20 kV, many small particles adhered to the surface of a larger particle form a larger agglomerate particle. These SEM images illustrate the morphology and broad particle size range of the nanoparticles after milling.

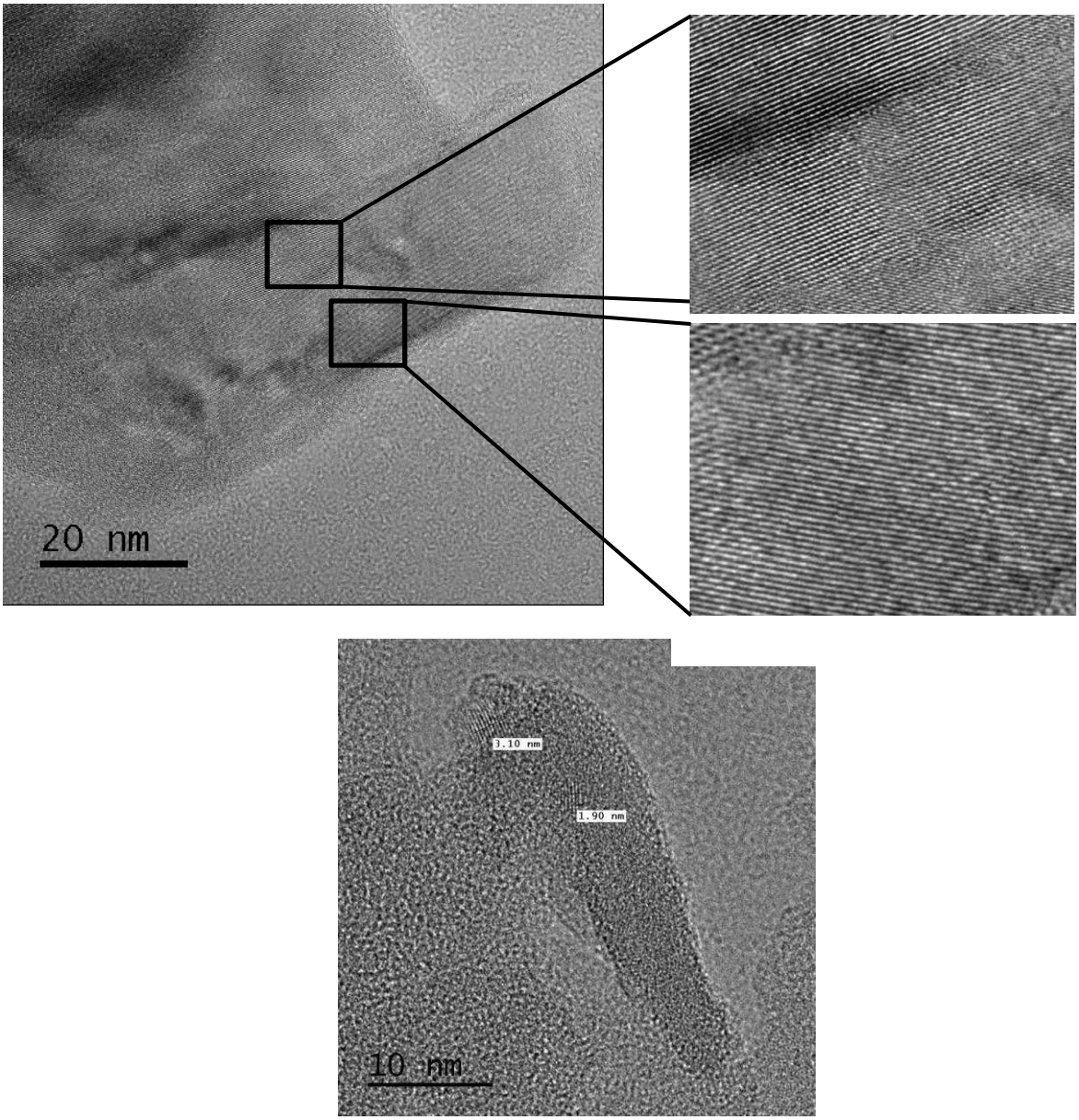

Figure 3.3. TEM images of A-H/M-5.5h aerobically milled MGS. Top Image: notice the different orientation of atoms in the same particle. Between these two regions is an area that is random and amorphous. These are multiple crystalline regions created/combined by the milling process with amorphous regions in-between the crystalline regions. Bottom Image: The sample is mostly amorphous with very small but identifiable Si crystallites imbedded in a continuous amorphous particle. Two crystallites were measured indicated by black lines, the top having a length of 3.10 nm and the bottom a length of 1.90 nm in the long dimension perpendicular to the image.

Table 3.2. Summary of Milling Experimental Details.

sample name	milled aerobic/ anaerobic	seal-fluid	mill-fluid	additives (wt/wt% of MGS)	mill time (h)	BET surface area (m^2g^{-1})	Si–C (at. % of Si by XPS)[a]	Si–O_x $x < 2$ (at. % of Si by XPS)[a]	SiO_2 (at. % of Si by XPS)[a]
hand ground 20-45 μm	—	—	—	—	—	0.7	0	9	35
A-M/P-5h	aerobic	mesitylene	mesitylene	pyrene 9.0	5	130	34	24	10
A-M/P-6h	aerobic	mesitylene	mesitylene	pyrene 9.0	6	140	—	—	—
AA-M/P-1h	anaerobic	mesitylene	mesitylene	pyrene 9.0	1	75	—	—	—
AA-M/P-2h	anaerobic	mesitylene	mesitylene	pyrene 9.0	2	162	—	—	—
AA-M/P-5h	anaerobic	mesitylene	mestiylene	pyrene 9.0	5	258	33	11	0
AA-M/P-6h	anaerobic	mesitylene	mesitylene	pyrene 9.0	6	206	—	—	—
A-H/M-5.5h	aerobic	mesitylene	heptane	—	5.5	243	13	27	14
AA-H/M-5.5h	anaerobic	mesitylene	heptane	—	5.5	295	38	9	0
AA-H-5.5h	anaerobic	heptane	heptane	—	5.5	70	23	5	0
A-H-5h	aerobic	heptane	heptane	—	5	169	19	20	33
AA-H-1h	anaerobic	heptane	heptane	—	1	44	12	7	0
AA-H-2h	anaerobic	heptane	heptane	—	2	45	—	—	—
AA-H-3h	anaerobic	heptane	heptane	—	3	33	17	6	0
AA-H-4h	anaerobic	heptane	heptane	—	4	36	—	—	—
AA-H-5h	anaerobic	heptane	heptane	—	5	40	18	6	0

[a] These are the percent of the observed silicon peak for these binding environments. The remaining fraction was Si^0.

3.2.2. Anaerobic Powder XRD

Due to the reactivity of some of the milled materials it was necessary to find a method to perform powder XRD analysis in an anaerobic or nearly anaerobic environment. The transfer of the samples and purging of the instrument X-ray protection enclosure would have been painstaking and still not afforded a sufficiently anaerobic environment for these materials. A different method was tested with known samples to determine its effect on the resulting data (See results in Figure 3.4). Rather than try to protect the dry sample throughout the transfer and during the powder XRD experiment it was decided that mixing the material in a high purity grease (Apiezon Type N) would keep the sample anaerobic during the powder XRD experiment. Apiezon grease is highly purified aliphatic only based grease. Since the samples were milled in heptane it was suspected that the Apiezon Type N grease would not react with the milled silicon samples. A control experiment was also performed where XRD patterns were obtained on a sample immediately after preparation and again on the same sample 52 days later to confirm that the grease was protecting the sample and no significant change in the observed powder XRD pattern had occurred (Figure 3.5). As expected, the powder XRD of samples mixed with Apiezon grease attenuated the peak height and slightly broadened the peak widths compared to samples dispersed on top of high-vacuum silicon grease. However, for the purposes of this study determination of crystallinity was still possible with the observed measurements (Figure 3.4, 3.5). Diffraction patterns for 1 h milled samples (AA-H-1h and AA-M/P-1h) showed decreased but measurable diffractions peaks, however, all samples milled for longer than 1 h showed very weak diffraction peaks.

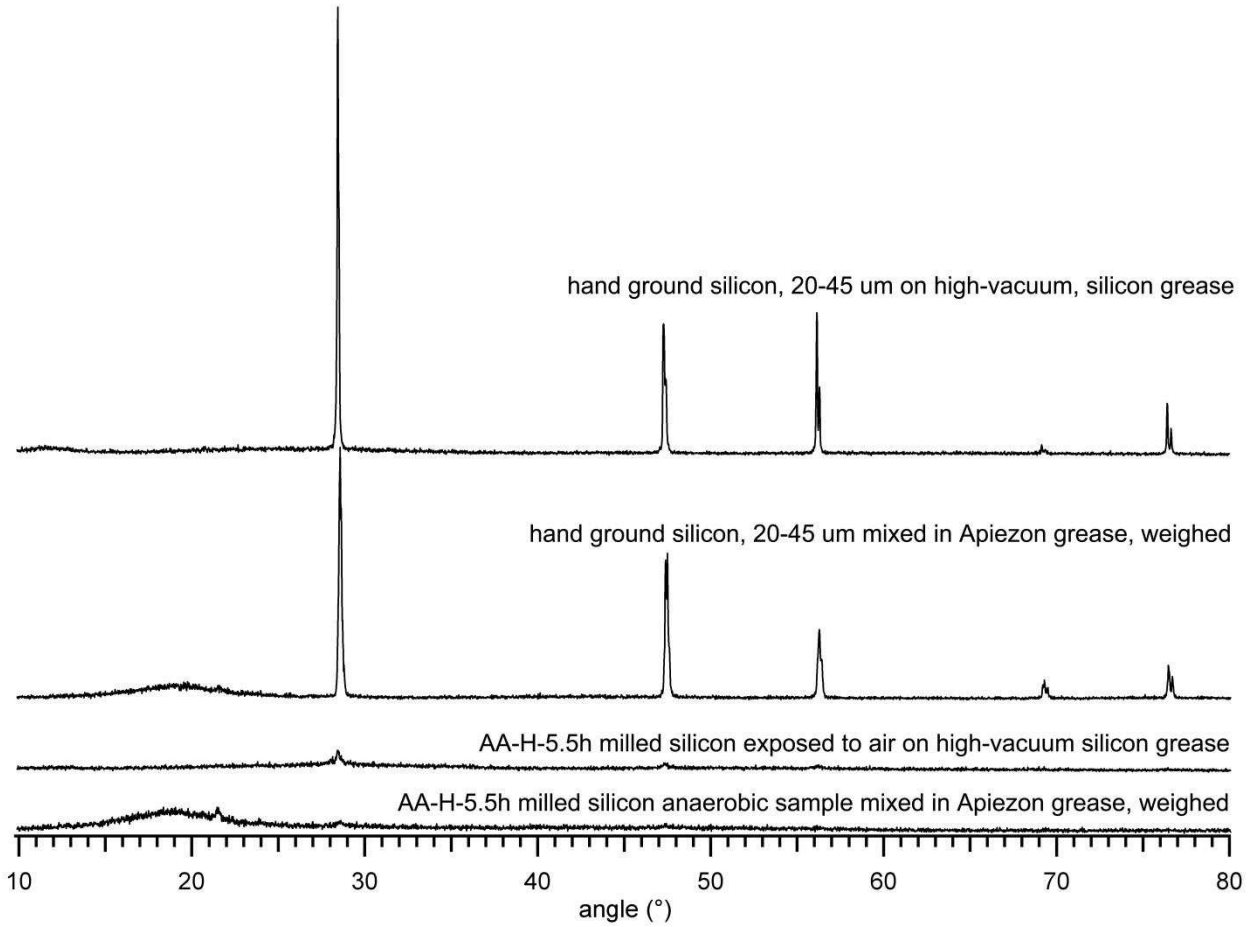

Figure 3.4. Comparison of two silicon powder samples analyzed by powder XRD to determine the effect of preparing the sample as a paste intimately mixed with Apiezon Type N grease. Hand ground metallurgical silicon ranging in size from 20–45 μm, and AA-H-5.5h dispersed onto a thin film of high-vacuum grease spread on a glass microscope slide compared to the same materials mixed with Apiezon Type N grease forming a homogenous paste and spread onto a glass microscope slide. The samples in Apiezon grease were weighed as well as the quantity of Apiezon grease, (the hand ground sample was mixed with Apiezon grease but not treated anaerobically). Notice the decrease in peak heights and broadening of peak widths for both the hand ground and AA-H-5.5h when mixed with Apiezon grease. While some signal attenuation was observed, this was acceptable to determine relative crystallinity of these samples while keeping the sample anaerobic during the XRD experiment.

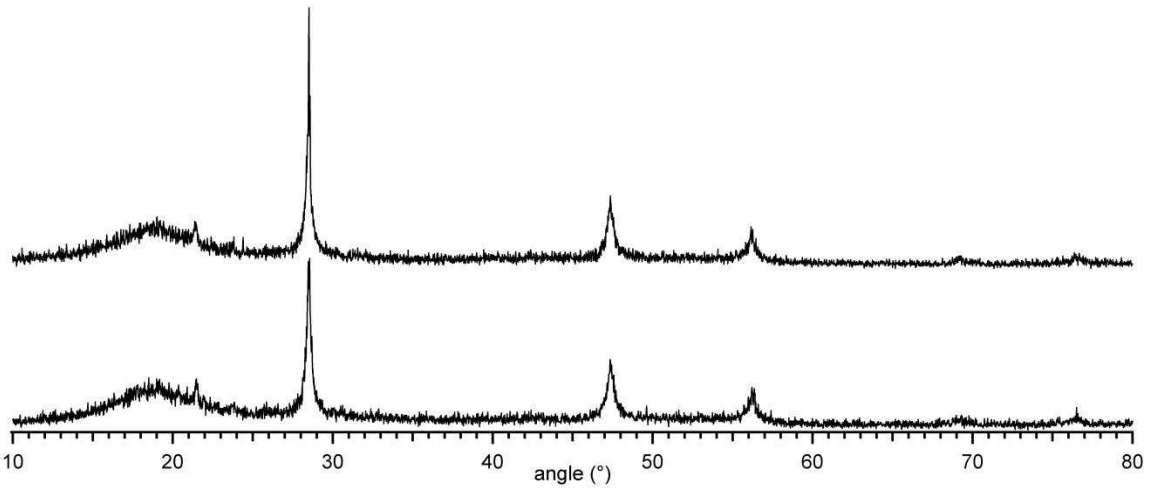

Figure 3.5. Powder XRD pattern of AA-H-1h in Apiezon Type N grease, the bottom pattern is from a sample prepared immediately after milling and drying the sample, the top pattern is the exact same powder XRD sample after 52 days; the sample was left intact, on the slide, in ambient air during those 52 days.

3.2.3. Anaerobic Milling in Heptane

The three milling experiments performed in dry, air-free heptane in an inert atmosphere glovebox produced dark gray to black solids that were reactive with oxygen. In addition to the three anaerobic milling experiments in dry, air-free heptane, two additional anaerobic experiments were performed to probe how much batch to batch contamination was transferred after normal cleaning; the first with dry, air-free heptane as the milling fluid and mesitylene as the seal fluid to determine "impurity" leeching from the seal fluid (AA-H/M-5.5h) and a second experiment with dry, air-free heptane as the seal fluid and mill fluid (AA-H-5.5h) to determine cross contamination between batches with small quantities of impurities. The AA-H-5.5h experiment was also meant to remove contaminants from the slurry lines and sonicator flow cell, and is included as further data.

The five samples free of deliberate and adventitious slurry stabilizing species had similar BET surface areas (Table 3.2, Figure 3.6) indicating mechano-chemical equilibrium was reached quickly. The surface area changed little with time while the crystallite size decreased rapidly; the AA-H-4h sample had almost an identical powder XRD pattern to the AA-H-5h sample, suggesting similar crystallite sizes Further evidence of decreasing crystallite size is given by

comparing TEM images of AA-H-1h to those of AA-H-5h (Figures 3.7 and 3.8). The TEM images demonstrate that the bulk of the particles were amorphous with the agglomerated particles having a size range on the order of 10-200 nm in size. The remaining crystallites embedded in the amorphous agglomerated particles identified by darkfield TEM (Figures 3.3, 3.7 and 3.8) range in size from 2-50 nm comparable to crystallites sizes observed in Si ball milling research.[52]

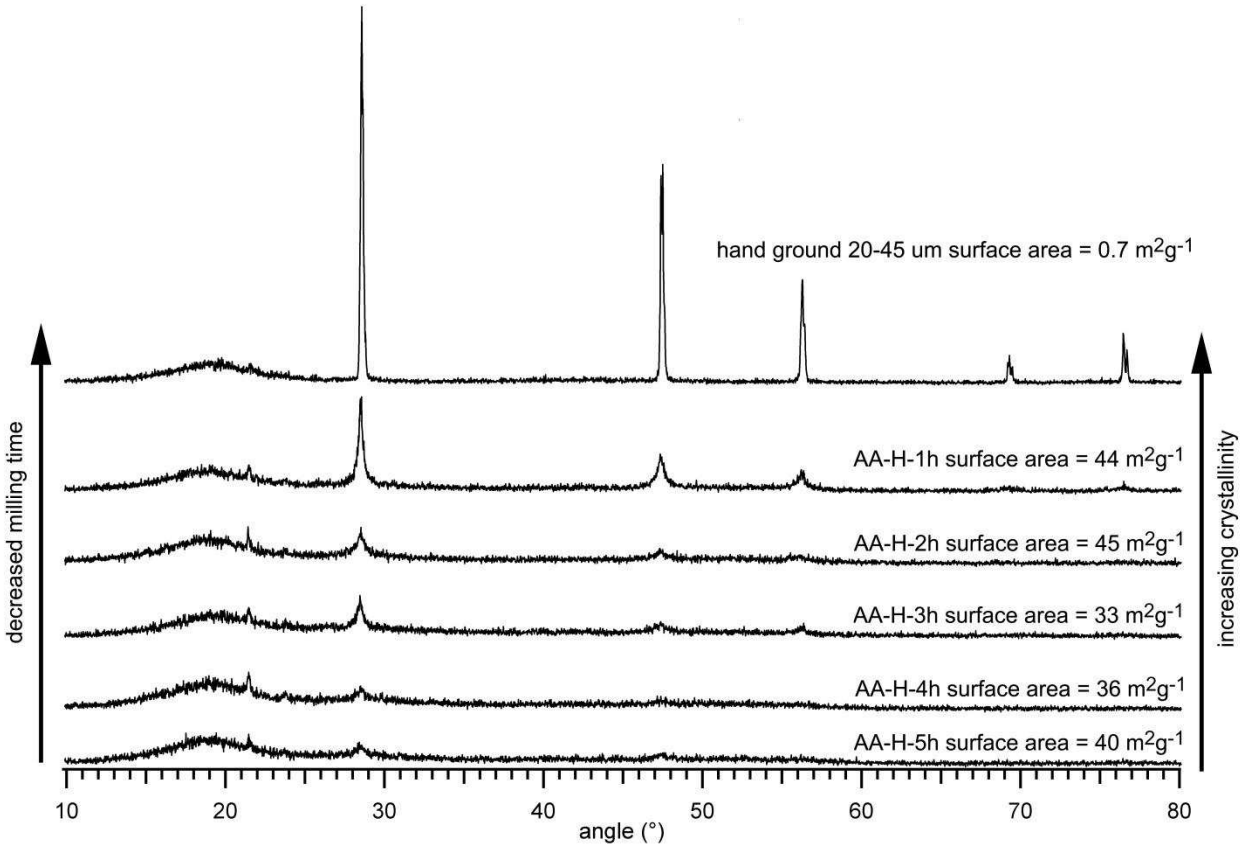

Figure 3.6. Anaerobic powder XRD of AA-H- 1–5 h compared to hand ground silicon powder ranging in particle size from 20–45 μm. The 1–5 h milled samples were milled anaerobically and treated rigorously anaerobic. The hand ground sample of metallurgical silicon was prepared by mixing in Apeizon Type N grease, same as the other 5 samples, but was not treated anaerobically. Note the similar surface areas for all 5 samples. Also note the decrease in crystallinity with increased milling time.

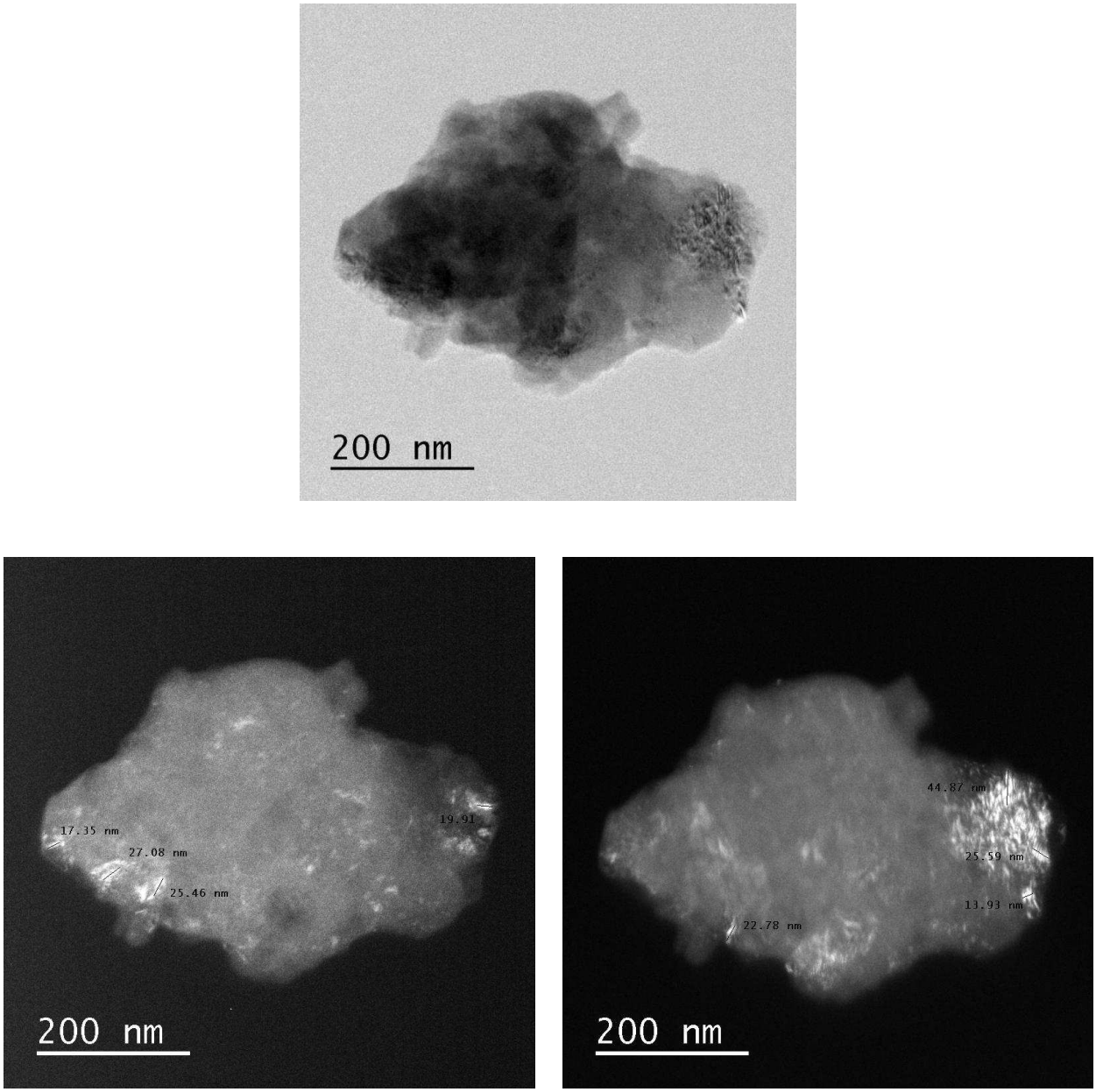

Figure 3.7. TEM images of AA-H-1h. Top: original agglomerate particle image. Bottom: Darkfield view of the same particle with the beam in 0° and 90° orientations highlighting the crystalline regions of the particle. The scale bar for the darkfield images is the same as for the normal view image. Note the crystalline regions are on the order of 10–50 nm in length.

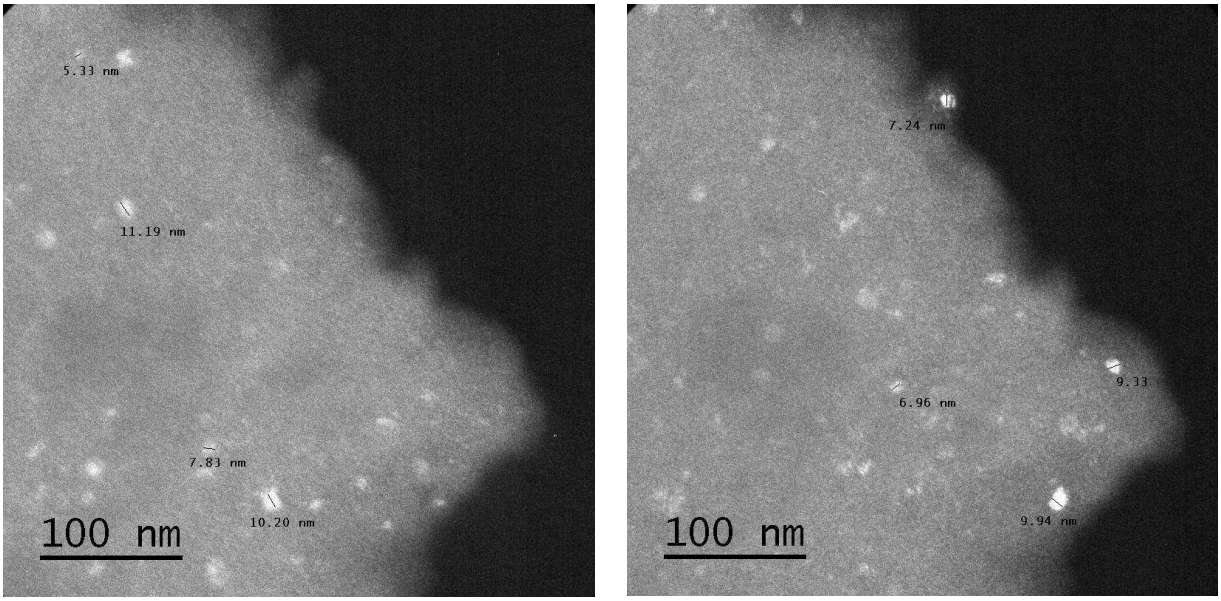

Figure 3.8. TEM images of AA-H-5h. Darkfield view images of the same particle with the beam in 0° and 90° orientations highlighting the crystalline regions of the particle. Note the crystalline regions (Some that only show up in the 0° orientation and some that only show up in the 90° orientation are on the order of 5–12 nm in length.)

The surface composition of the samples AA-H/M-5.5h, AA-H-5.5h, AA-H-1h, AA-H-3h, and AA-H-5h was examined using XPS. See Figure 3.9 for AA-H-1h, AA-H-3h, and AA-H-5h. All samples contained silicon, carbon, and oxygen and all samples except AA-H/M-5.5h and AA-H-1h had a small (≤ 5 atomic %) amount of fluorine present (Table 3.3). The silicon spectra contained 3 peaks: ca. 99.5 eV associated with Si^0,[42,46-48] ca. 100.5 eV assigned to Si–C,[41,44,50] and ca. 101.5 associated with Si_xO_y.[40,42] Sample AA-H/M-5.5h exhibits significantly different silicon binding than the other samples, of the silicon 38% is Si–C, 9% is Si–O, and 53% is Si^0. For all other samples milled anaerobically in heptane the silicon is in the same three bonding environments, but the amount of each is: Si–C 12–24%, Si–O 5–7%, and Si^0 72–81%. At one hour there is 12% Si–C and 7% Si–O and after that first hour there is a slight increase in the amount of Si–C to 17% and almost no change in the Si–O (6%) and these values are nearly the same after 5 hours (Table 3.2)

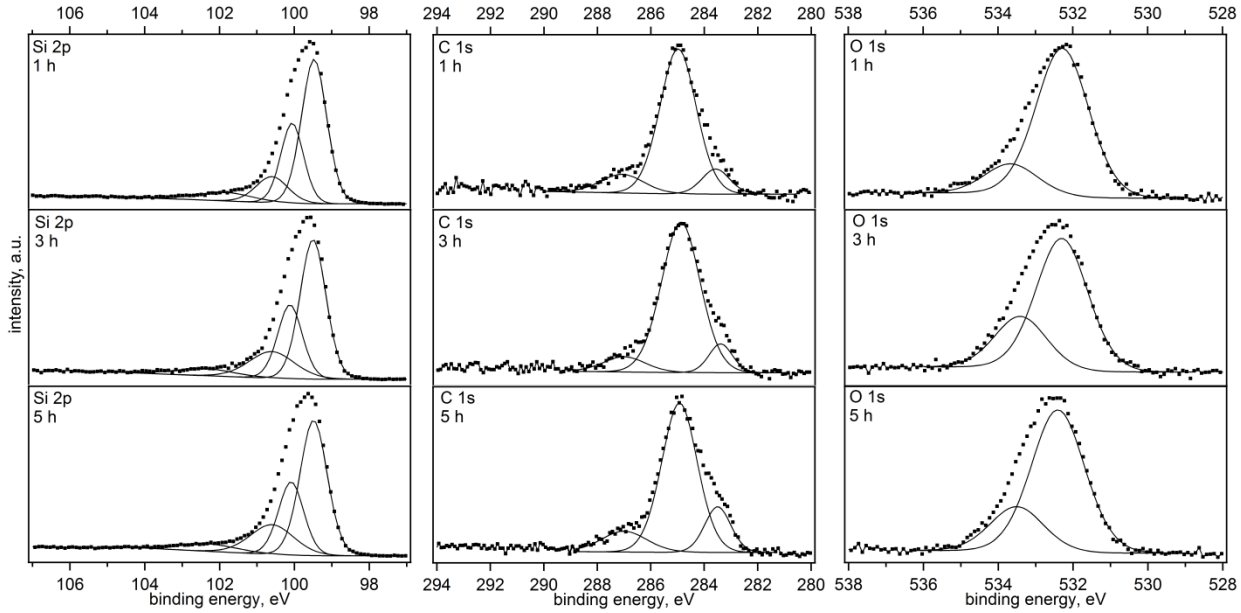

Figure 3.9. XPS of AA-H-1h (top), AA-H-3h (middle), and AA-H-5h (bottom). Few changes are observed in the XPS spectra of samples milled anaerobically in heptane for varying amounts of time. This indicates that there is little change in the surface composition after the first hour of milling anaerobically in heptane.

Table 3.3. Amounts of various elements in all samples studied by XPS.

sample	Si atomic %	C atomic %	O atomic %	F atomic %	N atomic %
A-M/P-5h	24	56	20	—	—
AA-M/P-5h	31	62	7	—	—
A-H/M-5.5h	33	35	32	—	—
AA-H/M-5.5h	38	55	6	1	—
AA-H-5.5h	53	38	8	2	—
AA-H-1h	67	22	11	—	—
AA-H-1h sputtered	70	16	8	3	3
AA-H-3h	62	23	11	3	—
AA-H-3h sputtered	66	18	10	5	1
AA-H-5h	59	26	12	4	—
AA-H-5h sputtered	65	19	8	3	4
A-H-5h	36	32	33	—	—

Three carbon binding environments were observed: ca. 283.5 eV for Si–C,[41,44] ca. 285.0 eV for C–C/C–H,[46,48] and ca. 286.5 eV for C–O.[47,48] Samples AA-H-1h, AA-H-3h, and AA-H-5h

were sputtered to remove surface hydrocarbon contamination (Figure 3.10). The amount of carbon did decrease for all samples, but all three binding environments remained. A small (≤ 4 atomic %) nitrogen peak was present after sputtering. Despite the fact that these samples were milled anaerobically, oxygen was present at 3–12% of the total and had two binding environments: C–O at ca. 532 eV[42] and Si–O at ca. 533.8 eV.

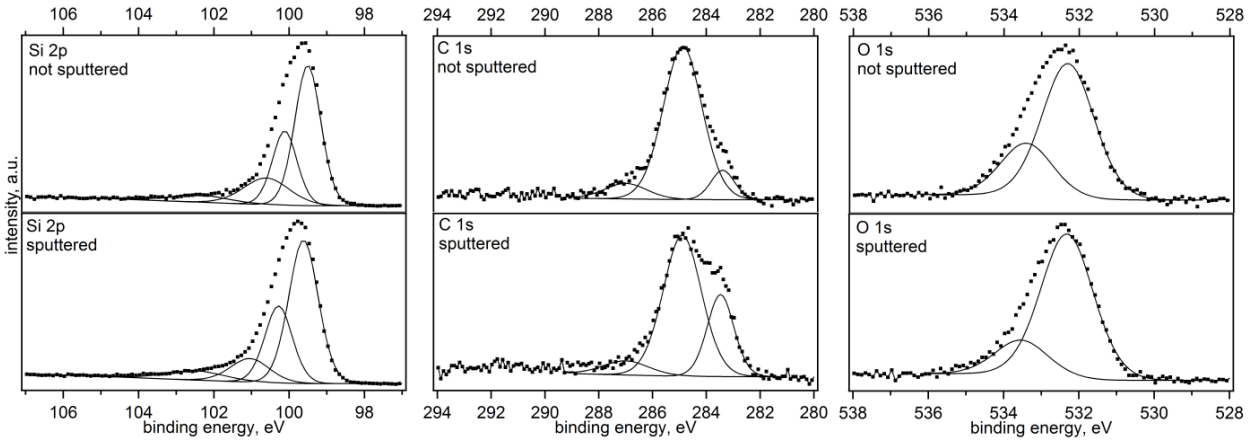

Figure 3.10. XPS of AA-H-3h as made (top) and sputtered (bottom). The Si–C peak is more pronounced in the C 1s spectrum after sputtering removed surface hydrocarbon contamination. Little change is observed in the other elements.

Attempts to understand the reactivity of the silicon surface of the anaerobically milled particles led to multiple gas uptake experiments of anaerobically milled Si powder with various gases. During the BET surface area analysis in N_2 (99.999%) samples did not exhibit any irreversible sorption of N_2 gas indicating no silicon nitride was rapidly being formed. Post treatment experiments of AA-H/M-5.5h (specific surface area = 295 m^2g^{-1}) with oxygen exhibited 5.1% by mass irreversible absorption in 5,128 min. Most of that mass was taken up quickly (Figure 3.11). Similar experiments by Butyagin et al.[28] with anaerobically milled silicon showed a 1.1% mass increase by mass until equilibrium pressure was reached (time not reported). While the oxygen uptake by AA-H/M-5.5h is ca. 4.6 times greater than in the Butyagin experiment, it should be noted that the AA-H/M-5.5h sample has ca. 110 times greater surface area than samples described by Butyagin. A second oxygen post treatment experiment

with AA-H-5.5h exposed to air showed a 2.6% mass increase in ca. 5,760 min (AA-H-5.5h specific surface area = 70 m^2g^{-1}). Interestingly the anaerobic AA-H-5.5h sample absorbed ca. 68% of the total oxygen mass in the first 10 min, and during this time the sample and containing vial warmed to the touch. A final experiment demonstrating the reactivity of these anaerobically milled samples with oxygen was simply pouring ca. 50 mg sample of anaerobic AA-H-5.5h from a vial (sample prepared in an argon atmosphere and filled with argon) through air causing orange sparks and an ensuing fireball. The resulting powder was a brown color instead of the original grey black color.

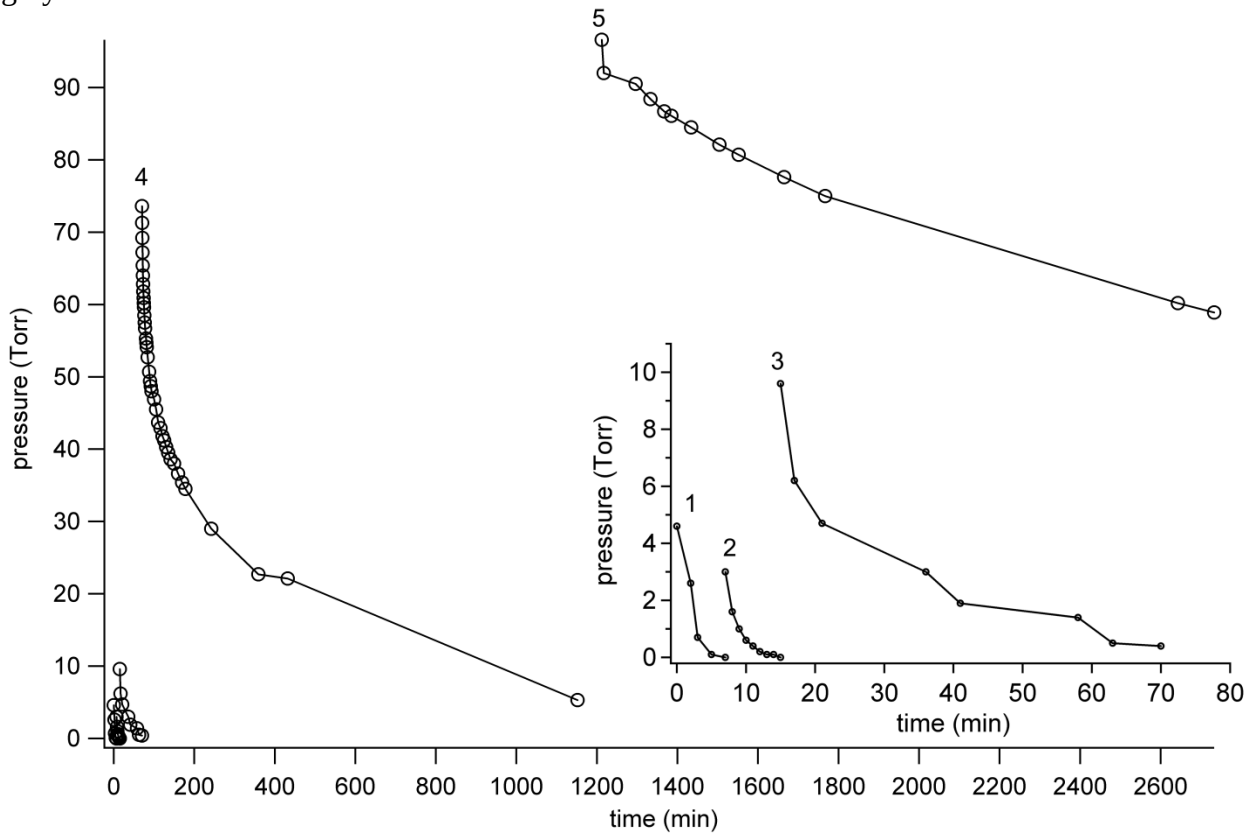

Figure 3.11. Post treatment of AA-H/M-5.5h with O_2. Rate of O_2 uptake of 5 doses of O_2 on a single sample (0.237 g) of AA-H/M-5.5h, order of doses indicated 1-5. The rate of uptake for each dose was graphed following one another. The expanded inset shows the first 3 doses and the rate of uptake over time for clarity.

To determine if water vapor in air was reacting at all with the anaerobically milled MGS, a fresh sample of anaerobic AA-H/M-5.5h was treated with ca. 4 Torr of water vapor (low vapor pressure of H_2O to inhibit condensing H_2O on the glass) and in ca. 6 h the pressure dropped 3.5

Torr. The sample itself did not actually take up mass, it is believed the observed pressure drop was due to exposing the rigorously dry glassware to the water vapor. A final experiment to determine if a sample treated with O_2 would then take up H_2O was also performed; again the total pressure of H_2O taken up was 8.85 Torr, but the mass of the sample only increased by 0.2%. Therefore it is likely that any mass uptake upon exposure to air is mostly due to oxygen.

3.2.4. Anaerobic Milling in Mesitylene with Pyrene Additive

Two anaerobic batches were milled in dry, air-free mesitylene with 9.0 wt/wt% pyrene additive (relative to Si mass) as an aromatic stabilizer to determine the effects aromatic compounds have on milling silicon. The two milling experiments performed in dry, air-free mesitylene in an inert atmosphere glovebox produced dark gray to black solids that were reactive with oxygen, but not to the extent that the heptane milled samples were reactive with oxygen. If rapidly exposed to air, the mesitylene/pyrene milled samples would warm and, in some instances, visible smoke was observed, the sample did change in color from grey/black to brown, no sparks or flame were observed. The two anaerobic batches (AA-M/P-1h, AA-M/P-2h, AA-M/P-5h, AA-M/P-6h) produced 4 samples exhibiting surface area growth with increased milling time; a trend commonly observed in attritor milling experiments. The 1, 2, and 5 hour milled samples had increasing BET surface areas while the 6 hour milled sample had a BET surface area lower than the 5 hour sample (Figure 3.12) indicating that particle agglomeration was becoming the dominant interaction stopping overall particle fracture. Also from Figure 3.12, as expected, the MGS continued to lose crystallinity from 1 to 6 h of milling time. Surface composition analysis of the AA-M/P-5h sample by XPS revealed a small amount of Si–O bonding (11% of the total Si), and significant Si–C bonding (33% of the total Si), no other species were observed.

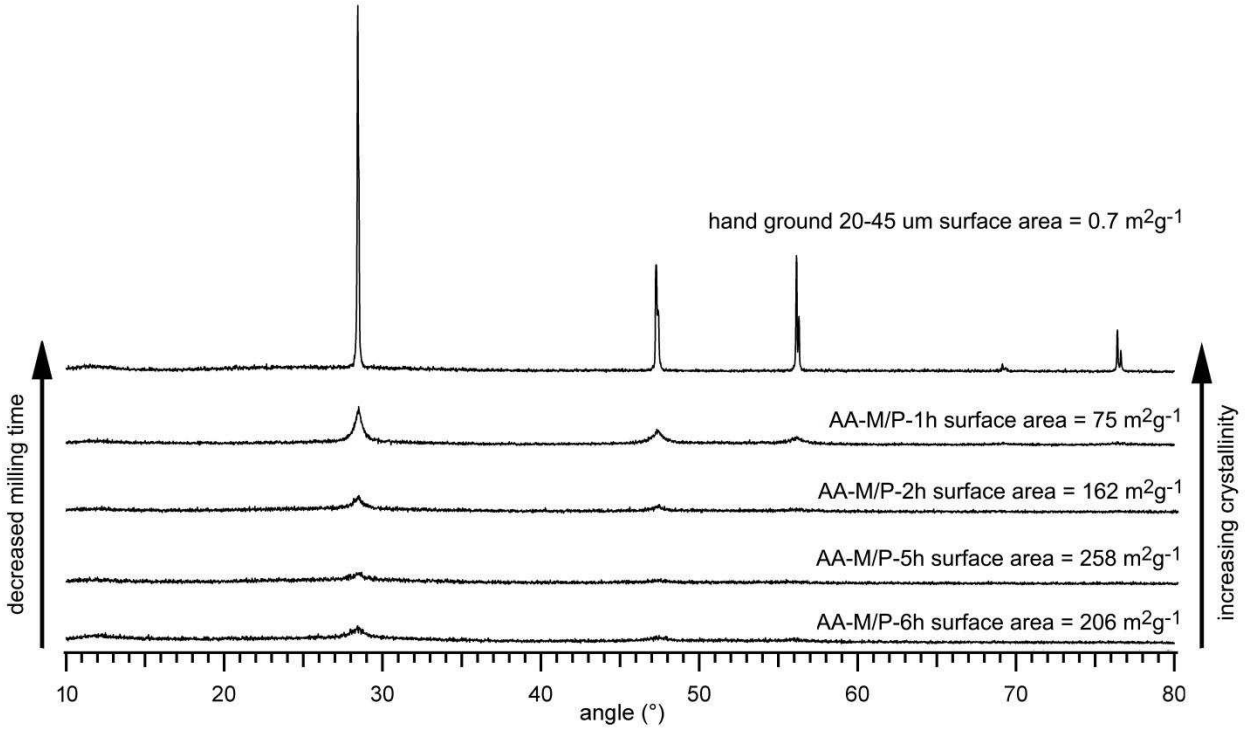

Figure 3.12. Anaerobic powder XRD of MGS milled in dry, air-free mesitylene with pyrene additive for 1, 2, 5, and 6 h compared to hand ground silicon powder ranging in particle size from 20–45 μm. Note these XRD samples were prepared by dispersion on high-vacuum silicon grease on a glass slide under aerobic conditions. The samples did discolor upon exposure to air, but no change was observed in the XRD pattern.

Post treatment of AA-M/P-5h with O_2 was performed, it displayed rapid initial uptake of O_2, but quickly stopped taking up O_2 (Figure 3.13). The O_2 was added in small quantifiable doses so an overall rate of O_2 uptake is not known, but the final amount of O_2 taken up equated to 0.9% by mass. This is ca. 18% of the O_2 taken up by AA-H/M-5.5h indicating the mesitylene/pyrene sample was more passivated towards O_2 reactions than anaerobic material milled only in heptane. No water uptake experiments were performed on mesitylene/pyrene milled samples.

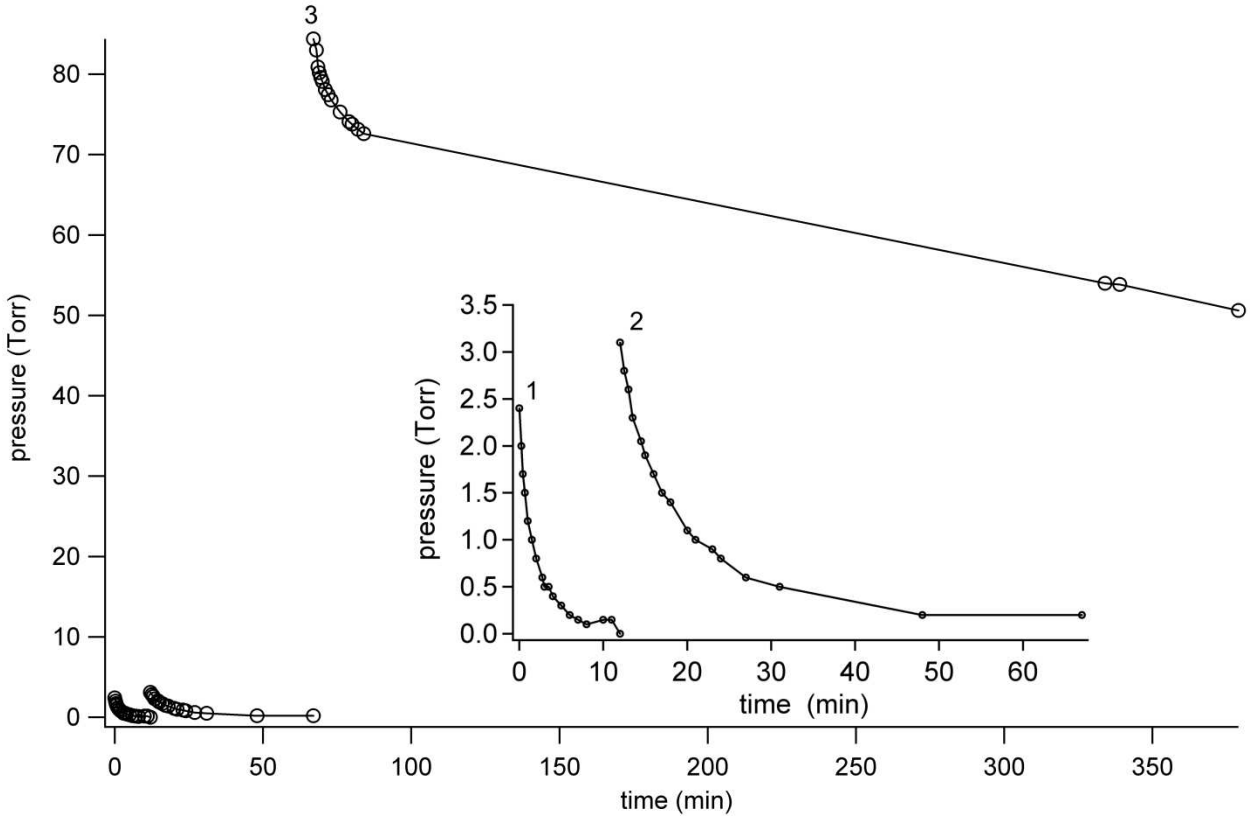

Figure 3.13. Post treatment of AA-M/P-5h with O_2. Rate of O_2 uptake of 3 doses of O_2 on a single sample (0.235 g) of AA-M/P-5h, order of doses indicated 1-3. The rate of uptake for each dose was graphed following one another. The expanded inset shows the first 2 doses and the rate of uptake over time for clarity.

The surface composition of AA-M/P-5h was studied with XPS (Figure 3.14). Silicon, carbon, and oxygen were all present in this sample with the same binding environments which were observed for the samples milled anaerobically in heptane. Of the silicon present 33% was Si–C, 11% was Si–O, and 56% was Si^0. Compared to the samples milled anaerobically in heptane AA-M/P-5h contained a much higher amount of carbon, 62% of the total elemental composition (Table 3.3).

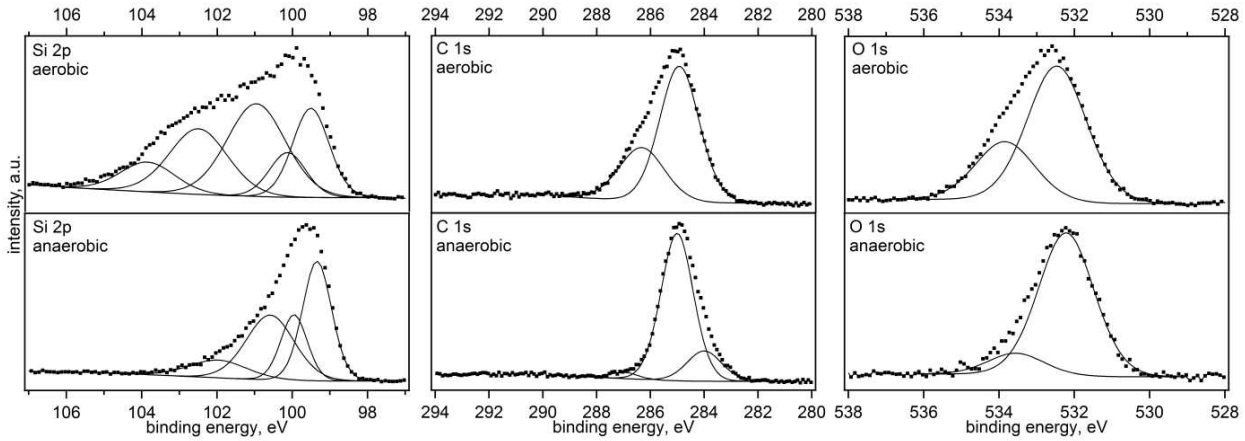

Figure 3.14. XPS of A-M/P-5h (top) and AA-M/P-5h (bottom). The aerobic sample contains SiO_2 (ca. 103.5 eV) that is not present in the anaerobic sample. The aerobic sample also had more silicon suboxide species (ca. 102 eV in Si 2p and ca. 533.5 eV in O 1s) than the anaerobic sample. For A-M/P-5h the Si–C peak in the C 1s spectrum is likely contained within the broader C–C/C–H peak.

Pyrene was chosen as an additive because it could physiochemically adsorb to the nascent Si surface, and during the continued milling in aromatic mesitylene solvent, act as a surface stabilizing additive allowing further particle break down. Previous studies have shown that aromatic compounds, typically benzene, interact with certain faces of Si when rigorously cleaned, and can form strong chemisorption interactions.[53] The pyrene was thought to react with or adsorb to the Si surface thereby protecting the Si surface and allowing further comminution. In a post-milling treatment, the pyrene could be exchanged later with a more desirable surface coating. Additionally, the adsorbed/reacted pyrene on the Si surface could be pyrolyzed thereby protecting the surface from atmospheric oxidation making the particles air-stable, however, this concept was not further investigated in this effort.

3.2.5. Aerobic Milling in Heptane

The aerobic milling in as received heptane yielded a brown powder that was not noticeably reactive with air. Both samples milled aerobically in heptane, A-H/M-5.5h and A-H-5h, were studied using XPS. Sample A-H/M-5.5h contained 33% silicon, 35% carbon, and 32% oxygen (Table 3.3). Sample A-H-5h contained 36% silicon, 32% carbon, and 33% oxygen (Table 3.3). The silicon spectra contained peaks for Si^0 at ca. 99.5 eV, Si–C at ca. 100.5 eV, Si_xO_y at ca. 102

eV, and a peak at ca. 103.5 eV for SiO_2.[40,42,44] The amounts of silicon for each type of bond in A-H/M-5.5h are: 46% Si^0, 13% Si–C, and 41% Si–O (Table 3.2). The amounts of silicon for each type of bond in A-H-5h are: 28% Si^0, 19% Si–C, and 53% Si–O (Table 3.2). In the carbon spectra, the same peaks are observed that were present in the anaerobically heptane milled samples. Sample A-H/M-5.5h contained the same two oxygen peaks (ca. 532 and 533.8 eV) that were seen in samples milled anaerobically. Sample A-H-5h contained three oxygen peaks at 531.5 eV, 533 eV, and 534.2 eV (Figure 3.15).

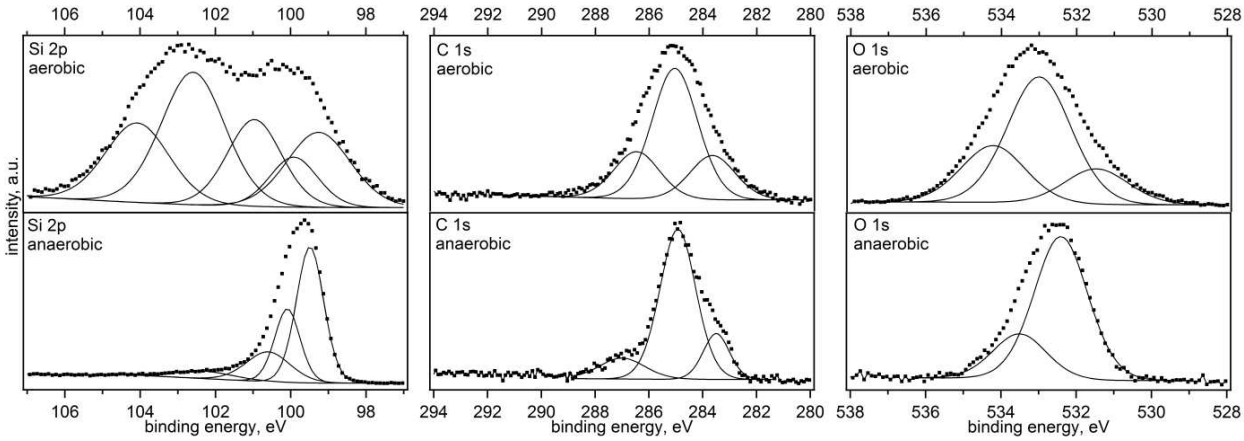

Figure 3.15. XPS of A-H-5h (top) and AA-H-5h (bottom). The aerobic sample contains SiO_2 (ca. 103.5 eV) which is not present in the anaerobic sample. The amounts of silicon suboxide species (ca. 102 eV) are also higher in the aerobic than the anaerobic. The Si-C shoulder (ca. 283.5 eV) is more evident in the anaerobic sample.

3.2.6. Aerobic Milling in Mesitylene with Pyrene Additive

The aerobic milling in as received mesitylene yielded a brown powder that was not noticeably reactive with air. Sample A-M/P-5h was studied by XPS (Figure 3.14). The silicon spectrum contained the same peaks as were seen in the aerobic heptane milled samples. The amounts of silicon were: Si^0 31%, Si–C 34%, Si–O 35%. The carbon spectrum contained two peaks at 285 eV and 286.4 eV, the Si–C peak is likely contained within the C–C/C–H peak at 285 eV. The oxygen spectrum contains two peaks at 532.5 eV and 533.8 eV.

3.2.7. DLS Particle Size Analysis of Samples

Comparable 1 h and 5 h milled MGS samples were tested for particle size range by DLS to ascertain the mean particle size and the total range of particle sizes. Shown in Figure 3.16 are the data compared for 5 samples compared, AA-H-1h, AA-H-5h, AA-M/P-1h, AA-M/P-5h, and A-H-5h (the distribution in Figure 3.16 is the average of 3 measurements for each sample). Notice from Figure 3.17 that all 5 samples, independent of additives and milling time, exhibit similar mean particle size and particle size distribution. For all samples measured by DLS the data obtained was considered "quality" by the Malvern software. Based on the DLS analysis in absolute EtOH, all of the samples measured had a minimum particle size starting around 70 ± 5 nm and depending on the additives a maximum particle size ranging up to 600 ± 175 nm.

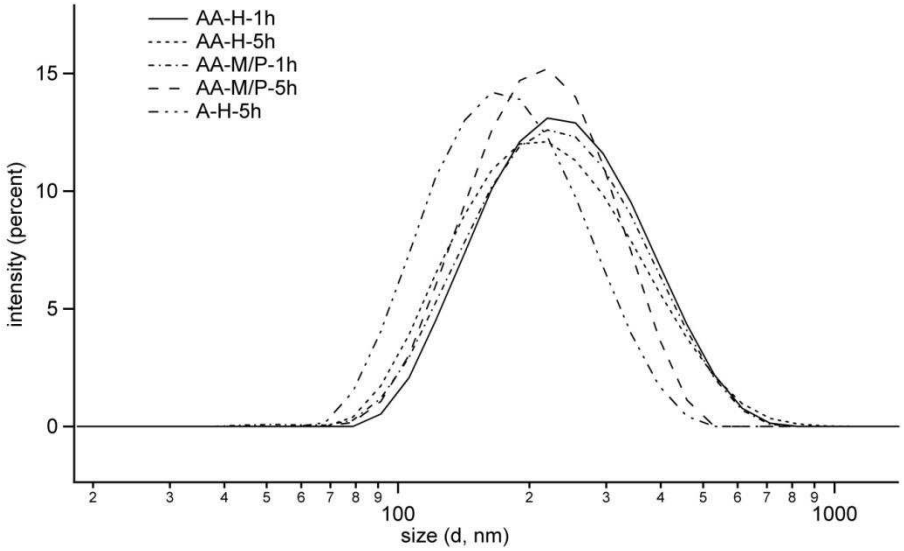

Figure 3.16. DLS analysis of 5 samples: AA-H-1h, AA-H-5h, AA-M/P-1h, AA-M/P-5h, and A-H-5h. Displayed graphs are the average of 3 measurements where each measurement consists of 12-15 runs each. Samples were hand ground to break up clumps, and then dispersed in absolute ethanol with a bath sonicator for 10-15 min per sample. The DLS measurement was performed at 25 °C after 2 min equilibration at 25 °C for each sample. All samples appeared to have similar particle size and particle size distributions.

3.3. Discussion

3.3.1. General

During the milling experiments there was purposefully a low volume percentage of sample compared to milling media to: 1) decrease time required to reach mechano-chemical equilibrium

in experiments where that was the desired target, 2) minimize particle-particle interaction/agglomeration, and 3) minimize changes in milling efficiency when multiple samples were removed. Milling efficiency is dependent on the ratio of milling media to sample. The milling media in the mill chamber on a percent volume basis started at ca. 94% for all experiments, and when samples, roughly half the mass of the original starting material were removed, the percent volume of milling media went up to 97%, a change of only 3%.

3.3.2. Anaerobic vs. Aerobic Without Surface Passivating Additives (AA-H-1h, AA-H-2h AA-H-3h AA-H-4h AA-H-5h, AA-H-5.5h compared to A-H-5h)

The apparent effect oxygen (or air) had on stabilizing the slurry against agglomeration was quite dramatic. The anaerobically milled MGS in dry, air-free heptane reached mechano-chemical equilibrium rapidly with little measurable change in surface area between the 1 h milling time and 5 h milling time for the five anaerobically milled samples (Figure 3.6). As expected, the increased milling time only led to further amorphization of the MGS (Figure 3.6) without significant changes to particle size as confirmed by BET surface area measurements. The A-H-5h sample had a similar amount of crystallinity compared to AA-H-5h as determined by powder XRD, but had a BET surface area over four times greater than the AA-H-5h sample. This would suggest that in aerobic conditions even though the MGS is being ground in a slurry of heptane, enough available oxygen is present to react with the silicon surface forming Si–O bonds and changing the surface composition of the particles. Additionally, the partially oxidized surface was mitigating inter-particle interaction and agglomeration allowing further particle fracture. The amount of oxide present on the MGS after milling was compared using XPS; when milled aerobically 35–53% of the total Si present was in the form of an oxide while after anaerobic milling 5–7% of the total Si present was bound to oxygen, whereas, anaerobic experiments were apparently forming more Si–C bonds observed at ca. 283.5 eV (Figures 3.9 and 3.15). One can reasonably assume that reaction of Si with heptane molecules in the heptane only milled samples is especially difficult, as it requires activation/cleavage of a strong C–H or C–C bond at near room temperature, a reaction that is likely to be thermodynamically

unfavorable under these conditions unless the freshly exposed Si surface is catalyzing such reaction. The XPS results confirm a low degree of Si–C bond formation in the anaerobically milled samples, indicating that the freshly exposed Si is likely not catalytically activating C–H or C–C bond cleavage based on the moderate percent of Si–C bonding present. However, under the conditions created during the milling process, it is likely more energetically favorable to cold-weld smaller particles together forming larger agglomerates minimizing the overall surface potential compared to the surface potential of an equal mass of smaller Si particles, explaining the time independent specific surface area for all anaerobic, heptane only milled samples. The cold-welding of smaller particles is likely the thermodynamically more stable way to minimize the surface potential but with such a high concentration of heptane the formation of Si–C bonds from reaction with heptane is likely a kinetic product. The ability of the nascent Si surface to activate C–H or C–C bonds at or near room temperature as evidenced by XPS is interesting and could be further utilized to protect the Si surface from rapid reaction with air.

Further evidence of the different surface chemistry for the anaerobically milled samples compared to the aerobically milled samples is shown by the differences in forming a suspension. After drying the AA-H-5h and A-H-5h samples, attempts to suspend the particles in dry, air-free heptane with a probe sonicator yielded different results; the AA-H-5h sample formed a suspension that did not settle out in a matter of tens of minutes compared with aerobic milled A-H-5h that settled out almost immediately. The AA-H-5h sample was shown by XPS to have very little oxygen (Si–O = 6% of the total Si), some Si–C bonding (18% of the total Si), indicating the addition of carbonaceous species to the surface of the MGS particles. The carbonaceous species groups were likely beneficial for suspending the particles in heptane. On the other hand, the A-H-5h sample had 53% of all Si in $Si–O_x$ ($x < 2$) or SiO_2 bonding environments on the surface, according to XPS analysis, and only 19% of all Si was in Si–C bonding environments (Figure 3.15). Based on this data, it is no surprise that the much more hydrophilic Si–O surface composition of the A-H-5h would not suspend in heptane despite the fact that both samples had similar amounts of Si–C bonding.

To examine how strongly carbonaceous groups are bound to the Si-surface, evacuation of the milled samples was carried out. Silicon–carbon bonds are present even after evacuating the milled sample on a high-vacuum line (ca. 10^{-5} Torr) for greater than 12 h which would remove any weakly bound or physisorbed heptane. XPS analysis was performed after the samples were evacuated. Once initial spectra were obtained the samples were sputtered and XPS analysis was repeated. After sputtering, while the total percent of carbon decreases, the Si–C peak is more pronounced suggesting that carbon surface contamination has been removed leaving behind mostly those carbonaceous species that exhibit Si–C bonds. No precedent has been found in the literature for the formation of bonds between silicon and aliphatic carbon compounds by mechanochemical means alone. The Mitchell group milled silicon with a ball mill in octane, 1-octene, and 1-octyne and found evidence of C–H bonds in the FT-IR spectra for 1-octene and 1-octyne milled silicon, but not in octane milled silicon.[36,37,54]

In all of the anaerobically milled samples there is no peak present at ca. 103.5 eV for SiO_2. However, there is typically a peak present at ca.102 eV which is likely due to a silicon suboxide species, i.e., Si_xO_y[40,42] (Figure 3.9). Despite the anaerobic milling conditions, some surface bound oxygen remains and it cannot be determined whether this is from the initial SiO_2 layer on MGS, due to reactions with the small amount ($\leq$ 5 ppm) O_2 in the milling atmosphere, or another unknown source of oxygen. Given that the starting hand-ground MGS material had 44% of the total Si in Si–O bonding environments, it seems likely that a large proportion of the remaining oxide is due to oxygen present in the MGS before milling.

When samples were milled anaerobically without the presence of surface reactive carbon species, most had a small ($\leq$ 5 atomic %) amount of fluorine present. The only fluorine source identified at this time is the Viton® tubing transporting the slurry from the overhead stirrer to the sonicator and back to the mill. One hypothesis is that the nascent silicon surface is so reactive after a short time in the mill that it can react with the normally inert Viton® tubing and start to leach or remove compounds from the tubing. In the C 1s spectra there is no evidence of C–F bonds, but given the low level of fluorine present, these peaks could be below the detection limit.

The high reactivity of nascent silicon surfaces is corroborated by the presence of fluorine and Si–C bonds in samples milled anaerobically in heptane.

Samples that were milled anaerobically (in a N_2 atmosphere) in heptane and then sputtered in the XPS also showed the presence of a small (≤ 4 atomic %) amount of nitrogen. Silicon will very slowly react with nitrogen during milling to form silicon nitrides.[55] The reason that this peak is only apparent after sputtering is not clear, but may be due to the hydrocarbon surface contamination.

3.3.3. Anaerobic Milling Without Surface Passivating Additives vs. Anaerobic Milling With Surface Passivating Additives (AA-H-5h, AA-M/P-5h)

All of the anaerobically milled samples appeared to be reactive with O_2 based on visual inspection when exposed to air and upon post-treatment with O_2 gas. Not surprisingly, the anaerobically milled material with surface passivating additives was less reactive with O_2, likely due to greater passivation of the nanoparticle surface. Direct comparison of XPS data for anaerobic milled samples with and without surface passivating additives shows similar small amounts of Si–O bonding (AA-H-5h Si–O = 6%, AA-M/P-5h Si–O = 11%) but a marked increase in Si–C bonding in the sample with surface passivating additives (AA-H-5h Si–C = 18%, AA-M/P-5h Si–C = 33%). The slowed rate of post-treatment O_2 reactivity and the greater Si–C bonding in the anaerobic milled sample with surface passivating additives indicates that in the absence of oxygen and in the presence of a reactive organic material more Si–C bonding will occur.

3.3.4. Milling Time for Anaerobic Milling Without Surface Passivating Additives vs. Anaerobic With Surface Passivating Additives (AA-H-1h, AA-H-2h AA-H-3h, AA-H-4h, AA-H-5h, AA-H-5.5h compared to AA-M/P-1h, AA-M/P-2h, AA-M/P-5h, AA-M/P-6h)

Milling time did not make much difference in the measured BET surface in the anaerobic experiments without surface passivating additives (AA-H-1h, AA-H-2h, AA-H-3h, AA-H-4h, AA-H-5h, AA-H-5.5h). In the 1-5 h series the crystallinity rapidly decreased forming mostly amorphous particles with small crystallites embedded in solid amorphous particles. In the AA-H-

5.5h sample, the BET surface area was 70 m^2g^{-1} compared to the 1-5 h series average BET surface area of 40 ± 5 m^2g^{-1}, which indicates a difference in these samples. As mentioned previously the AA-H-5.5h was run to remove contaminants from the slurry lines. The AA-H-5.5h experiment occurred after an experiment in which mesitlyene was used as the seal fluid and the relatively high surface area indicates that some aromatic compounds carried over between runs. While the percentages of Si–O and Si–C bonding are nearly the same for these samples based on the Si bonding environments, the overall carbon was 12% greater in the AA-H-5.5h sample. This additional carbon could be further mitigating particle agglomeration and allowing greater particle reduction without the formation of Si–C bonds. By XPS (Figure 3.9) these samples (AA-H-1h, AA-H-2h, AA-H-3h, AA-H-4h, AA-H-5h, AA-H-5.5h) all had less than 10% Si–O bonding (6.5 ± 0.5%) and Si–C bonding near 15% (15.0 ± 3.0%). The anaerobic samples milled for 1, 2, 3, 4, and 5 h in heptane had almost no increase in BET surface area indicating there was little to no stabilization of the slurry and therefore particle fracture quickly reached a maximum and particle agglomeration (likely through cold-welding) became the dominate process.

In contrast, the samples milled anaerobically with surface passivating additives did increase in measured BET surface area with increased milling time, going from 1 h = 75 m^2g^{-1} to 5 h = 258 m^2g^{-1}. The 6 h milled sample had a measured BET surface area of 205 m^2g^{-1}, decreased from the 5 h sample indicating minimum particle size had been reached and agglomeration was occurring due to increased inter-particle interactions. The aromatic surface passivating species were superior at stabilizing the slurry and allowing further particle reduction. The anaerobic samples milled for 1, 2 and 5 h with surface passivating species showed increases in BET surface area with increased milling time indicating further particle fracture was occurring between those times.

3.3.5. Anaerobic Milling With Surface Passivating Additives vs. Aerobic Milling With Surface Passivating Additives (AA-M/P-5, AA-M/P-6 compared to A-M/P-5, A-M/P-6)

Interestingly, samples milled anaerobically with the same surface passivating additives had measured BET surface areas greater than samples milled aerobically (AA-M/P-5h, AA-M/P-6h = 258 and 205 m^2g^{-1} respectively, A-M/P-5h, A-M/P-6h = 130 and 140 m^2g^{-1} respectively). However, the presence of oxygen does not appear to preclude or diminish formation of Si–C bonding; for aerobic milled MGS with surface passivating additives significant Si–O formed with nearly the same amount of Si–C bonding (AA-M/P-5h Si–O = 11%, Si–C = 33%, A-M/P-5h Si–O = 35%, Si–C = 34%) (Figure 3.14). Based on bond enthalpies, a Si–O bond is stronger by 67 kJ/mol compared to Si–C bond indicating the formation of significant Si–C is a kinetic phenomenon, likely arising due to the significantly greater concentration of carbon containing molecules compared to O_2 during milling. Once an MGS particle fractures exposing fresh reactive surface, the more readily available carbon additives and solvent react even though reaction with O_2 would be the energetically favored reaction. This result also indicates that while Si–O bonds are more thermodynamically favorable, they are not as good at mitigating surface potential allowing further particle size reduction compared with aromatic carbon compounds for MGS. This result regarding additives versus oxygen should be taken into account when milling any metal powder aerobically; the presence of oxygen and formation of metal oxide might be controlling the minimum particle size more than the intentional additives augmenting the surface potential.

Under the milling conditions presented here, regardless of oxygen, milling solvent, or surface passivating additives all samples milled for 5 or 5.5 h reached nearly the same level of amorphization (Figure 3.17). The specific surface area of each of these samples spans a range of over 7 times from the lowest specific surface area to the greatest. This wide range of surface area and corresponding particle sizes was produced by variations in additives, solvent, and oxygen presence.

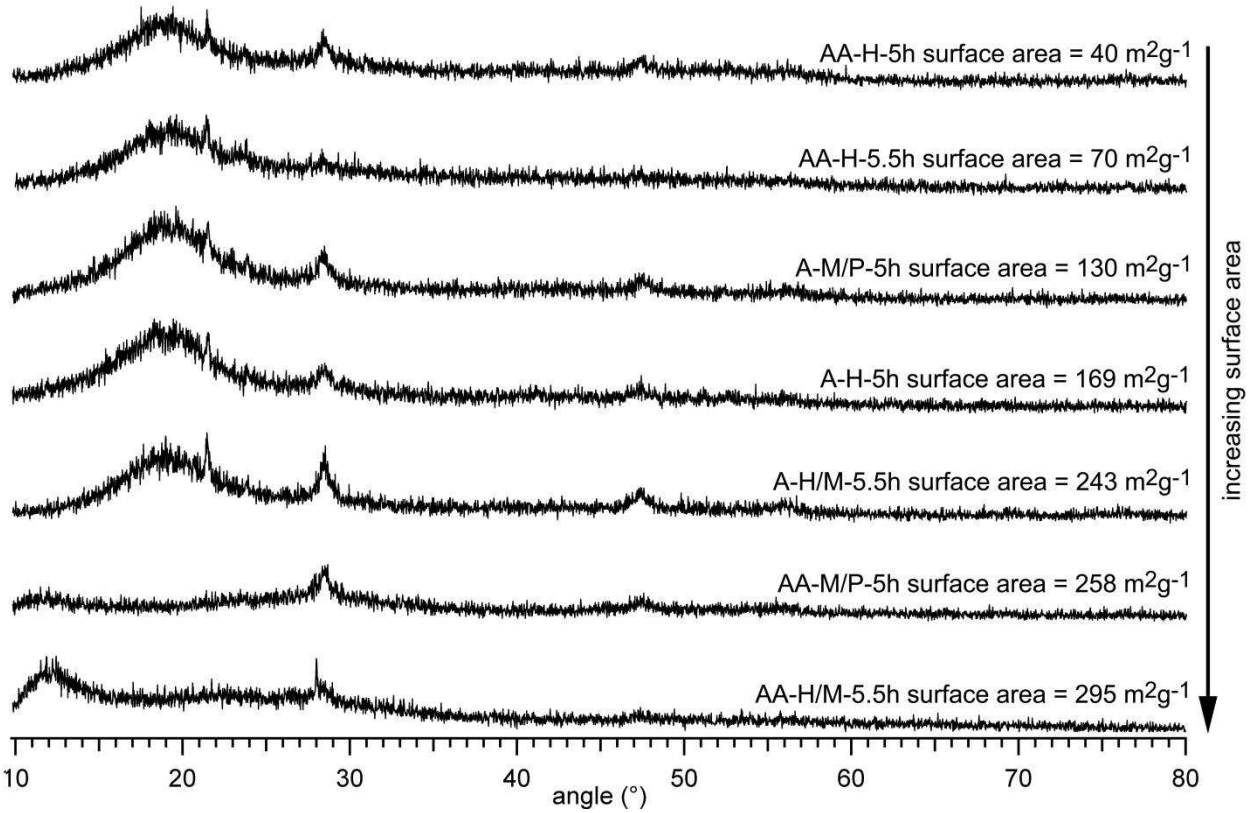

Figure 3.17. Anaerobic powder XRD of metallurgical silicon milled in dry, air-free heptane for 5–5.5 h. The AA-H/M-5.5h and AA-M/P-5h samples were exposed to air and spread on a thin film of high-vacuum grease; all other samples were mixed in Apiezon grease. Samples AA-H-5h, AA-H-5.5h, and AA-M/P-5h were treated rigorously anaerobic.

3.3.6. Comparing DLS Results With BET Surface Areas

For the 5 samples tested by DLS, the DLS particle size distribution measurements appear to be counter to the BET surface area measurements. This comparison is only valid if the assumption that the surface area can be directly correlated to particle size is valid (this assumption requires that the particles be non-porous, which appears to be the case for the samples inspected by TEM). Table 3.4 shows the results for samples measured by DLS, measured by BET surface area, calculated particle size based on BET specific surface area assuming solid spheres with monodisperse distribution, and the particle size range obtained by DLS in absolute ethanol. From Table 3.4 note the large disparity in calculated monodisperse particle size based on BET specific surface area and the mean DLS particle size for each sample, the DLS particle size is 3 to 23 times as large as the calculated size. These two methods for

deriving particle size do have a number of variables that could account for the observed differences.

Table 3.4. Estimated Particle Size from BET Surface Area Measurement Compared to DLS Particle Size

sample	BET surface area (m^2 g^{-1})	calculated particle size[a] (diameter nm)	DLS particle size[b] (mean, std dev nm)	estimated DLS particle[c] size range (nm)
AA-H-1h	44	58.5	235, 0.92	80-850
AA-H-5h	40	64.3	208, 1.58	70-900
AA-M/P-1h	75	34.3	224, 0.79	70-850
AA-M/P-5h	258	9.98	235, 3.71	75-550
A-H-5h	169	15.2	167, 1.13	65-550

[a] Particle size calculated assuming non-porous spheres with no size distribution. The particle size diameter was varied until the surface area was ± 0.1 m^2 g^{-1} of the measured surface area.
[b] DLS particle size mean was averaged from the three measurements using the Malvern software. The std. dev. is the standard deviation of the mean and was also calculated using the Malvern software.
[c] The estimated DLS particle size range is taken from the graph (Figure 3.17).

First, the calculated particle size based on BET specific surface area assumes the sample is comprised of spherical monodisperse particles, which is known to be untrue from SEM and TEM. In fact, SEM and TEM show thin plates of irregular shape which would have a much greater surface area to volume ratio compared to a sphere so small changes in actual particle size of thin irregular sheets would have a significant change in the surface area. Similarly, the calculations used to obtain particle size from the changes in scattering patterns in the DLS experiment assume spherical particles which, again, it is known these samples are not. Also, the samples were dispersed in ethanol which could be reacting with the reactive surface of the anaerobic samples or otherwise changing the surface potential of the samples causing agglomeration in the suspension and artificially increasing the particle size. Attempts to repeat the DLS measurement in air-free heptane resulted in unreliable data due to rapid particle settling, even at low concentrations. Based on the SEM and TEM images and the BET surface area

measurements it seems the DLS measurements in ethanol are not an accurate representation of the true particle size of these samples.

3.4. Conclusions

Stirred media mills can be used in a top-down approach method to produce irregularly shaped silicon nanoparticles. When milling silicon, the presence of surface passivating additives including oxygen or aromatic carbon containing species mitigates agglomeration and leads to a dramatic increase in specific surface area, and corresponding decrease in average particle size. Particle amorphization occurs rapidly in a stirred media mill, within two hours crystallite size is on the order of 2-50 nm regardless of whether surface passivating additives are present. Nascent silicon surfaces are sufficiently reactive to result in the formation of Si–C bonds even when milled in a relatively inert solvent such as heptane. Interestingly, when milled aerobically in either heptane or mesitylene the silicon still forms a significant amount of Si–C bonds as well as Si–O bonds, indicating selection of mill fluid and additives should be considered carefully and that when milling silicon, and likely all metalloids and metals, significant metal oxygen formation does occur without other surface passivation in stirred media mills. When milled anaerobically the silicon forms mostly Si–C bonds with very little Si–O and, due to the lack of surface passivation, the resulting material is highly reactive once dried to a solid in the absence of O_2/H_2O. The silicon milled anaerobically with aromatic additives is less reactive than silicon milled anaerobically in heptane, but does still exhibit some reactivity with residual O_2 in controlled experiments. Finally, the nascent silicon surface produced by this milling method was reactive with typically non-reactive solvents, any oxygen present, and aromatic additives; this empirically derived knowledge should be used as a guide when choosing milling conditions for producing silicon nanoparticles or any metal nanoparticle of an oxygen reactive metal with a particular particle size and chemically modified surface.

3.5. Experimental Details

3.5.1. General

The milling process and all subsequent manipulations of the anaerobic milled silicon took place in an N_2 or Ar atmosphere glovebox for anaerobic samples. The quality of the atmosphere (concentration of oxygen and solvent) was determined by the length of time an exposed 25 W tungsten filament light bulb stayed on in the glovebox.[56] The atmosphere was sufficiently pure to keep the light bulb on continuously for at least 24 h prior to any milling or handling of anaerobically milled silicon indicating combined concentrations of O_2 and H_2O at or below 5 ppm.[57] All milling operations were performed equally by the author and Mr. Eric V. Bukovsky and employed a continuous flow Netzsch MiniCer Laboratory stirred media mill with yttrium stabilized zirconium oxide lining, and Netzsch SiLi yttrium stabilized zirconium oxide milling media (0.3–0.4 mm). The grinding chamber (volume ca. 160 mL) with a cylindrical slotted mixer blade, a 150 μm separator screen, double mechanical seals separating the grinding tank from motor bearings by means of ca. 80 psi seal fluid, and an inline QSonica 700 W, 20 kHz sonicator with an 85 mL low-flow cell and a 1.27 cm diameter probe, was programmed to run periodically throughout the milling procedure for 3 min at 30% of peak amplitude in intervals every 10 min, see schematic and slurry flow direction in Figure 3.18.

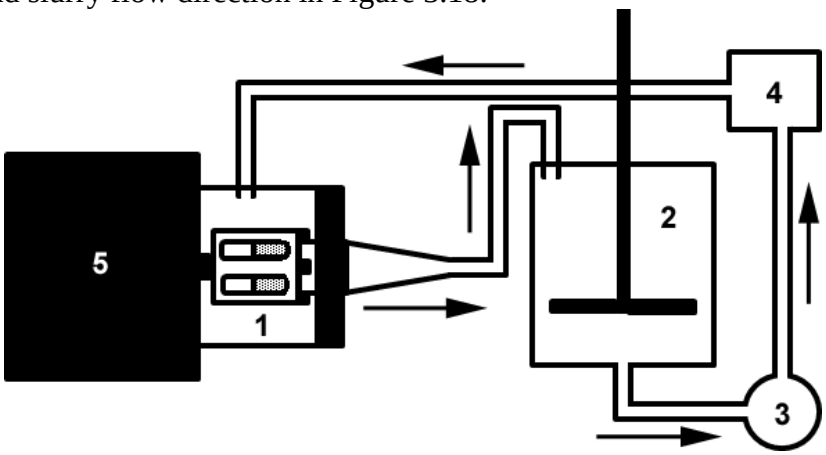

Figure 3.18. Schematic of Netzsch MiniCer Laboratory mill, arrows indicate direction of flow. 1) 160 mL water cooled milling chamber with double mechanical pressurized fluid seal, slotted cylinder mixer blade, 150 μm separator screen, 2) slurry tank with overhead mixer, samples and additives were added via slurry tank, 3) peristaltic slurry pump with 1/8” I.D. Viton® tubing, 4) low-flow sonicator cell with 1/2” diameter probe, 5) mill motor.

For anaerobically milled material the mill was adapted by Mr. Bukovsky and installed by the author, Mr. Bukovsky, and Mr. Brent M. Wyatt in an inert atmosphere glovebox requiring minor modifications to adapt; water cooling lines, inert gas pressure line, and 230 V electrical connections through the glovebox walls. The operation, function, and capabilities of the mill were otherwise unaffected by these adaptations. A Buchi RII rotary evaporator was also adapted for use in the same glovebox to remove solvent from milled samples, with the vacuum and solvent trap outside of glovebox. The heater bath was filled with Thomas Scientific dimethyl silicon fluid, SF96/50 (removed all volatiles at ca. 30×10^{-3} Torr for 48 h at 150 °C).

The MGS was obtained from Kratos LLC (Si = 98.9 ± 0.20%, major impurities Fe = 0.35 ± 0.30%, Al = 0.20 ± 0.15%, Ca = 0.12 ± 0.06%). Prior to milling, the silicon powder was hand ground in air with a mortar and pestle, and sieved to a size range of 45–90 μm.

3.5.2. Anaerobic Milling in Heptane

Dry, air-free heptane (Fisher, HPLC grade, submicron filtered) was prepared by refluxing over sodium metal for ca. 12 h, and then distilled under N_2. Except for sample AA-H/M-5.5h dry, air-free heptane was also used as the seal fluid in the Netzsch MiniCer mill. For sample AA-H/M-5.5h dry, air-free mesitylene was used as the seal fluid. The mill was charged with ca. 130 mL of 0.3–0.4 mm Netzsch SiLi beads. Once the mill was ramped up to 4104 rpm and the heptane was circulating, ground, sieved MGS powder (ca. 20 g) was added to the slurry tank over a 5 min period, followed by more heptane (ca. 150 mL). Once all MGS was added, the inline sonicator was started and continued until the end of the milling cycle. For the AA-H-1h and AA-H-2h experiment, after 1 h of milling, approximately half of the slurry material was removed from the mill by taking the outflow material till the slurry bucket was nearly empty, this produced sample AA-H-1h. An equal volume of dry, air-free heptane was added to the slurry bucket and the milling continued for an additional 1 h to make the AA-H-2h sample. The 2 h sample material was removed by taking the outflow material till the slurry bucket was nearly empty, adding dry, air-free heptane to the slurry tank, milling for 10 additional minutes, and then taking the outflow material until the slurry bucket was empty. Both of the second set of outflows

were collected and treated as the 2 h sample. These two slurries (1 h and 2 h) were collected in separate flasks and dried to a powder by rotary evaporation in the glovebox. A similar procedure was followed for milling, collecting and drying samples AA-H-3h and AA-H-4h. The AA-H-5h sample was milled, collected with two flushes of dry, air-free heptane, collected and dried as a single sample. After the samples were dried to a powder they were sealed in their respective flasks, removed from the glovebox and all volatiles were removed by vacuum ($<10^{-5}$ Torr) at 20 °C for ca. 15 h.

3.5.3. Anaerobic Milling in Mesitylene with Pyrene Additive

Dry, air-free mesitylene (Alfa Aesar, 98+%) was prepared by refluxing over sodium metal for ca. 12 h, and then distilled under N_2. Dry, air-free mesitylene was also used as the seal fluid in the Netzsch MiniCer mill. Pyrene (0.99 mmols, Alfa Aesar 98%, used as received) was mixed with ca. 460 mL of mesitylene for ca. 15 h in the glovebox. The mesitylene solution of pyrene was then added to the slurry tank following the same procedure described in the heptane milling experiments. Samples were removed following the heptane procedure as well, except with dry, air-free mesitylene to wash through the mill. Besides using a solution of pyrene in mesitylene all other milling parameters and handling procedures were the same as previously described. One batch was milled for 1 h, removed ca. half the slurry and the second portion was taken at 2 h (AA-M/P-1h and AA-M/P-2h respectively) and second batch was milled for 5 h, removed ca. half the slurry and the second portion was taken at 6 h (AA-M/P-5h and AA-M/P-6h respectively).

3.5.4. Aerobic Milling in Heptane

The aerobic milling of silicon took place outside of the glovebox using the same Netzsch MiniCer mill. Mesitylene was used as the seal fluid to mill sample A-H/M-5.5h. Heptane was used as the seal fluid to mill sample A-H-5h. The mill was operated as previously described with the following exceptions: heptane was used as received, rotary evaporation was performed outside the glovebox, powder XRD and BET samples were prepared in air, XPS sample films were transferred to the XPS sample chamber under aerobic conditions. The A-H/M-5.5h XPS

sample film was prepared in 1,2,3-trichloropropane (Alfa Aesar, 98+%) and the A-H-5h XPS sample film was prepared in heptane.

3.5.5. Aerobic Milling in Mesitylene with Pyrene Additive

The aerobic milling of silicon took place outside of the glovebox using the same Netzsch MiniCer mill and produced samples A-M/P-5h and A-M/P-6h. The mill was operated as previously described with the following exceptions: mesitylene was used as received, rotary evaporation was performed outside the glovebox, powder XRD and BET samples were prepared in air, XPS sample film was prepared in 1,2,3-trichloropropane and transferred to the XPS sample chamber under aerobic conditions.

3.5.6. BET

One method to probe particle size is to perform Brunauer, Emmett, and Teller specific surface area analysis (BET).[58] The sample is placed under vacuum and cooled to liquid nitrogen temperatures. The sample is then exposed to N_2 gas which adsorbs to the surface and the sample is allowed to equilibrate. From the difference in the starting pressure and equilibrium pressure, the number of moles of nitrogen adsorbed can be calculated. This process is repeated multiple times to create a trend which is evaluated by linear regression to determine the volume of a monolayer of adsorbed gas. From this volume, Avogadro's number, the cross-sectional area of the adsorbate gas, the molar volume of the gas, and the mass of the sample the specific surface area is calculated. The specific surface area can then be used to determine average particle size using the material density and assuming the particles are spherical and non-porous. Even for non-spherical particles, smaller particles will have large BET specific surface areas and as particle size increases BET specific surface area decreases. Therefore, even if it is known that the particles are non-spherical, BET analysis provides an assessment of relative particle sizes.

Anaerobic specific surface area analysis was performed via the BET method[58] by the author, Mr. Bukovsky, or Mr. Wyatt using specially designed air-free "pear-shaped" flasks. The flasks had narrow necks minimizing the volume of gas exposed to a gradient temperature (i.e. temperature change going from room temperature to liquid N_2 temperature). This method of BET

analysis required a two temperature measurement of the final pressure in the flask. The gas used was N_2 (Airgas, UHP, 99.999%) and the sample was cooled to liquid N_2 temperatures. The silicon sample was added to the flask in a glovebox and then further dried by vacuum (< 10^{-5} Torr) at 20 °C for at least 16 h. Samples were ca. 1.00 g in mass, and the sample volume was corrected for in the final pressure measurement. The data was plotted as $P_{eq}/n(P_0\text{-}P_{eq})$ vs. P_{eq}/P_0 and fit to a linear equation where the slope, intercept, and the moles of N_2 required to form a monolayer was calculated,[58] and the specific surface area was determined using a surface area for N_2 of 1.62×10^{-19} m^2 $molecule^{-1}$.[59] At least 5 nitrogen additions were performed per sample, more additions were performed when required to keep the P_{eq}/P_0 in the linear range of 0.05–0.30.[58] In all cases the linear fit through the 5 or more data points had a $r^2 > 0.999$.

3.5.7. H_2O and O_2 Gas Uptake Experiments

For oxygen uptake experiments industrial grade O_2 (Airgas, 99.5%) was used as received and these experiments were performed by Mr. Bukovsky and Dr. Steven H. Strauss. For water uptake experiments distilled deionized water (Barnstead Nanopure filtration and deionizer system, final resistance greater than 18 MΩ) was freeze, pump, thaw, degassed three times to remove any dissolved gases and the experiment was performed by Mr. Bukovsky. A fresh sample of milled, dried MGS was transferred to an air-free test tube in an N_2 or argon-filled glovebox and attached to a glass manifold with a #9 o-ring joint. Keeping the sample rigorously anaerobic all volatiles were again removed by vacuum, < 10^{-5} Torr for ca. 12 h. The sample was then exposed to measured doses of O_2 or H_2O. In the case of H_2O experiments, the H_2O was held isothermally at a temperature of 19 °C, just below room temperature to ensure no water vapor would condense in the air-free sample tube leading to erroneous mass changes.

3.5.8. Powder XRD

A powder is placed in the X-ray beam and the detector moves over a range of angles, collecting the intensity of the diffracted electrons as a function of the angle. Peaks occur when the lattice planes of crystalline regions diffract X-rays at the detection angle. When examining a material, the intensity and position of the peaks can be compared to known materials since the

combination of these two is unique to a particular phase of a material. A completely amorphous sample will not diffract electrons and will therefore produce a flat line pattern. Larger crystallites diffract more and produce more intense peaks. As crystallite size decreases peaks become shorter and broader.

Data were collected by Mr. Bukovsky on a Scintag X-2 powder X-ray diffractometer, with Cu Kα radiation (λ = 0.154 nm) at 40 mA and 45 kV, a tube divergent slit width of 2 mm, and a tube scatter slit width of 4 mm. The instrument is equipped with a Pelteir detector with a scatter slit width of 0.5 mm and a reference slit width of 0.2 mm. The experimental setup was a standard Bragg-Brentano geometry with a stationary sample stage. Each sample was scanned from 5° – 90° or 10° – 80° in 0.02° step increments with 1.00 s collection time per step. Samples that were aerobic were sprinkled onto a thin film of high vacuum silicon grease applied to a standard glass microscope slide or mixed in mortar and pestle with Apiezon Type N grease in air and spread as a paste to a standard microscope slide.

3.5.9. Air-free Powder XRD

Instrument and experimental set up were the same as previously described and were performed by Mr. Bukovsky. Samples were prepared by grinding/mixing a weighed sample of the milled MGS in a weighed amount of Apiezon Type N grease in a N_2 or argon filled glovebox. All milled MGS samples were 0.106 ± 0.008 g and all amounts of Apiezon Type N grease were 0.260 ± 0.007 g. The mixture of milled MGS powder and grease was ground in a clean, dry agate mortar and pestle inside the glovebox until a smooth brown paste formed. The paste was then removed from the glovebox and spread as a film covering ca. the middle half of the surface area on a standard glass microscope slide.

3.5.10. TEM

Transmission electron microscopy was performed by Mr. Bukovsky with the assistance of Dr. Roy Geiss on a JEOL JEM-2100F field emission transmission electron microscope. Samples were dispersed in ethanol (Pharmco-AAPER, 200 proof, ACS/USP grade) or isopropyl alcohol (Fisher, 99.999%) in air with a bath sonicator for ca. 10 min. The dispersion settled for ca. 1 min

then the solution was added drop-wise to TEM grids (Ted Pella, part #01840, pure carbon on 200 mesh Cu), and allowed to dry in air for ca. 10 min. The grids with samples were then attached to a double tilt holder and subjected to ca. 10^{-3} Torr vacuum until the pressure equilibrated (indicating little to no residual alcohol remained). Samples were imaged at 200 keV, images were captured and manipulated with Gatan Microscopy Suite, Version 2.31.734.0. To simplify crystalline region and crystallite size analysis most TEM images were collected in darkfield view with the beam at an arbitrary angle and then rotated 90° from the initial angle.

3.5.11. SEM

Scanning electron microscopy was performed by Mr. Bukovsky with the assistance of Dr. Geiss on a JEOL JSM-6500F field emission scanning electron microscope. Samples were dispersed in ethanol (Pharmco-AAPER, 200 proof, ACS/USP grade) or isopropyl alcohol (Fisher, 99.999%) in air with a bath sonicator for ca. 10 min. The dispersion settled for ca. 1 min then the solution was added drop-wise to TEM grids (Ted Pella, part #01840, pure carbon on 200 mesh Cu), and allowed to dry in air for ca. 10 min.

3.5.12. XPS

X-ray photoelectron spectroscopy (XPS) is used to examine the binding environments of atoms in a sample and was pioneered by Kai Siegbahn and co-workers.[60] It is related to the photoelectron spectroscopy that was described in an earlier chapter for measuring electron affinities, but uses X-rays to eject electrons because the binding energies of core electrons are higher than the binding energy of an extra electron. Samples are typically prepared as a film and placed into the analysis chamber, which is under high vacuum (< ca. 10^{-8} Torr). X-rays irradiate the surface of the sample and as they interact with atoms electrons are ejected. Emitted electrons are collected by either an electrostatic or a magnetic lens system. In the extraction lenses the electron energy is retarded to a specific energy, set by the user, known as the pass energy. Using a pass energy allows uniform energy resolution across the entire spectrum. Only electrons with the specified pass energy are sent into the concentric hemispherical analyzer which controls the path of electrons by setting negative potentials on the two hemispheres thereby directing

electrons around the hemisphere to the multichannel plate. The spectrum is scanned by varying the electric fields in the extraction lenses to retard electrons with differing initial kinetic energies. The binding energy of the detected electron is determined by subtracting the kinetic energy of the electron and the work function of the spectrometer from the X-ray source energy.

The binding energy of the electrons depends on the element, the orbital, and what other atoms are bound to the atom of interest. Electrons in atoms bound to other atoms with higher electronegativity will exhibit higher binding energies. Spin-orbit splitting is observed when electrons can have different angular momentum values (j), i.e., p, d, and f orbitals, and leads to two peaks in the spectrum. The observed spectrum is fit with peaks for the different binding environments likely present in the sample. XPS is considered a surface analytical technique, because only electrons which are able to escape the material detected. The depth of analysis is dependent on the inelastic mean free path of the ejected electron which, in turn, is dependent on the material being analyzed, but typically on the order of 10 nm or less.

X-ray photoelectron spectroscopy (XPS) experiments were performed by the author on a PHI-5800 system using a monochromatic Al Kα X-ray source. A takeoff angle of 45° was used for all analyses and an electron neutralizer set to 5 μA for anaerobic samples and 35 μA for aerobic samples was used to partially offset sample charging. High resolution spectra were collected using 0.1 eV/step, 100 ms/step, 23.50 eV pass energy, and a spot size of 0.8 × 2 mm. CasaXPS Version 2.3.16 was used to analyze all data. Silicon and carbon spectra were fit with a Tougaard background and oxygen spectra were fit with a Shirley background, using an average width of 5 and 70% Gaussian 30% Lorentzian peak shapes for all elements. After fitting the C 1s spectrum, all peaks were shifted by setting the C–C/C−H peak to 285.0 eV[46,48] to charge correct all binding energies. The metallic silicon Si^0 environment was fit with both $2p_{1/2}$ and $2p_{3/2}$ peaks, the other Si environments were fit with single peaks.

Anaerobic samples were loaded onto the sample holder in a N_2 or argon-atmosphere glovebox and transferred into either a transfer bag or a glass jar. When using a transfer bag, the bag was opened over the flush of nitrogen exiting the sample introduction chamber and the

sample holder transferred into the instrument and started under vacuum as quickly as possible, typically within 30 seconds. When using the glass jar with a plastic lid and the seam covered in parafilm, the glass jar was opened under a flush of argon and the sample holder transferred into the instrument under a flush of argon and then immediately started under vacuum. For samples that were sputtered to remove surface hydrocarbon contamination, an argon-ion gun within the XPS operated at 2 kV for 0.1 min was used.

3.5.13. DLS

Dynamic light scattering was performed by Mr. Bukovsky on a Malvern Zetasizer Nano ZS with a 633 nm laser source operating in backscatter mode with a source detector angle of 173°. Samples were dispersed in ethanol (Pharmco-AAPER, 200 proof, ACS/USP) by breaking up clumps in an agate mortar and pestle and then further dispersion with sonication for 10-15 min in a bath sonicator. Samples were diluted until a quality experiment was achieved. Samples were tested in 1.5 mL PMMA ISO 9001-14001 Certified, disposable cuvettes (GMBH, Cat. No. 759085D) at 25 °C and were held isothermally at 25 °C for 2 min prior to the experiment. For each sample 3 measurements of 12-15 runs per measurement were utilized (number of runs depending on sample concentration, determined by instrument for each sample).

CHAPTER 3 REFERENCES

(1) Balaz, P.: High-Energy Milling. In *Mechanochemistry in Nanoscience and Minerals Engineering*; Springer-Verlag Berlin Heidelberg, 2008; pp 413.

(2) Balaz, P.; Achimovicova, M.; Balaz, M.; Billik, P.; Cherkezova-Zheleva, Z.; Criado, J. M.; Delogu, F.; Dutkova, E.; Gaffet, E.; Gotor, F. J.; Kumar, R.; Mitov, I.; Rojac, T.; Senna, M.; Streletskii, A.; Wieczorek-Ciurowa, K.: Hallmarks of mechanochemistry: from nanoparticles to technology. *Chem. Soc. Rev.* **2013**, *42*, 7571-7637.

(3) Castro, C. L., Mitchell, B. S.: Nanoparticles from Mechanical Attrition. In *Synthesis, Functionallization and Surface Treatment of Nanoparticles*; Baraton, M. I., Ed.; Americn Scientific Publishers, 2002; pp 450.

(4) McMahon, B. W.; Perez, J. P. L.; Yu, J.; Boatz, J. A.; Anderson, S. L.: Synthesis of Nanoparticles from Malleable and Ductile Metals Using Powder-Free, Reactant-Assisted Mechanical Attrition. *ACS Appl. Mater. Interfaces* **2014**, *6*, 19579-19591.

(5) Xing, T.; Sunarso, J.; Yang, W.; Yin, Y.; Glushenkov, A. M.; Li, L. H.; Howlett, P. C.; Chen, Y.: Ball milling: a green mechanochemical approach for synthesis of nitrogen doped carbon nanoparticles. *Nanoscale* **2013**, *5*, 7970-7976.

(6) Kim, H. S.; Hong, S. J.: Microstructure and Thermoelectric Properties of N-type 95%Bi_2Te_3-5%Bi_2Se_3 compound Prepared by High Energy Milling and Hot Extrusion. *Current Nanosci.* **2014**, *10*, 118-122.

(7) Akdogan, N. G.; Hadjipanayis, G. C.; Sellmyer, D. J.: Anisotropic Sm-(Co,Fe) nanoparticles by surfactant-assisted ball milling. *J. Appl. Phys.* **2009**, *105*, 07A710.

(8) Monteiro, A.; Afolabi, A.; Bilgili, E.: Continuous production of drug nanoparticle suspensions via wet stirred media milling: a fresh look at the Rehbinder effect. *Drug Devel. Industrial Pharm.* **2013**, *39*, 266-283.

(9) Kwon, S. G.; Hyeon, T.: Formation Mechanisms of Uniform Nanocrystals via Hot-Injection and Heat-Up Methods. *Small* **2011**, *7*, 2685-2702.

(10) Ghorpade, U.; Suryawanshi, M.; Shin, S. W.; Gurav, K.; Patil, P.; Pawar, S.; Hong, C. W.; Kim, J. H.; Kolekar, S.: Towards environmentally benign approaches for the synthesis of CZTSSe nanocrystals by a hot injection method: a status review. *Chem. Comm.* **2014**, *50*, 11258-11273.

(11) Williams, J. V.; Kotov, N. A.; Savage, P. E.: A Rapid Hot-Injection Method for the Improved Hydrothermal Synthesis of CdSe Nanoparticles. *Indust. Eng. Chem. Res.* **2009**, *48*, 4316-4321.

(12) Kim, H. S.; Hong, S. J.: Microstructure and Thermoelectric Properties of N-type 95%Bi_2Te_3-5%Bi_2Se_3 compound PRepared by High Energy Milling and Hot Extrusion. *Current Nanoscience* **2014**, *10*, 118-122.

(13) Jankovic, A.: Variables affecting the fine grinding of minerals using stirred mills. *Minerals Eng.* **2003**, *16*, 337-345.

(14) Stenger, F.; Mende, S.; Schwedes, J.; Peukert, W.: Nanomilling in stirred media mills. *Chem. Eng. Sci.* **2005**, *60*, 4557-4565.

(15) Suryanarayana, C.: Mechanical alloying and milling. *Prog. Mater. Sci.* **2001**, *46*, 1-184.

(16) Mende, S.; Stenger, F.; Peukert, W.; Schwedes, J.: Mechanical production and stabilization of submicron particles in stirred media mills. *Powder Technol.* **2003**, *132*, 64-73.

(17) Peukert, W.; Schwarzer, H.-C.; Stenger, F.: Control of aggregation in production and handling of nanoparticles. *Chem. Eng. Processing: Process Intensification* **2005**, *44*, 245-252.

(18) Sommer, M.; Stenger, F.; Peukert, W.; Wagner, N. J.: Agglomeration and breakage of nanoparticles in stirred media mills—a comparison of different methods and models. *Chem. Eng. Sci.* **2006**, *61*, 135-148.

(19) Pourghahramani, P.; Altin, E.; Mallembakam, M. R.; Peukert, W.; Forssberg, E.: Microstructural characterization of hematite during wet and dry millings using Rietveld and XRD line profile analyses. *Powder Technol.* **2008**, *186*, 9-21.

(20) Knieke, C.; Sommer, M.; Peukert, W.: Identifying the apparent and true grinding limit. *Powder Technol.* **2009**, *195*, 25-30.

(21) Knieke, C.; Berger, A.; Voigt, M.; Taylor, R. N. K.; Röhrl, J.; Peukert, W.: Scalable production of graphene sheets by mechanical delamination. *Carbon* **2010**, *48*, 3196-3204.

(22) Knieke, C.; Steinborn, C.; Romeis, S.; Peukert, W.; Breitung-Faes, S.; Kwade, A.: Nanoparticle Production with Stirred-Media Mills: Opportunities and Limits. *Chem. Eng. Technol.* **2010**, *33*, 1401-1411.

(23) Knieke, C.; Romeis, S.; Peukert, W.: Influence of process parameters on breakage kinetics and grinding limit at the nanoscale. *AIChE Journal* **2011**, *57*, 1751-1758.

(24) Pradeep, P. R.; Pitchumani, B.: Effect of operating variables on the production of nanoparticles by stirred media milling. *Asia-Pacific J. Chem. Eng.* **2011**, *6*, 154-162.

(25) Kirby, B. J.: *Micro- and Nanoscale Fluid Mechanics. Transport in Microfluidic Devices*; First Edition ed.; Cambridge University Press, 2010.

(26) Nic, M. J., J.; Kosata, B.; Updates by Jenkins, A.: Electrochemical Potential. In *IUPAC. Compendium of Chemical Terminology, 2nd ed. (the "Gold Book"), XML on-line corrected version: http://goldbook.iupac.org (2006-)* McNaught, A. D. W., A., Ed.; Blackwell Scientific Publications, Oxford

(27) Larryisgood: Diagram of zeta potential and slipping planeV2. Wikimedia Commons: Online, 2015.

(28) Butyagin, P. Y.; Streletskii, A. N.; Berestetskaya, I. V.; Borunova, A. B.: Amorphization of Silicon during Mechanical Treatment of Its Powders: 3. Sorption of Gases. *Colloid J.* **2001**, *63*, 639-644.

(29) Van Devener, B.; Anderson, S. L.: Breakdown and Combustion of JP-10 Fuel Catalyzed by Nanoparticulate CeO_2 and Fe_2O_3. *Energy & Fuels* **2006**, *20*, 1886-1894.

(30) Van Devener, B.; Perez, J. P. L.; Jankovich, J.; Anderson, S. L.: Oxide-Free, Catalyst-Coated, Fuel-Soluble, Air-Stable Boron Nanopowder as Combined Combustion Catalyst and High Energy Density Fuel. *Energy & Fuels* **2009**, *23*, 6111-6120.

(31) Gan, Y.; Qiao, L.: Combustion characteristics of fuel droplets with addition of nano and micron-sized aluminum particles. *Combust. Flame* **2011**, *158*, 354-368.

(32) Tyagi, H.; Phelan, P. E.; Prasher, R.; Peck, R.; Lee, T.; Pacheco, J. R.; Arentzen, P.: Increased Hot-Plate Ignition Probability for Nanoparticle-Laden Diesel Fuel. *Nano Lett.* **2008**, *8*, 1410-1416.

(33) Beloni, E.; Hoffmann, V. K.; Dreizin, E. L.: Combustion of Decane-Based Slurries with Metallic Fuel Additives. *J. Propul. Power* **2008**, *24*, 1403-1411.

(34) Suryanarayana, C.; Ivanov, E.; Boldyrev, V. V.: The science and technology of mechanical alloying. *Mater. Sci. Eng.: A* **2001**, *304–306*, 151-158.

(35) Zhang, D. L.: Processing of advanced materials using high-energy mechanical milling. *Prog. Mater. Sci.* **2004**, *49*, 537-560.

(36) Heintz, A. S.; Fink, M. J.; Mitchell, B. S.: Mechanochemical Synthesis of Blue Luminescent Alkyl/Alkenyl-Passivated Silicon Nanoparticles. *Adv. Mater.* **2007**, *19*, 3984-3988.

(37) Heintz, A. S.; Fink, M. J.; Mitchell, B. S.: Silicon nanoparticles with chemically tailored surfaces. *Appl. Organometallic Chem.* **2010**, *24*, 236-240.

(38) Shen, T. D.; Shmagin, I.; Koch, C. C.; Kolbas, R. M.; Fahmy, Y.; Bergman, L.; Nemanich, R. J.; McClure, M. T.; Sitar, Z.; Quan, M. X.: Photoluminescence from mechanically milled Si and SiO_2 powders. *Phys. Rev. B* **1997**, *55*, 7615-7623.

(39) Barr, T. L.; Seal, S.: Nature of the use of adventitious carbon as a binding energy standard. *J. Vac. Sci. Technol.* **1995**, *13*, 1239-1246.

(40) Chockla, A. M.; Harris, J. T.; Akhavan, V. A.; Bogart, T. D.; Holmberg, V. C.; Steinhagen, C.; Mullins, C. B.; Stevenson, K. J.; Korgel, B. A.: Silicon nanowire fabric as a lithium ion battery electrode material. *J. Am. Chem. Soc.* **2011**, *133*, 20914-20921.

(41) Wheeler, D.; Pepper, S.: Angle-resolved X-ray photoelectron spectroscopy of epitaxially grown (100) β-SiC to 1300 °C. *Surf. Interface Anal.* **1987**, *10*, 153-162.

(42) Nguyen, T.; Lefrant, S.: XPS study of SiO thin films and SiO-metal interfaces. *J. Phys.: Condens. Matter* **1989**, *1*, 5197.

(43) Jaksa, G.; Stefane, B.; Kovac, J.: XPS and AFM characterization of aminosilanes with different numbers of bonding sites on a silicon wafer. *Surf. Interface Anal.* **2013**, *45*, 1709-1713.

(44) Shirahata, N.; Yonezawa, T.; Seo, W.-S.; Koumoto, K.: Photoinduced cleavage of alkyl monolayers on Si. *Langmuir* **2004**, *20*, 1517-20.

(45) Seal, S.; Krezoski, S.; Petering, D.; Barr, T. L.: Surface modification of silicon and silica in biological environment: an X-ray photoelectron spectroscopy study. *Appl. Surf. Sci.* **2001**, *173*, 339-351.

(46) Radvanyi, E.; De Vito, E.; Porcher, W.; Jouanneau Si Larbi, S.: An XPS/AES comparative study of the surface behaviour of nano-silicon anodes for Li-ion batteries. *J. Anal. Atomic Spec.* **2014**, *29*, 1120-1131.

(47) Philippe, B.; Dedryvere, R.; Gorgoi, M.; Rensmo, H.; Gonbeau, D.; Edstrom, K.: Role of the $LiPF_6$ Salt for the Long-Term Stability of Silicon Electrodes in Li-Ion Batteries - A Photoelectron Spectroscopy Study. *Chem. Mater.* **2013**, *25*, 394-404.

(48) Nie, M. Y.; Abraham, D. P.; Chen, Y. J.; Bose, A.; Lucht, B. L.: Silicon Solid Electrolyte Interphase (SEI) of Lithium Ion Battery Characterized by Microscopy and Spectroscopy. *J. Phys. Chem. C* **2013**, *117*, 13403-13412.

(49) Önneby, C.; Pantano, C. G.: Silicon oxycarbide formation on SiC surfaces and at the SiC/SiO_2 interface. *J. Vac. Sci. Technol. A* **1997**, *15*, 1597-1602.

(50) Miyoshi, K.; Buckley, D. H.: XPS, AES and friction studies of single-crystal silicon carbide. *Appl. Surf. Sci.* **1982**, *10*, 357-376.

(51) Smith, G. B.; McKenzie, D. R.; Martin, P. J.: An XPS study of chemical order in hydrogenated amorphous silicon-carbon alloy films. *Phys. Status Solidi B* **1989**, *152*, 475-480.

(52) Shen, T. D.; Koch, C. C.; McCormick, T. L.; Nemanich, R. J.; Huang, J. Y.; Huang, J. G.: The structure and property characteristics of amorphous/nanocrystalline silicon produced by ball milling. *J. Mater. Res.* **1995**, *10*, 139-148.

(53) Harikumar, K. R.; Polanyi, J. C.; Zabet-Khosousi, A.: A new strongly-bound chemisorption structure of benzene on Si(100). *Surface Sci.* **2012**, *606*, 1431-1434.

(54) Heintz, A. S.: A Mechanochemical Method for the Synthesis of Passivated Silicon Nanoparticles. Tulane Univeristy, 2008.
(55) Shaw, L. L.; Yang, Z.; Ren, R.: Mechanically Enhanced Reactivity of Silicon for the Formation of Silicon Nitride Composites. *J. Am. Ceramic Soc.* **1998**, *81*, 760-764.
(56) Eubanks, I. D.; Abbott, F. J.: Gas purification and pressure control system for inert atmosphere boxes. *Anal. Chem.* **1969**, *41*, 1708-1709.
(57) Shriver, D. F.: *The manipulation of air-sensitive compounds*; Wiley: New York, 1986.
(58) Brunauer, S.; Emmett, P. H.; Teller, E.: Adsorption of Gases in Multimolecular Layers. *J. Am. Chem. Soc.* **1938**, *60*, 309-319.
(59) Emmett, P. H.; Brunauer, S.: The Use of Low Temperature van der Waals Adsorption Isotherms in Determining the Surface Area of Iron Synthetic Ammonia Catalysts. *J. Am. Chem. Soc.* **1937**, *59*, 1553-1564.
(60) Siegbahn, K.: *ESCA; atomic, molecular and solid state structure studied by means of electron spectroscopy*; Almqvist & Wiksells, 1967; Vol. 20.

SUMMARY/CONCLUSIONS AND FUTURE CONSIDERATIONS

Summary/Conclusions

Three different classes of molecules/materials have been characterized in this dissertation. This work explored the ability to tune properties by altering either the molecular structure or the synthetic conditions. Careful study and analysis allows for conclusions to be drawn about what effects different changes have on the properties of interest.

In Chapter 1, a selection of fluorescent $C_{70}(CF_3)_n$ (n = 8 or 10) molecules were studied to determine the effect that addition pattern had on the photophysical properties. Since these molecules all had the same substituents any substituent effects could be ruled out. Additionally, pairs of molecules differed in the placement of a single trifluoromethyl group so the remaining pi systems were very similar. Through experimental and theoretical studies it has been determined that high fluorescence quantum yields are correlated with high oscillator strength, large Δ_{S1-T1} energy gaps, and smaller spatial extension of the $S_0 \rightarrow S_1$ excitation. Similarities in the fluorescence and singlet oxygen quantum yields for two compounds, **70-8-1** and $C_{70}Ph_8$, with the same addition pattern, but different substituents leads to the conclusion that the addition pattern and not the identity of the substituents affects the photophysical properties of fullerenes.

In Chapter 2, the effect of molecular shape on product distributions, the electrochemical properties of $PAH(CF_3)_n$ compounds, and the effects of donor or acceptor choice on CTCs were explored. In general, based on the selection of PAH cores studied in this work, when cores with 8–10 substitutable carbons are reacted with at least 10 equivalents of CF_3I the $PAH(CF_3)_n$ products will mostly have a range of n = 4–6. This synthetic technique worked equally well for the heterocyclic compound PHNZ. The addition of electron-withdrawing CF_3 groups to PAHs results in a regular, incremental increase in both the $E_{1/2}$ and EA as a function of the number of CF_3 groups. For a broad selection of PAH and $PAH(CF_3)_n$ compounds the relationship between reduction potentials and EAs is 0.74 V eV^{-1}. When $PAH(CF_3)_n$ compounds are mixed with

PAHs, CTCs can form and the energy of the CT band in solution is closely approximated by the difference in solution oxidation/reduction potentials of the donor and acceptor.

In Chapter 3 the first example of adapting a stirred media mill to operate in an inert atmosphere glovebox is presented. When milling silicon, the presence of surface passivating additives including oxygen or aromatic carbon containing species mitigates agglomeration and leads to a dramatic increase in specific surface area, and corresponding decrease in average particle size. Nascent silicon surfaces are sufficiently reactive to result in the formation of Si–C bonds even when milled in a relatively inert solvent such as heptane. After milling anaerobically in heptane the resulting silicon nanoparticles are very reactive with oxygen resulting in the production of sparks upon exposure to ambient air. Silicon milled in mesitylene and pyrene forms nearly the same amount of Si–C bonds whether it is milled aerobically or anaerobically.

Future Considerations

TMFs that exhibit high fluorescence quantum yields could have their electroluminescence quantum yields measured to determine whether they are suitable for use in organic light emitting diodes. TD-DFT can be used to calculate oscillator strengths and Δ_{S1-T1} energy gaps to search for new promising fullerene fluorophores. Additional study is needed to explain the reason that **70-8-1** has low fluorescence and singlet oxygen quantum yields while **70-8-2** exhibits relatively high fluorescence and singlet oxygen quantum yields. Preliminary experiments have demonstrated the proof of concept for using fullerene derivatives as leaf imaging agents, however, the solution was made at the limit of solubility for **70-10-2** in perfluorodecalin. Future leaf imaging experiments would be improved by using a molecule with either higher solubility or a higher fluorescence quantum yield. Theoretically higher solubility could be achieved with longer perfluoroalkyl chain length so it is recommended to target the synthesis of molecules with the same addition pattern as fluorescent TMFs, but longer perfluoroalkyl chain length. TMFs with high singlet oxygen quantum yields could be investigated for use as photodynamic therapy agents or photodisinfection.

To further understand the effect of five-membered rings on product composition in PAH$(CF_3)_n$ compounds, reactions of FLUR and FLRA with CF_3I should be performed with at least 10 equivalents of CF_3I gas. It is hypothesized that this will result in narrower product distributions and higher *n* value products. In instances where separation has largely been unsuccessful the use of methanol as the mobile phase will likely lead to increased interaction with the stationary phase and may then result in improved separation and the isolation of new, pure compounds. Measuring the gas-phase EA of FLRA-3-1, FLRA-3-2, PHEN-4-1, and PHEN-4-2 will further elucidate the relationship between reduction potential and EA for isomers where the reduction potential is significantly different. PHNZ$(CF_3)_n$ compounds where $n < 4$ could be tried in reactions to produce organometallic complexes. Different solvents could be used to crystallize CTCs to determine whether the crystallizing solvent or the intermolecular interactions play a more important role in solid-state stoichiometry.

Milling experiments with other metals or metalloids could be completed to determine whether the effects noted here are similar for other materials. The most enlightening experiment would be to determine the identity of the carbon species on the surface of the nanoparticles, but a method do to this has not yet been found. Pyrene in mesitylene was selected on the hypothesis that pyrene would selectively bind to the surface because of the steric hindrance for silicon to bind to mesitylene. To check whether the addition of pyrene results in more Si–C bond formation than mesitylene alone, milling experiments could be conducted with pure mesitylene as the mill fluid.